Structural Health Monitoring of Composite Structures: Low-Velocity Impact Localisation and Force Reconstruction

By

Dong Xiao

Thesis submitted in part fulfilment of the requirements for the degree of Doctor of Philosophy of Imperial College London

Department of Aeronautics
Faculty of Engineering
Imperial College London
2025

Declaration of Originality

I hereby confirm that the work presented in this thesis is my own. All else is appropriately referenced.

Copyright Declaration

Acknowledgements

Completing this Ph.D. has been a transformative journey filled with challenges, discoveries, and moments of introspection. It has shaped not only my academic perspective but also my understanding of resilience, gratitude, and the connections that make this journey meaningful. As I reflect on the path that brought me here, I am overwhelmed by the support, guidance, and encouragement I have received from many remarkable individuals.

First and foremost, I would like to extend my sincerest gratitude to my supervisors, Professor Zahra Sharif-Khodaei and Professor M.H. Aliabadi. Your mentorship has been the cornerstone of this journey. Your expertise, patience, and guidance have not only shaped the trajectory of my research but also influenced my approach to critical thinking and problem-solving. Thank you for your trust in my abilities and for challenging me to push the boundaries of my work. I am profoundly thankful for the countless discussions, constructive feedback, and unwavering support you have provided.

I would also like to thank not only the members of our research group but also my friends across the college—especially those I had the pleasure of sharing an office with—for their friendship, support, and shared moments throughout this journey. I am especially grateful to Feifei, Yingwu, Aldy, Francisco, Yuhang, Mengke, Fatih, Massimiliano, Haolin, Ilias, Samet, Valentin, Sina, Tongrui, Hongmin, Tafara, Ali, Haomiao, Guangxiao, Junjie, Kelly, and Elif. Your encouragement, insightful conversations, and daily companionship have made this experience not only intellectually rewarding but also genuinely enjoyable. The laughter, late-night discussions, and mutual support turned our workspaces into places of learning, inspiration, and lasting connection. It has been a true privilege to share this time with such an incredible group of friends.

I am deeply grateful to Imperial College London and the China Scholarship Council (CSC) for their generous financial support through the CSC–Imperial Scholarship (Grant No. [2021]339).

This joint scholarship provided me with an invaluable opportunity to pursue my doctoral studies in a world-leading research environment. Without their support, this academic journey would not have been possible.

To my parents, I owe everything. Your unwavering love, sacrifices, and belief in my potential have been the foundation of my life. Despite the challenges you have faced, you always prioritised my education and instilled in me the values of perseverance and integrity. I am forever indebted to your enduring support and strength.

To my extended family and the community that surrounded me in my early years, particularly my grandparents, I would like to express my gratitude for the profound influence your collective spirit and values have had on my outlook on life. You taught me resilience, humility, and the importance of relationships—lessons that have guided me through every stage of this journey.

Finally, I would like to express my gratitude to everyone who has supported me directly or indirectly. Each of you has played a part in shaping my academic and personal growth. This thesis is not just a product of my efforts but a reflection of the care, encouragement, and inspiration I have received from so many along the way.

As I conclude this chapter of my life, I am reminded of Shakespeare's timeless question: "To be, or not to be." For me, the answer lies in embracing the journey, valuing the relationships that give life its meaning, and striving to contribute positively to the world. To all who have walked this path with me, I am forever grateful.

Abstract

This thesis addresses key challenges in structural health monitoring (SHM) of composite structures using passive sensing, with a particular focus on solving the inverse problem of impact identification. It develops a comprehensive framework for robust, efficient, interpretable, and scalable methodologies for impact localisation and force reconstruction, integrating structural dynamics analysis, guided wave propagation, advanced signal processing, and machine learning.

To enhance impact localisation, several novel approaches are introduced. First, a data-driven method leveraging Gaussian Process Regression with composite kernel design and Bayesian model fusion is developed, ensuring high accuracy and robustness across varying environmental and operational conditions. Second, a hybrid physics-data approach combines wave propagation physics with data-driven techniques, significantly improving generalisability in complex composite structures. Third, a general Bayesian probabilistic framework for impact localisation is proposed, adaptable to structural complexity and available data. These methods are underpinned by rigorous theoretical analyses of wave propagation in composite plates using plate theories.

For impact force reconstruction, an adaptive wavelet-based regularisation technique is introduced to mitigate its ill-posed nature, enabling efficient and accurate force identification when the structural transfer functions are known. Furthermore, to achieve precise force estimation at any impact location using sparse impact data, an physics-guided impact identification method is developed. This approach integrates sparse data-driven physics modelling with data-augmented machine learning, enhancing interpretability and accuracy across diverse impact scenarios.

The proposed methodologies are rigorously validated through extensive experiments on representative composite structures. Results demonstrate their effectiveness, robustness, and scalability, marking a significant advancement in SHM for composite aerostructures. This research contributes to improving the reliability, safety, and sustainability of next-generation aerospace systems.

Publications and Presentations

Peer-Reviewed Journal Articles:

Xiao, D., Sharif-Khodaei, Z., & Aliabadi, M.H. (2025). Robust impact localisation on composite aerostructures using kernel design and Bayesian-inspired model averaging under environmental and operational uncertainties. *Structural Health Monitoring*, 14759217251362397. DOI: 10.1177/14759217251362397

Xiao, D., de Sá Rodrigues, F., Sharif-Khodaei, Z., & Aliabadi, M. H. (2025). A general probabilistic framework for impact localisation based on flexural wave propagation. *Mechanical Systems and Signal Processing*, 226, 112320. DOI: 10.1016/j.ymssp.2025.112320

Xiao, D., Sharif-Khodaei, Z., & Aliabadi, M. H. (2024). Impact force identification for composite structures using adaptive wavelet-regularised deconvolution. *Mechanical Systems and Signal Processing*, 220, 111608. DOI: 10.1016/j.ymssp.2024.111608

Xiao, D., Sharif-Khodaei, Z., & Aliabadi, M. H. (2024). Hybrid physics-based and data-driven impact localisation for composite laminates. *International Journal of Mechanical Sciences*, 274, 109222. DOI: 10.1016/j.ijmecsci.2024.109222

Manuscripts Under Review:

Xiao, D., Sharif-Khodaei, Z., & Aliabadi, M. H. (2025). Physics-guided impact localisation and force estimation in composite plates with uncertainty quantification. Submitted to *Composite Structures*. DOI: 10.48550/arXiv.2507.13376

Published Conference Papers:

Xiao, D., Sharif-Khodaei, Z., & Aliabadi, M. H. (2024). Time of arrival extraction for impact localisation on composite structures. *Proceedings of 11th European Workshop on Structural Health Monitoring* (EWSHM 2024), Potsdam, Germany. DOI: 10.58286/29601

Xiao, D., Sharif-Khodaei, Z., & Aliabadi, M. H. (2023). Impact identification based on surrogate-assisted efficient global optimisation. *Proceedings of 21st International Conference of Fracture and Damage Mechanics* (FDM 2023), London, UK. DOI: 10.1016/j.prostr.2023.12.067

Conference Papers in Preparation:

Xiao, D., Sharif-Khodaei, Z., & Aliabadi, M. H. (2025). Deep learning approaches for impact identification on composite structures under environmental and operational variabilities: a comparative study. *Proceedings of 22nd International Conference of Fracture and Damage Mechanics* (FDM 2025), Rodos, Greece. (First Draft).

Conference Presentations (Without Full Papers):

Xiao, D., Sharif-Khodaei, Z., & Aliabadi, M. H. (2023). An adaptive multi-fidelity impact identification method for composite structures. Oral presentation in *17th International Conference on Engineering Structural Integrity Assessment* (ESIA17-ISSI2023), Manchester, UK.

Contents

List of Figures

List of Tables

Nomenclature

Impact Dynamics

x, y, z	Coordinate system
u, v, w	Displacement components
$\mathbf{M}$	Mass matrix
$\mathbf{C}$	Damping matrix
$\mathbf{K}$	Stiffness matrix
$\mathbf{x}(t)$	Vector of displacements for all DOFs
$\mathbf{F}(t)$	Vector of forces acting on all DOFs
ω_m	Natural frequency of m-th mode
ϕ_m	Mode shape of m-th mode
$\mathbf{u}(t)$	Vector of modal coordinates
$g_m(t)$	Impulse response function of m-th mode
L	Locations of passive sensors
N_s	Number of passive sensors
q	Impact location
$f(t), \boldsymbol{f}$	Impact force history
$s(t), \boldsymbol{s}$	Impact-induced signal sensors
$h(t)$	Transfer function in time domain between impact force and sensor signal
Q	Reference impact locations
$F(t), \boldsymbol{F}$	Reference impact force histories
$S(t), \boldsymbol{S}$	Reference impact-induced sensor signals
N_i	Number of reference impacts

Plate Theory

a, b, d	Plate length, width, and depth
ρ	Material density
$u_0(x, y)$	Displacement of the midplane in the x-direction
$v_0(x, y)$	Displacement of the midplane in the y-direction
$w_0(x, y)$	Displacement of the midplane in the z-direction
$\varphi_x(x, y)$	Rotation of the normal to the midplane about the y-axis
$\varphi_y(x, y)$	Rotation of the normal to the midplane about the x-axis
$\boldsymbol{\epsilon_0}$	Midplane strains (vector)
$\boldsymbol{\gamma}$	Transverse shear strains (vector)
$\boldsymbol{\kappa}$	Plate curvatures (vector)
$\bar{\boldsymbol{Q}}$	Reduced stiffness matrix of lamina
$\boldsymbol{N}$	Normal force resultants (vector)
$\boldsymbol{M}$	Moment resultants (vector)
$\boldsymbol{Q}$	Shear force resultants (vector)
$\boldsymbol{A}$	Extensional stiffness (matrix)
$\boldsymbol{B}$	Bending-extensional coupling stiffness (matrix)
$\boldsymbol{D}$	Bending stiffness (matrix)
$\bar{\boldsymbol{A}}$	Shear stiffness (matrix)
I_1, I_2, I_3	Inertial terms
$\mathbf{d}$	Displacement vector of plate, e.g. $\mathbf{d} = [u_0,\ v_0,\ w_0,\ \varphi_x,\ \varphi_y]^T$ for FSDT plate
$\mathcal{L}$	Differential operator
U	Strain energy
T	Kinetic energy
V	Potential energy

Wave Propagation

ω	Wave angular frequency
k	Wavenumber
λ	Wavelength

θ	Wave propagation direction
v_p	Phase velocity
v_g	Group velocity
$v_g(\theta)$	Group velocity profile (GVP)
d_j	Wave propagation distance between impact point and sensor j
t_j	Wave propagation time from impact point to sensor j
$\Delta\mathbf{t}$	Vector of time differences of arrival
Δt_{ij}	Time difference of arrival between sensor i and sensor j

Signal Processing

f_s	Sampling frequency in Hertz
f_d	Dominant frequency
T_{win}	Sampling window length
t_{win}	Impact window covering the entire impact duration
n	Length of sensor signals
$\mathcal{F}$	Fourier transform operator
$\mathcal{F}^{-1}$	Inverse Fourier transform operator
$\hat{s}$	Signal's spectrum in frequency domain
$\hat{s}^*$	Complex conjugate of the spectrum $\hat{s}$
$\psi(t)$	Mother wavelet (wavelet function)
$\phi(t)$	Father wavelet (scaling function)
$\circ$	Convolution operator

Other Symbols

$\mathbb{N}_{mn}$	set of natural numbers from integer m to n
λ_{reg}	Regularisation parameter
$\mathbf{x}$	Variables of the design/parameterisation space
$\mathbf{B}$	Vector/matrix of basis functions

List of Acronyms

AIC	Akaike Information Criterion.
AWT	Adaptive Wavelet Regularisation.
BIMA	Bayesian-Inspired Model Averaging.
BMA	Bayesian Model Averaging.
BVID	Barely Visible Impact Damage.
CDF	Cumulative Distribution Function.
CFRP	Carbon Fibre Reinforced Plastic.
CNN	Convolutional Neural Network.
COMP	Composite.
COS	Cosine Similarity.
CPT	Classical Plate Theory.
CWT	Continuous Wavelet Transform.
CWTT	Continuous Wavelet Transform Threshold.
DD	Data-driven.
DOF	Degrees of Freedom.
EOV	Environmental and Operational Variability.
ET	Envelope Threshold.
FEA	Finite Element Analysis.
FFT	Fast Fourier Transform.
FP	Flat Panel.
FSDT	First-order Shear Deformation Theory.

FT Fourier Transform.

GA Genetic Algorithm.

GCV Generalised Cross Validation.

GNN Graph Neural Network.

GP Gaussian Process.

GPR Gaussian Process Regression.

GVP Group Velocity Profile.

HF High-Fidelity.

HGA Hybrid Genetic Algorithm.

HPD Hybrid Physics-based and Data-driven.

LC L-curve.

LF Low-Fidelity.

LS Least Squares.

LTI Linear Time-Invariant.

MCMC Markov Chain Monte Carlo.

MF Multi-Fidelity.

MLE Maximum Likelihood Estimation.

MLP Multi-Layer Perceptron.

NED Normalised Euclidean Distance.

NSET Normalised Smoothed Envelope Threshold.

PB Physics-based.

PoD Probability of Detection.

PSD Power Spectral Density.

PZT Piezoelectric Transducer.

RBF Radial Basis Function.

RNN Recurrent Neural Network.

SC Spearman's Correlation.

SD Standard Deviation.

SEK	Squared Exponential Kernel.
SF	Shape Function.
SHM	Structural Health Monitoring.
SNR	Signal-to-Noise Ratio.
SP	Stiffened Panel.
STFT	Short-Time Fourier Transform.
SWP	Sandwich Panel.
TCN	Temporal Convolutional Network.
TDOA	Time Difference of Arrival.
TOA	Time of Arrival.
TR	Time Reversal.
TRF	Trust-Region-Reflective.
WT	Wavelet Transform.
XFMR	Transformer.

Chapter 1

Introduction

The aviation industry's pursuit of higher performance and lower operational costs has driven the widespread adoption of lightweight yet high-strength Carbon Fibre Reinforced Plastic (CFRP) composite materials. These advanced materials offer exceptional mechanical properties, including high strength-to-weight ratios, corrosion resistance, and design flexibility, making them indispensable in modern aerostructures. Both Boeing and Airbus have progressively integrated CFRP composites into their fleets to enhance structural performance, fuel efficiency, and environmental sustainability.

For example, the Airbus A320 employs CFRP in critical components such as flaps, ailerons, spoilers, and the vertical and horizontal tail planes [1]. Similarly, the Boeing 777 introduced CFRP composites in its tail section [2]. Composite applications expanded further with the Airbus A380, which incorporated CFRP in the fuselage rear section, center wing box, and wing ribs [3]. This trend reached a milestone with the Airbus A350 XWB and Boeing 787, where over 50% of the airframes—including the fuselage and wing skins—are constructed from CFRP composites [1,2], as illustrated in Fig. 1.1. Such extensive integration of composites has significantly improved aircraft performance and reduced weight, but it also highlights the critical importance of reliable Structural Health Monitoring (SHM) systems to ensure safety and operational efficiency.

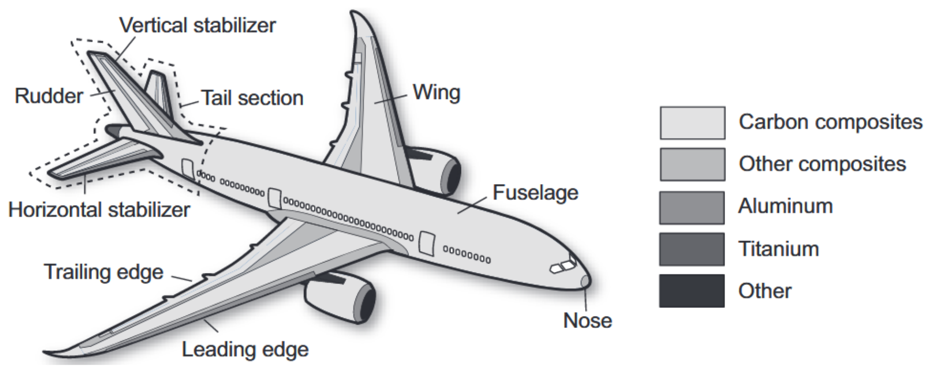

Figure 1.1: The composition of Boeing 787 [2].

One significant concern with composite aerostructures is their vulnerability to impact events, which can lead to various forms of damage, including matrix cracking [4], delamination [5], and fibre breakage [6]. Such damage can compromise the structural integrity and operational safety of aircraft. In real-world applications, composite aerostructures are exposed to a wide range of impact scenarios, including dropped tools during maintenance, debris strikes during takeoff and landing, hail strikes, and collisions with ground vehicles [7]. Fig. 1.2 illustrates the distribution of impact events across different parts of an Airbus A320 aircraft, highlighting the doors, wings, fuselage sections, and nose as the most frequently impacted areas.

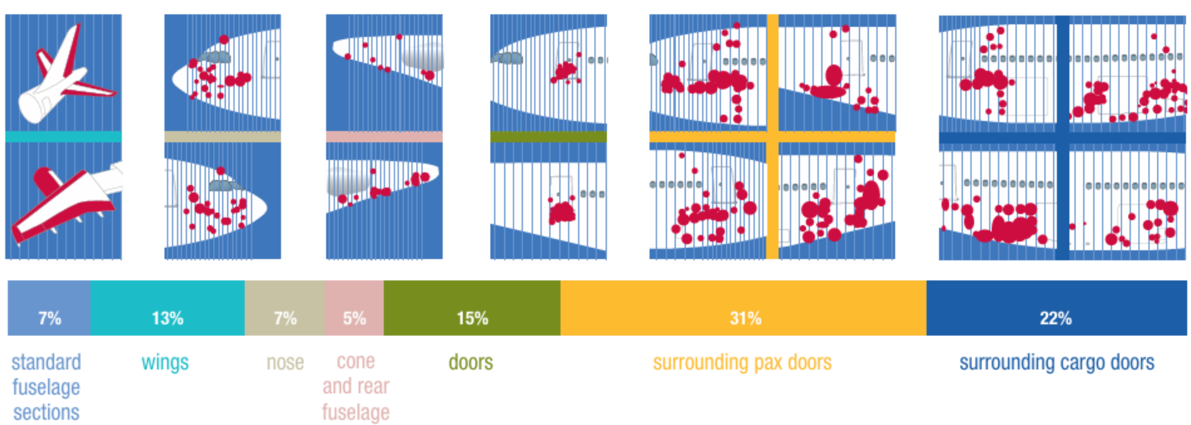

Figure 1.2: Distribution of impact events across different parts of an Airbus A320 aircraft [7].

Among the various impact types, low-velocity impacts are particularly problematic as they can cause Barely Visible Impact Damage (BVID) [8, 9]. BVID, while often undetectable through visual inspection, poses a significant threat to structural integrity due to its potential to propagate under operational loads. This hidden damage presents a critical challenge for aerospace safety, as undetected or inadequately assessed BVID can lead to catastrophic failure if not addressed promptly. Consequently, effective monitoring and assessment of impact damage are essential to ensuring the safety and reliability of composite aerostructures.

To address this challenge, advanced SHM technologies are essential for detecting and monitoring impact-induced damage [10]. Passive SHM techniques, which rely on sensors either affixed to the surface or embedded within the composite structures, offer a promising solution. These sensors enable continuous, real-time monitoring without the need for external excitation, making them highly effective for tracking the condition of composite aerostructures throughout their service life. Developing efficient, accurate, and generalisable methodologies for impact localisation, force estimation and damage assessment within this context is imperative for improving the reliability, safety, and performance of next-generation aerospace systems.

1.1 Passive Sensing for Impact Monitoring

Passive sensing offers a non-intrusive and cost-effective approach for monitoring aerostructures, characterised by its high sensitivity to dynamic events without the need for continuous external excitation. This feature makes it particularly advantageous for impact monitoring in composite aerostructures. Passive sensors, such as Piezoelectric Transducers (PZTs), strain gauges, and accelerometers, can be integrated during the manufacturing process or retrofitted onto existing structures. Together, these sensors form a distributed network capable of enabling continuous, real-time monitoring throughout the operational lifespan of the structure.

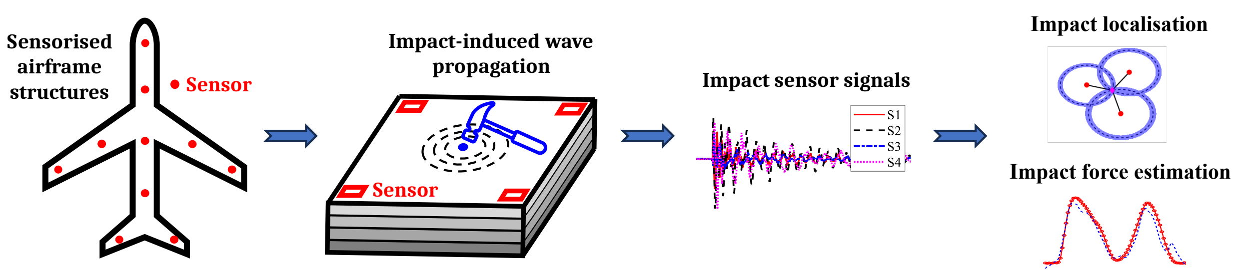

Figure 1.3: Passive sensing for impact monitoring. Passive sensors capture impact responses, forming the basis for reconstructing the impact event.

As illustrated in Fig. 1.3, an impact event on a sensorised composite aerostructure generates elastic waves that propagate through the material. These impact-induced waves, often referred to as impact-induced sensor signals, are captured by the passive sensors. The acquired data serves as the foundation for reconstructing key characteristics of the impact event, such as the impact location, q, and impact force, $\boldsymbol{f}$. (Note that both bold and italic symbols and the explicit (t) are used to represent time series, e.g. $\boldsymbol{f}$ and $f(t)$ are the same force history. Bold variables, such as $\mathbf{F}$, denote vectors and matrices). This enables the early detection of potential damage D and facilitates timely maintenance interventions, significantly enhancing the structural health management process.

Impact identification is formulated as an inverse problem that aims to determine the excitation inputs acting on the structure—specifically, the impact location q, the impact force $\boldsymbol{f}$ and the potential damage D—based on the observed outputs, namely the passive sensor signals. Denoting the sensor signals as $\boldsymbol{s}$, the impact identification process can be described probabilistically using Bayes' theorem:

$$P\left(q, \boldsymbol{f}, D | \boldsymbol{s}\right) \propto P\left(\boldsymbol{s} | q, \boldsymbol{f}, D\right), \tag{1.1}$$

where $P\left(q, \boldsymbol{f}, D | \boldsymbol{s}\right)$ represents the posterior probability of the impact location, force and damage given the sensor signals, and $P\left(\boldsymbol{s} | q, \boldsymbol{f}, D\right)$ is the likelihood of observing the sensor signals for a given impact scenario.

Solving this inverse problem in practice requires a combination of theoretical insight, numerical techniques, and practical expertise in handling specific types of impact and structural response data. The significant interdependence between impact location, force, and damage complicates the problem, necessitating a hierarchical solution approach. This hierarchical methodology divides the impact identification process into four stages: impact localisation, impact force reconstruction, detection of damage presence, and assessment of damage extent. Each preceding stage serves as a basis for the subsequent stage, thereby simplifying the inference process and improving computational efficiency.

To develop an SHM system capable of detecting and characterizing impact events on aircraft structures based on the recorded sensor responses, it is essential that the dynamic response of the structure to the probable external perturbations is well understood.

1.2 Governing Equation of Impact Dynamics

The behavior of composite aerostructures under dynamic loading, such as impact events, is governed by the structural dynamics equation. For a linear elastic structure with N Degrees of Freedoms (DOFs), as typically represented in Finite Element Analysis (FEA) modelling, the equation of motion can be formulated as:

$$\mathbf{M}\ddot{\mathbf{x}}(t) + \mathbf{C}\dot{\mathbf{x}}(t) + \mathbf{K}\mathbf{x}(t) = \mathbf{F}(t), \tag{1.2}$$

where $\mathbf{x}(t)$ denotes the structural displacement vector with N elements. $\mathbf{M}$, $\mathbf{C}$, and $\mathbf{K}$ represent the structural mass matrix, damping matrix, and stiffness matrix, each of size N by N, respectively. $\mathbf{F}(t)$ is the vector of external forces acting on the structure, which is nonzero if a force acts on the corresponding DOF.

In the context of impact dynamics, the governing equation Eq. (1.2) can be simplified by assuming a single force acting at a specific point (or node) of the structural system. This reflects a single-input and multiple-output (SIMO) system, where a single load applied at one node excites the entire structure, influencing all its nodes. Such an assumption is consistent with real-world scenarios, as the probability of multiple independent impacts occurring simultaneously on the same structure is exceedingly low.

Under this simplification, the force vector, $\mathbf{F}(t)$, contains at most M nonzero elements, corresponding to the DOFs of the impacted node. If the external impact is directed along a specific DOF, $\mathbf{F}(t)$ is further reduced to a single nonzero element. These assumptions allow for a more focused analysis of localised impact events and facilitate the development of practical, computationally efficient models for impact monitoring and analysis.

1.3 State-of-the-art Impact Identification Methodologies

Significant research efforts have been devoted to developing impact identification methodologies for composite aerostructures, considering their anisotropic and complex material properties. Depending on the required knowledge about the structures, these methodologies are broadly classified into two categories: physics-based methods and data-driven methods, as summerised in Table 1.1.

Table 1.1: Impact identification methodologies. Depending on the required structural knowledge, these methodologies can be broadly classified into physics-based and data-driven methods.

Method	**Bayes' expression**	**Required knowledge**	**Charact-eristics**	**Model / metamodel**
Physics-based	$P(q\|\boldsymbol{s},\mathcal{M},L)$ $P(q,\boldsymbol{f}\|\boldsymbol{s},\mathcal{M},L)$	Observed $\boldsymbol{s}$ Model $\mathcal{M}$ Sensors L	Model validation High generalisability	Finite Element Analysis [11–15] Modal analysis [16–18] Transfer function [19–24] Wave propagation [25–34]
Data-driven	$P(q\|\boldsymbol{s},Q,\boldsymbol{S})$ $P(\boldsymbol{f}\|\boldsymbol{s},\boldsymbol{F},\boldsymbol{S})$ $P(q,\boldsymbol{f}\|\boldsymbol{s},Q,\boldsymbol{F},\boldsymbol{S})$	Observed $\boldsymbol{s}$ Reference database $Q,\boldsymbol{F},\ \boldsymbol{S}$	Data acquisition Low generalisability	Multilayer Perceptron [35–42] Gaussian Process Regression [43–47] Convolutional Neural Network [48–53] Recurrent Neural Network [54, 55] Graph Neural Network [56–58] Transformers [59]

*q: impact location of target impact, $\boldsymbol{f}$: impact force history of target impact, $\boldsymbol{s}$: observed impact-induced sensor signals of target impact, $\mathcal{M}$: model, L: sensors configuration (type/numbers/locations of sensors), Q: reference impact locations, $\boldsymbol{F}$: reference impact forces, $\boldsymbol{S}$: reference impact-induced sensor signals.

1.3.1 Physics-based methods

Physics-based (PB) methods are founded on forward physical and mathematical representations of impact dynamics, denoted as $\mathcal{M}$. These representations can be categorised as either complete or incomplete. Complete models, such as FEA, modal analysis, and transfer functions, allow for the prediction of full structural responses, expressed as $\bar{\boldsymbol{s}} = \mathcal{M}(q,\boldsymbol{f},D,L)$. In contrast, incomplete models, such as wave propagation, focus on specific features of structural responses. For instance, wave propagation models can predict the theoretical wave travel time and are commonly used for impact localisation. Both categories play a critical role in advancing the understanding and identification of impacts on structural systems.

FEA is one of the most widely adopted forward models in structural dynamics. FEA-based models enable the identification of impact location and force through two primary approaches: optimisation and Time Reversal (TR) processing.

The optimisation approach identifies impacts by minimising discrepancies [11, 12] or maximising correlation coefficients [13] between predicted and measured responses. Various optimisation algorithms have been developed to improve efficiency and accuracy. For instance, Hu et al. [11] estimated strain responses using an FEA model combined with the mode superposition method and identified impact forces by minimising the differences between predicted and measured strain responses using direct parametric searches across all possible loading points. Similarly, Liu et al. [13] introduced a hierarchical method for identifying impact numbers, locations, and forces by constructing an FEA model. Their method employed partition optimisation and polynomial fitting techniques to enhance computational efficiency in impact localisation. Xiao et al. [12] addressed the computational challenges associated with FEA-based impact identification, noting that identifying a single impact event typically requires hundreds of simulations, even when utilising surrogate-assisted efficient global optimisation techniques.

In contrast, TR processing offers a computationally efficient alternative, as it eliminates the need for iterative or repetitive simulations. By performing a single multiple-input virtual TR simulation, both the impact location and the force shape can be identified. Yu et al. [14, 15] enhanced FEA-based methods by introducing virtual TR processing into time-domain spectral FEA. This approach enabled accurate localisation of impact sources and reconstruction of impact forces without relying on extensive optimisation iterations, thereby significantly reducing computational demands.

Modal analysis in structural dynamics is a technique used to determine the natural vibration characteristics of a structure, including its natural frequencies, mode shapes, and damping ratios [60]. These properties are essential for understanding how a structure responds to dynamic loads and can be utilised as physics for impact identification. Modal analysis highlights that the distinct contributions of individual modal modes to the structural response act as signatures for the impact location. Building on this insight, Goutaudier et al. [16, 17] and Zhang et al. [18] successfully identified both the impact location and force using a single accelerometer, effectively leveraging modal information.

Similar to modal information, the transfer function represents another fundamental physical characteristic of structural dynamics that can be leveraged for impact identification. The transfer function characterises how a structural node responds to an input excitation at another node, effectively capturing the dynamic relationship between them. Consequently, researchers often view the transfer function as a viable alternative to FEA models for forward impact simulation. It is frequently combined with optimisation algorithms or TR techniques to identify impacts. In scenarios employing optimisation algorithms, Atobe et al. [20] utilised a transfer function database and adopted a quadratic programming method to minimise the discrepancies between predicted and measured impact responses by iteratively updating the impact location and force. When using TR techniques, Ciampa et al. [21], Simone et al. [22], and Chen et al. [23] effectively identified impacts on a composite stiffened plate, composite flat plate, and aluminium plates, respectively, by leveraging TR techniques based on densely distributed transfer function data.

Wave propagation, based on the physical principle that the distance travelled by impact-induced waves is the product of wave velocity and propagation time, provides a practical triangulation approach for locating impacts. To make triangulation solvable, two main strategies have been explored: sensor clustering, which assumes a uniform group velocity from the impact point to a cluster of sensors [61–63], and pre-determined Group Velocity Profile (GVP), which is obtained in advance [25–32]. While the sensor clustering approach is resource-intensive, requiring a significant number of sensors and extensive impact data acquisition, pre-measuring the GVP offers a resource-efficient alternative. Notably, the wavefront velocity is independent of the structural boundary conditions, offering the advantage of boundary-condition-independent impact localisation. However, this independence also imposes a limitation: the impact force cannot be inferred from the wavefront information alone. Moreover, another critical limitation arises from the dispersive nature of impact-induced waves, in that wave velocities are inherently frequency-dependent. This frequency dispersion raises concerns about the accuracy of velocity predictions/measurements, particularly when a single group velocity is assumed across all frequencies, potentially compromising localisation accuracy.

Although physics-based methods offer straightforward and interpretable solutions, these physical models come with their own set of drawbacks and limitations. The FEA model, for instance, is heavily reliant on accurate knowledge of material properties [64] and boundary conditions [65], which can be difficult to obtain in real-world applications. Ensuring model accuracy often requires iterative updates [66], as well as rigorous validation and verification (V&V) [67]. Even after extensive updates and V&V, the FEA model may still fail to match laboratory experiments or, more critically, real-world operational structures. Furthermore, real-time impact localisation using FEA is often impractical, particularly for large-scale structures, due to the prohibitive computational cost of simulating their dynamic behaviour.

In contrast, the remaining physics-based methods—modal analysis, transfer functions, and GVP for impact identification—are typically determined through a combination of numerical simulations and experimental measurements. While numerical simulations, such as FEA, often struggle to accurately replicate real-world conditions, experiments, though more costly, provide higher accuracy. However, experimental approaches are inherently expensive, time-consuming and labour-intensive due to their meticulous setup, data acquisition, and post-processing requirements.

For instance, GVP estimation generally necessitates a large number of precisely placed sensors and strategically positioned impact excitations. In some setups, tens of sensors must be arranged along the circumference of a circle, with the impact excitation positioned at its centre [27, 68, 69]. Alternatively, sensors may be evenly distributed, with multiple impact excitations carefully aligned with pairs of passive sensors to estimate the wave velocity along a given path [26]. Similarly, experimental modal analysis [70] and transfer function estimation require dozens of sensors and multiple densely distributed tests, further increasing the complexity and cost of experimental procedures.

1.3.2 Data-driven methods

In contrast, Data-driven (DD) methods rely on surrogate models constructed from reference databases to map structural outputs (e.g., sensor signals) to impact inputs (e.g., location and force). Traditional approaches, such as Multi-Layer Perceptrons (MLPs) [37–40] and Gaussian Process Regression (GPR) [44–47], often rely on manually extracted features such as Time Difference of Arrival (TDOA) [71, 72], which are rooted in wave propagation principles. In contrast, modern deep learning techniques—including Convolutional Neural Networks (CNNs) [48–53], Recurrent Neural Networks (RNNs) [54, 55], Graph Neural Networks (GNNs) [56–58], and Transformers (XFMRs) [59]—can process raw time-series data directly, capturing complex patterns and nonlinear relationships.

Deep learning approaches have gained considerable attraction for impact identification due to their ability to address inverse problems in multivariate time series. However, their effectiveness is contingent on access to extensive, high-quality training datasets, which are often difficult to obtain in real-world SHM applications. Despite their advantages, deep learning and other data-driven methods still face several key challenges:

- High costs in reference data collection: While numerical simulations can generate training data at low cost, the resulting datasets often lack fidelity due to discrepancies between the simulated model and the actual structure. Conversely, experimental data collected from real structures provide high-fidelity training sets but are costly and labour-intensive to obtain. Validating data-driven impact identification models typically requires thousands of impact tests on a real structure for training and testing [49, 53, 56], further increasing costs.

- Poor generalisability: Variations in operational and environmental conditions pose significant challenges to the robustness of data-driven models. It is neither practical nor feasible to collect training data that encompasses all possible impact scenarios and the full spectrum of environmental variabilities, including a wide range of impact forces, locations, and environmental factors such as temperature, humidity, and structural loading. This limitation is exacerbated by the inherent unpredictability of real-world impacts, where factors like impact mass, velocity, and direction are often unknown. Furthermore, the influence of environmental factors on structural stiffness adds another layer of complexity, making it difficult to develop models that are both accurate and robust across varying conditions. As a result, achieving reliable generalisation in practical applications of impact identification remains an ongoing obstacle.

- Limited interpretability: Many deep learning models used for impact identification function as "black boxes", offering limited insight into the decision-making process or the internal representation of inverse impact dynamics. This lack of interpretability can hinder trust in the models and limit their adoption in practical SHM applications.

- Limited scalability: Data-driven methods often struggle to scale when applied to different structural configurations, especially as the number of sensors increases. Furthermore, as structural complexity increases—e.g., transitioning from a simple flat panel to a mono-stiffened panel and ultimately to a large-scale stiffened panel—new training data must be collected, and models must be retrained for each specific configuration. This requirement for repeated adaptation significantly limits the scalability of data-driven approaches.

1.4 Aims and Objectives

This thesis aims to develop next-generation methodologies for impact localisation and force reconstruction in composite structures, with an emphasis on robustness, efficiency, interpretability, and scalability. By integrating principles from structural dynamics, wave propagation, and data-driven modelling, the research targets solutions that not only address current technical limitations but also move toward practical relevance for real-world applications.

In pursuit of this goal, the thesis is structured around the following key research objectives: *Each contributes to narrowing the gap between theoretical innovation and applied structural health monitoring while recognising the challenges that remain for industrial integration.*

1. **Develop a robust data-driven impact localisation method that adapts to Environmental and Operational Variability (EOV)** [73]

    - This research tackles the challenge of achieving reliable impact localisation under EOVs, such as temperature changes, impactor mass differences, and varying energy levels. A novel composite kernel design and Bayesian model fusion framework are proposed to dynamically adapt to these conditions. While the method significantly improves localisation robustness compared to existing data-driven techniques, its full deployment on large-scale aerostructures will require further testing under a broader range of EOV scenarios, such as moisture or fatigue.

2. **Develop a hybrid physics-data method for impact localisation that reduces reliance on reference data and improves generalisability** [74]

    - A two-stage, gradient-based hybrid algorithm is introduced that incorporates wave propagation physics into the learning process to enhance generalisability and reduce the need for exhaustive training datasets. This method enables real-time localisation with improved physical interpretability. Though promising on coupon-level specimens, its applicability to more complex structures (e.g., fuselage panels with stiffeners or cut-outs) has yet to be fully demonstrated in operational environments.

3. **Develop a probabilistic framework for impact localisation that enables fast and accurate scalability from low to high structural complexity** [75]

   - A novel probabilistic framework is introduced to improve the scalability and accuracy of impact localisation across structures of varying complexities. This framework enables rapid estimation of GVPs using sparse sensor data from flat plates to more intricate composite assemblies. While the framework shows significant potential, additional experimental validation is required to confirm its robustness on large-scale and anisotropic composite components found in real-world aerospace structures.

4. **Develop an efficient impact force reconstruction using adaptive wavelet-regularised method** [76]

   - This objective introduces a wavelet-regularised force reconstruction method that improves both computational efficiency and reconstruction accuracy. Adaptive time–frequency resolution and energy-based filtering enable real-time performance on simplified test specimens. However, the method assumes linear elasticity and undamaged states, and its robustness in the presence of damage or under varying environmental conditions remains a subject for future extension.

5. **Develop sparse data-driven impact force identification and localisation with enhanced interpretability and generalisability** [77]

   - This study proposes a physics-guided data-driven framework based on the First-order Shear Deformation Theory (FSDT) plate model that enables both impact localisation and force identification from sparse sensor data. By learning structural and boundary conditions from data, the method facilitates extrapolation to untrained scenarios and improves interpretability. While the integration of physical insight and data sparsity improves generalisability compared to black-box models, further work is needed to demonstrate its reliability in complex, operationally variable environments.

The methods presented are evaluated on representative composite panels under controlled laboratory conditions, demonstrating marked improvements over existing approaches. However, the ultimate deployment of these techniques in operational settings—such as full-scale aircraft structures—will require further validation, particularly under more complex EOV conditions.

1.5 Thesis Overview

An overview of the thesis structure is illustrated in Fig. 1.4. The figure visually represents the logical progression of the chapters, beginning with foundational concepts in Chapter 2, which form the basis for the development of impact localisation methods in Chapter 3–5. These methods are further extended to force identification in Chapter 6 and Chapter 7, ultimately leading to the conclusions presented in Chapter 8.

A summary of the key contents and novel contributions of each chapter is provided below:

- **Chapter 2: Fundamentals of impact dynamics, plate theory and impact-induced waves.** This chapter establishes the theoretical foundation for impact identification by introducing key concepts of impact dynamics, structural vibration, and wave propagation. Structural modal analysis is presented as a link between FEA models and measured responses, providing insight into passive sensor signals and transfer functions. Plate theories, including First-Order Shear Deformation Theory (FSDT) and Classical Plate Theory (CPT), are introduced as efficient alternatives to FEA for modelling plate-like structures. Using these theories, the characteristics of impact-induced wave propagation—such as multiple wave types, modes, and dispersion—are examined. Furthermore, the chapter reviews existing signal processing and physics-based impact identification approaches using sparse sensor networks. This chapter lays a foundational basis for the novel hybrid and data-driven techniques developed in later chapters.

- **Chapter 3: Robust impact localisation under environmental and operational**

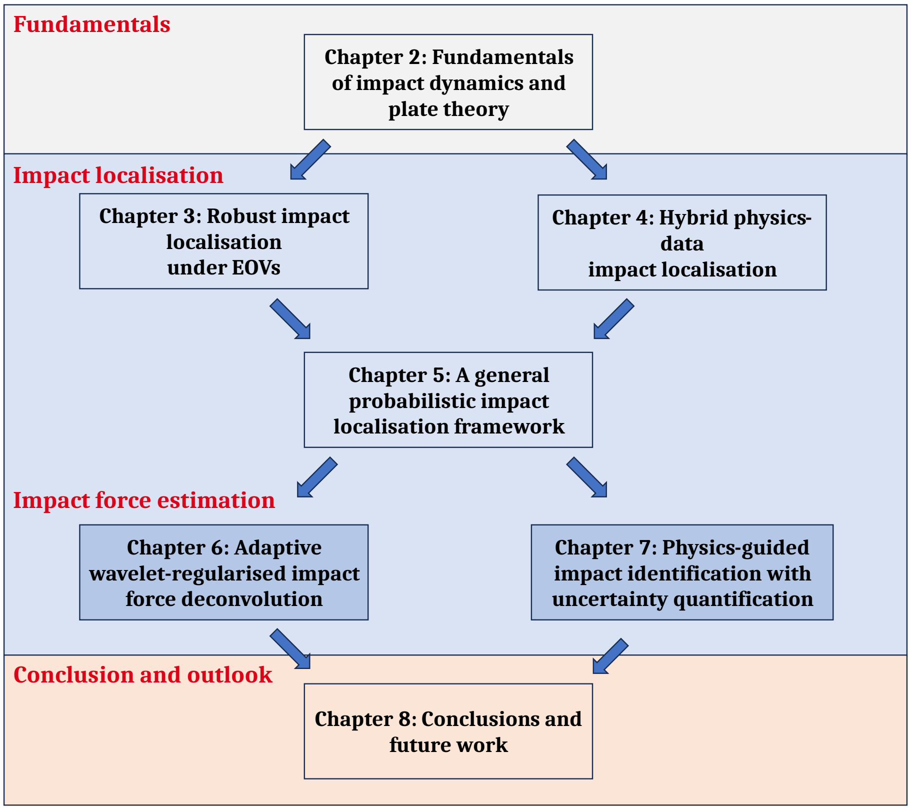

Figure 1.4: An overview of the thesis structure.

variabilities. This chapter introduces a novel composite-kernel Gaussian Process Regression (GPR) method for impact localisation that is explicitly designed to address operational and environmental variability. A key contribution is the physics-guided design of a composite kernel informed by wave propagation characteristics, enabling improved robustness across different structural and environmental conditions. Additionally, a Bayesian-inspired model averaging strategy is proposed to dynamically fuse multiple kernel predictions, adaptively weighting them based on the confidence under each condition. The integration of physics-informed kernel design with data-driven uncertainty quantification represents a significant step beyond existing GPR-based localisation methods. Experimental results on composite structures demonstrate the method's robustness and adaptability under simulated variabilities in laboratory conditions.

- Chapter 4: **Hybrid physics-data impact localisation for enhanced generalisability.** This chapter proposes, for the first time, a hybrid localisation framework that combines analytically derived dispersion relations from the FSDT plate theory with data-driven learning for real-time impact localisation. A novel two-stage gradient-based optimisation algorithm is developed to identify the GVP as a function of wave frequency and stiffness. This method enables the adaptive incorporation of material and frequency-dependent dispersion into triangulation-based localisation, significantly improving generalisability across materials and geometries. The hybrid formulation demonstrates substantial gains in accuracy and speed over conventional purely data-driven or physics-based methods. This contribution represents a novel formulation that extends the state of the art in SHM by tightly coupling physical insight with learning algorithms.

- **Chapter 5: A general probabilistic impact localisation framework.** This chapter develops a unified probabilistic framework for impact localisation that integrates physics-based, data-driven, and hybrid approaches within a Bayesian inference paradigm. A novel contribution lies in the introduction of a Bayesian inferred GVP estimation method that operates effectively with sparse data and limited sensor networks. By embedding uncertainty quantification into both the velocity estimation and the TDOA measurements, the framework provides reliable probabilistic localisation outputs. Moreover, it supports multi-frequency analysis, allowing more reliable impact identification under dispersive wave propagation. This comprehensive probabilistic approach represents an advancement over deterministic localisation strategies as it enhances interpretability and adaptability to different structural configurations.

- **Chapter 6: Adaptive wavelet-regularised impact force deconvolution.** This chapter addresses the ill-posed nature of the impact force reconstruction problem by introducing an adaptive wavelet-based regularisation framework. A novel formulation is presented wherein multi-resolution wavelet decomposition is used to construct an impact-adaptive window, selectively filtering wavelet components based on energy contribution to improve temporal accuracy while reducing noise. The method advances state-of-the-art deconvolution techniques by providing a dynamic regularisation mechanism tuned to the characteristics of the measured signal. Experimental studies confirm its effectiveness even under significant structural deformation, marking a novel application of wavelet regularisation in SHM.

- **Chapter 7: Physics-guided impact identification with uncertainty quantification.** This chapter presents a novel sparse data-driven framework for impact identification that integrates data-driven FSDT modelling. A key innovation is the simultaneous identification of material properties and boundary conditions directly from sensor data—material stiffness is inferred via dispersion analysis, while boundary conditions are estimated from modal characteristics. This is the first known application of constructing a sparse data-driven FSDT model to generate synthetic training data for impact localisation and to adaptively regularise the force deconvolution process. The framework demonstrates high localisation and reconstruction accuracy even with limited training data and sparse sensors, thereby significantly extending the applicability of data-driven methods to resource-constrained conditions

- **Chapter 8: Conclusions and future work.** This chapter summarises the key findings of the thesis and highlights the contributions made to the field of impact identification. The limitations of the developed methodologies are discussed, and potential directions for future research are outlined, with an emphasis on extending the proposed frameworks to more complex structural configurations and real-world aeronautical applications.

1.6 Assumptions and Limitations

This thesis develops novel methodologies for impact localisation and force reconstruction in composite structures based on wave propagation and deconvolution technique. To ensure conceptual clarity and define the boundaries of the work, it is important to outline the key assumptions and limitations adopted in this research:

1. Linear elasticity assumption: All proposed methods assume that the structure behaves according to linear elastic theory. Both wavefront propagation used for TDOA estimation and inverse methods for force deconvolution rely on this linearity. Material nonlinearities—such as those induced by matrix cracking, delamination, or plastic deformation—are not modelled explicitly.

2. Neglect of structural damage effects: While TDOA-based localisation assumes that wavefront propagation is unaffected by subsequent impact damage—a claim supported by recent

literature [78]—this assumption may break down in cases of extensive damage. Furthermore, while this thesis experimentally validates force deconvolution under significant geometric deformation (e.g., large-mass impacts), the presence of structural damage (e.g., delamination or perforation) during the force reconstruction process remains unaddressed.

3. Partial coverage of EOV: This research focuses primarily on temperature variation and impact-related variabilities (e.g., mass and energy). Other relevant EOVs—such as moisture ingress, pre-stress, cyclic fatigue, and dynamic loading—are not incorporated, which may influence signal propagation and system response in real-world deployments.

4. Validation on representative composite panels: The methodologies developed are validated on coupon-level composite structures with simplified geometries. While the frameworks are designed to be scalable to full-scale aerostructures (e.g., stiffened fuselage), such application is assumed rather than demonstrated and will require further validation and refinement.

5. Ideal sensor conditions and placement: The research assumes ideal sensor behaviour with no degradation, noise beyond baseline measurement error, or failure. The effects of sensor placement variability and signal-to-noise ratio under harsh environments have not been systematically evaluated.

6. Passive sensing paradigm: All methodologies rely on passive sensing (i.e., no active excitation). While this approach is suited for impact monitoring, it may not generalise directly to other SHM tasks requiring high spatial resolution or active interrogation.

By articulating these assumptions and limitations at the outset, this thesis aims to clarify its scope and guide the reader in understanding the contexts in which the proposed methods are most applicable.

Chapter 2

Fundamentals of Impact Dynamics, Plate Theory and Impact-induced Wave

Highlights:

- Introduce structural modal analysis to relate Finite Element Analysis models to measured responses via passive sensing and transfer functions.
- Present Classical Plate Theory and First-order Shear Deformation Theory as efficient analytical alternatives for modelling composite plate-like structures.
- Explore the propagation characteristics of impact-induced waves, including wave types, modes and dispersion.
- Describe impact identification using sparse sensor networks, covering signal processing, localisation, and force reconstruction techniques.

2.1 Impact Dynamics through Modal Analysis

2.1.1 Modal analysis as a bridge between FEA and transfer function

The equation of motion for linear Finite Element Analysis (FEA), as presented in Eq. (1.2), can be decoupled by expressing the structural displacements $\mathbf{x}(t)$ in terms of modal coordinates $u_m(t)$

and eigenvectors (mode shapes) ϕ_m:

$$\mathbf{x}(t) = \sum_{m=1}^{N} \phi_m u_m(t) = \mathbf{\Phi}\mathbf{u}(t),\ \mathbf{\Phi} = [\phi_1,\ \phi_2,\ ...,\ \phi_N], \mathbf{u}(t) = [u_1(t),\ u_2(t),\ ...,\ u_N(t)]^\top. \tag{2.1}$$

Here, each mode shape ϕ_m is an N-dimensional column vector, forming the mode shape matrix $\mathbf{\Phi}$ of size $N \times N$. The mode shapes ϕ_m are obtained by solving the undamped eigenvalue problem:

$$(\mathbf{K} - \omega_m^2 \mathbf{M})\phi_m = 0, \tag{2.2}$$

where ω_m is the natural frequency associated with mode shape ϕ_m. The mode shapes are mass-normalised such that:

$$\phi_m^\top \mathbf{M} \phi_n = \delta_{mn},\ \phi_m^\top \mathbf{K} \phi_n = \omega_m^2 \delta_{mn}, \tag{2.3}$$

where δ_{mn} is the Kronecker delta.

Substituting Eq. (2.1) into Eq. (1.2), the equation of motion can be reformulated in terms of modal coordinates $\mathbf{u}(t)$ as follows:

$$\mathbf{\Phi}^\top \mathbf{M} \mathbf{\Phi} \ddot{\mathbf{u}}(t) + \mathbf{\Phi}^\top \mathbf{C} \mathbf{\Phi} \dot{\mathbf{u}}(t) + \mathbf{\Phi}^\top \mathbf{K} \mathbf{\Phi} \mathbf{u}(t) = \mathbf{\Phi}^\top \mathbf{F}(t) = \mathbf{P}(t). \tag{2.4}$$

Assuming proportional (Rayleigh) damping, the damping matrix $\mathbf{C}$ preserves orthogonality in modal coordinates, and the modal transformation of the equation of motion yields:

$$\ddot{u}_m(t) + 2\zeta_m \omega_m \dot{u}_m(t) + \omega_m^2 u_m(t) = p_m(t), \tag{2.5}$$

where ζ_m represents the damping ratio ($0 < \zeta_m < 1$ for an underdamped system), and $p_m(t) = \phi_m^\top \mathbf{F}(t)$ is the modal force acting on the m-th mode. The modal response $u_m(t)$ is given by the convolution of the modal force $p_m(t)$ with the impulse response function $g_m(t)$:

$$\begin{aligned} &\mathbf{u}(t) = \mathbf{g}(t) \circ \mathbf{P}(t) \leftrightharpoons u_m(t) = g_m(t) \circ p_m(t), \\ &g_m(t) = \frac{1}{\omega_d} e^{-\zeta_m \omega_m t} \sin(\omega_d t),\ \mathbf{g}(t) = [g_1(t),\ g_2(t),\ ...,\ g_N(t)]^\top, \end{aligned} \tag{2.6}$$

where $\omega_d = \omega_m \sqrt{1 - \zeta_m^2}$ is the damped natural frequency, and the circle $\circ$ represents the convolution operator. The vector of impulse response functions is denoted as $\mathbf{g}(t) = [g_1(t), g_2(t), \ldots, g_N(t)]^\top$.

Substituting back to physical coordinates yields the structural response:

$$\mathbf{x}(t) = \mathbf{\Phi}\mathbf{u}(t) = \mathbf{\Phi}\mathbf{g}(t) \circ \mathbf{P}(t). \tag{2.7}$$

Assuming a point impact force $f(t)$ at location q in the z-direction, the modal force becomes:

$$p_m(t) = \phi_m^w(q) f(t), \tag{2.8}$$

where $\phi_m^w(q)$ denotes the w-component of the m-th mode shape along the z-direction at location q. When a piezoelectric transducer (PZT) sensor at location L measures the in-plane strain combination $\varepsilon_{xx} + \varepsilon_{yy}$, the sensor output $s(t; L)$ is related to the force by a transfer function:

$$h(t; q, L) = \sum_{m=1}^{N} \left(\frac{\partial \phi_m^u}{\partial x}(L) + \frac{\partial \phi_m^v}{\partial y}(L) \right) \phi_m^w(q) g_m(t), \;\; s(t; L) = h(t; q, L) \circ f(t). \tag{2.9}$$

Here, ϕ_m^u and ϕ_m^v are the displacement mode shapes in the x and y directions, respectively. The transfer function $h(t; q, L)$ characterises the contribution of each mode to the measured strain signal, enabling reconstruction or interpretation of the force input from sensor outputs.

This modal decomposition reveals how structural modes contribute to the observed dynamic response, and allows the development of interpretable and efficient models for structural health monitoring (SHM) and impact characterisation.

2.1.2 Insights into impact dynamics and impact identification

The FEA model, modal properties, and transfer functions collectively define how a structure responds to external excitations. These components are inherently dependent on the structural configuration and, once accurately identified, enable complete characterisation of the system—a process known as structural system identification.

As outlined in Section 1.3, reliable system identification often requires detailed prior knowledge of the structure, extensive model updating, or dense experimental data coverage. Given the lack of a standardised methodology for integrating FEA into SHM, this thesis introduces a unified conceptual framework (see Fig. 2.1) that systematically links FEA, modal analysis, transfer functions, dispersion relations, and wave propagation modelling. This framework provides a cohesive and interpretable strategy for impact identification and damage detection.

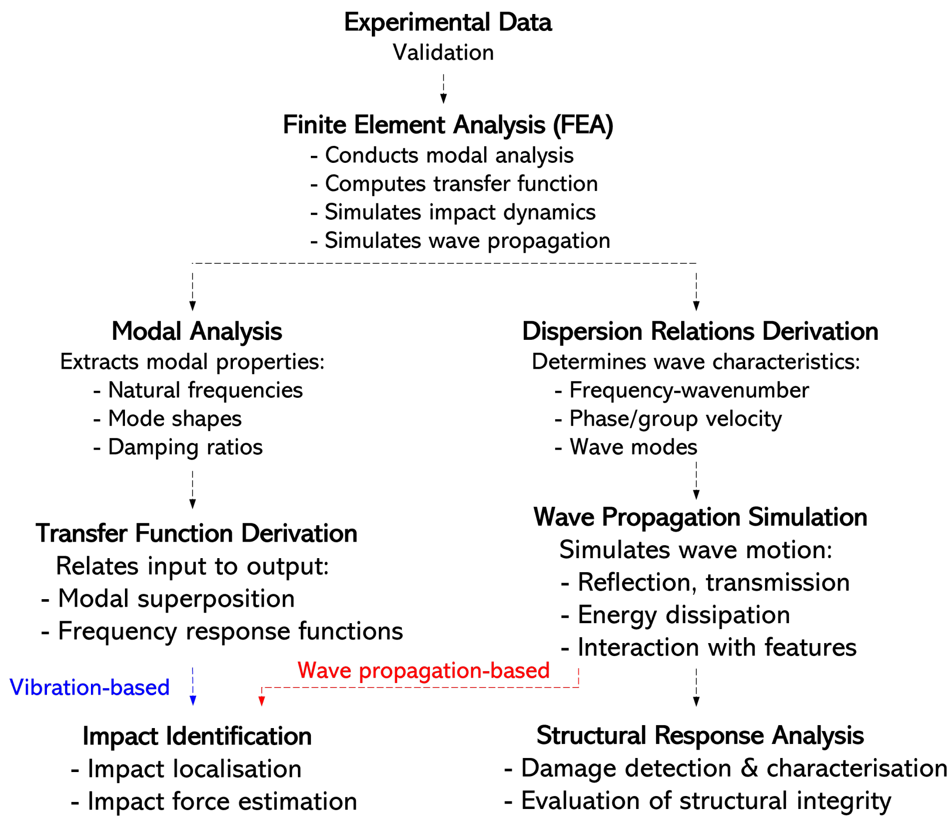

Figure 2.1: The conceptual diagram between FEA, modal analysis, transfer function, dispersion relation and impact identification.

Within this framework, FEA serves as the computational foundation, supporting two complementary analytical pathways:

1. **Vibration**: FEA → Modal Analysis → Transfer Function Derivation → Impact Identification

2. **Wave Propagation**: FEA → Dispersion Relations Derivation → Wave Propagation Simulation → Structural Response Analysis

These pathways are interconnected: modal analysis captures global structural dynamics, while dispersion-based wave propagation modelling addresses localised wave phenomena. Their integration facilitates accurate impact localisation and force reconstruction, enabling robust and interpretable SHM and damage assessment. This proposed framework contributes an integrated perspective on leveraging FEA within SHM and aims to bridge the gap between physics-based modelling and data-driven diagnostics.

The response of passive sensors to an impact event is governed by the interplay between the applied impact force and its location. These influences can be analysed through modal properties and transfer functions, which describe how different structural modes contribute to the measured response. For a given sensor and a fixed impact force, variations in the impact location affect the modal contributions to the sensor signals. This dependency is captured by the weighting term $\mathbf{\Phi}^w(q)$ in Eq. (2.9), which represents the modal displacements evaluated at the impact location q. A shift in impact location alters the relative excitation of different modes, leading to a distinctive signal signature at each sensor. Consequently, modal displacements—defined as evaluation of mode shapes at a specific point in the structure—serves as a key indicator of impact location.

Similarly, different sensors positioned at various locations exhibit distinct responses to the same impact event. This variation arises due to differences in modal participation at different sensor positions, mathematically characterised by $\frac{\partial \mathbf{\Phi}^u(L)}{\partial x} + \frac{\partial \mathbf{\Phi}^v(L)}{\partial y}$ in Eq. (2.9). The spatial sensitivity of each sensor to specific modes means that some sensors may detect stronger responses for particular impacts, while others may register attenuated signals. Understanding this spatial variation is crucial for optimising sensor placement in impact detection systems.

When both the impact location and the sensor position are fixed, the measured strain response is primarily influenced by the spectral distribution of the impact force $f(t)$. Each mode contributes to the response according to its resonance characteristics, meaning that the frequency content of the measured signal reflects both the impact force spectrum and the structural modal properties. Consequently, time-frequency analysis techniques—such as wavelet transforms or Fourier transforms—can be employed to extract spectral information about the impact force and provide insights into the underlying structural dynamics.

Furthermore, if the transfer function between the impact force and the sensor response is known, the impact force history can be deconvoluted. This process, often referred to as impact force deconvolution, involves solving an inverse problem to estimate the force input from the measured sensor signals. Such an approach is particularly valuable in SHM, where precise force estimation can aid in assessing the severity of impact events and their potential to cause damage.

2.1.3 Dominance of low-frequency modes in impact dynamics

In practical impact dynamics, the loading and unloading phases of structural impacts lead to a finite contact duration T and force histories characterised by relatively simple shapes [79]. According to the Paley-Wiener-Schwartz theorem [80, 81], the Fourier-Laplace transform amplitudes of compactly supported functions are bounded and exhibit decay properties. This spectral behaviour plays a crucial role in determining the frequency content (modes excited) of impact-induced excitations.

For instance, considering an impact force with a half-sine waveform, where the impulse is defined as $f(t) = A\sin(\omega_f t)$ for $0 \leq t \leq T$ with $T = \pi/\omega_f$, its frequency spectrum can be obtained using the Fourier transform [82]:

$$\hat{f}(\omega) = \frac{A_f(1 + e^{-2\pi^2 ri})}{1 - 4\pi^2 r^2}, \tag{2.10}$$

where i represents the imaginary unit, $r = \omega/\omega_f$ denotes the frequency ratio. $A_f = AT/\pi$ is the half maximum amplitude of the impulse spectrum, depending on the impulse amplitude A and the impulse duration T. The normalised amplitude spectrum is visualised in Fig. 2.2, showing the rapid decay of spectral components at higher frequencies. Specifically, when $r = 1$ and 2, the spectral amplitude decreases to approximately 2.35% and 0.4% of the maximum spectrum amplitude, respectively. Consequently, such impact loads predominantly excite low-frequency structural modes, while the influence of higher-order modes—those with natural frequencies significantly exceeding the fundamental loading frequency ω_f is limited. This characteristic spectral distribution is particularly relevant for analysing wave propagation in composite aerostructures, where low-frequency wave modes tend to dominate the response.

2.2 Plate Theories for Efficient Structural Modelling

Most composite aerostructures—such as fuselages, wings, and stabilisers—can be effectively idealised as plates or thin shells, where the thickness d is much smaller than the in-plane dimensions,

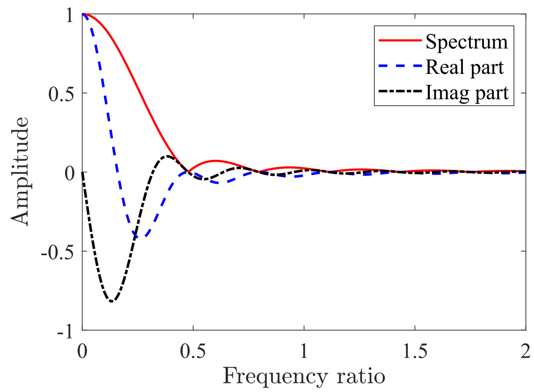

Figure 2.2: Spectrum of half-sine impulse.

i.e., length a and width b. This geometric characteristic allows the use of plate theories to efficiently model impact dynamics while maintaining a balance between computational tractability and mechanical accuracy.

As illustrated in Fig. 2.3, a sensorised composite plate is subjected to an impact event. The resulting structural response involves complex interactions among guided wave propagation, localised deformation, and potential damage initiation—all significantly affected by the anisotropic and layered nature of composite laminates. Despite these complexities, plate theory offers a robust and computationally efficient framework for capturing the dominant physical behaviours, enabling accurate analysis and predictive modelling of impact responses in composite aerostructures.

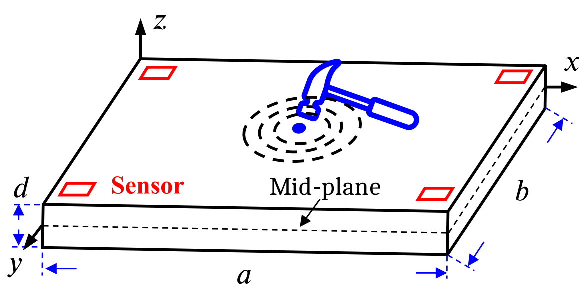

Figure 2.3: Illustration of a thin plate. Impact dynamics of composite aerostructures can be efficiently analysed using plate theories.

2.2.1 First-order Shear Deformation Theory (FSDT)

The First-order Shear Deformation Theory (FSDT) [83] is widely used for modelling moderately thick plates. FSDT assumes constant transverse shear strains ϵ_{xz} and ϵ_{yz} along the plate thickness coordinate, while neglecting transverse normal strain ϵ_{zz}. These assumptions result in the following displacement field:

$$\begin{aligned} u(x,y,z) &= u_0(x,y) + z\varphi_x(x,y), \\ v(x,y,z) &= v_0(x,y) + z\varphi_y(x,y), \\ w(x,y,z) &= w_0(x,y), \end{aligned} \tag{2.11}$$

where u_0, v_0, and w_0 are the displacement components of the plate midplane, while φ_x and φ_y denote the rotations of the normal to the midplane about the y- and x-axes, respectively. The strain-displacement relationships for plates are then derived as follows:

$$\begin{bmatrix} \epsilon_{xx} \\ \epsilon_{yy} \\ \epsilon_{xy} \end{bmatrix} = \begin{bmatrix} \frac{\partial u_0}{\partial x} \\ \frac{\partial v_0}{\partial y} \\ \frac{\partial u_0}{\partial y} + \frac{\partial v_0}{\partial x} \end{bmatrix} + z \begin{bmatrix} \frac{\partial \varphi_x}{\partial x} \\ \frac{\partial \varphi_y}{\partial y} \\ \frac{\partial \varphi_x}{\partial y} + \frac{\partial \varphi_y}{\partial x} \end{bmatrix} = \boldsymbol{\epsilon}_0 + z\boldsymbol{\kappa}, \quad \begin{bmatrix} \epsilon_{xz} \\ \epsilon_{yz} \end{bmatrix} = \begin{bmatrix} \frac{\partial w_0}{\partial x} + \varphi_x \\ \frac{\partial w_0}{\partial y} + \varphi_y \end{bmatrix} = \begin{bmatrix} \gamma_x \\ \gamma_y \end{bmatrix} = \boldsymbol{\gamma}. \tag{2.12}$$

Here, $\boldsymbol{\epsilon}_0$, $\boldsymbol{\gamma}$, and $\boldsymbol{\kappa}$ represent the midplane strains, transverse shear strains, and plate curvatures, respectively.

To model out-of-plane response of a composite laminated plate subjected to low-velocity impacts, this study assumes a linear structural response with a perpendicular point impact on the plate surface. Additionally, perfect bonding between lamina layers is assumed, with each lamina behaving as a linearly elastic orthotropic material [84, 85]. The stress-strain relations for such materials are expressed as:

$$\begin{bmatrix} \sigma_{xx} \\ \sigma_{yy} \\ \sigma_{xy} \end{bmatrix} = \begin{bmatrix} \bar{Q}_{11} & \bar{Q}_{12} & \bar{Q}_{16} \\ \bar{Q}_{12} & \bar{Q}_{22} & \bar{Q}_{26} \\ \bar{Q}_{16} & \bar{Q}_{26} & \bar{Q}_{66} \end{bmatrix} \begin{bmatrix} \epsilon_{xx} \\ \epsilon_{yy} \\ \epsilon_{xy} \end{bmatrix}, \tag{2.13}$$

where $\bar{Q}_{ij}$ are the reduced stiffness of lamina. Consequently, the normal force resultants $\boldsymbol{N}$, moment resultants $\boldsymbol{M}$ and shear force resultants $\boldsymbol{Q}$ are obtained as:

$$\begin{aligned} \boldsymbol{N} &= [N_x, N_y, N_{xy}]^\top = \int_{-d/2}^{d/2} [\sigma_{xx}, \sigma_{yy}, \sigma_{xy}]^\top dz, \\ \boldsymbol{M} &= [M_x, M_y, M_{xy}]^\top = \int_{-d/2}^{d/2} [\sigma_{xx}, \sigma_{yy}, \sigma_{xy}]^\top z dz, \\ \boldsymbol{Q} &= [Q_x, Q_y]^\top = \int_{-d/2}^{d/2} [\sigma_{xz}, \sigma_{yz}]^\top dz. \end{aligned} \tag{2.14}$$

Substituting the strain-displacement relations Eq. (2.12) and stress-strain relations Eq. (2.13) into Eq. (2.14), the force resultants are reformulated as:

$$\boldsymbol{N} = \boldsymbol{A}\boldsymbol{\epsilon}_0 + \boldsymbol{B}\boldsymbol{\kappa},\ \boldsymbol{M} = \boldsymbol{B}\boldsymbol{\epsilon}_0 + \boldsymbol{D}\boldsymbol{\kappa},\ \boldsymbol{Q} = \bar{\boldsymbol{A}}\boldsymbol{\gamma}, \tag{2.15}$$

In these constitutive equations, $\boldsymbol{A}$, $\boldsymbol{B}$, $\boldsymbol{D}$, and $\bar{\boldsymbol{A}}$ are symmetric stiffness matrices representing extensional, bending-extensional coupling, bending, and shear stiffness, respectively. These stiffness are defined as follows:

$$\begin{aligned}
A_{ij} &= \sum_k \bar{Q}_{ij}|_k(z_k - z_{k-1}), i,j = 1,2,6.\\
B_{ij} &= \frac{1}{2}\sum_k \bar{Q}_{ij}|_k(z_k^2 - z_{k-1}^2), i,j = 1,2,6.\\
D_{ij} &= \frac{1}{3}\sum_k \bar{Q}_{ij}|_k(z_k^3 - z_{k-1}^3), i,j = 1,2,6.\\
\bar{A}_{ij} &= \alpha_i\alpha_j\sum_k \bar{Q}_{ij}|_k(z_k - z_{k-1}), i,j = 4,5.
\end{aligned} \tag{2.16}$$

Here, α_i and α_j are shear correction factors used to account for the non-uniform distribution of shear strain across the plate thickness. Typically, this factor is taken as $\pi^2/12$ [86].

Applying Hamilton's principle yields the equations of motion in terms of force and moment resultants [87], assuming that only an out-of-plane external impact force $f(t)$ is applied:

$$\begin{aligned}
&\frac{\partial N_x}{\partial x} + \frac{\partial N_{xy}}{\partial y} = I_1\frac{\partial^2 u_0}{\partial t^2} + I_2\frac{\partial^2 \varphi_x}{\partial t^2},\\
&\frac{\partial N_{xy}}{\partial x} + \frac{\partial N_y}{\partial y} = I_1\frac{\partial^2 v_0}{\partial t^2} + I_2\frac{\partial^2 \varphi_y}{\partial t^2},\\
&\frac{\partial Q_x}{\partial x} + \frac{\partial Q_y}{\partial y} + f(t) = I_1\frac{\partial^2 w_0}{\partial t^2},\\
&\frac{\partial M_x}{\partial x} + \frac{\partial M_{xy}}{\partial y} - Q_x = I_3\frac{\partial^2 \varphi_x}{\partial t^2} + I_2\frac{\partial^2 u_0}{\partial t^2},\\
&\frac{\partial M_{xy}}{\partial x} + \frac{\partial M_y}{\partial y} - Q_y = I_3\frac{\partial^2 \varphi_y}{\partial t^2} + I_2\frac{\partial^2 v_0}{\partial t^2},
\end{aligned} \tag{2.17}$$

where inertial terms I_1, I_2, I_3 are defined in terms of the material density ρ and plate thickness d:

$$(I_1, I_2, I_3) = \int_{-d/2}^{d/2} \rho(1, z, z^2)dz. \tag{2.18}$$

By substituting the force and moment resultants with the constitutive equations Eq. (2.15) and the strain-displacement relations Eq. (2.12), the equations of motion can be further expressed in terms of the displacement components $u_0, v_0, w_0, \psi_x, \psi_y$. These equations can be expressed using a differential operator as follows:

$$\mathcal{L}\mathbf{d} = \mathbf{F}, \quad \mathbf{d} = [u_0,\ v_0,\ w_0,\ \varphi_x,\ \varphi_y]^\top, \quad \mathbf{F} = [0,\ 0,\ -f(t),\ 0,\ 0]^\top, \tag{2.19}$$

where $\mathcal{L}$ denotes a symmetric differential operator, $\mathbf{d}$ is the displacement vector, and $\mathbf{F}$ represents the external force. In this study, only the force component in the out-of-plane direction is considered. The operator $\mathcal{L}$ is a 5×5 matrix, as there are five differential equations corresponding to five displacement variables. Further details on the derivation of the governing equations for laminated plates using FSDT can be found in [85, 87–89]. The independent matrix elements $\mathcal{L}_{ij}$ of the symmetric operator $\mathcal{L}$ are provided in Appendix A.

2.2.2 Classical Plate Theory (CPT)

Classical Plate Theory (CPT) [83] neglects the effects of shear deformation (i.e., zero shear strains ϵ_{xz} and ϵ_{yz}), rotational inertia (zero I_3), and transverse normal strain (zero ϵ_{zz}). Consequently, the functions γ_x and γ_y in Eq. (2.12) vanish, leading to $\varphi_x = -\frac{\partial w_0}{\partial x}$ and $\varphi_y = -\frac{\partial w_0}{\partial y}$. While the midplane strains remain unchanged, the plate curvatures κ are reformulated in terms of w_0 as follows:

$$\kappa = \left[-\frac{\partial^2 w_0}{\partial x^2},\ -\frac{\partial^2 w_0}{\partial y^2},\ -2\frac{\partial^2 w_0}{\partial x \partial y}\right]^\top,\ \gamma = 0,\ I_3 = 0. \tag{2.20}$$

Substituting Eq. (2.20) into the last three equations of Eq. (2.17) yields the equations of motion for CPT in terms of force and moment resultants [90]:

$$\begin{aligned}
&\frac{\partial N_x}{\partial x} + \frac{\partial N_{xy}}{\partial y} = I_1 \frac{\partial^2 u_0}{\partial t^2} - I_2 \frac{\partial^3 w_0}{\partial t^2 \partial x}, \\
&\frac{\partial N_{xy}}{\partial x} + \frac{\partial N_y}{\partial y} = I_1 \frac{\partial^2 v_0}{\partial t^2} - I_2 \frac{\partial^3 w_0}{\partial t^2 \partial y}, \\
&\frac{\partial^2 M_x}{\partial x^2} + 2\frac{\partial^2 M_{xy}}{\partial x \partial y} + \frac{\partial^2 M_{yy}}{\partial y^2} + f(t) = I_1 \frac{\partial^2 w_0}{\partial t^2} + I_2 (\frac{\partial^3 u_0}{\partial t^2 \partial x} + \frac{\partial^3 v_0}{\partial t^2 \partial y}).
\end{aligned} \tag{2.21}$$

Thus, there are three differential equations governing the motion of CPT plates. The differential operator for CPT is a 3×3 matrix, corresponding to the three independent displacements u_0, v_0, w_0:

$$\mathcal{L}\mathbf{d} = \mathbf{F}, \quad \mathbf{d} = [u_0,\ v_0,\ w_0]^\top, \quad \mathbf{F} = [0,\ 0,\ f(t)]^\top. \tag{2.22}$$

The equations of motion in terms of displacements for angle-ply laminates based on CPT are provided in Appendix B.

2.3 Characteristics of Impact-induced Waves

2.3.1 Wave types, modes and dispersion

Impact-induced waves in plate-like structures can manifest in several forms [91], depending on the geometry, material properties, and impact conditions. These waves include bulk waves—longitudinal and shear waves [92,93]—as well as guided waves, such as Lamb waves [89,94,95], shear horizontal (SH) waves [96,97], and Rayleigh-like surface waves [92,98].

Among these, bulk waves primarily dominate the near-field response immediately after impact but undergo multiple reflections at the plate's boundaries [99], giving rise to guided waves [100]. Rayleigh-like surface waves, which are confined to the plate's surface, may also emerge; however, their prominence is diminished in plate structures due to finite thickness effects [92].

Shear horizontal (SH) waves and Lamb waves are the primary guided wave types in plate-like structures, each exhibiting distinct propagation characteristics. SH waves, characterised by in-plane shear motion perpendicular to the propagation direction, do not involve out-of-plane displacements [101]. This unique property makes them less susceptible to boundary reflections and mode conversions, providing a more stable wave propagation in certain applications. SH waves are particularly advantageous in the inspection of composite and anisotropic materials, where their polarisation enhances sensitivity to specific structural features [97]. However, in impact scenarios where out-of-plane motion dominates, SH waves play a less significant role.

Lamb waves, on the other hand, involve both in-plane and out-of-plane particle motion and are strongly influenced by the plate thickness and material properties. They exist in two fundamental types: symmetric (S) and antisymmetric (A) modes [102], with multiple higher-order modes emerging at higher frequencies. Due to their multimodal and dispersive nature, Lamb waves are highly sensitive to structural discontinuities, such as cracks, delaminations, and impact-induced damage [103]. These characteristics make them widely used for non-destructive evaluation (NDT) and SHM in aerospace and civil engineering applications. However, their complexity, including mode coupling and wave dispersion, often requires advanced signal processing techniques for accurate interpretation.

Dispersion describes the frequency dependence of wave velocity, meaning that different frequency components of a wave propagate at different speeds. To illustrate the mode diversity of Lamb waves, Fig. 2.4 presents the dispersion curves, which depict the relationship between phase velocity and wave frequency for isotropic aluminium alloy 1100. These curves are obtained by numerically solving the Helmholtz decomposition of the Lamé-Navier equation using the open-source software Dispersion Calculator [104].

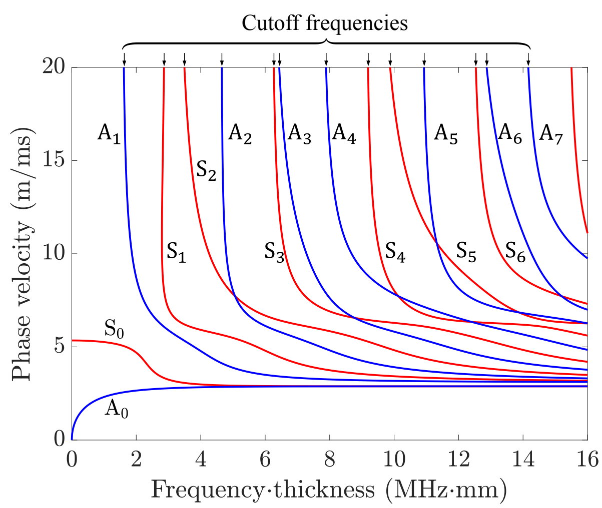

Figure 2.4: Dispersion curves of Lamb wave in an isotropic plate (aluminium alloy 1100).

The figure clearly illustrates multiple symmetric (S) and antisymmetric (A) modes, represented by solid red and blue curves, respectively. Each mode is characterised by a distinct cutoff frequency, above which it begins to propagate. Notably, the fundamental modes, A0 and S0, have zero cutoff frequencies, allowing them to propagate across the entire frequency spectrum. In contrast, higher-order modes exhibit positive cutoff frequencies, meaning they only emerge beyond specific frequency thresholds. As a result, in the low-frequency range, only the A0 and S0 modes are present.

The dispersion characteristics of Lamb waves fundamentally govern wave propagation behaviour in composite plate-like structures. As discussed in Section 2.1.3, low-frequency structural modes dominate the impact response, with low-order Lamb waves (A0 and S0 modes) playing a crucial role in impact-induced wave propagation. Experimental studies have confirmed that impact events in composite laminated structures generate both in-plane waves (S0 mode) and out-of-plane flexural waves (A0 mode) [105, 106].

However, in practical low-velocity impact scenarios, in-plane waves (S0 mode) tend to have relatively low amplitudes, often making them difficult to detect [107]. Even in cases of oblique impacts at 45 degrees, experimental evidence has shown that flexural waves (A0 mode) dominate the response, while the amplitude of in-plane waves (S0 mode) remains significantly small [107], particularly when the impact occurs at a considerable distance from the sensor. Detecting these in-plane waves typically requires a high sampling frequency [30, 108, 109], which may not always be feasible in practical applications. Given these observations, this research focuses on out-of-plane flexural waves (A0 mode), as they are more prominent, more easily captured by sensors, and carry critical information about the impact event.

2.3.2 Spectrum/dispersion relation derivation based on plate theory

2.3.2.1 Spectrum relation derivation

While plate theories inherently simplify shear deformation across the plate thickness, they effectively capture the behaviour of low-order wave modes. For instance, the FSDT, which includes five displacement components $(u_0, v_0, w_0, \varphi_x, \varphi_y)$, is capable of modelling the fundamental symmetric (S0), antisymmetric (A0), shear-horizontal (SH0), and higher-order A1 and SH1 wave modes (consistent with the assertion in [110] that the FSDT captures two symmetric and three antisymmetric modes). In contrast, the CPT, which considers only three displacement components (u_0, v_0, w_0), is limited to modelling the S0, SH0, and A0 modes.

To derive the dispersion relations based on plate theory, the harmonic wave propagating in an infinite laminated plate can be expressed as:

$$\mathbf{d} = [u_0, v_0, w_0, \varphi_x, \varphi_y]^\top = [U_0, V_0, W_0, \Phi_x, \Phi_y]^\top e^{i(k_x x + k_y y - \omega t)}, \tag{2.23}$$

where $\mathbf{D} = [U_0, V_0, W_0, \Phi_x, \Phi_y]^\top$ represents the wave amplitude components, k_x, k_y are the wavenumbers along the x and y directions, respectively, i is the imaginary unit, ω denotes the angular frequency. Based on this representation, key wave propagation characteristics can be derived, including the phase velocity v_p and its propagation direction θ, group velocity vector $\mathbf{v_g}$ (which represents the rate of energy transport) and the group velocity direction θ_g, which indicates the direction of energy flow.

$$v_p = \frac{\omega}{\sqrt{k_x^2 + k_y^2}},\ \tan\theta = \frac{k_y}{k_x},\ \mathbf{v_g} = [\frac{\partial\omega}{\partial k_x},\ \frac{\partial\omega}{\partial k_y}],\ \tan\theta_g = \frac{\partial\omega/\partial k_y}{\partial\omega/\partial k_x},\ v_g = \sqrt{(\frac{\partial\omega}{\partial k_x})^2 + (\frac{\partial\omega}{\partial k_y})^2}. \tag{2.24}$$

From the waveform expression in Eq. (2.23), it follows that only real wavenumbers result in waves with positive group velocity propagating efficiently in a laminated plate. A positive imaginary component in the wavenumber signifies an evanescent wave, which undergoes amplitude decay and does not sustain energy transmission over long distances. Conversely, a negative imaginary component would correspond to an exponentially growing wave, which is non-physical in real-world scenarios.

To simplify the mathematical formulation, instead of solving for complex wavenumbers k_x and k_y in the complex plane—where they may have different phases—for a given frequency ω, wavenumbers k_x, k_y are assumed to be real positive, aiding in definition of real phase velocity direction $\theta = \arctan\frac{k_y}{k_x}$ and real wavenumber $k = \sqrt{k_x^2 + k_y^2}$. By adopting this approach, the computational complexity is significantly reduced. The phase velocity v_p, group velocity vector $\mathbf{v_g}$ and group velocity direction θ_g with respect to k and θ can be derived using chain rule:

$$\begin{aligned}
&v_p = \frac{\omega}{k},\ k = \sqrt{k_x^2 + k_y^2},\ \theta = \arctan\frac{k_y}{k_x},\\
&\mathbf{v_g} = [\frac{\partial\omega}{\partial k_x},\ \frac{\partial\omega}{\partial k_y}] = [\frac{\partial\omega}{\partial k}\frac{\partial k}{\partial k_x} + \frac{\partial\omega}{\partial\theta}\frac{\partial\theta}{\partial k_x},\ \frac{\partial\omega}{\partial k}\frac{\partial k}{\partial k_y} + \frac{\partial\omega}{\partial\theta}\frac{\partial\theta}{\partial k_y}] = [\frac{k_x}{k}\frac{\partial\omega}{\partial k} - \frac{k_y}{k^2}\frac{\partial\omega}{\partial\theta},\ \frac{k_y}{k}\frac{\partial\omega}{\partial k} + \frac{k_x}{k^2}\frac{\partial\omega}{\partial\theta}],\\
&\tan\theta_g = \frac{\frac{k_y}{k}\frac{\partial\omega}{\partial k} + \frac{k_x}{k^2}\frac{\partial\omega}{\partial\theta}}{\frac{k_x}{k}\frac{\partial\omega}{\partial k} - \frac{k_y}{k^2}\frac{\partial\omega}{\partial\theta}} = \frac{kk_y\frac{\partial\omega}{\partial k} + k_x\frac{\partial\omega}{\partial\theta}}{kk_x\frac{\partial\omega}{\partial k} - k_y\frac{\partial\omega}{\partial\theta}} = \frac{k\sin\theta\frac{\partial\omega}{\partial k} + \cos\theta\frac{\partial\omega}{\partial\theta}}{k\cos\theta\frac{\partial\omega}{\partial k} - \sin\theta\frac{\partial\omega}{\partial\theta}},\ v_g = \sqrt{(\frac{\partial\omega}{\partial k})^2 + \frac{1}{k^2}(\frac{\partial\omega}{\partial\theta})^2}.
\end{aligned} \tag{2.25}$$

For flat plates, the phase velocity direction θ aligns with the group velocity direction θ_g [111]. This occurs because the influence of directional anisotropy for flat plate without curvature, quantified by $\frac{1}{k}\frac{\partial\omega}{\partial\theta}$, is typically much smaller than that of wave dispersion, represented by $\frac{\partial\omega}{\partial k}$. Consequently, the group velocity v_g, as given in Eq. (2.25), can be approximated by $\frac{\partial \omega}{\partial k}$. This approximation simplifies wave propagation analysis for anisotropic flat plates. By substituting k_x, k_y in Eq. (2.23) with $k\cos\theta, k\sin\theta$, respectively, the waveform is re-parameterised by k, ω, θ.

By substituting this reformulated waveform parameterised by k, θ into governing equation of motion in terms of displacements and neglecting external forces, the governing equations describing wave propagation in laminated plate are obtained:

$$\mathbf{G}\mathbf{D} = 0 \implies \det \mathbf{G} = P(k, \omega; \theta) = 0. \tag{2.26}$$

Here, the matrix $\mathbf{G}$ is derived by replacing the differential operators $\mathcal{L}$ in the governing equation with their wavenumber representations. Specifically, the second-order partial derivatives $\frac{\partial^2}{\partial x^2}$, $\frac{\partial^2}{\partial x \partial y}$, and $\frac{\partial^2}{\partial y^2}$ are substituted with $-k^2\cos^2\theta$, $-k^2\cos\theta\sin\theta$, and $-k^2\sin^2\theta$, respectively. Similarly, the first-order derivatives $\frac{\partial}{\partial x}$ and $\frac{\partial}{\partial y}$ are replaced by $ik\cos\theta$ and $ik\sin\theta$.

For a non-trivial solution $\mathbf{D}$, the matrix $\mathbf{G}$ must be singular, which leads to the spectrum relation $\det \mathbf{G} = P(k, \omega; \theta) = 0$, where $P(k, \omega; \theta)$ is a polynomial in terms of wavenumber k and frequency ω. This spectrum relation establishes the fundamental relationship between wavenumber k and frequency ω for an arbitrary velocity direction θ, describes the propagation characteristics of guided waves in laminated plates

2.3.2.2 Dispersion relation derivation

For a given frequency ω and propagation direction θ, the corresponding wavenumber k can be obtained by solving Eq. (2.26), thereby generating the spectrum relation curve expressed as $\omega = sr(k; \theta)$. The phase velocity in direction θ is then given by $v_p(\theta) = \omega/k$. To calculate the group velocity, denoted as $v_g(\theta) = \partial\omega/\partial k$, one method involves utilising the difference operation $v_g(\theta) \approx \Delta\omega/\Delta k$ with dense sampling points on the spectrum relation curve $\omega = sr(k; \theta)$. However, this method is computationally costly, and its accuracy depends on the difference step size. Previous studies [74, 87, 112] do not analytically derive the group velocity from the spectrum relations. In this thesis, instead of relying on numerical approximations, the group velocity is analytically derived by implicit differentiation, which takes the partial derivative of Eq. (2.26) with respect to the wavenumber k for a given wave direction θ:

$$\frac{\partial}{\partial k}\det[\mathbf{G}] = \frac{\partial \det[\mathbf{G}]}{\partial k} + \frac{\partial \det[\mathbf{G}]}{\partial \omega}\frac{\partial \omega}{\partial k} = 0. \tag{2.27}$$

Simplifying Eq. (2.27) yields analytical group velocity v_g:

$$v_g = \frac{\partial \omega}{\partial k} = -\frac{\partial \det[\mathbf{G}]/\partial k}{\partial \det[\mathbf{G}]/\partial \omega} = -\frac{\mathrm{tr}\left[\mathrm{adj}(\mathbf{G})\frac{\partial \mathbf{G}}{\partial k}\right]}{\mathrm{tr}\left[\mathrm{adj}(\mathbf{G})\frac{\partial \mathbf{G}}{\partial \omega}\right]}, \tag{2.28}$$

where $\mathrm{tr}(\cdot)$ denotes the trace operator, $\mathrm{adj}(\mathbf{G})$ is the adjugate of the matrix $\mathbf{G}$, $\frac{\partial \mathbf{G}}{\partial k}$ and $\frac{\partial \mathbf{G}}{\partial \omega}$ are the element-wise derivatives of the matrix $\mathbf{G}$ with respect to k and ω, respectively.

The derivation of the spectrum and dispersion relations based on CPT can also be implemented using the approach outlined above, leading to the same governing equations of spectrum relation Eq. (2.26) and dispersion relation Eq. (2.28). However, due to the simplifying assumptions of CPT, the dimensionality of the system is reduced. Specifically, the size of the matrix $\mathbf{G}$ and the displacement vector $\mathbf{D}$ decrease from 5, as in FSDT, to 3 in CPT.

2.3.3 Dispersion relations for symmetrically-laminated plates

Since symmetrical laminates are widely employed in practical applications [87], this research focuses on symmetrically laminated composites, which does not impose a significant limitation on generality. In a symmetrically laminated plate, the bending-extensional coupling stiffness $\boldsymbol{B}$ and the inertial term I_2 vanish, leading to a complete decoupling of in-plane and out-of-plane motions [87]. The governing equations of motion for symmetrical laminates are detailed in Appendix C for the FSDT and in Appendix D for the CPT.

Utilising the dispersion relation derivation framework outlined earlier, the matrix $\mathbf{G}$ for symmetrical laminates is obtained for both FSDT and CPT plates. Due to the decoupling of in-plane and out-of-plane motions, the matrix $\mathbf{G}$ is partitioned into two independent blocks: a 2×2 submatrix $\mathbf{G}_i$ governing in-plane waves and a separate submatrix $\mathbf{G}_o$ governing out-of-plane waves:

$$\mathbf{G} = \begin{bmatrix} \mathbf{G}_i & \mathbf{0} \\ \mathbf{0} & \mathbf{G}_o \end{bmatrix}, \tag{2.29}$$

where the square matrix $\mathbf{G}_o$ has dimensions of 1×1 for CPT and 3×3 for FSDT.

2.3.3.1 Non-dispersive in-plane waves based on CPT and FSDT

Notably, the in-plane submatrix $\mathbf{G}_i$ remains identical for both plate theories, as the primary differences between CPT and FSDT arise from variations in shear strain distribution along the thickness. The in-plane matrix $\mathbf{G}_i$ is derived as [87, 113]:

$$\begin{aligned}
&\mathbf{G}_i = k^2 \begin{bmatrix} C_{11} - I_1 v_p^2 & C_{12} \\ C_{12} & C_{22} - I_1 v_p^2 \end{bmatrix}, \ \mathbf{G}_i \begin{bmatrix} U_0 \\ V_0 \end{bmatrix} = 0, \\
&C_{11} = A_{11}\cos^2\theta + A_{66}\sin^2\theta + 2A_{16}\sin\theta\cos\theta, \\
&C_{12} = A_{16}\cos^2\theta + A_{26}\sin^2\theta + (A_{12} + A_{66})\sin\theta\cos\theta, \\
&C_{22} = A_{66}\cos^2\theta + A_{22}\sin^2\theta + 2A_{26}\sin\theta\cos\theta.
\end{aligned} \tag{2.30}$$

Here, $A_{ij}, i, j = 1, 2, 6$ represent the extensional stiffness components, as defined in Section 2.2.1. For a non-trivial solution, the determinant of the coefficient matrix $\mathbf{G}_i$ must be zero ($\det \mathbf{G}_i = 0$), yielding the direction-dependent phase velocity solution:

$$v_p^2 = \frac{-C_b \pm \sqrt{C_b^2 - 4C_aC_c}}{2C_a}, \ C_a = I_1^2, \ C_b = -I_1(C_{11} + C_{22}), \ C_c = C_{11}C_{22} - C_{12}^2. \tag{2.31}$$

The operation $\pm$ corresponds to two distinct wave modes with different phase velocities. These two solutions precisely represent the in-plane extensional wave (S0 mode) and the in-plane shear wave (SH0 mode), where the extensional wave is associated with the larger velocity value.

2.3.3.2 Dispersive flexural waves based on CPT

For CPT, the out-of-plane submatrix $\mathbf{G}_o$ in Eq. (2.29) contains an element. Therefore, when setting $\det \mathbf{G}_o = 0$, the spectrum relation for the flexural wave (A0 mode) is given by [87]:

$$I_1 \frac{\omega^2}{k^4} = D_{11}\cos^4\theta + 4D_{16}\sin\theta\cos^3\theta + 2(D_{12} + 2D_{66})\sin^2\theta\cos^2\theta + 4D_{26}\sin^3\theta\cos\theta + D_{22}\sin^4\theta. \tag{2.32}$$

This expression reveals a non-linear relationship between wave frequency ω and wavenumver k. Specifically, wave frequency ω is directly proportional to the square of wave number k, indicating that higher-frequency waves propagate at greater speeds than their lower-frequency counterparts. The flexural wave (A0 mode) exhibits strong dispersion.

2.3.3.3 Dispersive flexural waves based on FSDT

For FSDT, the out-of-plane submatrix $\mathbf{G}_o$ is a 3×3 symmetric matrix given by [86–89, 112, 114]:

$$\mathbf{G}_o = \begin{bmatrix} g_{11} & g_{12} & g_{13} \\ g_{12} & g_{22} & g_{23} \\ g_{13} & g_{23} & g_{33} \end{bmatrix}, \; \mathbf{G}_o \begin{bmatrix} W_0 \\ \Phi_x \\ \Phi_y \end{bmatrix} = 0. \tag{2.33}$$

For a symmetrically laminated composite plate, the elements g_{ij}, for $i, j = 1, 2, 3$, of the coefficient matrix $\mathbf{G}_0$ are given by:

$$\begin{aligned} g_{11} &= -(A_{44}\sin^2\theta + A_{55}\cos^2\theta + 2A_{45}\sin\theta\cos\theta)k^2 + I_1\omega^2, \\ g_{12} &= i(A_{55}\cos\theta + A_{45}\sin\theta)k, \; g_{13} = i(A_{45}\cos\theta + A_{44}\sin\theta)k, \\ g_{22} &= (D_{11}\cos^2\theta + 2D_{16}\sin\theta\cos\theta + D_{66}\sin^2\theta)k^2 + A_{55} - I_3\omega^2, \\ g_{23} &= [(D_{12} + D_{66})\sin\theta\cos\theta + D_{16}\cos^2\theta + D_{26}\sin^2\theta]k^2 + A_{45}, \\ g_{33} &= (D_{22}\sin^2\theta + D_{66}\cos^2\theta + 2D_{26}\sin\theta\cos\theta)k^2 + A_{44} - I_3\omega^2, \end{aligned} \tag{2.34}$$

where i denotes the imaginary unit ($i^2 = -1$). For a non-trivial solution, the determinant of the matrix $\mathbf{G}_o$ must be zero:

$$\det \mathbf{G}_o = 0, \tag{2.35}$$

leading to a sextic polynomial equation in terms of the wave frequency ω, which contains only even-degree terms. For each wavenumber k, there are three positive frequency solutions to this polynomial equation, corresponding to three values of phase velocity $v_p = \omega/k$ and three wave modes A0, A1, and SH1.

2.4 Impact Identification with a Sparse Sensor Network

2.4.1 Signal processing techniques for impact-induced waves

The impact-induced waves are recorded by passive sensors integrated within the composite structure, producing time-series sensor signals. Given their inherently dispersive and multimodal nature, these signals often exhibit complex propagation characteristics, making accurate and efficient impact identification challenging. To extract meaningful information, advanced signal processing techniques are essential.

2.4.1.1 De-noising

One fundamental yet effective approach is de-noising, which mitigates the influence of measurement noise and environmental disturbances. By enhancing the Signal-to-Noise Ratio (SNR), de-noising techniques improve the clarity of wave features, thereby facilitating more accurate impact localisation and characterisation.

A straightforward method involves subtracting the mean of a noise-only segment from the signal to ensure the noise component has a zero mean. Building upon this, more sophisticated techniques such as wavelet thresholding, empirical mode decomposition (EMD) [115], and adaptive filtering can be employed to further enhance signal quality. These advanced methods selectively suppress noise while preserving critical waveform characteristics, making them particularly effective for processing dispersive and multimodal impact-induced sensor signals. However, the choice of de-noising method should be guided by the specific objectives of the analysis, as different techniques offer varying trade-offs between noise suppression and signal distortion, depending on the intended application of the impact-induced sensor signals.

2.4.1.2 Spectral analysis

The spectral analysis of impact-induced sensor signals is fundamentally based on the Fourier Transform (FT) [116], one of the most powerful tools in signal processing. The FT decomposes a signal into its constituent frequencies, converting it from the time domain to the frequency domain. This transformation not only reveals the spectral content of the signal but also simplifies convolution operations, as the convolution of two functions in the time domain is equivalent to the element-wise product of their Fourier transforms in the frequency domain.

This convolution relationship between the impact-induced sensor signal $s(t)$, the impact force history $f(t)$ and the transfer function $h(t)$ for a linear structural system can be expresses:

$$\begin{aligned} s(t) = f(t) \circ h(t) = \int_0^t f(t)h(t-\tau)d\tau \;\leftrightharpoons\; \hat{s}(\omega) = \hat{f}(\omega)\hat{h}(\omega), \\ \hat{s}(\omega) = \mathcal{F}(s(t)) = \int_{-\infty}^{\infty} s(t)e^{-i\omega t}dt, \end{aligned} \tag{2.36}$$

where $\mathcal{F}$ denotes the Fourier transform operator, ω represents angular frequency, and variables with a hat (e.g., $\hat{s}$) represent their corresponding frequency-domain spectra.

By analysing the spectral distribution of impact-induced sensor signals $s(t)$, structural modes and their associated natural frequencies can be identified. Fig. 2.5(a) presents an impact-induced sensor signal, along with its Power Spectral Density (PSD), for a real-world hammer impact on a composite laminated plate recorded by a PZT sensor. This signal was captured at a sampling frequency of 2 MHz over a 20 ms sampling window. In computing the PSD, the number of Fast Fourier Transform (FFT) [117] points was set equal to the signal length. Additionally, a Hanning window of the same length as the signal was applied to mitigate spectral leakage and minimise aliasing effects.

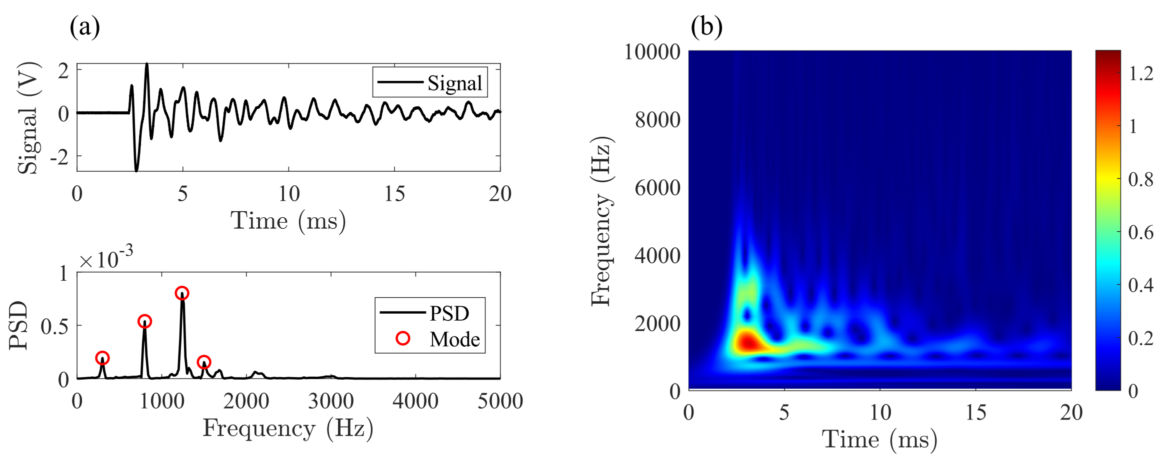

Figure 2.5: Spectral and time-frequency analysis of impact-induced sensor signal: (a) sensor signal and its PSD calcuated by FFT, (b) time-frequency analysis of sensor signal by wavelet transform.

The PSD plot confirms the dominance of low-frequency components in the impact-induced sensor signal, consistent with the discussion in Section 2.1.3. The finite-duration impact force predominantly excites low-frequency modes, which are identified as spectral peaks marked by red circles in the PSD plot.

2.4.1.3 Time-frequency analysis

However, FFT-based spectral analysis lacks temporal resolution, meaning it does not capture how frequency components evolve over time. To incorporate temporal information into the analysis, advanced time-frequency techniques such as the Short-Time Fourier Transform (STFT) and Wavelet Transform (WT) [118] have been developed. Unlike the FFT, which provides a global frequency representation, the wavelet transform offers a localised time-frequency representation, making it particularly suitable for analysing transient and non-stationary signals.

The WT employs a compactly supported wavelet function, which is characterised by two key parameters: the scaling parameter a_c, which adjusts the frequency range, allowing for the examination of both high- and low-frequency components; the shifting parameter b_s, which controls the time localisation of the wavelet function. Mathematically, the WT is defined as the inner product of the signal with a scaled and shifted wavelet function:

$$W_s(a_c, b_s) = \frac{1}{\sqrt{a_c}} \int_{-\infty}^{\infty} s(t)\psi_{a_c,b_s}(t)dt,\ \psi_{a_c,b_s}(t) = \frac{1}{\sqrt{a_c}}\psi(\frac{t-b_s}{a_c}), \tag{2.37}$$

where $\psi_{a_c,b_s}(t)$ represents the wavelet function at a given scaling parameter a_c and shifting parameter b_s, and $W_s(a_c, b_s)$ is the corresponding wavelet coefficients evaluated at this wavelet function. By continuously adjusting these parameters, a time-frequency analysis of the signal can be performed, offering a more detailed representation of transient events.

Fig. 2.5(b) illustrates the wavelet analysis of the impact-induced sensor signal shown in (a). The broadband low-frequency spectrum of the impact-induced sensor signals is reaffirmed, consistent with previous spectral analysis. Additionally, the WT enables not only the identification of dominant frequencies but also the precise determination of when these frequencies appear within the signal. This capability provides a deeper understanding of the time-dependent characteristics of impact-induced wave propagation.

2.4.1.4 Feature extraction

A signal feature is defined as a key piece of information that can be extracted from a signal to characterise its behaviour. Common examples include signal energy, maximum amplitude, dominant frequency, signal envelope, and the time at which the maximum amplitude occurs. These features serve as fundamental descriptors in signal analysis and play a crucial role in various applications, including impact identification.

In impact identification, certain features exhibit strong correlations with physical impact parameters. For instance, both signal energy and maximum amplitude are positively correlated with the impact energy level and impact peak force. Experimental studies, such as those conducted by Seno et al. [44], have validated a linear relationship between impact peak force and maximum amplitude of the signal. This relationship has been effectively utilised to estimate peak impact forces in composite structures.

Among the various features extracted from impact-induced sensor signals, the most critical for impact localisation is the time difference of arrival (TDOA). Accurate TDOA estimation is essential for determining the impact source location using triangulation-based methods. Numerous techniques have been developed to extract TDOA from impact-induced sensor signals with high precision, including: Akaike Information Criterion (AIC) [36, 62], Continuous Wavelet Transform (CWT) [26, 28, 32], Envelope Threshold (ET) [37, 40, 68], and Normalised Smoothed Envelope Threshold (NSET) [35, 43].

A comparative experimental study conducted in [72] comprehensively evaluated these methods for their accuracy and consistency in TDOA extraction. The results demonstrated that the NSET method achieved the highest precision in estimating TDOA across different impact locations.

Due to the dispersive nature of impact-induced waves, as analysed in Section 2.3, the extracted TDOA is inherently frequency-dependent. In the case of an impact event on a composite structure, the TDOA values obtained from impact-induced waves using the aforementioned methods form a frequency-dependent vector of size N_s, where N_s represents the total number of passive sensors in the network:

$$\begin{aligned}&\Delta\mathbf{t}(\omega) = [\Delta t_{i1}(\omega),\ \Delta t_{i2}(\omega),\ \Delta t_{i3}(\omega),\ \cdots,\ \Delta t_{iN_s}(\omega)]^\top,\\&\Delta t_{ij}(\omega) = t_j(\omega) - t_i(\omega),\ i, j \in \mathbb{N}_{1N_s},\ \mathbb{N}_{1N_s} = \{1, 2, 3, ..., N_s\},\end{aligned} \tag{2.38}$$

where $t_j(\omega)$ denotes the time taken for the wave to propagate from the impact point to the j-th sensor at frequency ω. A specific sensor i, where $i \in \mathbb{N}_{1N_s}$, is designated as the anchor sensor, serving as the reference point for computing relative time differences. For brevity, the notation $\mathbb{N}_{mn}, m \leqslant n$ is introduced to denote the set of natural numbers from integer m to n.

2.4.2 Physics-based impact localisation via triangulation

Triangulation [119] is a widely used method for impact localisation based on the propagation of impact-induced waves, given known sensor locations. It leverages the fundamental physical relationship that the distance travelled by a wave equals the product of its group velocity and travel time.

As illustrated in Fig. 2.6, four sensors are positioned at the corners of a composite plate. Prior studies on sensor placement optimisation have shown that optimal impact identification performance is achieved when the sensor network maximises the coverage area [120–122]. Upon impact, dispersive waves are generated and propagate outward from the impact location to the surrounding sensors. This wave propagation satisfies the fundamental Time of Arrival (TOA) equation for each sensor:

$$d_j = v_g(\theta_j, \omega) t_j(\omega), \ j \in \mathbb{N}_{1N_s}, \tag{2.39}$$

where d_j is the distance from the impact point to the j-th sensor, $v_g(\theta_j, \omega)$ is the wave group velocity along the corresponding path at frequency ω, and $t_j(\omega)$ is the wave arrival time at the sensor at frequency ω.

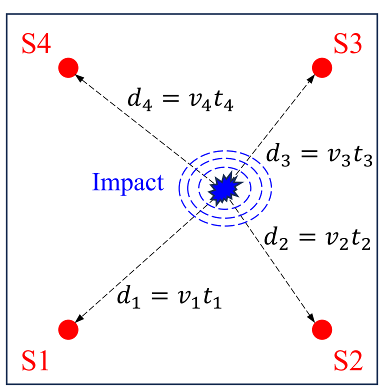

Figure 2.6: Impact localisation using triangulation on plate structures.

By subtracting the wave propagation time at an anchor sensor (say sensor 1) from those at the other sensors, a system of $N_s - 1$ nonlinear equations is formulated, relating the unknown impact location (x, y), sensor coordinates (x_j, y_j), TDOA and and direction-dependent Group Velocity Profile (GVP) $v_g(\theta)$ as follows [25]:

$$\Delta t_{1j}(\omega) = t_j(\omega) - t_1(\omega) = \frac{\sqrt{(x - x_j)^2 + (y - y_j)^2}}{v_g(\theta_j, \omega)} - \frac{\sqrt{(x - x_1)^2 + (y - y_1)^2}}{v_g(\theta_1, \omega)}, \; j \in \mathbb{N}_{2N_s}. \quad (2.40)$$

In anisotropic composite structures, the group velocity at a given frequency ω is direction-dependent, meaning that the triangulation system involves $N_s + 2$ unknowns: the two impact location coordinates x, y and N_s group velocities $v(\theta_j, \omega)$, where $j \in \mathbb{N}_{1N_s}$. As a result, the system is underdetermined and cannot be directly solved without additional constraints.

To make the triangulation solvable, two main strategies have been explored: sensor clustering, which assumes a uniform group velocity from the impact point to a cluster of sensors [61,62], and pre-determined GVP, which is obtained in advance [27–29]. While the sensor clustering approach is resource-intensive, requiring a significant number of sensors and extensive impact data acquisition, pre-measuring the GVP offers a resource-efficient alternative. If more than three sensors are deployed, the system with known GVP becomes overdetermined.

In addition, it is essential to recognize that the GVP $v_g(\theta)$ within a structure is fundamentally governed by the structure's inherent properties and remains unaffected by external impacts as long as no damage occurs. This highlights the high generalisability of GVP for impact localisation across varying impact conditions. Upon a damaging impact, wave propagation initiates at the point of contact, before any damage is present. Consequently, the initial segment of the impact-induced wave reflects the characteristics of wave propagation in an undamaged structure. However, considering the viscoelastic properties of laminated composites, this segment may also include non-propagating wave modes with complex wave numbers that decay with distance. By analysing this initial segment, it is possible to extract the TDOA of the propagating flexural wave mode, which can then be used to locate the impact with the known GVP.

2.4.3 Physics-based impact force reconstruction via deconvolution

As outlined in Section 2.1.2, if the transfer function $h(t; q, L_j)$ between the impact force at location q and the response at sensor L_j is known, the impact force can be recovered through deconvolution of the measured sensor signals. This relies on the assumption of linearity, where the sensor output is the convolution of impact force and corresponding transfer function, as described by Eq. (2.36).

Force deconvolution is most efficiently performed in the frequency domain, where convolution operations reduce to simple multiplication, facilitating straightforward inversion [22, 123]:

$$\hat{f}(\omega; q) = \frac{\sum_{j=1}^{N_s} \hat{s}(\omega; L_j)\hat{h}^*(\omega; q, L_j)}{\sum_{j=1}^{N_s} \left|\hat{h}(\omega; q, L_j)\right|^2}, \; f(t; q) = \mathcal{F}^{-1}(\hat{f}(\omega; q)), \tag{2.41}$$

where the asterisk $*$ denotes the complex conjugate, $|\cdot|$ the absolute operator (modulus), and $\mathcal{F}^{-1}$ represents the inverse Fourier transform operator,

However, this inverse problem is inherently ill-posed: small perturbations in sensor signals (e.g., due to noise) can lead to significant errors in the reconstructed force. To address this, regularisation techniques are employed to stabilise the solution. One widely adopted method is Tikhonov regularisation, or Wiener deconvolution [22, 123, 124], which introduces a penalty on high-frequency amplification by incorporating a regularisation parameter λ_{reg}:

$$\hat{f}(\omega; q, \lambda_{reg}) = \frac{\sum_{j=1}^{N_s} \hat{s}(\omega; L_j)\hat{h}^*(\omega; q, L_j)}{\sum_{j=1}^{N_s} \left|\hat{h}(\omega; q, L_j)\right|^2 + \lambda_{reg}}. \tag{2.42}$$

This formulation can be interpreted as a regularised least-squares optimisation problem:

$$\hat{f}(\omega; q, \lambda_{reg}) = \underset{\hat{f}(\omega; q)}{\operatorname{argmin}} \sum_{j=1}^{N_s} \left\|\hat{s}(\omega; q, L_j) - \hat{f}(\omega; q)\hat{h}(\omega; q, L_j)\right\|^2 + \lambda_{reg} \left\|\hat{f}(\omega; q)\right\|^2, \tag{2.43}$$

where λ_{reg} governs the trade-off between fidelity to the measured data and suppression of unstable high-frequency components.

2.4.4 Data-driven impact identification via surrogate modelling

As outlined in Section 1.3.2, data-driven impact identification involves constructing surrogate models that map impact-induced sensor signals or their extracted features (serving as model inputs) to impact location and impact force (serving as model outputs). These surrogate models include MLPs [37–40] and GPR [44–47] for feature-based mapping, as well as deep learning architectures such as CNNs [48–52], Temporal Convolutional Networks (TCNs) [53], RNNs [54, 55], GNNs [56–58], and XFMRs [59] for time series-based mapping.

Among these approaches, GPR [125] stands out as a Bayesian machine learning technique particularly well-suited for regression tasks. Its ability to provide not only accurate predictions but also reliable uncertainty quantification makes it highly valuable for impact identification, where robustness and confidence estimation are critical. Furthermore, GPR's non-parametric nature allows it to flexibly model complex, nonlinear relationships without requiring a predefined functional form, enhancing its applicability in real-world scenarios with limited training data.

GPR models an unknown function $g(\mathbf{x})$ as a Gaussian Process (GP), characterised by a mean function $\mu(\mathbf{x})$ and a covariance function (kernel) $k(\mathbf{x}, \mathbf{x}')$. The GP prior is expressed as:

$$g(\mathbf{x}) \sim \mathcal{GP}\left(\mu(\mathbf{x}), k(\mathbf{x}, \mathbf{x}')\right). \tag{2.44}$$

Given training data (X, Y) where X is the input matrix and Y is the corresponding output vector, and a test input $\mathbf{x}^*$, the posterior predictive distribution of $g(\mathbf{x}^*)$ is Gaussian:

$$P\left(g(\mathbf{x}^*)|X, Y, \mathbf{x}^*\right) \sim \mathcal{N}\left(\mu(\mathbf{x}^*), \sigma^2(\mathbf{x}^*)\right), \tag{2.45}$$

where the posterior mean and variance given by:

$$\begin{aligned} \mu(\mathbf{x}^*) &= m(\mathbf{x}^*) + k(\mathbf{x}^*, X)[K(X, X) + \sigma_n^2 I]^{-1}(Y - m(\mathbf{x}^*)), \\ \sigma^2(\mathbf{x}^*) &= k(\mathbf{x}^*, \mathbf{x}^*) - k(\mathbf{x}^*, X)[K(X, X) + \sigma_n^2 I]^{-1} k(X, \mathbf{x}^*), \end{aligned} \tag{2.46}$$

where I represents the identity matrix, $K(X, X)$ is the kernel matrix evaluated over the training inputs X, $k(\mathbf{x}^*, X)$ is the vector of covariances between the test input $\mathbf{x}^*$ and training points in X,

σ_n^2 represents the noise variance in the observations, reflecting the model's handling of noisy data.

The kernel $k(\mathbf{x}, \mathbf{x}')$ encodes the similarity between input points and is fundamental in defining key properties of the GP model, such as smoothness, periodicity, and response to input variations [126]. Two widely used kernels in GPR are the squared exponential kernel (also known as the Radial Basis Function (RBF)) and the Cosine Similarity (COS) kernel:

$$k_{rbf}(\mathbf{x}, \mathbf{x}') = \exp\left(-\frac{\|\mathbf{x} - \mathbf{x}'\|^2}{2l_{rbf}^2}\right), \ k_{cos}(\mathbf{x}, \mathbf{x}') = l_{cos}^2 \frac{\mathbf{x}^\top \mathbf{x}'}{\|\mathbf{x}\| \, \|\mathbf{x}'\|}. \tag{2.47}$$

The RBF kernel is a popular choice for modeling smooth and continuous functions. It is characterised by the lengthscale parameter l_{rbf}, which determines the kernel's sensitivity to input differences. A smaller l_{rbf} allows the model to capture finer details in the data, while a larger l_{rbf} promotes smoother and more generalized predictions. The COS kernel measures the angular similarity between input vectors, ignoring their magnitudes. It computes the cosine of the angle between vectors and is scaled by the lengthscale parameter l_{cos}. This kernel is particularly useful when the relative orientation or proportional relationships between inputs carry more significance than their absolute values.

Building on the advantages of GPR, several studies have employed this technique for data-driven impact localisation [45–47] and peak force estimation [44]. One of the most widely used features for impact localisation is the TDOA, which is strongly correlated with impact location and enables high localisation accuracy. For impact peak force estimation, a key feature is the maximum amplitude of the sensor signal, as it directly reflects the intensity of the impact event. In both cases, GPR's ability to model complex, nonlinear relationships while providing uncertainty quantification makes it particularly effective for improving the reliability and interpretability of real-time impact identification systems.

Chapter 3

Robust Impact Localisation under Environmental and Operational Variabilities

Highlights:

- Propose a robust, data-driven impact localisation framework that implicitly accounts for environmental and operational variabilities.
- Offer practical guidance for sensor network design by quantifying the effect of sensor density on localisation performance.
- Investigate model sensitivity to training data variability by analysing how the representativeness of reference impacts influences prediction accuracy.
- Examine generalisation capability by evaluating model performance on untrained impact locations and unseen environmental or operational conditions.

3.1 Introduction

A fundamental challenge in both physics-based and data-driven impact localisation approaches is their limited ability to generalise from controlled laboratory conditions to real-world operational environments. As illustrated in Fig. 3.1, passive sensors are embedded into a composite aircraft structure during the laboratory or factory stage to enable in-service impact monitoring. Ensuring the long-term reliability of the sensing network requires rigorous calibration and validation in both controlled laboratory environments and real-world operational conditions. Laboratory calibration typically involves controlled impact tests at predefined locations and force levels, allowing for the systematic assessment of sensor sensitivity and accuracy under repeatable conditions. Field testing, in contrast, evaluates the robustness of the sensing network in realistic operational settings, where variations in temperature, mechanical vibrations, and acoustic noise introduce additional complexities. However, extensive field testing on in-service aircraft structures is often impractical due to operational constraints, such as limited access to critical components and the difficulty of replicating controlled impact scenarios under real-world conditions.

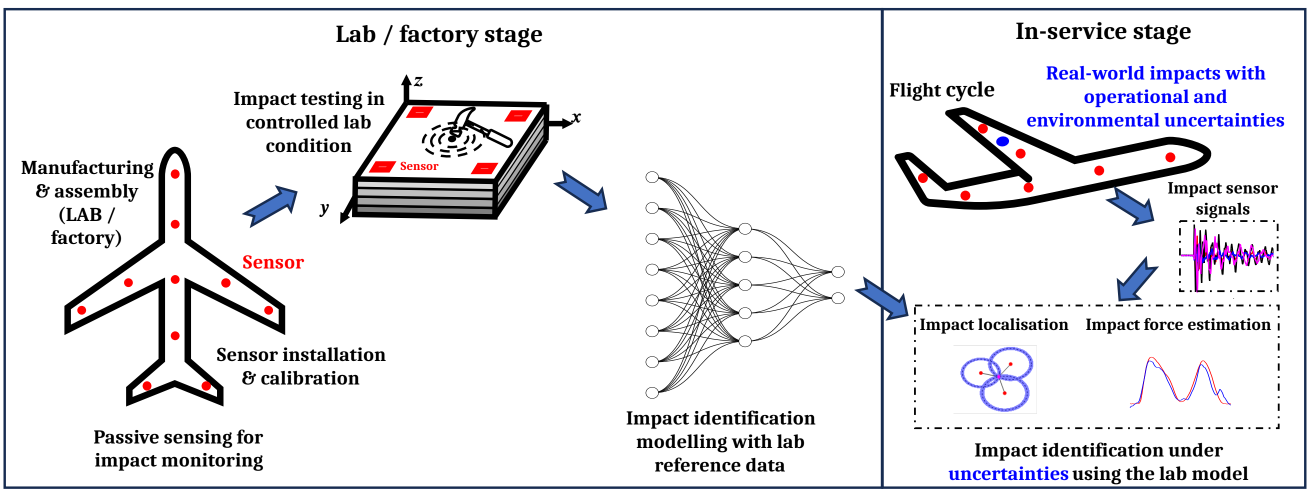

Figure 3.1: Passive sensing for impact monitoring from laboratory to operational conditions.

Given these challenges, both physics-based and data-driven impact localisation methods are typically validated or trained using laboratory-generated datasets, as shown in Fig. 1.3. While controlled experiments provide valuable insights and demonstrate the feasibility of these methods, their direct applicability to real-world conditions remains limited. Real-world impacts are inherently unpredictable, involving variations in multiple parameters, including impactor mass, velocity, angle, and environmental conditions such as significant fluctuations in temperature. These variabilities pose considerable challenges for data-driven models, which often rely on consistent patterns in training data for accurate predictions.

For instance, even minor temperature variations can influence wave propagation velocities, introducing errors in time difference of arrival (TDOA)-based localisation. Furthermore, substantial changes in impact mass can significantly alter the spectral distribution of sensor signals, affecting the extraction and interpretation of impact features. While Seno et al. [35, 36] experimentally demonstrated that small variations in TDOA occur due to changes in impact mass, height, and angle using the same impactor, these studies were limited to minor perturbations. Such findings are insufficient to address the challenges posed by significant variations in impact mass and environmental temperature, which require more robust and adaptable localisation methodologies.

This research seeks to address these challenges by advancing data-driven impact localisation under environmental and operational variabilities (EOVs). A key insight leveraged in this study is the inherent invariance in the relative order of TDOA across sensors under such variabilities. For example, temperature variations predominantly scale wave propagation velocities proportionally, preserving the relative TDOA order. Additionally, substantial changes in impact mass modify the frequency spectrum of impact responses, enabling TDOA extraction at different dominant frequencies, which scale proportionally due to flexural wave dispersion.

Building on these observations, a Composite (COMP) kernel is developed for Gaussian Process Regression (GPR), integrating the complementary strengths of the Radial Basis Function (RBF) and Cosine Similarity (COS) kernels. The RBF kernel effectively captures complex nonlinear relationships, while the COS kernel models linear and angular dependencies in TDOA, enhancing the model's robustness to environmental and operational variations. To further improve adaptability, Bayesian-Inspired Model Averaging (BIMA) is employed to dynamically fuse these kernels, assigning context-sensitive weights that optimise model reliability and accuracy in varying operational conditions. This novel approach provides a more robust framework for impact localisation, closing the gap slightly between controlled laboratory conditions and real-world applications.

3.2 TDOA Analysis under EOVs

The reference impact dataset, collected under controlled laboratory conditions, forms the basis for training the impact localisation model. In this controlled environment, critical factors such as impact mass, velocity, impactor material, angle, temperature, mechanical vibrations, and other environmental variables are meticulously regulated and maintained at constant levels. This rigorous control ensures a consistent and repeatable dataset, enabling precise extraction of TDOA values essential for model development and validation.

Within this controlled framework, the extracted TDOA at frequency ω for an impact at location q, along with the corresponding Group Velocity Profile (GVP), are denoted as $\Delta\bar{\mathbf{t}}(\omega)$ and $\bar{v}_g(\theta, \omega)$, respectively. In contrast, under real-world in-service conditions—characterized by EOVs—the extracted TDOA and GVP are represented as $\Delta\mathbf{t}(\omega)$ and $v_g(\theta, \omega)$. These two representations highlight the discrepancies between idealised laboratory data and real-world data influenced by factors such as temperature variations, structural vibrations, and sensor noise. The ability to generalise the impact localisation model from the controlled laboratory setting to practical in-service applications fundamentally depends on the similarity between $\Delta\bar{\mathbf{t}}(\omega)$ and $\Delta\mathbf{t}(\omega)$.

While operational variabilities, such as variations in impact mass, velocity, angle, and impactor material, do not directly alter the GVP (which depends on structural and environmental properties), they significantly influence the characteristics of the impact force and the frequency content of sensor signals. This relationship arises from the linear system property, where the frequency spectrum of the sensor signal, $\hat{s}(\omega)$, is linearly related to the impact force spectrum, $\hat{f}(\omega)$, through the system transfer function $\hat{h}(\omega)$, as $\hat{s}(\omega) = \hat{h}(\omega)\hat{f}(\omega)$. Several studies have explored the effects of impact-related properties. Olsson [127] demonstrated that the frequency content of sensor signals is primarily determined by the mass ratio between the impactor and the plate, rather than by the impact velocity. Additionally, Seno et al. [36] showed that the material of the impactor significantly affects the impact force history. For instance, replacing a steel impactor head with a rubber one increases the contact time, reduces the peak force, and shifts the frequency content towards lower frequencies.

Operational variabilities often result in substantial changes to the frequency content of impact sensor signals compared to those observed in laboratory conditions. These changes complicate the extraction of TDOA, which relies on consistent frequency components for accurate estimation due to wave dispersion. To address this, it is critical to identify a frequency ω that serves as a shared dominant frequency in both laboratory and real-world impacts. Advanced time-frequency analysis techniques, such as wavelet analysis, facilitate the identification of such shared dominant frequencies.

In extreme cases where the dominant frequencies of laboratory and real-world impacts do not overlap, alternative strategies must be employed. One such approach involves extracting TDOA values at distinct dominant frequencies for each condition. Specifically, TDOA values can be extracted at frequency ω for laboratory impacts, denoted as $\Delta\bar{\mathbf{t}}(\omega)$, and at the dominant frequency ω^* for real-world impacts, denoted as $\Delta\mathbf{t}(\omega^*)$.

The relationship between wave frequency and group velocity in symmetrically laminated composite plates, derived from CPT in Section 2.3.3, provides crucial insights for addressing such scenarios. In the low-frequency range, substituting wavenumber k with ω/v_p in Eq. (2.32), the phase velocity $v_p(\theta, \omega)$ is found to be proportional to the square root of wave frequency [87]:

$$I_1 \frac{v_p^4(\theta)}{\omega^2} = D_{11}\cos^4\theta + 4D_{16}\sin\theta\cos^3\theta + 2(D_{12} + 2D_{66})\sin^2\theta\cos^2\theta + 4D_{26}\sin^3\theta\cos\theta + D_{22}\sin^4\theta. \tag{3.1}$$

The group velocity is obtained by differentiating the dispersion relation with respect to the wavenumber:

$$v_g(\theta) = \frac{\partial\omega}{\partial k} = \frac{\partial[kv_p(\theta)]}{\partial k} = v_p(\theta) + k\frac{dv_p(\theta)}{dk} = 2v_p(\theta), \tag{3.2}$$

which demonstrates that the group velocity is exactly twice the phase velocity and follows the same proportional relationship to the square root of the wave frequency:

$$v_g(\theta, \omega) \propto \sqrt{\omega},\ v_g(\theta, \omega) = \alpha v_g(\theta, \omega^*),\ \alpha = \sqrt{\frac{\omega}{\omega^*}}, \tag{3.3}$$

where α is the frequency-dependent scaling factor. This proportionality reveals that while frequency scales the GVP, it does not alter its directional characteristics. Consequently, this scaling property extends naturally to the extracted TDOA values. By substituting Eq. (3.3) into the TDOA expression in Eq. (2.38), it follows that frequency similarly scales the TDOA values without affecting their relative order:

$$\Delta t_{ij}(\omega^*) = t_j(\omega^*) - t_i(\omega^*) = \alpha\left[t_j(\omega) - t_i(\omega)\right] = \alpha\Delta t_{ij}(\omega). \tag{3.4}$$

In practice, TDOA measurements are subject to errors arising from both numerical inaccuracies in the extraction methods and random noise in the signals. However, these errors are generally negligible compared to the dominant contribution from the dispersion relation, ensuring that the proportional scaling property remains a reliable characteristic for real-world implementations.

Environmental variabilities, particularly uniform temperature variations, can be systematically incorporated into the proposed framework. Temperature-induced changes are generally assumed to cause uniform scaling in material properties and structural dimensions, leading to corresponding changes in wave propagation speeds. This assumption has been supported both theoretically and experimentally. Specifically, the linear relationship between wave velocity and temperature has been theoretically investigated in [128], and experimentally validated across a wide operational range from –50 °C to 70 °C in [129], and further extended to 85 °C in [130]. This validated temperature range encompasses most practical scenarios encountered in aerospace applications.

This thermal effect results in a scaled GVP, with TDOA values scaled by a factor proportional to the temperature change, consistent with Eq. (3.4). Crucially, although the absolute TDOA values are affected by temperature, their relative ordering remains consistent under uniform scaling, preserving the robustness of TDOA-based localisation.

In addition to thermal variations, other environmental influences, such as mechanical vibrations induced by aerodynamic loads, engine operations, or onboard machinery, can introduce stochastic noise into the sensor signals. These disturbances often manifest as low-frequency oscillatory components confined to specific frequency bands and can be identified through time-frequency analysis techniques such as spectral decomposition or wavelet transforms. By characterising the spectral content of these noise sources, their impact on TDOA extraction can be effectively mitigated when the signal-to-noise ratio (SNR) is moderate to high.

One practical approach involves applying targeted bandpass filtering to isolate frequency components that are minimally affected by noise. For example, Seno et al. [35] experimentally investigated the effects of low-frequency vibration noise (below 2 kHz) on TDOA estimation. Their study demonstrated that even with a moderate SNR—where the noise amplitude is approximately 5% of the signal amplitude—reliable TDOA values can still be obtained by applying Butterworth filtering to isolate higher-frequency components. This highlights the robustness of TDOA-based methods under realistic vibrational noise conditions and reinforces the applicability of the proposed approach to operational environments encountered in aerospace structures.

3.3 Gaussian Process Regression with Kernel Design and Bayesian Fusion

3.3.1 Kernel design for impact localisation considering EOVs

In the context of impact localisation using GPR and TDOA as input features, the kernel design is critical for addressing EOVs. The kernel determines how the GPR model interprets relationships within the data, enabling it to capture patterns induced by various sources of variability. Specific considerations include:

1. Temperature variations: Temperature changes typically cause uniform scaling in the extracted TDOA values due to the thermal expansion or contraction of the structure. To account for this, a kernel that incorporates linear components, such as the COS kernel, is essential. The COS kernel ensures the model can capture these proportional relationships, enabling it to generalise effectively across temperature-induced variations. This is critical for maintaining accuracy in dynamic operational environments.

2. Frequency variability: Operational variabilities often lead to the extraction of TDOA values at different frequencies. According to the dispersion relations in plate structures, wave group velocities scale predictably with frequency. A kernel that can model such frequency-induced linear relationships, like the COS kernel, is indispensable. This allows the GPR model to adapt to frequency-dependent TDOA variations and maintain robust performance across diverse impact scenarios.

3. Simulation errors in TDOA extraction methods [28]: Errors in TDOA extraction methods introduce non-linear variations in the extracted values. These non-linear effects, often resulting from noise or inconsistencies in the extraction algorithms, require a kernel capable of capturing such complexities. The RBF kernel is well-suited for this purpose, as it excels at modeling smooth, non-linear relationships in the data.

4. Zero TDOA and singularity point: A singularity point is defined as a structural location where the analytical TDOA forms a zero vector—for instance, the centre of a rectangular

sensor array on isotropic plates. In regions near the singularity point, TDOA values approach zero and exhibit robustness against scaling effects caused by frequency variability and temperature variations. The RBF kernel is particularly suitable for impact localisation in this area, as it relies on the magnitudes of TDOA values. Introducing an irregularly placed sensor to the array can effectively eliminate this singularity, thereby improving localisation performance.

5. Multitask regression: Impact localisation involves predicting a two-dimensional output for plate-like structures, namely the spatial coordinates (x, y) of the impact location. Each coordinate pair corresponds uniquely to a TDOA vector through the GVP, as expressed in Eq. (2.40). Modeling these outputs independently using separate GP may fail to capture the inherent interactions between the coordinates. Leveraging multitask regression techniques allows the model to learn and exploit similarities between the outputs simultaneously [131], improving accuracy and efficiency.

In scenarios where smooth non-linear variations and linear trends coexist—such as when EOVs simultaneously affect TDOA values—a composite (COMP) kernel that integrates the strengths of the RBF and COS kernels can be effectively utilised. The composite kernel is defined as:

$$k_{comp}(\mathbf{x}, \mathbf{x}') = k_{rbf}(\mathbf{x}, \mathbf{x}') * k_{cos}(\mathbf{x}, \mathbf{x}'). \tag{3.5}$$

This formulation enables the GPR model to address both local, non-linear effects (captured by the RBF component) and global, proportional relationships (captured by the COS component). The RBF kernel effectively models fine-grained variations and smooth non-linearities, while the COS kernel accounts for angular similarity and linear scaling effects in the TDOA vectors.

By selecting the sensor at which the wave first arrives as the anchor sensor for calculating time differences, the TDOA vector $\Delta\mathbf{t}(\omega)$ is inherently non-negative, always containing at least one zero element. This property ensures that the individual kernel outputs for the COS and RBF kernels are naturally constrained within the ranges $[0, l_{cos}^2]$ and $[0, 1]$, respectively. Without preprocessing the TDOA vectors to include negative values, the composite input kernel also remains confined within $[0, l_{cos}^2]$. A high composite kernel value reflects a strong similarity not only in the magnitudes of two TDOA vectors but also in their relative ordering, making it particularly suitable for capturing both amplitude and directional consistency.

To fully capture the dependencies between output coordinates, an output kernel is defined for each task (x- and y-coordinate prediction). A task covariance kernel is employed using a parameterised low-rank matrix, enabling the joint modelling of outputs. The covariance between two data points ($\mathbf{x}$, $\mathbf{x}'$) and their respective tasks (i, j) is defined as:

$$k([\mathbf{x}, i], [\mathbf{x}', j]) = k_{inputs}(\mathbf{x}, \mathbf{x}') * k_{tasks}(i, j), \tag{3.6}$$

where where k_{inputs} is the kernel function over the input space, which can be a COMP, RBF or COS kernel, k_{tasks} is the task covariance matrix, which encodes the correlations between tasks. Importantly, this task covariance matrix k_{tasks} is not predefined—it is learned from data during model training. This multitask approach effectively learns shared structures and correlations between tasks, resulting in improved localisation performance. By integrating both input and task covariance kernels, the GPR model captures a comprehensive understanding of the relationships in the data, delivering robust and accurate predictions under diverse environmental and operational conditions.

3.3.2 Bayesian-inspired model averaging (BIMA) for kernel fusion

Given the availability of multiple input kernels, a key challenge is to determine which kernel is most effective for localising a target impact $\mathbf{x}^*$. The optimal kernel choice is inherently dependent on the prevailing conditions affecting the target impact, such as environmental variations or signal noise characteristics. For instance, when the target impact is subject to environmental factors like varying temperature or impact mass, the COS kernel tends to yield more accurate localisation results due to its ability to capture angular similarities. In contrast, under noisy conditions with random signal fluctuations, the RBF kernel typically offers more reliable performance due to its robustness to noise and smoothness assumptions.

Rather than selecting a single optimal kernel, this study proposes a Bayesian-inspired model averaging (BIMA) framework that fuse predictions from all candidate kernels to enhance localisation robustness. In the context of multi-task regression with N_{task} output dimensions (tasks), each kernel k_i yields:

- A predictive mean vector $\boldsymbol{\mu}_i(\mathbf{x}^*) \in \mathbb{R}^{N_{task}}$, and
- A predictive covariance matrix $\boldsymbol{\Sigma}_i(\mathbf{x}^*) \in \mathbb{R}^{N_{task} \times N_{task}}$.

The BIMA strategy integrates two complementary weighting criteria:

- Marginal likelihood (ML): Quantifies the model's goodness-of-fit to the training data.
- Predictive uncertainty: Encoded in the covariance $\boldsymbol{\Sigma}_i(\mathbf{x}^*)$, capturing local confidence in the prediction at $\mathbf{x}^*$.

These metrics are combined to form adaptive fusion weights that reflect both global model relevance and local prediction reliability.

In classical Bayesian Model Averaging (BMA) [132], the posterior probability of kernel k_i given data $\mathcal{D}$ is computed as:

$$P(k_i|\mathcal{D}) = \frac{P(\mathcal{D}|k_i)P(k_i)}{\sum_j P(\mathcal{D}|k_j)P(k_j)}, \tag{3.7}$$

where $P(k_i)$ is the prior probability of kernel k_i, and $P(\mathcal{D}|k_i)$ is the marginal likelihood. In the absence of prior preference or domain-specific knowledge, uniform priors across all kernels are assumed, i.e., $P(k_i) = 1/N_k$ for N_k kernels. This yields posterior weights that are directly proportional to the marginal likelihoods:

$$w_i^{\text{ml}} = \frac{P(\mathcal{D}|k_i)}{\sum_j P(\mathcal{D}|k_j)}. \tag{3.8}$$

This produces a marginal likelihood weight vector $\boldsymbol{w}^{\text{ml}} \in \mathbb{R}^{N_{task}}$, expressing how well each kernel explains the observed training data.

To integrate local predictive reliability, an uncertainty-based weight is introduced, inversely proportional to the determinant of the predictive covariance matrix. This determinant reflects the volume of the confidence ellipsoid and thus captures both the variance and task correlations:

$$w_i^{\text{unc}} = \frac{1/\det \boldsymbol{\Sigma}_i(\mathbf{x}^*)}{\sum_j 1/\det \boldsymbol{\Sigma}_j(\mathbf{x}^*)}. \tag{3.9}$$

This formulation favours kernels with tighter predictive distributions (i.e., higher confidence), resulting in an uncertainty weight vector $\boldsymbol{w}^{\mathrm{unc}} \in \mathbb{R}^{N_{task}}$.

The final weight w_i assigned to kernel k_i combines these two criteria using a conditional fusion strategy. Specifically, if the maximum marginal likelihood weight $\max(\boldsymbol{w}^{\mathrm{ml}})$ and the maximum uncertainty weight $\max(\boldsymbol{w}^{\mathrm{unc}})$ occur at the same index, the final weight is defined as the normalised product of the two. Otherwise, to prioritise model evidence over conflicting uncertainty, the final weight defaults to the marginal likelihood weight:

$$w_i = \begin{cases} \dfrac{w_i^{\mathrm{ml}} \cdot w_i^{\mathrm{unc}}}{\sum_j w_j^{\mathrm{ml}} \cdot w_j^{\mathrm{unc}}}, & \text{if } \arg\max_j w_j^{\mathrm{ml}} = \arg\max_j w_j^{\mathrm{unc}}, \\ w_i^{\mathrm{ml}}, & \text{otherwise.} \end{cases} \tag{3.10}$$

This conditional rule ensures synergy when both weighting schemes agree, while defaulting to marginal likelihood when predictive uncertainty conflicts with global model evidence, preventing over-reliance on potentially misleading uncertainty estimates.

The BIMA predictive mean is then obtained as the weighted average:

$$\boldsymbol{\mu}_{\mathrm{BIMA}}(\mathbf{x}^*) = \sum_{i=1}^{N_k} w_i \cdot \boldsymbol{\mu}_i(\mathbf{x}^*). \tag{3.11}$$

The fused predictive covariance captures both aleatoric uncertainty within each model and epistemic uncertainty across models:

$$\boldsymbol{\Sigma}_{\mathrm{BIMA}}(\mathbf{x}^*) = \sum_{i=1}^{N_k} w_i \cdot \boldsymbol{\Sigma}_i(\mathbf{x}^*) + \sum_{i=1}^{N_k} w_i \cdot [\boldsymbol{\mu}_i(\mathbf{x}^*) - \boldsymbol{\mu}_{\mathrm{BIMA}}(\mathbf{x}^*)][\boldsymbol{\mu}_i(\mathbf{x}^*) - \boldsymbol{\mu}_{\mathrm{BIMA}}(\mathbf{x}^*)]^\top. \tag{3.12}$$

Here, the first term models per-kernel variance, while the second captures model disagreement, enabling more informative and cautious uncertainty quantification—essential for safety-critical structural health monitoring (SHM) applications.

Prediction accuracy at a test input $\mathbf{x}^*$ is evaluated using the root sum squared error (RSSE):

$$\varepsilon = \|\mathbf{y}^* - \boldsymbol{\mu}(\mathbf{x}^*)\|, \tag{3.13}$$

where $\mathbf{y}^*$ is the ground truth, $\boldsymbol{\mu}(\mathbf{x}^*)$ is the predicted mean from a single kernel or from BIMA.

To assess the calibration of the predictive variance, the empirical coverage probability P_λ is computed using the Mahalanobis distance, which quantifies the proportion of true target values $\mathbf{y}_j^*$) that lie within the λ confidence region (e.g., $\lambda = 0.95$) of the predictive multivariate Gaussian distribution:

$$P_\lambda = \frac{1}{N_{test}} \sum_{j=1}^{N_{test}} \mathbb{I}\left[(\boldsymbol{\mu}_j(\mathbf{x}^*) - \mathbf{y}_j^*)^\top \boldsymbol{\Sigma}_j(\mathbf{x}^*)^{-1}(\boldsymbol{\mu}_j(\mathbf{x}^*) - \mathbf{y}_j^*) \leq \chi^2_{N_{task},\lambda}\right]. \tag{3.14}$$

Here, $\mathbb{I}[\cdot]$ is the indicator function, returning 1 if the condition is true and 0 otherwise. $\chi^2_{N_{task},\lambda}$ is the 100λ-th percentile of the chi-squared distribution with N_{task} degrees of freedom. A well-calibrated probabilistic model under the multivariate Gaussian assumption $\mathbf{y}^* \sim \mathcal{N}(\boldsymbol{\mu}(\mathbf{x}^*), \boldsymbol{\Sigma}(\mathbf{x}^*))$, is indicated by $P_\lambda \approx \lambda$. A value $P_\lambda > \lambda$ reflects a conservative uncertainty estimate, which is particularly desirable in SHM for reducing the risk of missed detections or false negatives in damage localisation. In this study, a 90% confidence level is used for uncertainty calibration: $\lambda = 0.9$.

Similarly, the Probability of Detection (PoD) is used to evaluate localisation accuracy. It is defined as the localisation error threshold below which 90% of prediction errors fall—an established benchmark in SHM uncertainty analysis [37, 44]:

$$\varepsilon_{90\%} = \inf\left\{\varepsilon \in \mathbb{R}\geq 0 : \mathrm{CDF}_\varepsilon(\varepsilon) \geq 0.9\right\}, \tag{3.15}$$

where $\mathrm{CDF}_\varepsilon(\cdot)$ is the Cumulative Distribution Function (CDF) of the localisation error ε, inf denotes the infimum (greatest lower bound) of the set. This metric provides a statistically meaningful and interpretable indicator of the model's detection capability under uncertainty.

This Bayesian-inspired fusion strategy extends classical Bayesian model averaging by integrating both global model fit (via marginal likelihood) and local predictive confidence (via inverse variance) into the weighting scheme. As a result, the model can dynamically adapt its reliance on different kernels based on the data context, improving robustness and generalisation under diverse operational and environmental conditions.

3.3.3 Data pre-processing: two standardisation methods

This study investigates the effects of standardisation techniques on the performance of the GPR model for impact localisation under uncertain conditions. Two commonly used standardisation approaches are considered: sample standardisation (SS) and feature standardisation (FS). These techniques can be applied to the input matrix $X \in \mathbb{R}^{N \times M}$, where N is the number of impact samples and M is the number of input features (e.g., TDOA measurements across sensors). The two standardisation schemes are defined as follows:

$$X_{ss}(i,:) = \frac{X(i,:)}{\|X(i,:)\|},\ X_{fs}(:,j) = \frac{X(:,j) - \mathrm{mean}[X(:,j)]}{\mathrm{std}[X(:,j)]}, \tag{3.16}$$

where $\|\cdot\|$ denotes the Euclidean norm, $\mathrm{mean}(\cdot)$ and $\mathrm{std}(\cdot)$ denote the mean and standard deviation, respectively.

In SS, each input vector (i.e., each row of X) is normalised to unit norm, preserving the internal directional structure (i.e., the relative order of TDOA components) while eliminating magnitude differences between samples. This is particularly advantageous for impact localisation tasks, as environmental and operational conditions—such as temperature changes or varying impact energies—primarily affect the scale of the TDOA vectors. SS ensures that the GPR model receives consistently scaled inputs, improving its ability to generalise across varying test conditions.

In contrast, FS normalises each column (i.e., each feature across all samples) to zero mean and unit variance. While this method ensures comparability across sensors, it may inadvertently disrupt the internal ordering of TDOA components within each input vector. This is because FS applies independent linear transformations to each sensor's readings, potentially distorting the geometric structure of the input vector that encodes key localisation information.

Although both standardisation methods enhance numerical stability and model convergence, SS is better aligned with the physical characteristics of the problem and the nature of TDOA-based localisation. It preserves the directional information essential for kernel-based modelling while mitigating the effects of input scale variability introduced by uncertain conditions.

Algorithm 3.1: Implement of GPR-BIMA-based impact localisation.

Off-line Stage:

$Q, S(t)$; /* Reference impact locations Q, sensor signals $S(t)$ */

$\omega \leftarrow S(t)$; /* Dominant frequency analysis of $S(t)$ */

$\Delta\mathbf{t}(\omega) \leftarrow S(t), \omega$; /* TDOA extraction from $S(t)$ at ω */

$\Delta\mathbf{t}_{ss}(\omega) \leftarrow \Delta\mathbf{t}(\omega)$; /* TDOA sample standardisation */

$\mathcal{M}_{comp}, P(\mathcal{D}|k_{comp}) \leftarrow \Delta\mathbf{t}_{ss}(\omega), Q$; /* Train GPR model with COMP kernel */

$\mathcal{M}_{cos}, P(\mathcal{D}|k_{cos}) \leftarrow \Delta\mathbf{t}_{ss}(\omega), Q$; /* Train GPR model with COS kernel */

$\mathcal{M}_{rbf}, P(\mathcal{D}|k_{rbf}) \leftarrow \Delta\mathbf{t}_{ss}(\omega), Q$; /* Train GPR model with RBF kernel */

$\boldsymbol{w}^{\mathrm{ml}} \leftarrow P(\mathcal{D}|k_{comp}), P(\mathcal{D}|k_{cos}), P(\mathcal{D}|k_{rbf})$; /* Marginal likelihood-based weights */

Online Stage:

$s(t)$; /* Target impact detection and data acquisition */

$\omega^* \leftarrow s(t)$; /* Dominant frequency analysis of $s(t)$ */

$\Delta\mathbf{t}(\omega^*) \leftarrow s(t), \omega^*$; /* TDOA extraction from $s(t)$ at ω^* */

$\Delta\mathbf{t}_{ss}(\omega^*) \leftarrow \Delta\mathbf{t}(\omega^*)$; /* TDOA sample standardisation */

$\boldsymbol{\mu}_{comp}, \boldsymbol{\Sigma}_{comp} \leftarrow \mathcal{M}_{comp}, \Delta\mathbf{t}_{ss}(\omega^*)$; /* Location prediction with pre-trained GPR-COMP model */

$\boldsymbol{\mu}_{cos}, \boldsymbol{\Sigma}_{cos} \leftarrow \mathcal{M}_{cos}, \Delta\mathbf{t}_{ss}(\omega^*)$; /* Location prediction with pre-trained GPR-COS model */

$\boldsymbol{\mu}_{rbf}, \boldsymbol{\Sigma}_{rbf} \leftarrow \mathcal{M}_{rbf}, \Delta\mathbf{t}_{ss}(\omega^*)$; /* Location prediction with pre-trained GPR-RBF model */

$\boldsymbol{w}^{\mathrm{unc}} \leftarrow \boldsymbol{\Sigma}_{comp}, \boldsymbol{\Sigma}_{cos}, \boldsymbol{\Sigma}_{rbf}$; /* Predictive uncertainty-based weights */

$\boldsymbol{w} \leftarrow \boldsymbol{w}^{\mathrm{ml}}, \boldsymbol{w}^{\mathrm{unc}}$; /* Final kernel weights */

$\boldsymbol{\mu}_{\mathrm{BIMA}} \leftarrow \boldsymbol{w}, \boldsymbol{\mu}_{comp}, \boldsymbol{\mu}_{cos}, \boldsymbol{\mu}_{rbf}$; /* Mean prediction by BIMA */

$\boldsymbol{\Sigma}_{\mathrm{BIMA}} \leftarrow \boldsymbol{w}, \boldsymbol{\Sigma}_{comp}, \boldsymbol{\Sigma}_{cos}, \boldsymbol{\Sigma}_{rbf}, \boldsymbol{\mu}_{\mathrm{BIMA}}, \boldsymbol{\mu}_{comp}, \boldsymbol{\mu}_{cos}, \boldsymbol{\mu}_{rbf}$; /* Variance prediction by BIMA */

3.3.4 Implement of GPR-BIMA-based impact localisation.

Algorithm 3.1 outlines the implementation of the GPR-based impact localisation framework, which comprises an offline training phase and an online prediction phase.

In the offline phase, reference impact experiments are conducted to acquire sensor signals $S(t)$ and their corresponding locations Q. Dominant frequency analysis identifies the principal frequency component ω, facilitating the extraction of TDOA features $\Delta\mathbf{t}(\omega)$ for reference impacts. These features are used to train three GPR models based on COMP, COS, and RBF kernels. The models are implemented using GPyTorch [133], a Python-based Gaussian process library, with training performed via the Adam optimiser [134]. The marginal likelihoods of these models, $P(\mathcal{D}|k)$, determine the likelihood-based weights $\boldsymbol{w}^{\mathrm{ml}}$, reflecting each kernel's effectiveness in capturing the underlying data patterns.

In the online phase, sensor signals $s(t)$ from a new impact are processed similarly to extract ω^* and the corresponding TDOA features $\Delta\mathbf{t}(\omega^*)$. Each trained GPR model provides a probabilistic impact location estimate, characterised by a mean $\boldsymbol{\mu}$ and covariance matrix $\boldsymbol{\Sigma}$. Predictive uncertainty-based weights $\boldsymbol{w}^{\mathrm{unc}}$ are derived from the model covariance to account for confidence in predictions. The final kernel weights $\boldsymbol{w}$ are computed by integrating both marginal likelihood-based and uncertainty-based weighting. BIMA then fuses the individual predictions, yielding a final impact location estimate $\boldsymbol{\mu}_{\text{BIMA}}$ and associated covariance matrix $\boldsymbol{\Sigma}_{\text{BIMA}}$. This approach ensures an optimally weighted combination of multiple GPR models, enhancing the localisation accuracy and robustness.

3.4 Experimental Validation

Experimental impact tests were conducted under controlled laboratory conditions to generate reference datasets for model training and validation. The tests were performed on a sensorized fibre-reinforced composite plate using three different impact delivery methods—drop tower, small hammer, and guided drop mass—selected to introduce variability in impact mass, energy, and contact characteristics. The composite plate, fabricated from M21/T800 prepreg material, measured $290 \times 200 \times 4$ mm and had a quasi-isotropic layup of $[0/+45/-45/90]_{2s}$.

To capture the transient wave responses induced by the impacts, six PZT sensors (PIC 255) were surface-mounted on the panel in an optimised spatial configuration. These sensors provided high-fidelity voltage signals in response to elastic wave propagation generated by the impact events. Detailed mechanical and piezoelectric properties of the composite panel and PZT sensors are available in prior studies [43, 74, 75].

Based on the material properties and laminate layup, the critical load associated with delamination onset can be estimated using strain energy release rate models developed in [5, 135]. While the detailed formulations are omitted for brevity, the delamination threshold for the composite panel under study was calculated to be 4524.3 N, assuming an interlaminar fracture toughness of $G_{IIc} = 700$ J/m^2 [124]. Importantly, previous studies have shown that this threshold is largely insensitive to boundary conditions [136], which supports the broader applicability of the estimate across different structural configurations. In this study, the drop tower impact setup was specifically designed to generate forces near this critical threshold, ensuring that the experimental conditions reflect realistic damage-inducing scenarios relevant to aerospace composite structures.

3.4.1 Impact testing using drop tower and small hammer

To simulate large-mass impacts with peak forces approaching the delamination threshold, a drop tower machine (Instron-CEAST 9350) was used. The impactor was a spherical mass of 5.5 kg and 2 cm diameter. The impact energy was precisely controlled at 6 J by adjusting the drop height. Post-impact inspection using ultrasonic C-scan confirmed that no internal damage occurred, ensuring the structural integrity of the specimen. For comparison, small-mass impacts were generated using a handheld hammer (PCB Piezotronics 086C03) at the same location. The hammer, which weighed 160 g, had a flat tip with a diameter of 0.63 cm. The experimental setup, including the composite plate, drop tower and handheld hammer, is illustrated in Fig. 3.2.

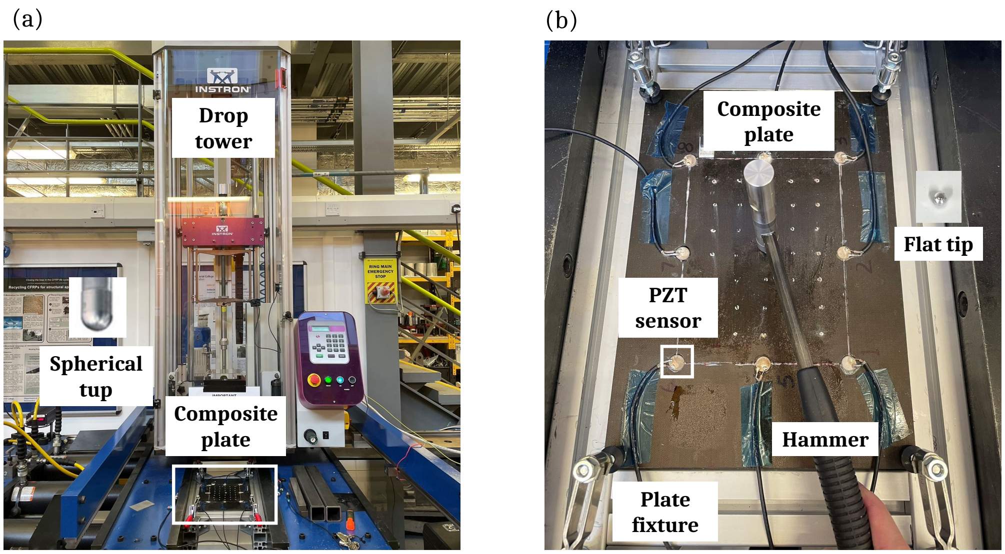

Figure 3.2: Experimental setup: (a) drop tower (DT) impact testing, (b) small hammer (HA) impact testing. The primary variabilities investigated were impact mass and impactor type.

The composite plate was simply supported along its two longitudinal edges, with supports placed 4 mm inside the edge from both sides, and clamped at four rectangular corners using fixtures beneath the drop tower, as depicted in Fig. 3.2. Impact-induced wave signals were captured during the experiments using four PZT sensors positioned at the vertices of the rectangle, labeled S1 to S4 in Fig. 3.3. These signals were recorded using an 8-channel PXI-5105 oscilloscope with a sampling frequency of 200 kHz. The sensors were connected to the oscilloscope through 100x attenuation probes to ensure high-fidelity data acquisition.

For clarity, Fig. 3.3 presents the layout of the composite plate, including the sensor placements and the impact location of the drop tower and hammer, marked as 'D'. Impacts at location D were

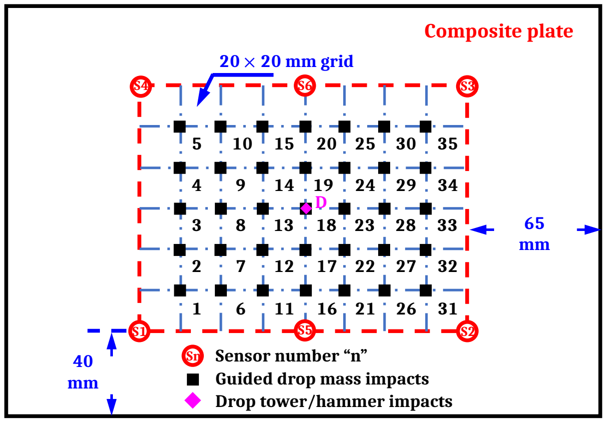

Figure 3.3: Layout of the composite plate used for impact testing.

conducted successively using the drop tower at 6 J and the handheld hammer. After each impact, ultrasonic C-scan inspection confirmed that the composite plate remained undamaged. Despite the absence of visible damage, the substantial difference in impactor mass between the two cases resulted in markedly different dynamic responses, as evidenced by the PZT sensor signals shown in Fig. 3.4(a). Specifically, the drop tower (DT) impact—characterised by a larger mass—produced signals with energy concentrated in lower-frequency components and exhibited significantly higher amplitudes due to its higher impact energy. For clarity and comparison, both the DT impact force and sensor signal amplitudes have been scaled down by a factor of 10 in the figure.

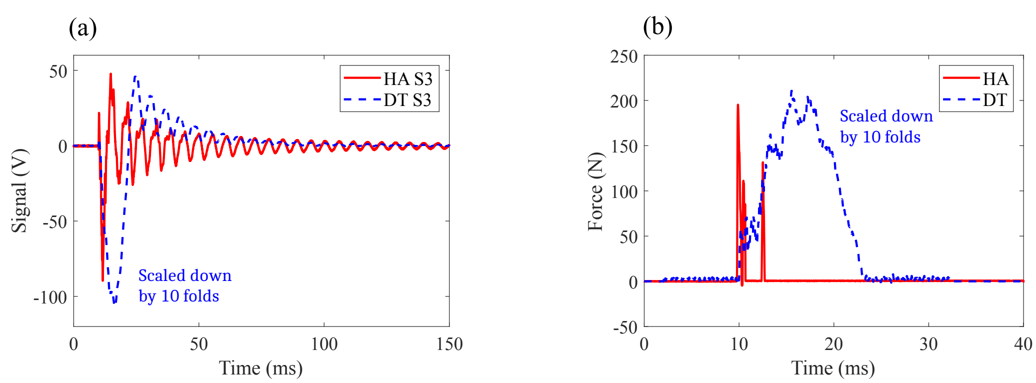

Figure 3.4: Sensor signals and impact force histories of DT and HA impacts. For comparison, the DT impact signal and force were scaled down by a factor of 10.

Table 3.1 summarises the conducted impact scenarios, where large-mass drop tower and small-mass hammer impacts are denoted as 'DT' and 'HA', respectively. The corresponding contact durations, extracted from the measured force histories in Fig. 3.4(b), further highlight the contrast between the two impact types. The DT impact, reaching a peak force of 2143.8 N, exhibit longer contact durations and predominantly excite low-frequency response modes. Conversely, the HA impact, with a peak force below 200 N, generates a shorter contact duration and excites higher-frequency modes. For hammer impacts, the reported contact duration corresponds to the first prominent peak in the impact force profile, which often exhibits multiple sine-like peaks. This experimental design facilitated the assessment of how impact mass and impactor influence signal characteristics, providing valuable insights into the structural response under varying conditions.

Table 3.1: Impact testing conducted using drop tower and small hammer, accounting variabilities in impact mass and impactor material.

Impact case	Impact mass (g)	Peak force (N)	Contact duration (ms)	No. of impacts
DT	5500	2143.8	13.66	1
HA	160	195.2	0.56	1

3.4.2 Impact testing using guided drop mass

To investigate the effects of impact angle, height, and temperature variation on the composite plate and the accuracy of impact localisation, experiments were conducted using a guided drop mass system. As shown in Fig. 3.5, the plate was clamped along its longitudinal edges, while the drop mass was released along a guided rail, providing precise control over both impact angle and height. This setup ensured high repeatability and minimized variability caused by unintended deviations, enabling a systematic examination of how these parameters influence the dynamic response of the plate. In addition, a heating pad was installed on the underside of the plate, facilitating controlled temperature adjustments. During the guided drop mass testing, six sensors, numbered 1 to 6 in Fig. 3.3, were employed to capture the impact-induced responses. These sensors were connected to a PXI-5105 oscilloscope operating at a sampling frequency of 2 MHz.

Four different impact cases were performed on the composite panel using the guided drop mass, as detailed in Table 3.2. The reference (REF) impacts were conducted perpendicularly at 35 evenly distributed locations, numbered 1-35 in Fig. 3.3, using a 100 g impact mass dropped from a height of 1 cm at room temperature (24 °C). In contrast, three additional cases introduced variations in height, angle and temperature: impact height increased to 2 cm (HEI), impact angle adjusted to 45 ° (ANG), and temperature elevated to 70 °C (TEM). To mitigate the influence of experimental

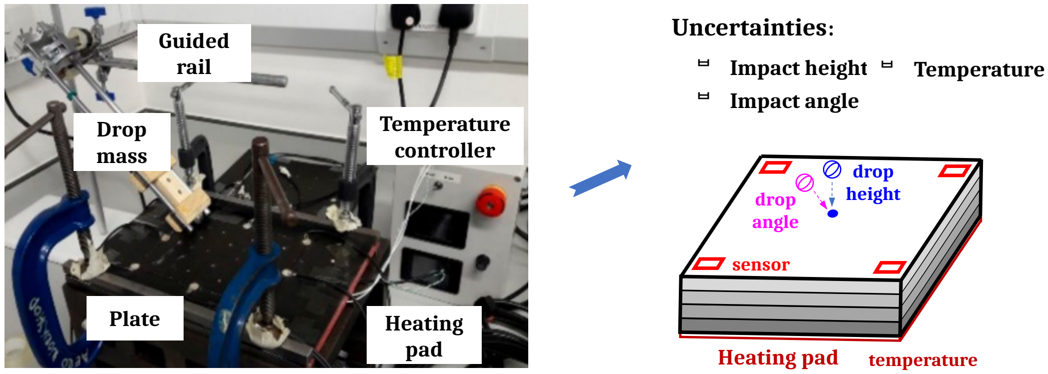

Figure 3.5: Experimental setup for guided drop mass impact testing, considering variabilities in impact height, angle and temperature.

randomness, each case was repeated two times, ensuring robust and reliable data collection.

Table 3.2: Impact testing conducted using guided drop mass accounting variabilities of impact height, angle and temperature.

Impact case	Temperature (°C)	Mass (g)	Height (cm)	Angle	Number of impacts
REF	24	100	2.5	90°	35 * 2 Rep
HEI	24	100	5	90°	35 * 2 Rep
ANG	24	100	2.5	45°	35 * 2 Rep
TEM	70	100	2.5	90°	35 * 4 Rep

*Note: REF = reference, HEI = height, ANG = angle, TEM = temperature, Rep = repetitions.

The data collected under temperature variations (TEM case) was generated by Dr. Aldyandra Hami Seno, a former Ph.D. student in the SI&HM group. Detailed information on experimental data collection under temperature variations can be found in [35, 44].

3.5 TDOA Extraction under EOVs

A reliable TDOA extraction method capable of consistently estimating TDOA under various variabilities is critical for robust, wave propagation-based, data-driven impact identification. While the Normalized Smoothed Envelope Threshold (NSET) method [35, 43] has demonstrated high accuracy and consistency in TDOA extraction for fixed impact scenarios with specific parameters [72], its robustness under significant variabilities—such as variations in impact mass and impactor—requires experimental validation.

3.5.1 TDOA uncertainties under variabilities in impact mass and impactor

Since impact mass and impactor material significantly affect impact responses [127], two distinct impact scenarios were considered: large-mass drop tower impacts (DT) and small-mass hammer impacts (HA), both conducted at location D, as shown in Fig. 3.3.

Fig. 3.6(a) compares the Power Spectral Density (PSD) of normalised impact sensor signals recorded by sensors 1 and 3 for DT and HA impacts. The results are consistent with the dynamics of the impacts. Large-mass DT impacts are dominated by low-frequency components, with PSD values decreasing sharply as the frequency increases. Most of the signal energy is concentrated below 0.5 kHz. In contrast, small-mass HA impacts exhibit a broader range of dominant frequencies (below 2 kHz) with a more gradual decline in PSD.

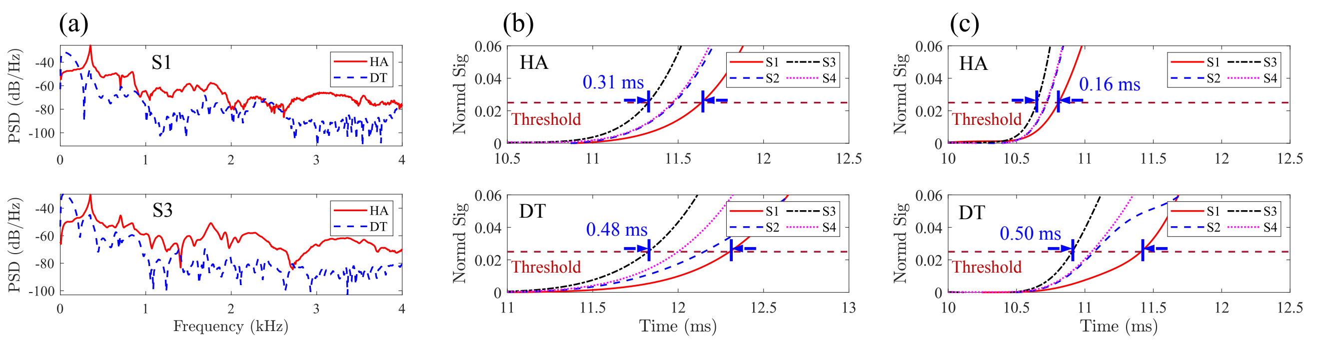

Figure 3.6: Signal PSD (a) and TDOA extracted by NSET method for HA and DT impacts at same location D with frequencies: (b) 1 kHz, (c) 2 kHz.

These spectral differences have a pronounced effect on TDOA. The TDOA values extracted using the NSET method for HA and DT impacts at location D at frequencies of 0.5 kHz and 1 kHz, with a threshold of 2.5% of the maximum signal amplitude, are presented in Fig. 3.6(b)-(c). The results indicate that the TDOA order remains consistent across variations in impact mass, with waves consistently arriving first at sensor 3 and last at sensor 1. However, the magnitude of the TDOA varies significantly, reflecting challenges in maintaining precise distance consistency.

For a fixed threshold, the maximum time difference of arrival between the first- and last-arriving sensors (Δt_{31}) is significantly greater for large-mass DT impacts compared to small-mass HA impacts—exceeding by 55% at 0.5 kHz (0.48 ms vs. 0.31 ms) and by over 200% at 1 kHz (0.50 ms vs. 0.16 ms). This trend contradicts the expected behavior of flexural wave dispersion, where higher frequencies travel faster, resulting in shorter TDOA intervals. While HA impacts follow this dispersion principle, DT impacts deviate from it between 0.5 kHz to 1 kHz.

This deviation stems from differences in the dominant frequency components present in the early portions of the filtered sensor signals. HA impacts generate a broad spectrum of frequencies, enabling dispersion-consistent TDOA estimation below 2 kHz. In contrast, DT impacts exhibit negligible signal energy at 1 kHz, causing the extracted TDOA to be governed by lower-frequency content, which naturally leads to larger delays. These results highlight the impact of frequency-dependent signal characteristics on TDOA estimation and emphasise the need for localisation algorithms that adapt to spectral variations. Such adaptability is essential for maintaining robustness and accuracy in scenarios with varying impactor masses and energy levels.

3.5.2 TDOA uncertainties under variabilities in impact height, angle and temperature

The four guided drop mass impact cases were used to examine TDOA uncertainties arising from variations in impact height, angle, and temperature. Fig. 3.7 presents the TDOA values extracted using the NSET method for these scenarios, with both 4 and 5 sensors, respectively. As shown in Fig. 3.7(a)-(b), the maximum TDOA differences across all 35 impact locations, induced by changes in impact height (HEI), impact angle (ANG), and a 46 °C temperature increase (TEM), consistently remain within approximately ±0.05 ms of the reference (REF) impacts, regardless of the number of sensors used. For impacts with a maximum TDOA below 0.1 ms using 4 sensors, the differences between impact cases are more pronounced. However, when an additional sensor (sensor 5) is introduced between sensor 1 and sensor 2, the lower bound of the maximum TDOA increases (exceeding 0.1 ms), indicating a reduced singularity in TDOA, as discussed in Section 3.3.1.

This reduction in singularity is also reflected in the cosine similarity between the REF impacts and the HEI, ANG, and TEM cases, which measures the order similarity of TDOAs. As shown in Fig. 3.7(c)-(d), the contour plots of cosine similarity across the plate indicate that the cosine similarity consistently exceeds 0.9 and 0.95 for 4 and 5 sensors, respectively. Impacts located closer to the sensors, where variations in impact-to-sensor distances are larger and TDOA values are higher, exhibit greater cosine similarity. Conversely, in the central region of the plate, where

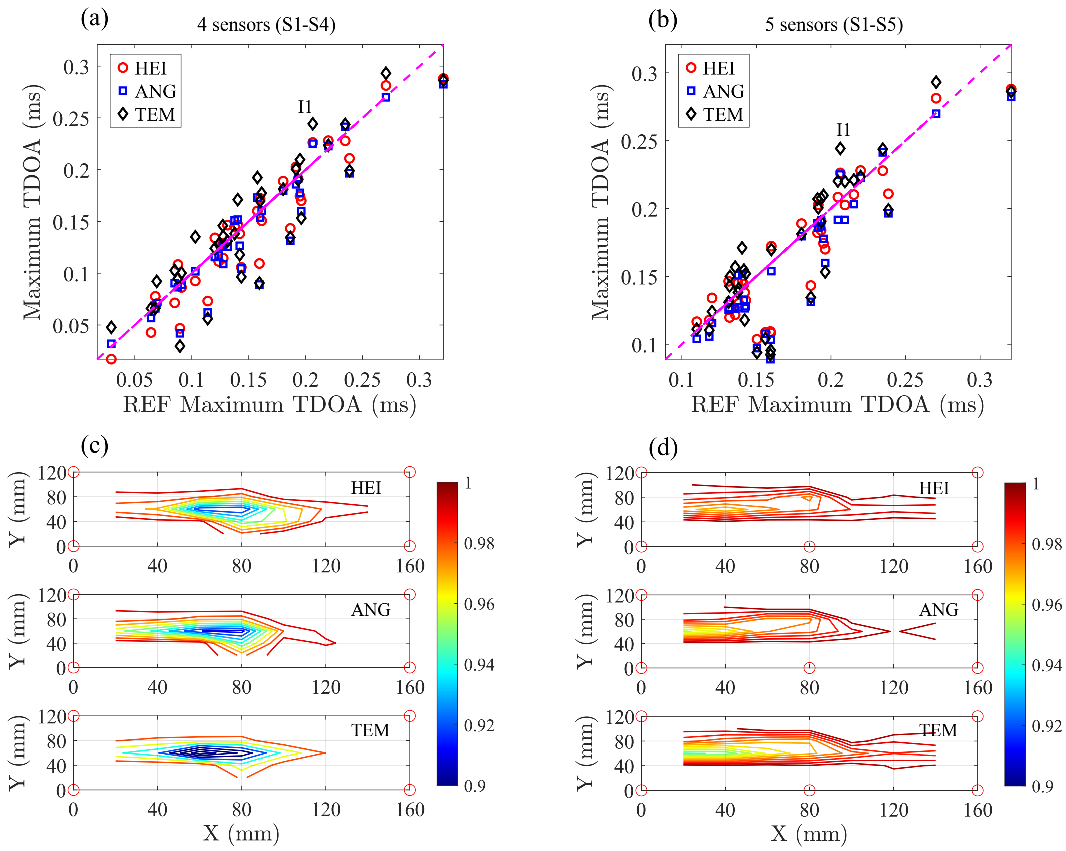

Figure 3.7: TDOA values extracted using the NSET method for four cases of drop mass impact testing: (a)-(b) maximum TDOA differences, (c)-(d) cosine similarity of TDOA between REF impacts and the HEI, ANG, and TEM cases, with 4 and 5 sensors, respectively.

impact-to-sensor distances are nearly identical and TDOA values are minimal, the cosine similarity decreases slightly. This behavior aligns with the proposed analysis regarding the influence of singularity point on TDOA consistency.

The effects of environmental temperature on TDOA differ significantly from those of impact height and angle. From a thermal expansion perspective, an increase in temperature reduces bending stiffness of the structure, which in turn decreases wave propagation velocities and increases TDOA values. However, as shown in Fig. 3.7(a)-(b), this trend is not consistently observed across all impact locations. Approximately two-thirds of the impacts follow this trend, showing the highest TDOA values in the TEM case. This can be attributed to two primary factors: First, for impacts near the singularity point, characterized by smaller TDOA values, the TDOA measurements become more sensitive to signal noise and errors in the TDOA extraction method. Second, the threshold used to extract TDOA in the NSET method is set to 2.5% of the signal peak, which varies for each impact. This adaptive threshold can result in either overestimation or underestimation of the TDOA, depending on the amplitude of the signal peak.

Similar to the findings for DT impacts, impact localisation solely based on distance similarity of TDOA values proves insufficient to address variabilities related to impact mass and temperature. However, the high similarity in TDOA order, as denoted by the cosine similarity in Fig. 3.7(b), suggest a promising avenue for improving localisation accuracy and reliability. By employing a composite input kernel that combines distance similarity (RBF kernel) with order similarity (COS kernel), it is anticipated that the robustness of the localisation process under variabilities can be significantly enhanced.

3.6 Impact Localisation under EOVs

This section presents the experimental validation and analysis of impact localisation on aircraft structures using various kernels and BIMA under EOVs.

3.6.1 Comparative analysis of GPR-BIMA for impact localisation

To investigate the influence of kernel choice in GPR-based localisation under environmental variability, the TEM case—characterised by the greatest deviation in TDOA values from the REF case due to temperature effects—was analysed. Three input kernels were considered: COS, RBF, and COMP kernel formed by element-wise multiplication of COS and RBF. Additionally, the proposed BIMA method was used to fuse predictions from multiple kernels. All TDOA inputs were normalised using sample standardisation (i.e., dividing each input vector by its L2 norm), while output impact locations remained in physical units (mm) without transformation.

As shown in Fig. 3.8(a), the negative marginal log-likelihood (MLL) values converged after 2000 Adam iterations across all models. The COMP kernel achieved the lowest MLL, benefiting from its ability to combine directional and amplitude-based similarity. Consequently, BIMA assigned it the highest marginal likelihood weight (0.47), compared to 0.35 for COS and 0.18 for RBF, confirming its superior model fit. The corresponding localisation results for each method are presented in Fig. 3.8(b)–(f), where red circles denote sensor locations, black squares indicate the true impact positions, and magenta diamonds represent the predicted impact locations. Each prediction is accompanied by an uncertainty ellipse, constructed using the marginal standard deviations from the predictive covariance, to visualise the spatial confidence of the estimation.

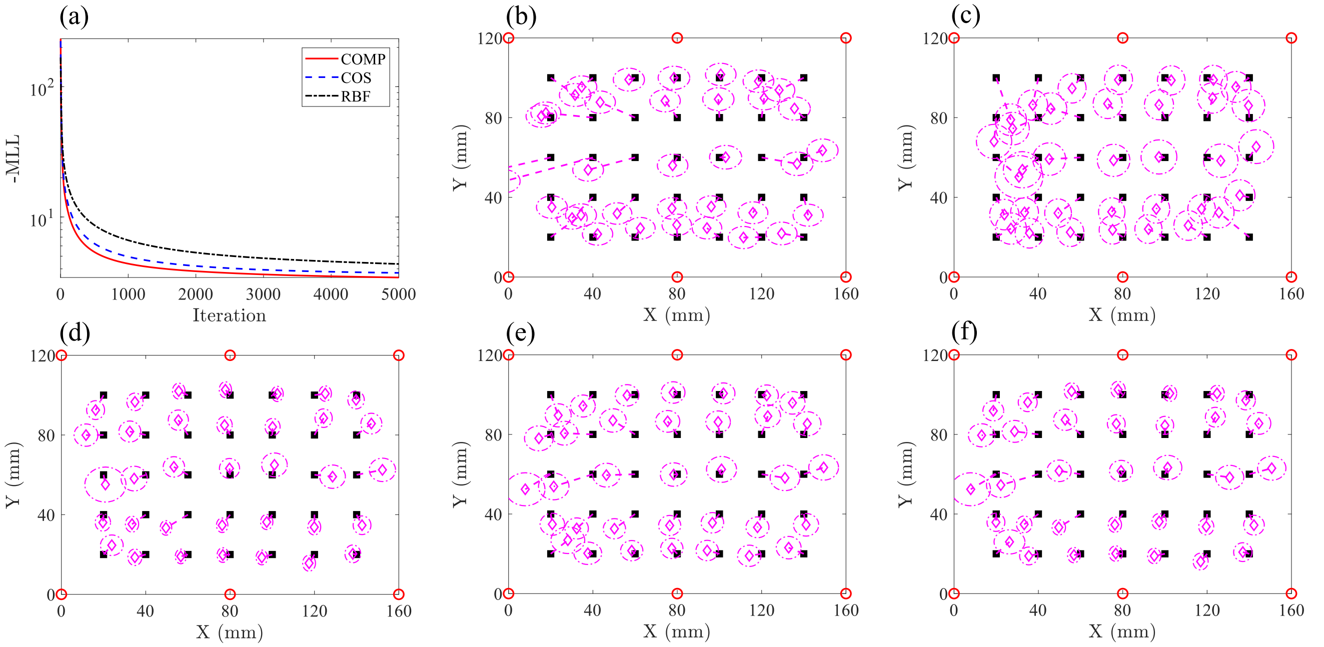

Figure 3.8: Multitask impact localisation for TEM impacts based on REF impacts using different input kernels, with 6 passive sensors: (a) Marginal log likelihood (MLL) convergence in GPR model training, (b) COS kernel, (c) RBF kernel, (d) COMP kernel, (e) BMA, (f) BIMA.

The COS kernel yielded high accuracy near sensors but performed poorly in the TDOA singularity region (e.g., along the line $Y = 60$ mm) due to its sensitivity to low TDOA amplitudes. In contrast, the RBF kernel performed better in these central regions but showed weaker accuracy near the sensors. The COMP kernel successfully integrated the strengths of both, achieving the best overall localisation with the highest accuracy and confidence (i.e., the smallest localisation variance). The BMA and BIMA results shown in Fig. 3.8(e)–(f) were nearly identical to those of the COMP kernel, reflecting their effectiveness in assigning greater weight to stronger-performing kernels. Compared to traditional BMA, the proposed BIMA more closely approximated the COMP kernel, indicating that the introduction of uncertainty-based weights in BIMA enabled greater emphasis on the COMP kernel, which consistently delivered superior localisation performance.

The optimised lengthscales provided further insight into the kernel behaviours. For the COMP kernel, the learned values were $l_{cos} = 14.90$ and $l_{rbf} = 0.73$, compared to $l_{cos} = 15.46$ and $l_{rbf} = 0.43$ in their respective standalone models. The shorter l_{cos} in COMP suggested more localised angular sensitivity, while the larger l_{rbf} indicated reduced sensitivity to small TDOA noise, thereby helping to mitigate overfitting. As the COMP kernel was constructed as the element-wise product of COS and RBF, its resulting covariance matrix suppressed off-diagonal elements, which enhanced interpolation contrast and improved generalisability across sparse reference samples.

The empirical CDF of localisation errors for all 35 TEM impacts using six passive sensors is presented in Fig. 3.9(a). Among the individual kernels, the COMP kernel achieved the best performance, yielding a mean localisation error of 6.1 mm and a 90% PoD error $\varepsilon_{90\%}$ of 8.7 mm, outperforming the RBF kernel (mean: 9.0 mm, PoD: 14.6 mm) and the COS kernel (mean: 11.1 mm, PoD: 18.3 mm). The classical BMA approach assigned the highest marginal likelihood weight (0.47) to the COMP kernel. Consequently, BMA produced intermediate performance (mean error: 7.5 mm; PoD error: 12.6 mm), reflecting a weighted average between the COMP and RBF models. In contrast, the proposed BIMA framework increased the weight assigned to the COMP kernel, driven by its lower predictive variance. As a result, BIMA achieved a mean error of 6.9 mm and a PoD error of 11.1 mm, closely approximating the performance of the COMP kernel while maintaining robustness through adaptive fusion of multiple models under uncertainty.

Uncertainty calibration was evaluated using the empirical coverage probability $P_{90\%}$, as defined in Eq. (3.14). The COS kernel exhibited underconfident uncertainty estimates, with $P_{90\%} = 0.743$, indicating that its predictive variances systematically underestimated the true localisation errors. In contrast, both the RBF and COMP kernels produced conservative estimates, each with $P_{90\%} = 0.943$. However, the source of this conservatism differed: for the RBF kernel, it stemmed from its relatively large predictive variances, while for the COMP kernel, it was due to its superior localisation accuracy, despite having slightly smaller predictive variances than RBF. The classical BMA and proposed BIMA models yielded $P_{90\%}$ values of 0.886 and 0.943, respectively. As both methods aggregate predictions through weighted averaging across kernels, their coverage probabilities generally fall within the range defined by the individual kernels. The BIMA model achieved a slightly conservative estimate by assigning higher weights to the more accurate COMP kernel—reflecting the positive correlation between localisation accuracy and empirical coverage. In contrast, classical BMA, which relies solely on marginal likelihood for weighting, assigned lower importance to COMP, resulting in a less conservative and slightly underconfident estimate.

To further assess model robustness, localisation performance was evaluated for the same set of TEM impacts under reduced sensor configurations, as illustrated in Fig. 3.9(b)–(c). With five sensors, the COMP kernel continued to yield the best localisation accuracy, closely followed by the proposed BIMA model, which benefited from its adaptive kernel weighting strategy. However, under the more constrained four-sensor configuration, the COS and RBF kernels surpassed COMP in terms of lower PoD errors ($\varepsilon_{90\%}$). In response, BIMA adaptively increased the weights assigned to COS and RBF, thereby outperforming COMP. This outcome underscores the importance of adaptive model averaging: no single kernel consistently delivered optimal localisation performance across all sensor configurations and data conditions. Specifically, BIMA's PoD errors increased from 11.1 mm (six sensors) to 13.4 mm (five sensors) and 17.4 mm (four sensors), while COMP's corresponding errors were 8.7 mm, 13.5 mm, and 19.7 mm, respectively. Despite performance degradation with fewer sensors, BIMA remained competitive due to its robustness to kernel selection under changing information content.

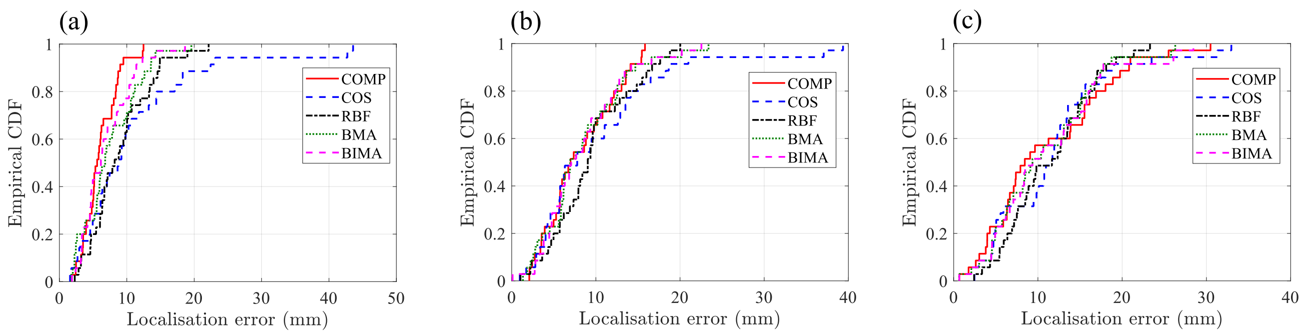

Figure 3.9: Empirical CDF of localisation error for TEM impacts based on REF impacts, under variations in sensors: (a) 6 sensors (S1-S6), (b) 5 sensors (S1-S5), (c) 4 sensors (S1-S4).

Uncertainty calibration was further assessed for the reduced sensor configurations. While the RBF, COMP, and BIMA models exhibited conservative uncertainty estimates under the full six-sensor configuration, all methods became increasingly underconfident as the number of sensors was reduced. With five sensors, the empirical $P_{90\%}$ values for COS, RBF, COMP, classical BMA, and BIMA were 0.771, 0.886, 0.747, 0.827, and 0.800, respectively. These values further declined under the four-sensor configuration to 0.771, 0.857, 0.627, 0.771, and 0.714, respectively. Notably, the COMP kernel consistently yielded the lowest empirical coverage among all models in both reduced sensor scenarios, revealing a significant underestimation of predictive uncertainty. This underconfidence can be attributed to the fact that the degradation in localisation accuracy with fewer sensors outpaced the growth of predicted variance. In contrast, the proposed BIMA model maintained relatively stable and moderately calibrated uncertainty by dynamically reweighting the base kernels in response to sensor sparsity. These results underscore the critical role of sensor density in achieving accurate impact localisation, while also highlighting the BIMA approach's ability to balance accuracy and confidence under constrained configurations.

3.6.2 Data preprocessing: sample standardization vs. feature standardisation

As demonstrated in Section 3.6.1, normalising the input TDOA vectors using sample standardisation yielded high accuracy in impact localisation. To further evaluate the effectiveness of different preprocessing strategies, a comparative study was conducted between sample standardisation (SS) and feature standardisation (FS) applied to the input TDOAs. Fig. 3.10 presents the empirical CDF of localisation errors for TEM impacts, comparing these preprocessing methods using the COMP kernel and BIMA. In the legend, 'I' and 'O' denote the input TDOAs (in milliseconds) and output location coordinates (in millimetres), respectively. 'SSI' refers to sample standardisation applied to inputs, whereas 'FSI' and 'FSO' indicate feature standardisation applied to inputs and outputs, respectively.

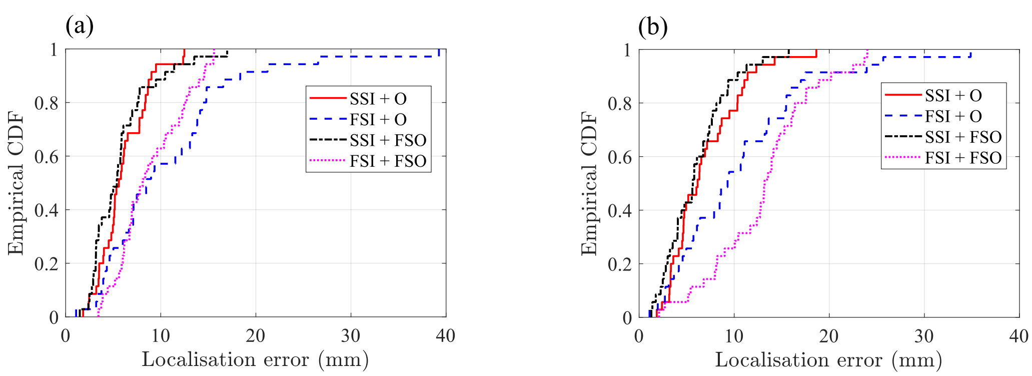

Figure 3.10: Empirical CDF of localisation error for TEM impacts based on REF impacts, comparing different data preprocessing approaches with: (a) COMP kernel, (b) BIMA.

The results showed that for both the COMP kernel and BIMA fusion, sample standardisation of the inputs (SSI) significantly outperformed feature standardisation (FSI) in achieving accurate TDOA-based impact localisation. Specifically, the mean localisation errors obtained using SSI with the COMP kernel and BIMA fusion ('SSI + O') were 6.1 mm and 6.9 mm, respectively, compared to 10.6 mm and 10.7 mm for the corresponding 'FSI + O' configurations. This advantage of SSI was also reflected in the PoD error $\varepsilon_{90\%}$, where the COMP kernel and BIMA fusion ('SSI + O') achieved $\varepsilon_{90\%}$ values of 8.7 mm and 11.1 mm, respectively, outperforming 16.6 mm and 17.0 mm for 'FSI + O'. This superior performance of SSI was attributed to its ability to preserve the relative ordering within the TDOA vectors while effectively addressing scale variations.

The underperformance of FSI stemmed from its disruption of order similarity, which is critical for the COS kernel, and its inability to adequately handle scale variations, a key factor for the RBF kernel. By preserving order similarity and consistently normalising TDOA magnitudes, SSI ensured compatibility with both order- and distance-based kernels, thereby improving impact localisation accuracy.

In addition, the effects of feature standardisation on output coordinates were examined. As shown in Fig. 3.10, applying feature standardisation to the output locations (FSO) slightly improved localisation performance when the input TDOAs were preprocessed using either SS or FS. This improvement was particularly evident in the reduction of maximum localisation errors, as illustrated by comparisons between 'SSI + O' and 'SSI + FSO', and between 'FSI + O' and 'FSI + FSO'.

Following output standardisation, the BIMA fusion method achieved a mean localisation error of 6.0 mm and PoD error $\varepsilon_{90\%}$ of 9.4 mm for the 'SSI + FSO' case, compared to 6.9 mm and 11.1 mm for 'SSI + O'. This improvement was attributed to enhanced numerical stability, as FSO helped alleviate kernel matrix ill-conditioning and accelerated the convergence of the marginal log-likelihood during training. Furthermore, BIMA fusion assigned greater weights to more accurate kernels, thereby improving the robustness of the predictions. Taken together, these findings support the recommendation of applying feature standardisation to output coordinates as a complementary preprocessing step, in consideration of numerical stability, model interpretability, and overall performance.

3.6.3 Impact localisation under various variabilities

To evaluate the performance of impact localisation under variabilities in impact height and angle, the ANG and HEI impacts were localised using the reference (REF) impacts recorded with six sensors. As shown in Fig. 3.11(a)-(b), the proposed BIMA demonstrated high accuracy in localising these impact cases under uncertain conditions.

For the ANG case, BIMA achieved a mean localisation error and PoD error $\varepsilon_{90\%}$ of 6.3 mm and 9.8 mm, respectively. Although these results were slightly worse than those of the COMP kernel (mean: 5.6 mm, PoD: 9.2 mm), BIMA outperformed the classical BMA method (mean: 6.9 mm, PoD: 12.4 mm). This outcome further confirmed BIMA's effectiveness in adaptively assigning higher averaging weights to the best-performing kernels. Similarly, for the HEI case, BIMA achieved a mean error of 6.0 mm and a PoD error $\varepsilon_{90\%}$ of 10.1 mm, which again was marginally inferior to the COMP kernel (mean: 5.4 mm, PoD: 8.0 mm) but superior to classical BMA (mean: 6.7 mm, PoD: 11.4 mm).

Uncertainty calibration was assessed using the empirical coverage probability $P_{90\%}$. For the ANG impacts, the COS, RBF, COMP, BMA, and BIMA kernels achieved $P_{90\%}$ values of 0.771, 0.914, 0.857, 0.943, and 0.914, respectively. In comparison, the corresponding values for the HEI impacts were 0.800, 0.943, 0.914, 0.971, and 0.943. These results indicate that individual kernels such as COS and COMP can exhibit underconfident estimates, while classical BMA tends to be slightly overconfident due to marginal likelihood-based weighting. In contrast, the proposed BIMA method consistently yielded better-calibrated uncertainty estimates, with empirical coverage probabilities closely matching those of the best-performing individual kernels. Notably, BIMA maintained stable and balanced coverage across both impact scenarios, underscoring its robustness in adaptively fusing base kernels by jointly considering predictive accuracy and uncertainty.

The normalisation methods for input TDOAs, specifically sample standardisation (SSI) and feature standardisation (FSI), were evaluated for the ANG and HEI impacts. The empirical CDFs of localisation errors, shown in Fig. 3.11(c)-(d), enabled a comparative analysis. In these figures, solid lines represented SSI, while dashed lines corresponded to FSI. Different colors distinguished the various methods, including individual kernels as well as BMA and BIMA.

Across all methods, the solid lines (SSI) consistently appeared slightly to the left of the dashed lines (FSI) up to a CDF value of 0.9 for the same method, indicating that SSI resulted in improved localisation accuracy. This outcome demonstrated the superior effectiveness of SSI for impact localisation, despite FSI also achieving comparatively high accuracy. Additionally, the COMP kernel's

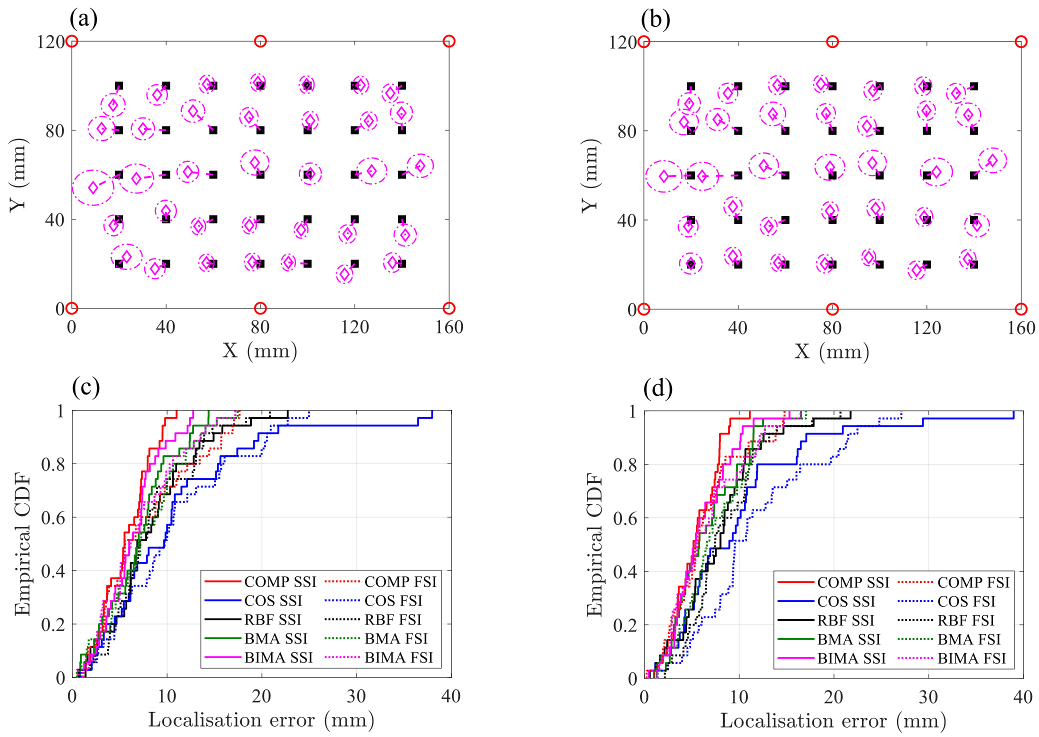

Figure 3.11: Localisation of ANG and HEI impacts based on REF impacts: (a)-(b) localisation illustration of ANG and HEI impacts using BIMA with SDI, respectively, (c)-(d) empirical CDF of localisation errors for ANG and HEI impacts, respectively, comparing SDI and FSI.

superior performance was reaffirmed, as it outperformed both the COS and RBF kernels. This advantage was further reflected in the BIMA fusion results, which surpassed the individual COS, RBF kernels, and classical BMA in localisation accuracy, highlighting the benefits of combining well-designed kernels with adaptive fusion strategies for robust impact localisation.

3.6.4 Impact localisation under varying boundary condition and impact mass

TDOA-based impact localisation methods were generally expected to remain effective regardless of structural boundary conditions, provided that the direct wave paths from the impact point to the sensors were not affected by reflections from the boundaries. This condition was typically satisfied when the sensor configuration ensured that the impact-induced wavefront reached the sensors before any boundary-reflected waves. To validate this hypothesis, drop tower (DT) impacts were localised using guided drop mass (REF) impacts as references. As illustrated in Section 3.4, the DT impacts were conducted on a plate simply supported along its longitudinal edges, whereas the

REF impacts were performed on the same plate but fully clamped along those edges. Additionally, as shown in Section 3.5.1, the substantial difference in impact mass between the two cases resulted in distinct spectral distributions of the impact responses. This experiment also aimed to assess the performance of localisation under variabilities arising from variations in impact mass (5500 g vs. 100 g) and energy (6000 mJ vs. 25 mJ).

Fig. 3.12 presents the localisation results for DT impacts using various kernel designs and the BIMA fusion, with a comparison between sample standardisation (SSI) and feature standardisation (FSI). Due to the substantially larger TDOA magnitudes observed in DT impacts compared to REF impacts, SSI consistently outperformed FSI in terms of localisation accuracy across all three kernels and the BIMA fusion. Specifically, the localisation errors achieved with SSI for the COS, RBF, and COMP kernels, and BIMA were 25.4 mm, 21.2 mm, 16.1 mm, and 19.6 mm, respectively. In contrast, the corresponding errors with FSI were significantly higher: 42.1 mm, 21.9 mm, 35.9 mm, and 34.6 mm, respectively. The classical BMA method was not plotted in this comparison, as its predictions coincided with those of BIMA due to disagreement between the kernel yielding the smallest predictive variance (COS) and the one with the highest marginal likelihood (COMP), leading the marginal likelihood weighting mechanism to dominate.

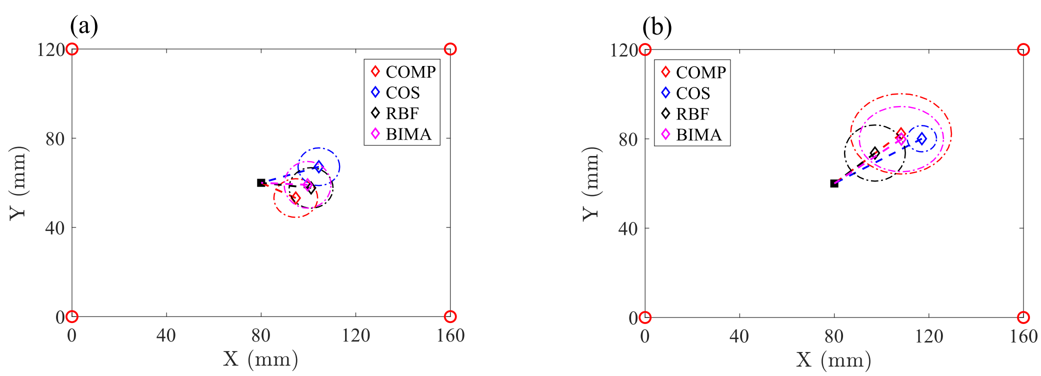

Figure 3.12: Localisation of DT impact based on REF impacts by kernel design and BIMA: (a) sample standardisation (SSI), (b) feature standardisation (FSI).

Moreover, when using SSI, both the RBF and COMP kernels produced smaller predictive variances, indicating higher confidence in localisation, compared to FSI. Since only one DT impact case was available, the empirical coverage probability P_λ could only take the value of 0 or 1, where 1 indicated that the true impact location fell within the predicted λ confidence interval. Except for the COS kernel, all methods achieved $P_{90\%} = 1$ under both SSI and FSI, suggesting well-calibrated predictive uncertainties. Notably, the COS kernel yielded the lowest variance but the highest localisation error, revealing a key limitation of relying solely on predictive variances as indicators of localisation accuracy. This finding further justified the conditional weighting mechanism employed in BIMA, as defined in Eq. (3.10), where uncertainty-based weighting was only applied when a kernel exhibits both lowest variance prediction and highest marginal likelihood.

These findings underscored the critical role of sample standardisation (SSI) in achieving accurate and reliable impact localisation under conditions of varying impact mass and energy. By effectively addressing scale variations in TDOAs, SSI enhanced compatibility across kernels and led to improved localisation accuracy and robust performance in kernel fusion strategies.

3.6.5 Influence of variability in reference impact data set

The preceding analysis of the impact localisation methodology was developed and validated using 35 reference impacts (RI) uniformly distributed on a composite plate in a 20 mm $\times$ 20 mm grid. To examine the influence of reference impact density on localisation performance, two additional RI subsets were systematically derived by reducing the number of impacts to 15 and 9, respectively, from the original set of 35. Fig. 3.13(a) illustrates the three RI configurations: black solid squares denote the full set of 35 RI, blue diamonds indicate the 15 RI subset, and magenta hexagrams represent the 9 RI subset.

The 15 RI subset was formed by selecting reference impacts from the first, fourth, and seventh columns of the full dataset, whereas the 9 RI subset was created by further excluding impacts from the second and fourth rows, thereby forming a subset of the 15 RI configuration. Owing to the increased density of RI in the second and fourth rows, the 15 RI configuration was expected to yield improved localisation accuracy in those regions compared to the sparser 9 RI setup.

Notably, all three RI configurations spanned the same rectangular area, ensuring that the localisation of all test impacts remained within an interpolation regime—denoted as ‘Int’ in the figure legend. This experimental design enabled a focused investigation into the trade-offs between the density of reference impacts and the achievable localisation accuracy under interpolation conditions, providing valuable insights for the efficient deployment of sensor-reference impact networks in practical SHM applications.

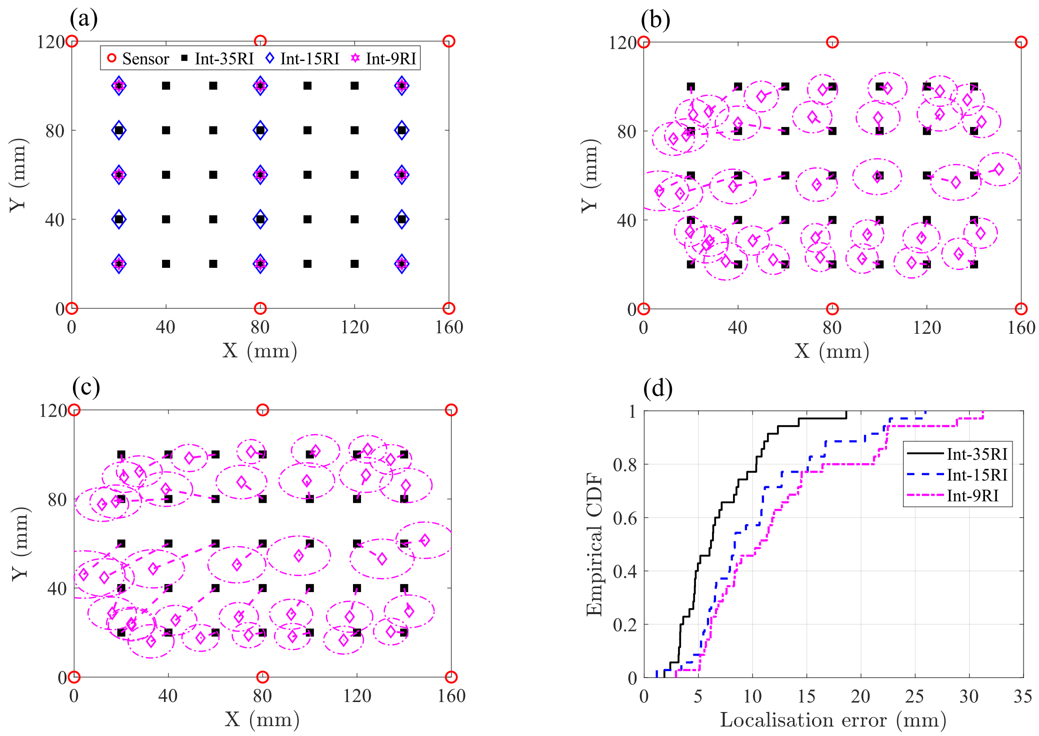

Figure 3.13: Interpolated localisation of TEM impacts using different sizes of reference impact (RI) sets with kernel design and BIMA fusion: (a) illustration of the three RI sets, (b) impact localisation with 15 RI using BIMA fusion, (c) impact localisation with 9 RI using BIMA fusion, (d) empirical CDF of impact localisation errors for the three RI sets using BIMA fusion.

The impact localisation results for the TEM impacts using the 15 RI and 9 RI configurations are presented in Fig. 3.13(b) and (c), respectively. When these results are compared with those obtained using the full set of 35 RIs—shown in Fig. 3.8(d)—and the empirical CDFs of localisation errors across the three RI sets—depicted in Fig. 3.13(d)—a clear trend emerges: increasing the number of reference impacts consistently improved localisation accuracy.

As anticipated, the 15 RI configuration yielded enhanced accuracy in the second and fourth rows, where its increased spatial sampling density provided a notable advantage over the sparser 9 RI configuration. Quantitatively, the 15 RI configuration achieved a mean localisation error and PoD error ($\varepsilon_{90\%}$) of 10.3 mm and 16.7 mm, respectively, while the 9 RI configuration resulted in higher errors of 12.2 mm and 22.3 mm. In comparison, the full set of 35 RIs significantly improved the overall performance, reducing the mean and PoD errors to 6.9 mm and 11.1 mm, respectively.

Despite the reduction in reference data, the mean localisation errors across all three configurations remained around 10 mm, demonstrating the robustness and high accuracy of the proposed impact localisation methodology. As detailed in Section 3.6.1, this strong performance was primarily attributed to the use of the COMP kernel—which effectively integrated the complementary strengths of the COS and RBF kernels—and the BIMA fusion strategy, which adaptively assigned greater weights to more accurate kernel predictions.

Fig. 3.14 presents the impact localisation results for the TEM impacts using 9 RI and three different kernel designs: COS, RBF, and COMP. The COS kernel performed poorly in regions associated with smaller TDOA values but exhibited better performance in regions with larger TDOA values. In contrast, the RBF kernel yielded higher accuracy in regions with smaller TDOA values but underperformed in regions where TDOAs were large. The COMP kernel successfully integrated the complementary strengths of both COS and RBF kernels, thereby achieving consistently high localisation accuracy across the entire sensing region.

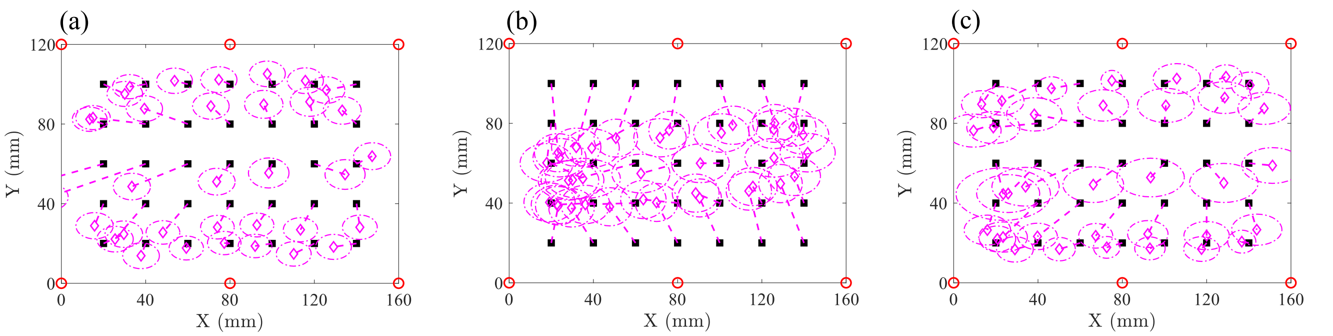

Figure 3.14: Interpolated localisation of TEM impacts with 9 RI using three different kernels: (a) COS kernel, (b) RBF kernel, and (c) COMP kernel.

This analysis further reinforced the robustness and effectiveness of the proposed composite kernel design and the BIMA fusion strategy. Together, they provided a reliable and adaptable framework for accurate impact localisation under varying conditions of uncertainty and with different densities of reference impacts.

3.6.6 Impact localisation: interpolation (int) vs. extrapolation (ext)

The preceding impact localisation tasks represented interpolation problems, in which all target (testing) impacts were located within the spatial coverage of the reference impacts (RI). To evaluate the capability of the proposed localisation framework in extrapolation scenarios, an alternative subset consisting of the 9 innermost reference impacts—referred to as 'Ext-9RI'—was constructed. As illustrated in Fig. 3.15(a), this set (marked by blue diamonds) formed a smaller rectangular region compared to the 'Int-9RI' configuration (marked by magenta hexagrams), which spanned the full coverage area of the original 35 RI. Consequently, any testing impact falling outside the boundary of the 'Ext-9RI' set was categorised as an extrapolation case.

Fig. 3.15(b)–(e) shows the extrapolated localisation results using the 'Ext-9RI' set with three individual kernels and the BIMA fusion. The corresponding empirical CDFs of localisation errors, shown in Fig. 3.15(f), revealed that the RBF kernel performed poorly under extrapolation conditions. It failed to accurately localise impacts outside the RI coverage, resulting in substantial localisation errors and inflated predictive variances.

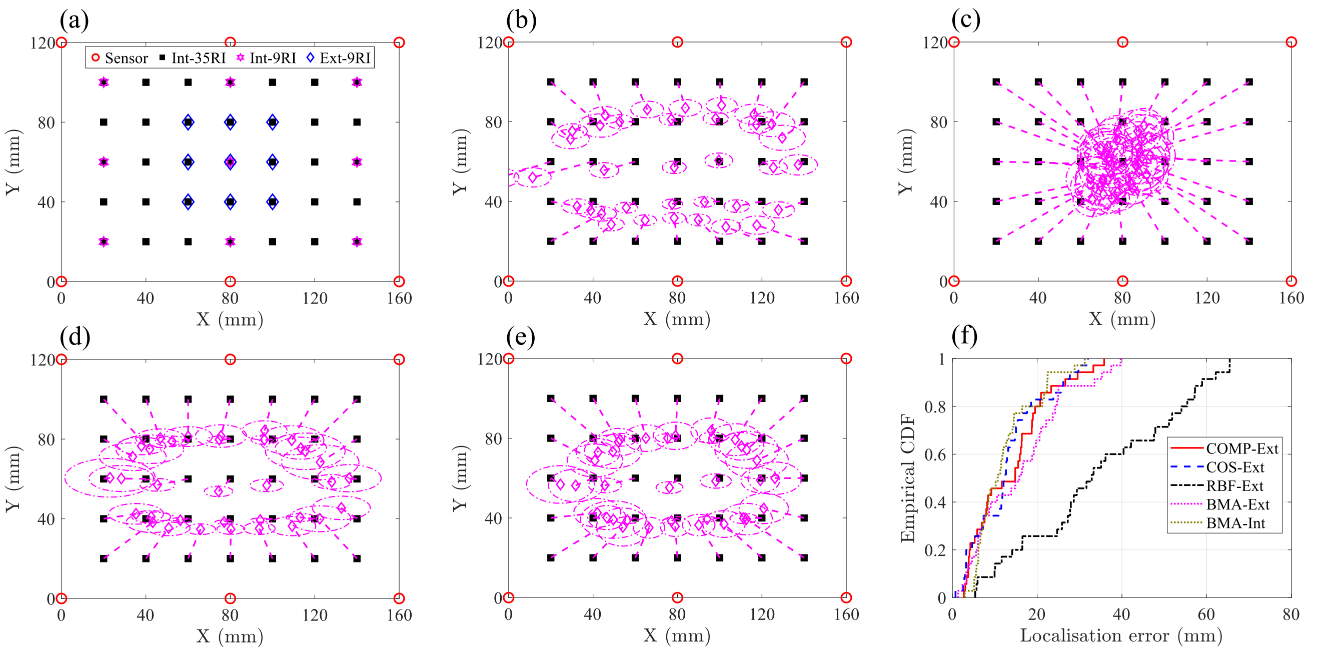

Figure 3.15: Extrapolated localisation of TEM impacts with the 9 innermost reference impacts (RI), referred to as 'Ext-9RI': (a) illustration of the RI set for extrapolation, denoted as 'Ext-9RI', (b) localisation results using the COS kernel, (c) localisation results using the RBF kernel, (d) localisation results using the COMP kernel, (e) localisation results using BIMA fusion, (f) empirical CDF of localisation errors for the 'Ext-9RI' reference set.

In contrast, the COS and COMP kernels demonstrated a degree of extrapolation capability, largely attributable to their reliance on TDOA order rather than absolute TDOA magnitudes. This allowed them to make more reasonable predictions beyond the reference domain. The BIMA fusion method effectively leveraged these strengths by adaptively weighting the COS and COMP kernels more heavily, based on their lower predictive variances. Consequently, BIMA inherited their extrapolation ability and achieved improved localisation performance in regions outside the training set coverage.

Compared to the interpolation scenario using the 'Int-9RI' set, which included nine reference impacts, the extrapolation scenario with the 'Ext-9RI' set exhibited reduced localisation accuracy. Specifically, the 'Ext-9RI' configuration resulted in a mean localisation error of 15.8 mm and a PoD error ($\varepsilon_{90\%}$) of 25.0 mm, whereas the 'Int-9RI' case achieved lower errors of 12.2 mm and 22.3 mm, respectively. These results highlight the inherent advantage of surrogate models in solving interpolation problems, where the test inputs lie within the span of the training data, as opposed to extrapolation tasks that require predictions beyond the training domain.

Uncertainty calibration was further assessed using the empirical coverage probability $P_{90\%}$. In the interpolation case ('Int-9RI'), the COS, RBF, COMP, and BIMA models yielded $P_{90\%}$ values of 0.771, 0.657, 0.829, and 0.857, respectively. In contrast, these values dropped significantly in the extrapolation case ('Ext-9RI'), with COS, RBF, COMP, and BIMA yielding 0.486, 0.257, 0.543, and 0.571, respectively. BIMA consistently produced higher coverage than the individual kernels in both scenarios, due to its ability to account for epistemic uncertainty through model disagreement, which increases the predictive variance. As illustrated in Fig. 3.14 and Fig. 3.15(b)-(d), the predictions from the three base kernels diverged significantly, especially in extrapolation, reflecting greater uncertainty. However, despite this increase in variance, the much larger localisation errors in the extrapolation case led to poorer uncertainty calibration overall.

These findings underscore the importance of ensuring that reference impacts are spatially distributed to comprehensively span the expected impact domain. Such coverage promotes interpolation-dominant conditions, enabling more accurate and better-calibrated predictions in data-driven impact localisation applications.

3.6.7 Impact localisation: CNN vs. GPR-BIMA

The convolutional neural network (CNN) model, whose model architecture is detailed in [73], was employed to validate the performance of the DNN-based impact localisation framework under real-world variabilities. The CNN models were trained using reference (REF) impact data, with raw sensor signals of 20,000 samples—corresponding to a 10 ms time window—used as input. These pre-trained CNN models were then applied to predict the locations of test (TEM) impacts.

To assess the influence of sensor count and the number of reference impacts on localisation performance, three configurations were examined: 6S-35RI, 4S-35RI, and 6S-9RI, where 'S' denotes the sensors and 'RI' refers to the reference impacts used for training. In all cases, the mean squared error (MSE) loss decreased rapidly during the initial training epochs and subsequently stabilised within a fluctuating range of [0.001, 0.007], indicating convergence of the learning process.

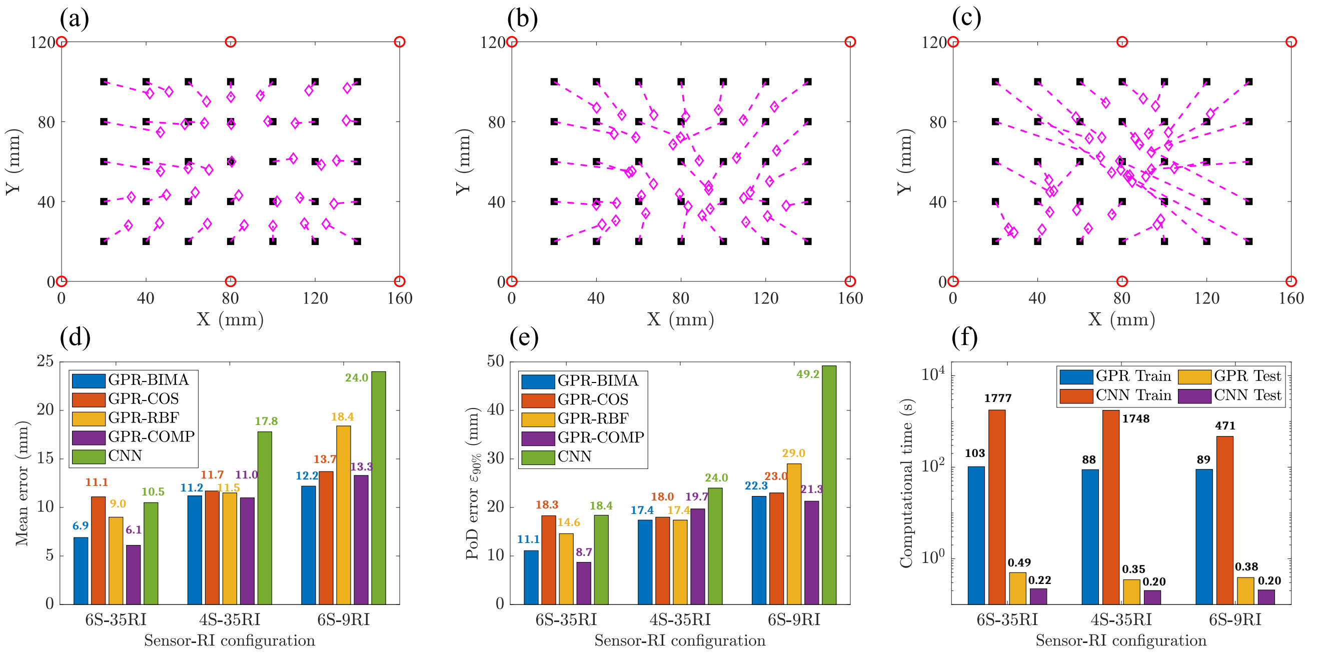

Figure 3.16: Localisation of TEM impacts using CNN model trained on REF impacts: (a)-(c) localisation illustration with 6S-35RI, 4S-35RI, and 6S-9RI, respectively, (d) localisation mean errors compared to GPR models, (e) localisation PoD errors $\varepsilon_{90\%}$ compared to GPR models, (f) computational times for training and testing of GPR and CNN models.

The localisation results for the TEM impacts under the three configurations are illustrated in Fig. 3.16(a)–(c). When using six sensors and 35 reference impacts, as shown in Fig. 3.16(a), the CNN model achieved moderate localisation accuracy, with a PoD error $\varepsilon_{90\%}$ of approximately 18.4 mm. However, reducing the number of sensors from 6 to 4 ($\varepsilon_{90\%}$=24.0 mm) or decreasing the number of reference impacts from 35 to 9 ($\varepsilon_{90\%}$=49.2 mm) significantly degraded the localisation performance. This deterioration was attributed to the reduced spatial coverage of sensor measurements and the limited training data, which constrained the CNN model's ability to generalise to unseen impact locations. In particular, the reduction in reference impacts led to poor feature representation, making it more difficult for the model to learn the underlying relationships between the impact signals and their spatial positions.

Fig. 3.16(d)–(e) presents a comparative analysis of localisation errors across three sensor-impact configurations, evaluating the CNN model against GPR models using the COS, RBF, and COMP kernels, as well as the BIMA fusion strategy. The CNN model produced mean localisation errors of 10.5 mm, 17.8 mm, and 24.0 mm, with PoD errors $\varepsilon_{90\%}$ of 18.4 mm, 24.0 mm, and 49.2 mm, respectively, across the three configurations. In contrast, the GPR model with BIMA fusion achieved substantially lower mean errors of 6.9 mm, 11.2 mm, and 12.2 mm, and corresponding PoD errors of 11.1 mm, 17.4 mm, and 22.3 mm. Notably, the BIMA fusion approach consistently produced error levels closest to the minimum obtained among the individual kernels (COS, RBF, COMP), highlighting its effectiveness in adaptively assigning the highest weights to the most suitable kernel for each scenario. These results demonstrated the enhanced accuracy and robustness of the GPR-based approach, particularly under sparse data conditions, where it consistently outperformed the CNN across different sensor counts and reference impact densities.

The computational efficiency of CNN and GPR was assessed by comparing the training and testing times on a desktop equipped with an Intel i7-10700 processor, as shown in Fig. 3.16(f). Across all three configurations, CNN required substantially longer training times due to its greater model complexity and the need for extensive hyperparameter tuning to extract temporal features. For the cases with 6S-35RI and 4S-35RI, training three GPR models with different kernels took approximately 100 seconds, whereas CNN training required 1750 seconds. Reducing the number of reference impacts to 9 (6S-9RI), lowered the CNN training time, but it still remained over five times longer than that of GPR. In contrast, model testing was highly efficient for both methods: predicting 35 TEM impacts required only 0.3 seconds, demonstrating real-time feasibility. Notably, GPR—with fewer than 10 hyperparameters—exhibited superior data efficiency, robust localisation performance, and real-time prediction capability under EOVs.

3.7 Summary

This chapter presents a robust data-driven framework for impact localisation in composite aircraft structures, targeting the challenges posed by EOV. A key insight underpinning the approach is the observed invariance of the relative TDOA order across sensors, even under varying temperatures and impact conditions. Building on this, a composite kernel (COMP) is developed for GPR, combining the spatial sensitivity of the RBF kernel with the order-preserving characteristics of the

COS kernel. To further enhance adaptability under changing conditions, a BIMA mechanism is introduced, dynamically adjusting kernel contributions based on the current operational context.

Experimental validation on a composite panel demonstrates the effectiveness of the proposed framework—referred to as GPR-BIMA—under partially covered EOV scenarios. Compared with two baselines—a CNN and a conventional GPR-RBF model—the proposed approach consistently delivers superior localisation accuracy across different sensor configurations and varying numbers of reference impacts, as summarised in Fig. 3.16(e)-(f). Without explicit temperature compensation and trained solely under baseline (REF) conditions, the GPR-BIMA model achieves 90% PoD errors of 6.9 mm and 11.2 mm using six and four sensors, respectively, under a 46°C temperature shift. In contrast, the CNN yields errors of 10.5 mm and 17.8 mm, while GPR-RBF results in 9.0 mm and 11.5 mm under the same conditions.

These results highlight the scalability and partial generalisability of the proposed method, with improved performance from increased sensor density and reference coverage. The integration of physically informed kernel design with adaptive probabilistic fusion contributes to enhanced robustness against uncertain and variable operating environments.

While these findings indicate strong potential for advancing in-service SHM in aerospace applications, it is important to note that the proposed framework has been validated only under limited EOV conditions and in controlled experimental settings. Moreover, the approach assumes a uniform scale of the GVP, an assumption that may not hold for complex composite structures—particularly those featuring non-uniform layups or intricate stiffener configurations—where wave propagation velocities can vary significantly across the structure. Such variability could compromise localisation accuracy and necessitate further model adaptation. Consequently, additional development, refinement, and large-scale validation under a wider range of EOVs are required to assess the framework's robustness and readiness for operational deployment. The proposed GPR-BIMA method therefore represents a promising, yet preliminary, step toward real-world SHM implementation.

Chapter 4

Hybrid Physics-data Impact Localisation for Enhanced Generalisability

Highlights:

- Develop a hybrid impact localisation framework that enhances robustness and generalisability by embedding dispersion relations derived from First-order Shear Deformation Theory.
- Strengthen the physical foundation of wave-based localisation by characterising key dispersive properties of flexural waves in laminated composites, including wave modes, cut-off frequencies, limiting velocities, and monotonicity.
- Overcome extrapolation limitations of purely data-driven models by integrating physical insights into the learning process.
- Enable real-time localisation through the development of efficient, gradient-based optimisation algorithms for fast and accurate prediction.

4.1 Introduction

As validated in Chapter 3, data-driven impact localisation methods encounter significant challenges when extrapolating to impact locations beyond the coverage area of the training dataset. Moreover, their performance is highly dependent on the extent and density of the training dataset. Achieving high localisation accuracy typically requires a large number of training impacts distributed densely across the structure, making data collection both impractical and costly.

To mitigate the expenses associated with collecting extensive training impact data, recent studies have explored techniques such as multi-fidelity data augmentation [43] and transfer learning [68]. These approaches enable the integration of inexpensive low-fidelity training data—typically derived from analytical models or numerical simulations—with high-fidelity experimental data, thereby reducing reliance on costly physical experiments.

For instance, Seno et al. [43] developed a multi-fidelity Gaussian Process Regression (GPR) surrogate model for impact localisation by combining numerical and experimental training data. Their study demonstrated that supplementing experimental data with low-cost numerical simulations can significantly reduce the need for expensive impact experiments while maintaining reliable localisation performance. Similarly, Kalimullah et al. [68] incorporated wave propagation physics into a multi-fidelity MLP model using transfer learning techniques. They first measured the Group Velocity Profile (GVP) through active sensing experiments and then integrated this information, along with experimental impact data, to improve model generalisability. While their GVP measurement was based on extensional waves, it effectively captured essential wave propagation physics, enhancing localisation performance across the entire structure.

The improved generalisability of such approaches stems from the fundamental physical principles governing impact dynamics, which remain valid regardless of the specific impact properties. Regardless of impact location or force, the fundamental relationship—that the distance travelled by impact-induced waves is the product of wave propagation velocity and propagation time—always holds. However, experimental GVP measurement typically requires a large number of precisely positioned sensors and strategically selected impact excitations. For example, some experimental setups involve arranging tens of sensors along the circumference of a circle, with the impact excitation positioned at its centre [27, 68, 69]. Alternatively, sensors may be evenly distributed, with multiple impact excitations carefully aligned with any two passive sensors to estimate wave velocity along a given line [26]. These demanding requirements significantly hinder the practical implementation of experimental GVP estimation, necessitating the development of more efficient approaches that reduce the number of required sensors and impact excitations.

In real-world aviation applications, composite structures are designed with safety margins and manufactured using selected lamina to ensure structural strength exceeds operational requirements. Consequently, the material properties of individual lamina and the stacking sequences of composites are generally known, albeit with some interval uncertainties. This roughly known information can be leveraged to construct Finite Element Analysis (FEA) models, though unknown boundary conditions can pose challenges requiring boundary condition identification and FEA updating. However, since the propagation of impact-induced wave fronts is independent of boundary conditions, these known material and structural properties can serve as prior physical knowledge to enhance the generalisability of data-driven impact localisation methods. By incorporating physical information into data-driven models, hybrid approaches can achieve improved localisation performance while mitigating the need for extensive experimental data collection.

This chapter introduces a novel Hybrid Physics-based and Data-driven (HPD) impact localisation method, which integrates the physical characteristics of impact-induced flexural waves into the localisation process. The proposed approach leverages a GVP governed by a dispersion equation analytically derived from First-order Shear Deformation Theory (FSDT) plate theory [83]. This dispersion equation provides a parametric representation of the GVP as a function of material stiffness and wave frequency, embedding physical knowledge into the impact localisation framework.

Unlike conventional data-driven methods, which approximate the GVP using black-box models, the HPD approach explicitly formulates and optimises the GVP with respect to material stiffness and wave frequency, based on training impact data. To achieve this, a two-stage optimisation process is proposed, which exploits the partial derivatives of the dispersion equation to refine GVP estimation. This process is efficiently solved using gradient-based optimisation techniques, including Newton's method and the Trust-Region-Reflective (TRF) algorithm [137], ensuring rapid convergence.

Once the optimised velocity profile is obtained, triangulation is employed for impact localisation using the TRF algorithm. Because the proposed HPD method relies entirely on computationally efficient gradient-based optimisation, it facilitates real-time localisation with minimal computational overhead—potentially even at the level of individual sensor nodes.

4.2 Impact-induced Flexural Wave Analysis based on FSDT

Given the widespread application of symmetric laminates in plate structures [87], this study focuses on symmetric composite laminates. The dispersion characteristics of flexural waves in such laminates, based on the FSDT, are presented in Section 2.3.3.3. This formulation yields three antisymmetric wave modes: A0, A1, and SH1. The propagation characteristics and spectral properties of these modes are analysed in detail in this section.

4.2.1 Cutoff frequencies and flexural wave modes

By Laplace expansion, this spectrum equation Eq. (2.35) is reformulated as:

$$\det \mathbf{G}_o = g_{11}(g_{22}g_{33} - g_{23}^2) + g_{12}(g_{13}g_{23} - g_{12}g_{33}) + g_{13}(g_{12}g_{23} - g_{13}g_{22}) = 0. \tag{4.1}$$

where $g_{ij}, i, j = 1, 2, 3$ are provided in Eq. (2.34). This dispersion equation is a sextic polynomial in terms of the frequency ω, containing only even-degree terms. For each wavenumber k, there are three positive frequency solutions to this equation, corresponding to three values of phase velocity $v_p = \omega/k$ and three antisymmetric wave modes A0, A1 and SH1. To evaluate the limit of Eq. (4.1) as the wavelength becomes infinite ($k \to 0$), the terms solely related to k are omitted. The cut-off frequencies of these three wave modes are the solutions to:

$$I_1\omega^2[(A_{55} - I_3\omega^2)(A_{44} - I_3\omega^2) - A_{45}^2] = 0. \tag{4.2}$$

The solution $\omega_c = 0$ corresponds to the lowest mode A0 of the flexural waves, which has a velocity of zero as $k \to 0$. Other two solutions ($\omega_c > 0$) represent two higher modes A1 and SH1 whose phase velocities become infinite as $k \to 0$.

It is worth noting that in the absence of shear modulus information, G_{23} and G_{13} are usually assumed to be equal to G_{12}. In this case, $G_{23} = G_{13}$ leads to $A_{44} = A_{55}$ and $A_{45} = 0$. From Eq. (4.1), the cutoff frequencies of these two higher modes are identically equal to $\sqrt{A_{44}/I_3}$. Due to the lack of information and for the sake of simplicity, the following analysis will adhere to the assumption that $G_{23} = G_{13} = G_{12}$. This assumption simplifies the $\mathbf{G}$ matrix from Eq. (2.34) to (replacing k with ω/v_p):

$$\begin{aligned}
g_{11} &= -A_{44}\frac{\omega^2}{v_p^2} + I_1\omega^2,\ g_{12} = iA_{44}\frac{\omega}{v_p}\cos\theta,\ g_{13} = iA_{44}\frac{\omega}{v_p}\sin\theta, \\
g_{22} &= (D_{11}\cos^2\theta + 2D_{16}\sin\theta\cos\theta + D_{66}\sin^2\theta)\frac{\omega^2}{v_p^2} + A_{44} - I_3\omega^2, \\
g_{23} &= [(D_{12} + D_{66})\sin\theta\cos\theta + D_{16}\cos^2\theta + D_{26}\sin^2\theta]\frac{\omega^2}{v_p^2}, \\
g_{33} &= (D_{22}\sin^2\theta + D_{66}\cos^2\theta + 2D_{26}\sin\theta\cos\theta)\frac{\omega^2}{v_p^2} + A_{44} - I_3\omega^2.
\end{aligned} \tag{4.3}$$

4.2.2 Limiting velocities and monotonicity of flexural waves

As the wavenumber/frequency tends to infinity, the phase velocities for these three wave modes A0, A1 and SH1 approach constant values. Evaluating the limit of Eq. (4.1) when the frequency becomes infinite ($\omega \to +\infty$) by omitting the lower-order terms of ω except ω^6 results in an equation:

$$\omega^6\left(\frac{A_{44}}{v_p^2} - I_1\right)\left[\left(\frac{b_{22}}{v_p^2} - I_3\right)\left(\frac{b_{33}}{v_p^2} - I_3\right) - \frac{b_{23}^2}{v_p^2}\right] = 0. \tag{4.4}$$

These intermediate parameters b_{22}, b_{33} and b_{23} extracted from their corresponding g_{ij} are given by:

$$\begin{aligned}
b_{22} &= D_{11}\cos^2\theta + 2D_{16}\sin\theta\cos\theta + D_{66}\sin^2\theta, \\
b_{23} &= (D_{12} + D_{66})\sin\theta\cos\theta + D_{16}\cos^2\theta + D_{26}\sin^2\theta, \\
b_{33} &= D_{22}\sin^2\theta + D_{66}\cos^2\theta + 2D_{26}\sin\theta\cos\theta.
\end{aligned} \tag{4.5}$$

The velocity solution $\bar{v}_{p,A0} = \sqrt{A_{44}/I_1} = \alpha\sqrt{G_{12}/\rho}$ from Eq. (4.4) represents the limiting phase velocity value of the lowest flexural wave mode A0 as the frequency tends to infinity. This velocity is solely dependent on the shear modulus and density of the laminates. However, the limiting velocities of the other two higher modes A1 and SH1 also depend on the wave propagation direction θ. The limiting velocities of the two higher modes as the frequency approaches infinity are derived as:

$$\bar{v}_{p,A1,SH1}^2 = \frac{(b_{22}+b_{33})I_3 + b_{23}^2 \pm \sqrt{[(b_{22}+b_{33})I_3 + b_{23}^2]^2 - 4b_{22}b_{33}I_3^2}}{2I_3^2} \geq \frac{\min(b_{22}, b_{33})}{I_3} \geq \frac{G_{12}}{\rho} > \bar{v}_{p,A0}^2, \tag{4.6}$$

The holding of inequality in the above equation can be analysed firstly in the $\theta = 0$ direction, with $b_{22} = D_{11}$, $b_{23} = D_{16}$ and $b_{33} = D_{66}$. Consider a unidirectional lamina whose stiffness matrix $\bar{Q}_{ij}, i, j = 1, 2, 6$ is calculated based on the principal fibre orientation ($\phi = 0$), $\bar{Q}_{11}$ reaches its maximum ($\bar{Q}_{11} = Q_{11} = E_1/(1-\nu_{12}\nu_{21})$), $\bar{Q}_{66}$ reaches it minimum ($\bar{Q}_{66} = Q_{66} = G_{12}$) and $\bar{Q}_{16}$ vanishes ($\bar{Q}_{16} = 0$). Consequently, the limiting velocity of one of the two higher modes A1 and SH1 takes its minimal value $\sqrt{\frac{D_{66}}{I_3}} = \sqrt{\frac{\bar{Q}_{66}}{\rho}} = \sqrt{\frac{G_{12}}{\rho}}$, which remains slightly larger than that of the lowest mode A0 ($\bar{v}_{p,A0} = \alpha\sqrt{G_{12}/\rho}$) as the frequency approaches infinity. Laminates with multiple plies placed in different orientations increase the average stiffness D_{66} compared to a unidirectional laminate, resulting in a greater limiting velocity for higher modes. Varying the principal directions of the laminates from the fibre direction also increases the D_{66}. Since the rotations of principal directions of laminates ϕ are equivalent to the change of wave propagation direction θ in the dispersion equation concerning the calculation of phase velocity, the limiting velocities of the higher modes in every wave propagation direction exceed that of the lowest mode ($\bar{v}_{p,A0} = \alpha\sqrt{G_{12}/\rho}$). Therefore, due to the nature of the laminates, $b_{22} > I_3\bar{v}_{p,A0}^2 > 0$ and $b_{33} > I_3\bar{v}_{p,A0}^2 > 0$ are maintained for all wave propagation directions θ since $\bar{v}_{p,A1}, \bar{v}_{p,SH1} \geq \bar{v}_{p,A0}$. Furthermore, a simple transformation on $(b_{22}/v_p^2 - I_3)(b_{33}/v_p^2 - I_3) - b_{23}^2/v_p^2 > 0$ demonstrates $g_{22}g_{33} - g_{23}^2 > 0$ if $v_p \in (0, \bar{v}_{p,A0})$.

Intuitively, the phase velocity of the lowest mode A0 of flexural waves increases monotonically with frequency and is bounded in $(0, \bar{v}_{p,A0})$. To prove this, assuming $v_p \in (0, \bar{v}_{p,A0})$, the first-order partial derivative of wave velocity with respect to frequency, $\frac{\partial v_p}{\partial \omega}$, should be positive. Typically, D_{16} is relatively small, which does not influence the sign of $\frac{\partial v_p}{\partial \omega}$, especially for symmetric cross-ply laminates ($D_{16} = 0$). By disregarding D_{16} and setting $\theta = 0$ ($g_{13} = g_{23} = 0$), Eq. (4.1) can be reformulated as:

$$g_{11}g_{22} - g_{12}^2 = 0,\ g_{11} = -A_{44}\frac{\omega^2}{v_p^2} + I_1\omega^2,\ g_{22} = D_{11}\frac{\omega^2}{v_p^2} + A_{44} - I_3\omega^2,\ g_{12} = iA_{44}\frac{\omega}{v_p}. \tag{4.7}$$

The derivative of wave phase velocity with respect to frequency is calculated as:

$$\frac{\partial v_p}{\partial \omega} = \frac{v_p}{\omega} \frac{g_{11}(g_{22} - A_{44})}{g_{11}(g_{22} - A_{44} + I_3\omega^2) - g_{22}I_1\omega^2} > 0. \tag{4.8}$$

When $v_p \in (0, \bar{v}_{p,A0})$, g_{11} is negative. Moreover, given that $b_{22} = D_{11} > I_3\bar{c}^2 > 0$, g_{22} exceeds A_{44}. Consequently, both the numerator and denominator in Eq. (4.8) are negative, resulting in a positive derivative. This confirms the monotonically increasing relationship between the phase velocity of the lowest flexural wave mode A0 and the frequency.

It can be observed from Eq. (4.1) and Eq. (4.8) that the phase velocity of flexural waves varies with the wavenumber/frequency. Particularly for the lowest mode A0, as the wavenumber (or frequency) increases, the phase velocity also increases, indicating the dispersive nature of flexural waves. Although Eq. (4.1) describes these dispersion relations, there is no explicit algebraic solution to this dispersion equation. However, approximate numerical solutions for the wave velocity of the lowest mode A0 can be obtained for any wavenumber or frequency using methods such as the bisection method or Newton's method, as the phase velocity v_p of the lowest-mode flexural waves, bounded within the range $(0, \bar{v}_{p,A0})$, monotonically increases with frequency.

4.2.3 Illustrative example of flexural waves in a laminated composite plate

To demonstrate the dispersive nature of flexural waves, an analysis was conducted on flexural wave propagation in a symmetric cross-ply laminate with a layup of $[0/90]_{4s}$. The material properties of the unidirectional ply are outlined in Table 4.1 within Section 4.4. Figure 4.1(a) illustrates the spectrum relations, which portray the relationship between frequency and wavenumber, for the three modes of flexural waves in the $\theta = 0$ direction. In this illustration, the wavenumber k and frequency ω are nondimensionalised by the laminate thickness d and velocity $\sqrt{G_{12}/\rho}$, respectively. As the wavenumber k increases, the frequency of the flexural wave modes also rises. For a specific wavenumber k, the higher mode corresponds to a greater frequency ω (or a higher phase velocity v_p). This nonlinear relationship between frequency and wavenumber underscores the dispersive nature of flexural waves.

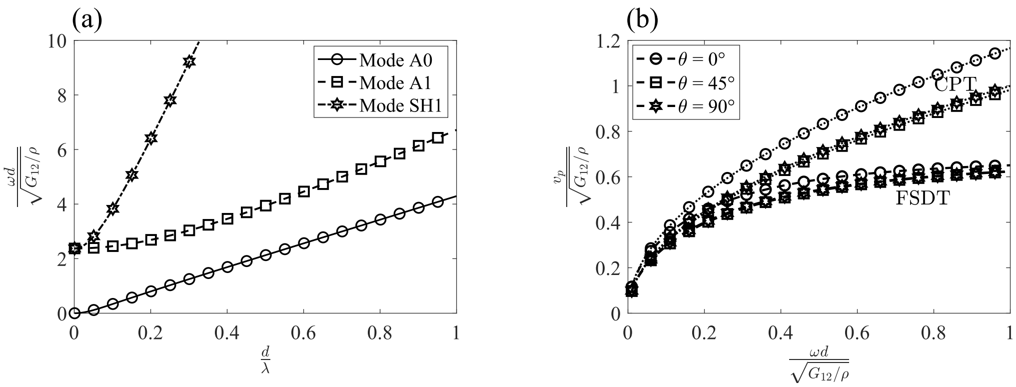

Figure 4.1: The modes and dispersion of flexural waves: (a) spectrum relations of three modes, (b) dispersion relations (A0 mode) along three directions.

To further explore the behavior of the lowest wave mode A0, which is the focus of this study, dispersion relations (plots of phase velocity as a function of frequency, $v_p = dr(\omega)$) are depicted in Fig. 4.1(b). These relations include velocity comparisons between Classical Plate Theory (CPT) and FSDT for wave propagation directions of 0, 45, and 90 degrees.

As frequency increases, phase velocities also increase in all directions, indicating a monotonically increasing relationship and confirming the dispersive property of flexural waves. Additionally, it's observed that CPT tends to overestimate wave velocity compared to FSDT due to its neglect of shear deformation and rotational inertia effects. However, for low wave frequencies, CPT can serve as an approximation of FSDT for phase velocity calculations. The dispersion relations for flexural waves based on CPT are depicted in Eq. (3.1), where phase velocity increases linearly with the square root of frequency and is unbounded.

4.3 Hybrid Physics-data Impact Localisation

4.3.1 Group velocity parameterisation using dispersion relations

The focus of this study lies on the lowest mode A0 of flexural waves, which carries the majority of impact-induced wave energy, particularly when the dominant frequency of the impact-induced waves remains below the cut-off frequency. Referring back to Eq. (4.1), the phase velocity $v_p(\theta, \omega)$ can be estimated by solving Eq. (4.1) for any given wave direction θ and wave frequency ω, substituting wavenumber k with $\frac{\omega}{v_p}$.

However, the group velocity $v_g(\theta, \omega) = \frac{\partial \omega}{\partial k}$, which is crucial for wave propagation-based impact localisation, requires an additional differentiation of the dispersion equation Eq. (4.1)—expressed in terms of wavenumber k and freqeuncy ω-with respect to k. This differentiation significantly increases the complexity of velocity calculations, making it challenging to derive closed-form partial derivatives of the group velocity concerning frequency and material properties.

An insightful observation is that the GVP, $v_g(\theta, \omega)$, and the phase velocity profile, $v_p(\theta, \omega)$, exhibit nearly identical directional dependence at a given frequency ω, differing primarily in absolute magnitude. This relationship is particularly evident in CPT, where the group velocity is precisely twice the phase velocity, as derived in Eq. (3.2). Consequently, in the low-frequency range, the dispersion equation expressed in terms of phase velocity serves as an effective parametric representation for the GVP of impact-induced flexural waves.

By modifying material stiffness or wave frequency, the wave velocity profile $v(\theta)$ is adjusted accordingly. Here, $v(\theta)$ denotes the parameterised GVP for clarity. Assuming independence of material stiffness components, the number of independent design variables for this parameterisation method amounts to eight:

$$\mathbf{x} = (D_{11}, D_{12}, D_{16}, D_{22}, D_{26}, D_{66}, A_{44}, \omega). \tag{4.9}$$

The first-order partial derivative of wave velocity $v(\theta)$ with respect to the n-th design variable is derived from this dispersion equation Eq. (4.1) as:

$$\frac{\partial \det \mathbf{G}_o}{\partial x_n} = \operatorname{tr}\left(\operatorname{adj}(\mathbf{G}_o)\frac{\partial \mathbf{G}_o}{\partial x_n}\right) = 0, \tag{4.10}$$

where $\operatorname{tr}(\cdot)$ denotes the trace operator, $\operatorname{adj}(\mathbf{G}_o)$ is the adjugate of the matrix $\mathbf{G}_o$, $\frac{\partial \mathbf{G}_o}{\partial x_n}$ is the element-wise derivatives of the matrix $\mathbf{G}_o$ with respect to x_n.

An example is presented here to illustrate the computation of the first-order partial derivative $\frac{\partial v}{\partial \omega}$. By setting $x_n = \omega$ in Eq. (4.10), the term $\frac{\partial \mathbf{G}_o}{\partial \omega}$, representing the element-wise derivatives of the matrix $\mathbf{G}_o$ with respect to ω, must be determined. This requires evaluating $\frac{\partial g_{ij}}{\partial \omega}$ based on Eq. (4.3), where $i, j = 1, 2, 3$:

$$\frac{\partial g_{11}}{\partial \omega} = -2A_{44}[\frac{\omega}{v^2} - \frac{\omega^2}{v^3}\frac{\partial v}{\partial \omega}] + 2I_1\omega,\ \frac{\partial g_{12}}{\partial \omega} = iA_{44}\cos\theta(\frac{1}{v} - \frac{\omega}{v^2}\frac{\partial v}{\partial \omega}),\ \frac{\partial g_{22}}{\partial \omega} = 2b_{22}(\frac{\omega}{v^2} - \frac{\omega^2}{v^3}\frac{\partial v}{\partial \omega}) - 2I_3\omega,$$
$$\frac{\partial g_{13}}{\partial \omega} = iA_{44}\sin\theta(\frac{1}{v} - \frac{\omega}{v^2}\frac{\partial v}{\partial \omega}),\ \frac{\partial g_{23}}{\partial \omega} = 2b_{23}(\frac{\omega}{v^2} - \frac{\omega^2}{v^3}\frac{\partial v}{\partial \omega}),\ \frac{\partial g_{33}}{\partial \omega} = 2b_{33}(\frac{\omega}{v^2} - \frac{\omega^2}{v^3}\frac{\partial v}{\partial \omega}) - 2I_3\omega. \tag{4.11}$$

By substituting $\frac{\partial g_{ij}}{\partial \omega}, i, j = 1, 2, 3$ into Eq. (4.10) and rearranging the equation to isolate $\frac{\partial v}{\partial \omega}$ on the right-hand side, the expression for $\frac{\partial v}{\partial \omega}$ is obtained.

4.3.2 Impact location relates TDOA and wave velocity

To integrate the parameterisation of the GVP, derived from the dispersion relations of the A0 mode flexural waves, into the impact localisation framework, the fundamental physical relationship expressed in Eq. (2.40)—which links impact location, time-difference-of-arrival (TDOA), and wave propagation velocity—is reformulated as:

$$\Delta t_{1j} = t_j - t_1 = \frac{d_j}{v(\theta_j;\ \mathbf{x})} - \frac{d_1}{v(\theta_1;\ \mathbf{x})} = \frac{\sqrt{(x-x_j)^2 + (y-y_j)^2}}{v(\theta_j;\ \mathbf{x})} - \frac{\sqrt{(x-x_1)^2 + (y-y_1)^2}}{v(\theta_1;\ \mathbf{x})},\ j \in \mathbb{N}_{2N_s}, \tag{4.12}$$

where (x, y) denotes the impact location (source), (x_j, y_j) represent the locations of the j-th sensors, and $v(\theta_j; \mathbf{x})$ are the impact-induced wave propagation group velocities parameterised by $\mathbf{x}$ along the paths from the impact to j-th sensors, respectively.

In practice, TDOA data are extracted from impact-induced sensor signals. Widely used data-driven methods for impact localisation typically construct a model—often through techniques such as surrogate modelling [126]—to establish a mapping between the TDOA values and impact locations based on training impacts. However, these methods approximate the relationship in Eq. (4.12) as a black-box function, disregarding the underlying physical information on GVP and sensor locations.

Rather than relying on a purely data-driven black-box approach, this study explicitly utilises the physical relationship in Eq. (4.12) for impact localisation by incorporating the parameterised GVP and known sensor positions. To effectively combine physics and data, the GVP—parameterised by the dispersion relation—is optimised with respect to wave frequency and material stiffness using training impact data. The objective function R (objective loss function) for optimising the GVP is defined as the sum of squared errors between the estimated and actual TDOA values from the training dataset. Consequently, the optimisation problem can be formulated as:

$$\mathbf{x}_{opt} = \arg\min_{\mathbf{x}} R = \arg\min_{\mathbf{x}} \sum_{i=1}^{N_i} \sum_{j=2}^{N_s} r^2,\ r = t_j^i - t_1^i - \Delta t_{1j}^i = \left(\frac{d_{ij}}{v(\theta_{ij};\ \mathbf{x})} - \frac{d_{i1}}{v(\theta_{i1};\ \mathbf{x})}\right) - \Delta t_{1j}^i,$$
$$v_{opt}(\theta) = v(\theta;\ \mathbf{x}_{opt}), \tag{4.13}$$

where r represents the difference between the estimated and actual TDOA, N_i and N_s are the number of training impacts and sensors, respectively. d_{ij} and θ_{ij} denote the known distance and wave propagation direction from the i-th training impact to j-th sensor, respectively. $v(\theta_{ij}, \mathbf{x})$ represents the wave propagation velocity along the direction θ_{ij} given the parameters $\mathbf{x}$ obtained by solving Eq. (4.1). In the definition of objective loss function for minimisation, sensor 1 is designated as the anchor sensor. TDOA are calculated between sensor $j, j \in \mathbb{N}_{2N_s}$ and sensor 1. Therefore, Δt_{1j}^i, $t_j^i - t_1^i$ represent the extracted TDOA and estimated TDOA from impact-induced sensor signals and GVP, repsectively, between sensor $j, j \in \mathbb{N}_{2N_s}$ and sensor 1 for i-th training impact.

4.3.3 Wave velocity profile optimisation: A two-stage approach

The optimisation of the GVP, as depicted in Eq. (4.13), can be achieved through heuristic optimisation algorithms such as Genetic Algorithm (GA) [138]. However, solving this eight-dimensional optimisation problem using GA necessitates a substantial number of objective function evaluations, making the process time-consuming. Moreover, enhancing the wave propagation velocity can be achieved by either adjusting the design variables associated with stiffness $A_{44}, D_{ij}, i, j = 1, 2, 6$ or by augmenting the wave frequency ω. Since these stiffness are intrinsic material properties, which are typically approximately known beforehand, it is preferable to scale the wave velocity by optimising the wave frequency ω and and fine-tune the shape of the GVP by optimising the stiffness $A_{44}, D_{ij}, i, j = 1, 2, 6$ within their confidence regions. Therefore, a two-stage approach is proposed to address this GVP optimisation problem.

4.3.3.1 Stage 1: scale the GVP by optimising the wave frequency

To scale the GVP by optimising the wave frequency ω, the first-order and second-order partial derivatives of objective loss function R with respect to the frequency ω are derived using the chain rule. This first-order partial derivative $\frac{\partial R}{\partial \omega}$ is derived as:

$$\begin{aligned}
&\frac{\partial R}{\partial \omega} = \frac{\partial \sum_{i=1}^{N_i} \sum_{j=2}^{N_s} r^2}{\partial \omega} = \sum_{i=1}^{N_i} \sum_{j=2}^{N_s} 2r \frac{\partial r}{\partial \omega} = 2 \sum_{i=1}^{N_i} \sum_{j=2}^{N_s} r (\frac{\partial r}{\partial v} \cdot \frac{\partial v}{\partial \omega}), \\
&\frac{\partial r}{\partial v} = [-\frac{d_{ij}}{v^2(\theta_{ij};\omega)}, \frac{d_{i1}}{v^2(\theta_{i1};\omega)}], \ \frac{\partial v}{\partial \omega} = [\frac{\partial v(\theta_{ij};\omega)}{\partial \omega}, \frac{\partial v(\theta_{i1};\omega)}{\partial \omega}],
\end{aligned} \tag{4.14}$$

where $\cdot$ represents the dot product operation. Both $\frac{\partial r}{\partial v}$ and $\frac{\partial v}{\partial \omega}$ are vectors with 2 elements, as r is related to v in both θ_{ij} and θ_{i1} directions. The second-order partial derivative of the objective loss function R with respect to the frequency ω is further derived as:

$$\begin{aligned}
&\frac{\partial^2 R}{\partial \omega^2} = 2 \sum_{i=1}^{N_i} \sum_{j=2}^{N_s} (\frac{\partial r}{\partial v} \cdot \frac{\partial v}{\partial \omega})^2 + r[\frac{\partial^2 r}{\partial v^2} \cdot (\frac{\partial v}{\partial \omega})^2 + \frac{\partial r}{\partial v} \cdot \frac{\partial^2 v}{\partial \omega^2}], \\
&\frac{\partial^2 r}{\partial v^2} = 2[\frac{d_{ij}}{v^3(\theta_{ij};\omega)}, -\frac{d_{i1}}{v^3(\theta_{i1};\omega)}], \ \frac{\partial^2 v}{\partial \omega^2} = [\frac{\partial^2 v(\theta_{ij};\omega)}{\partial \omega^2}, \frac{\partial^2 v(\theta_{i1};\omega)}{\partial \omega^2}].
\end{aligned} \tag{4.15}$$

The dependence of the second-order partial derivatives $\frac{\partial^2 R}{\partial \omega^2}$ on the TDOA Δt_{1j}^i in r is noted. The convexity of the objective loss function R with respect to the frequency ω remains uncertain. Utilising the Newton's method for optimisation based solely on these derivatives may lead to convergence to a local minimum.

Given that the frequency ω predominantly controls the scaling of the GVP, transitioning from ω_1 to ω_2 scales the velocity profile from $v_1(\theta)$ to $v_2(\theta)$. This scaling can be approximated by a velocity scale factor β, where $v_2(\theta)$ is approximately $v_1(\theta)/\beta$. Therefore, instead of optimising the frequency ω, the velocity scale factor β can also be employed to scale the GVP to best align with the training impact locations and TDOA data. With ω_b held constant, the baseline velocity profile calculated from Eq. (4.1) is denoted as $v_b(\theta)$, maintaining a constant value for each wave propagation direction θ. The optimisation of the objective loss function R with respect to velocity scale factor β is expressed as follows:

$$\beta_{opt} = \arg\min_{\beta} R = \arg\min_{\beta} \sum_{i=1}^{N_i} \sum_{j=2}^{N_s} [(\frac{d_{ij}}{v_b(\theta_{ij})} - \frac{d_{i1}}{v_b(\theta_{i1})})\beta - \Delta t_{1j}^{i}]^2. \tag{4.16}$$

The first and second-order partial derivatives of the objective loss function R with respect to β are derived as follows:

$$\begin{aligned} \frac{dR}{d\beta} &= 2\sum_{i=1}^{N_i} \sum_{j=2}^{N_s} [(\frac{d_{ij}}{v_b(\theta_{ij})} - \frac{d_{i1}}{v_b(\theta_{i1})})\beta - \Delta t_{1j}^{i}](\frac{d_{ij}}{v_b(\theta_{ij})} - \frac{d_{i1}}{v_b(\theta_{i1})}), \\ \frac{d^2R}{d\beta^2} &= 2\sum_{i=1}^{N_i} \sum_{j=2}^{N_s} (\frac{d_{ij}}{v_b(\theta_{ij})} - \frac{d_{i1}}{v_b(\theta_{i1})})^2 \geq 0. \end{aligned} \tag{4.17}$$

As the second-order partial derivatives of the objective loss function with respect to β are non-negative, this optimisation problem is convex, allowing for efficient solution using methods like the steepest descent or Newton's method. The Newton's method iteratively minimises R with respect to β:

$$\beta_{k+1} = \beta_k - \frac{R'(\beta_k)}{R''(\beta_k)}. \tag{4.18}$$

The optimised β_{opt} can then be utilised to update the frequency ω_b and adjust the velocity profile baseline $v_b(\theta)$ using the inverse dispersion relations $\omega = idr(v)$. These relations are derived from the dispersion relations $v = dr(\omega)$ illustrated in Fig. 4.1. The inverse dispersion relations represent a monotonic increasing function between wave frequency and phase velocity. The updates for the frequency ω_b and velocity profile baseline $v_b(\theta)$ are given by:

$$\omega_b = idr(v_b(\theta;\omega_b)/\beta_{opt}),\ v_b(\theta) = v(\theta;\omega_b). \tag{4.19}$$

Repeating such a convex optimisation with respect to the velocity scale factor β, and the update processes of the frequency ω_b and the velocity profile baseline $v_b(\theta)$ indirectly lead to the optimisation of the GVP and the identification of the optimal frequency. The pseudocode for this indirect optimisation approach is illustrated in Algorithm 4.1.

Algorithm 4.1: GVP optimisation with respect to frequency ω using Newton's method

```
Input: E_1, E_2, G_12, ν_12, ρ, Φ, Q, L, S, f_NSET
Output: ω_opt
Δt^i_1j ← S, f_NSET ;          /* TDOA extraction from impact-induced sensor signals by NSET method */
d_ij, θ_ij ← Q, L ;            /* Impact-to-sensor distances and angles */
D, A ← E_1, E_2, G_12, ν_12, ρ, Φ ;   /* Plate stiffness calculation based FSDT */
ω_b ← 2π f_NSET ;              /* Initial baseline angular frequency */
β_opt ← 2 ;                    /* Initial optimised β */
while | β_opt − 1 | ≥ 0.01 do
    v_b(θ) ← v(θ; ω_b, D, A) ;   /* Update/calculate baseline GVP by solving Eq. (4.1) */
    R ← Σ_{i=1}^{N_i} Σ_{j=2}^{N_s} [(d_ij / v_b(θ_ij) − d_i1 / v_b(θ_i1)) β − Δt^i_1j]^2 ;   /* Objective function */
    β_0 ← 1 ;                    /* Initial guess of β */
    β_opt ← arg min_β R ;        /* Solve optimisation problem Eq. (4.16) by Newton's method */
    ω_b ← idr(c_b(θ; ω_b)/β_opt) ;   /* Update baseline angular frequency */
end
ω_opt ← ω_b ;                  /* Optimised angular frequency */
```

4.3.3.2 Stage 2: fine-tune the GVP by optimising the stiffness

The amplitude of the GVP, optimised with respect to the frequency, closely approximates its real value. Next, the shape of the GVP can be fine-tuned by minimising the objective loss function with respect to the stiffness matrix $\boldsymbol{D}$ (where $\boldsymbol{D}$ represents $D_{11}, D_{12}, D_{16}, D_{22}, D_{26}, D_{66}$) and the stiffness A_{44} constrained within its confidence region. This second-stage optimisation problem is formulated as:

$$
\begin{gathered}
\boldsymbol{D}^{opt}, A_{44}^{opt} = \underset{\boldsymbol{D}, A_{44}}{\arg\min} R = \underset{\boldsymbol{D}, A_{44}}{\arg\min} \sum_{i=1}^{N_i} \sum_{j=2}^{N_s} r^2,\ r = \left(\frac{d_{ij}}{v(\theta_{ij};\, \boldsymbol{D}, A_{44}, \omega_{opt})} - \frac{d_{i1}}{v(\theta_{i1};\, \boldsymbol{D}, A_{44}, \omega_{opt})}\right) - \Delta t_{1j}^{i}, \\
v_{opt}(\theta) = v(\theta;\, \boldsymbol{D}^{opt}, A_{44}^{opt}, \omega_{opt}).
\end{gathered}
\tag{4.20}
$$

To avoid the computational expense of using a GA for solving this seven-dimensional optimisation problem, the TRF algorithm [137] is employed. This method utilises the partial derivatives of the objective loss function with respect to the design variables (stiffness parameters $\boldsymbol{D}$, A_{44}), enabling more efficient convergence.

By applying the chain rule, the first-order partial derivative of the objective loss function R with respect to the stiffness variable $x_n \in (\boldsymbol{D}, A_{44})$ is expressed in terms of intermediate derivatives

Algorithm 4.2: GVP optimisation with respect to stiffness (D, A_{44}) by TRF algorithm

Input: $E_1, E_2, G_{12}, \nu_{12}, \Phi, Q, L, \Delta t^i_{1j}, \omega_{opt}$
Output: $v_{opt}(\theta)$
$d_{ij}, \theta_{ij} \leftarrow Q, L$; /* Impact-to-sensor distances and angles */
$\boldsymbol{D}, A_{44} \leftarrow E_1, E_2, G_{12}, \nu_{12}, \Phi$; /* Stiffness to be optimised and its initial values */
$[\boldsymbol{D}^{lb}, \boldsymbol{D}^{ub}] \leftarrow \boldsymbol{D}, [A^{lb}_{44}, D^{ub}_{44}] \leftarrow A_{44}$; /* Stiffness bounds */
$N_{iter} \leftarrow 10000, i_{iter} \leftarrow 1$; /* Optimistaion maximum iteration and iterator */
$r \leftarrow (\frac{d_{ij}}{v(\theta_{ij}; \boldsymbol{D}, A_{44}, \omega_{opt})} - \frac{d_{i1}}{v(\theta_{i1}; \boldsymbol{D}, A_{44}, \omega_{opt})}) - \Delta t^i_{1j}$; /* Residual function */
$R \leftarrow \sum_{i=1}^{N_i} \sum_{j=2}^{N_s} r^2$; /* Objective function (loss) */
$\Delta R \leftarrow 1, \Delta x \leftarrow 1$; /* Iterative changes of objective function and design variables */
while $i_{iter} \leq N_{iter}$ & $\Delta R > 10^{-6}$ & $\Delta x > 10^{-6}$ **do**
  $\frac{\partial v}{\partial x_n}, \frac{\partial^2 v}{\partial x_n \partial x_m} \leftarrow \boldsymbol{D}, A_{44}, \omega_{opt}$; /* Intermediate derivatives */
  $\frac{\partial R}{\partial x_n}, \frac{\partial^2 R}{\partial x_n \partial x_m} \leftarrow \frac{\partial v}{\partial x_n}, \frac{\partial^2 v}{\partial x_n \partial x_m}$; /* Derivatives of objective function */
  $[\delta \boldsymbol{D}, \delta A_{44}] \leftarrow R, \frac{\partial R}{\partial x_n}, \frac{\partial^2 R}{\partial x_n \partial x_m}$; /* Updating direction by TRF */
  $p \leftarrow R, \frac{\partial R}{\partial x_n}, \frac{\partial^2 R}{\partial x_n \partial x_m}$; /* Updating step size by TRF */
  $[\boldsymbol{D}, A_{44}] \leftarrow [\boldsymbol{D}, A_{44}] - p[\delta \boldsymbol{D}, \delta A_{44}]$; /* Update stiffness */
  $r \leftarrow (\frac{d_{ij}}{v(\theta_{ij}; \boldsymbol{D}, A_{44}, \omega_{opt})} - \frac{d_{i1}}{v(\theta_{i1}; \boldsymbol{D}, A_{44}, \omega_{opt})}) - \Delta t^i_{1j}$; /* Update residual */
  $\Delta R \leftarrow R - \sum_{i=1}^{N_i} \sum_{j=2}^{N_s} r^2$; /* Iterative change of objective function */
  $R \leftarrow \sum_{i=1}^{N_i} \sum_{j=2}^{N_s} r^2$; /* Update objective function */
  $\Delta x \leftarrow |p[\delta \boldsymbol{D}, \delta A_{44}]|$; /* Iterative change of design variables */
  $i_{iter} \leftarrow i_{iter} + 1$; /* Update iterator */
end
$\boldsymbol{D}_{opt} \leftarrow \boldsymbol{D}, A^{opt}_{44} \leftarrow A_{44}$; /* Optimised stiffness */
$v(\theta) \leftarrow v(\theta; \boldsymbol{D}_{opt}, A^{opt}_{44}, \omega_{opt})$; /* Optimised GVP */

$\frac{\partial r}{\partial v}$ and $\frac{\partial v}{\partial x_n}$:

$$\frac{\partial R}{\partial x_n} = \sum_{i=1}^{N_i} \sum_{j=2}^{N_s} 2r \frac{\partial r}{\partial x_n} = 2 \sum_{i=1}^{N_i} \sum_{j=2}^{N_s} r (\frac{\partial r}{\partial v} \cdot \frac{\partial v}{\partial x_n}),$$
$$\frac{\partial r}{\partial v} = [-\frac{d_{ij}}{v^2(\theta_{ij}; \boldsymbol{D}, A_{44}, \omega_{opt})}, \frac{d_{i1}}{v^2(\theta_{i1}; \boldsymbol{D}, A_{44}, \omega_{opt})}], \; \frac{\partial v}{\partial x_n} = [\frac{\partial v(\theta_{ij}; \boldsymbol{D}, A_{44}, \omega_{opt})}{\partial x_n}, \frac{\partial v(\theta_{i1}; \boldsymbol{D}, A_{44}, \omega_{opt})}{\partial x_n}]. \tag{4.21}$$

The general formulation of the intermediate derivative $\frac{\partial v(\theta)}{\partial x_n}$, applicable for any stiffness combination $(\boldsymbol{D}, A_{44})$ and frequency ω, is provided in Eq. (4.10).

The implementation of the above optimisation problem is depicted in Algorithm 4.2. Here, the first-order partial derivative $\frac{\partial R}{\partial x_n}$ is utilised to minimise the residual R with respect to the stiffness $\boldsymbol{D}$ and A_{44} using the TRF algorithm. In practice, the optimisation is executed using the "fmincon" function in Matlab. Termination conditions include reaching the maximum number of iterations ('MaxIterations'), ensuring the change in design variables is below the 'StepTolerance', and ensuring the reduction in the objective loss function is below the 'FunctionTolerance'.

4.3.4 Triangulation: impact localisation based on the optimised GVP

Once the GVP $v(\theta; \boldsymbol{D}_{opt}, A_{44}^{opt}, \omega_{opt})$ of the impact-induced flexural waves has been optimised based on training impacts, the location of the target impact can be estimated using the triangulation method, which involves minimising the difference between the estimated TDOA from the optimised GVP and the extracted TDOA from sensor signals. This optimisation problem for impact localisation is expressed as:

$$
\begin{aligned}
&x, y = \underset{x,y}{\arg\min} R = \underset{x,y}{\arg\min} \sum_{j=2}^{N_s} r^2,\ r = t_j - t_1 - \Delta t_{1j} = \frac{d_j}{v(\theta_j)} - \frac{d_1}{v(\theta_1)} - \Delta t_{1j},\\
&d_j = \sqrt{(x - x_j)^2 + (y - y_j)^2},\ \theta_j = \arccos\frac{x_j - x}{d_j}, j \in \mathbb{N}_{1N_s},
\end{aligned}
\tag{4.22}
$$

where (x, y) represent the location coordinates of the target impact, (x_j, y_j) denotes the location coordinates of the j-th sensor, d_j indicates the distance between the target impact and the j-th sensor, θ_j is the direction from the target impact location to the j-th sensor, and $v(\theta_j)$ is the optimised wave velocity in the θ_j direction.

To avoid the use of the time-consuming GA algorithm, the TRF algorithm is employed to address this optimisation problem efficiently. The first and second-order derivatives $\frac{\partial R}{\partial x}$, $\frac{\partial R}{\partial y}$, $\frac{\partial^2 R}{\partial x^2}$, $\frac{\partial^2 R}{\partial y^2}$, $\frac{\partial^2 R}{\partial x \partial y}$ of the objective loss function R with respect to the impact location coordinates x and y are derived using the chain rule:

$$
\begin{aligned}
&\frac{\partial R}{\partial x} = \sum_{j=2}^{N_s} 2r\frac{\partial r}{\partial x},\ \frac{\partial R}{\partial y} = \sum_{j=2}^{N_s} 2r\frac{\partial r}{\partial y},\ \frac{\partial^2 R}{\partial x^2} = \sum_{j=2}^{N_s} 2(\frac{\partial r}{\partial x})^2 + 2r\frac{\partial^2 r}{\partial x^2},\\
&\frac{\partial^2 R}{\partial y^2} = \sum_{j=2}^{N_s} 2(\frac{\partial r}{\partial y})^2 + 2r\frac{\partial^2 r}{\partial y^2},\ \frac{\partial^2 R}{\partial x \partial y} = \sum_{j=2}^{N_s} 2\frac{\partial r}{\partial x}\frac{\partial r}{\partial y} + 2r\frac{\partial^2 r}{\partial x \partial y}.
\end{aligned}
\tag{4.23}
$$

These intermediate partial derivatives $\frac{\partial r}{\partial x}$, $\frac{\partial r}{\partial y}$, $\frac{\partial^2 r}{\partial x^2}$, $\frac{\partial^2 r}{\partial y^2}$, $\frac{\partial^2 r}{\partial x \partial y}$ can be derived using the chain rule in conjunction with the dispersion equation Eq. (4.1) and the optimised parameters $\boldsymbol{D}_{opt}$, A_{44}^{opt}, ω_{opt}. The detailed derivations of these derivatives are provided in [74]. Based on this derivative information, Algorithm 4.3 illustrates the implementation of impact localisation using the triangulation method and the TRF algorithm based on the optimised GVP.

The initial impact location in this optimisation can be estimated from the TDOA data. By

Algorithm 4.3: Triangulation method to locate impacts based on the optimised GVP

Input: $\boldsymbol{D}_{opt}, A_{44}^{opt}, \omega_{opt}, L(x_j, y_j), \boldsymbol{s}, f_{NSET}, [x_{lb}, x_{ub}], [y_{lb}, y_{ub}]$
Output: x, y, σ_{xy}

```
Δt_1j, j ∈ ℕ_2Ns ← s, f_NSET ;                          /* TDOA extraction for target impact */
v(θ) ← D_opt, A_44^opt, ω_opt ;                                         /* Optimised GVP */
x, y ← Δt_j1 ;                                                /* Initial impact location */
d_j, θ_j ← x, y, x_j, y_j ;                   /* Impact-to-sensor distances and directions */
R ← Σ_{j=2}^{Ns} [(d_j/c(θ_j) − d_1/c(θ_1)) − Δt_1j]^2 ;          /* Objective function (loss) */
N_iter ← 10000, i_iter ← 1 ;                  /* Optimistaion maximum iteration and iterator */
ΔR ← 1, Δd ← 1 ;            /* Iterative changes of objective function and design variables */
while i_iter ≤ N_iter & ΔR > 10^-6 & Δx > 10^-6 do
    ∂v(θ_j)/∂x, ∂v(θ_j)/∂y ← D_opt, A_44^opt, ω_opt ;                 /* Intermediate derivatives */
    ∂²v(θ_j)/∂x², ∂²v(θ_j)/∂y², ∂²v(θ_j)/∂x∂y ← ∂v(θ_j)/∂x, ∂v(θ_j)/∂y ; /* Intermediate derivatives */
    ∂R/∂x, ∂R/∂y, ∂²R/∂x², ∂²R/∂y², ∂²R/∂x∂y ← v(θ) ;            /* Derivatives of objective function */
    [δx, δy] ← R, ∂R/∂x, ∂R/∂y, ∂²R/∂x², ∂²R/∂y², ∂²R/∂x∂y ;         /* Updating direction by TRF */
    p ← R, ∂R/∂x, ∂R/∂y, ∂²R/∂x², ∂²R/∂y², ∂²R/∂x∂y ;                /* Updating step size by TRF */
    [x, y] ← [x, y] − p[δx, δy] ;                                   /* Update impact location */
    d_j, θ_j ← x, y, x_j, y_j ;          /* Update impact-to-sensor distances and directions */
    ΔR ← R − Σ_{j=2}^{Ns} [(d_j/v(θ_j) − d_1/v(θ_1)) − Δt_1j]^2 ; /* Iterative change of objective function */
    R ← Σ_{j=2}^{Ns} [(d_j/v(θ_j) − d_1/v(θ_1)) − Δt_1j]^2 ;        /* Update objective function */
    Δd ← |p[δx, δy]| ;                                /* Iterative change of design variables */
    i_iter ← i_iter + 1 ;                                                 /* Update iterator */
end
σ_xy ← x, y, v(θ), Δt_1j ;                                          /* Localisation uncertainty */
```

analysing the TDOA values, the sensor closest to the impact, indicated by the minimum TOA, and the sensor farthest from the impact, indicated by the maximum TOA, can be identified. This information offers a reasonable estimate of the impact location. To enhance the robustness of the localisation process, two initial impact locations are generated in this study. One is positioned inside the sensor network between the closest and farthest sensors, while the other is situated outside the sensor network near the nearest sensor.

Additionally, the uncertainty of the estimated impact location (x, y) can be quantified based on the triangulation method. For every pair of sensors, such as sensor i and sensor j, where $j > i$, there exists at least one location solution (x_{ij}, y_{ij}) that satisfies the condition for the estimated TDOA $\Delta\bar{t}_{ij} = t_j - t_i = d_j/v(\theta_j) - d_i/v(\theta_i)$ to match the actual TDOA Δt_{ij}.

$$\Delta\bar{t}_{ij} = t_j - t_i = \frac{d_j}{v(\theta_j)} - \frac{d_i}{v(\theta_i)} = \frac{\sqrt{(x_{ij} - x_j)^2 + (y_{ij} - y_j)^2}}{v(\theta_j)} - \frac{\sqrt{(x_{ij} - x_i)^2 + (y_{ij} - y_i)^2}}{v(\theta_i)} = \Delta t_{ij}. \tag{4.24}$$

The solution of the equation above, closest to the estimated impact location (x, y), indicates how the estimated impact location should adjust to nullify the TDOA difference ($\Delta\bar{t}_{ij} = \Delta t_{ij}$). Every pair of sensors (varying i and j) provides a location (x_{ij}, y_{ij}) bounding the estimated impact location (x, y) that satisfies $\Delta\bar{t}_{ij} = \Delta t_{ij}$. The uncertainty (Standard Deviation (SD)) of the estimated impact location can be defined as the average distance between the estimated impact location (x, y) and the bounding locations (x_{ij}, y_{ij}).

$$\sigma_{xy} = \frac{2}{N_s(N_s-1)} \sum_{i=1}^{N_s-1} \sum_{j=i+1}^{N_s} \sqrt{(x_{ij}-x)^2 + (y_{ij}-y)^2}. \tag{4.25}$$

4.4 Experimental Validation

To validate the proposed hybrid physics-data impact localisation method, experimental impact tests were conducted on a sensorised composite laminate Flat Panel (FP) (same flat panel used for experimental validation in Chapter 3) and a sensorised mono-stringer Stiffened Panel (SP). The experimental setup for these impact tests is depicted in Fig. 4.2. Both the FP and SP used were quasi-isotropic carbon fibre-reinforced laminates (M21/T800s). The stacking sequence of the FP was $[0/+45/45/90]_{2s}$, with each ply having a thickness of 0.25 mm. Conversely, the mono-stringer SP had a stacking sequence of $[-45/45/0/0/90/0]_s$ for both the single plate region without a stringer and the stringer, with a ply thickness of 0.125 mm. The material properties of a unidirectional, transversely isotropic lamina are provided in Table 4.1, essential for the analytical calculation of the wave propagation velocity profile.

Table 4.1: Material properties of a unidirectional, transversely isotropic lamina (M21/T800s).

Property	E_1 (MPa)	E_2 (MPa)	G_{12} (MPa)	G_{23} (MPa)	ν_{12}	ν_{23}	ρ (kg/m^3)
Value	171000	11470	4830	3720	0.33	0.33	1600

*E_1: elastic modulus in the fibre direction, E_2: elastic modulus perpendicular to the fibre direction, G_{12}, G_{23}: shear modulus, ν_{12}, ν_{23}: Poisson's ratio, ρ: density.

The FP (290 mm × 200 mm) was equipped with 4 PZT sensors (PIC 255) bonded to the top side of the plate (impact side), while the stiffened plate (475 mm × 250 mm) had 4 PZT sensors (PIC DuraAct) bonded to the bottom side of the plate to simulate potential sensor installation on the inside of a stiffened aircraft structure. The coverage area of these 4 PZT sensors, both for the

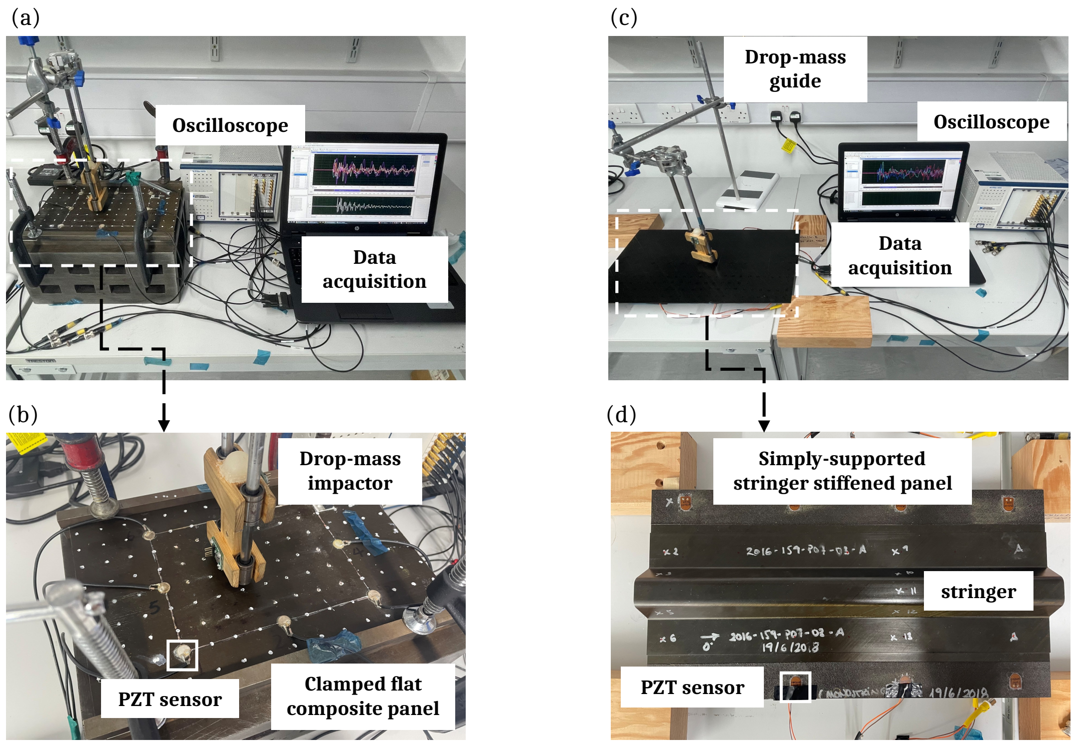

Figure 4.2: Experimental setup for impact testing, utilising a drop mass along a guide rail: (a)-(b) composite laminate FP, clamped along its longitudinal edges while the transverse edges remain free, (c)-(d) composite laminate SP, supported simply on the four corners of the panel.

FP and the SP, formed a rectangular area.

Impacts were induced by dropping a 20 mm diameter round steel head impactor perpendicular to the panels along the guide rails, as illustrated in Fig. 4.2(a) and (b). The impactor had a mass of 100 g and was dropped from a height of 20 mm. During impact testing, the FP was fully clamped along two opposite longitudinal edges, while the remaining two edges were left free. The SP, however, was simply supported at its four corners, with a support area measuring 20 mm by 20 mm.

The layout of the impact locations and sensor positions is depicted in Fig. 4.3 for both the flat and stiffened panels. A total of 35 drop mass impacts, numbered from 1 to 35, were applied to the composite laminate FP, evenly distributed on a 20×20 mm grid and all within the sensor network. Conversely, 25 drop mass impacts, numbered 1 to 25, were conducted on the composite laminate SP. Impacts numbered 1 to 5 and 21 to 25 were slightly outside the sensor network. Additionally, these impacts on the SP were categorised into three groups based on impact location: 10 impacts on the single panel region without a stringer (numbered 1:5:21, 5:5:25), 10 impacts on the stringer toes (numbered 2:5:22, 4:5:24), and 5 impacts on the panel region between the stringer toes (numbered 3:5:23).

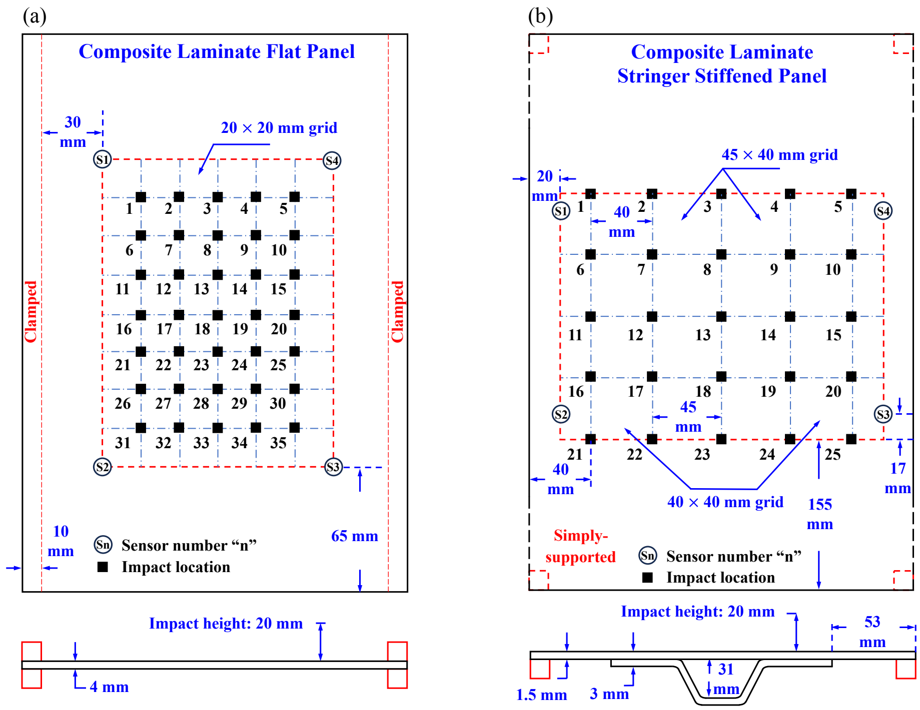

Figure 4.3: Layout of composite laminate flat and stiffened panels, (a) FP, (b) SP.

An NI PXI-5105 8-channel oscilloscope and NI SignalExpress software were utilised for sensor signal acquisition. Each PZT sensor was connected to an individual channel of the oscilloscope. The sampling frequency for recording the impact-induced sensor signals was set at 200 kHz, with a fixed sampling window of 50 ms. Each impact was repeated twice for consistency. A total of 70 impact-induced sensor signals were collected from the FP, while 50 were collected from the mono-stringer SP. Details of these impact tests are summarised in Table 4.2, where 'FP' and 'SP' represent the flat and stiffened panels, respectively.

Table 4.2: Impact tests conducted on FP and SP using guided drop mass.

Impact case	Impact machine	Parameters	Number of impacts
FP	Drop mass	m = 100 g, h = 20 mm	70 (loc 1-35 × 2 rpt)
SP	Drop mass	m = 100 g, h = 20 mm	50 (loc 1-25 × 2 rpt)

*m: impact mass, h: impact height, loc: location, rpt: repetitions.

It is important to highlight that the dispersion relations governing the wave profile are derived analytically for simple plates, based on the FSDT. A recent study by Correas [139] presented an analytical impact spring model for predicting impact behaviors of stringer-stiffened composite laminates, utilising the FSDT. In this model, the global stiffness of the SP is represented by combining the stiffness of its flat plate component and the stringer component. Validation of this analytical impact spring modeling was conducted using FEA, which demonstrated a close estimation of the impact force history.

Building upon this work, stringer-stiffened composite laminates can be effectively approximated by a simplified plate model, where the equations of motion of simple plates approximately govern the motions of the stringer-stiffened composite laminates using the global stiffness. In other words, the dispersion relations derived from the equations of motion of simple plates can also be used to parameterise the GVP of the stringer-stiffened composite laminates. The purpose of conducting impact tests on the mono-stringer SP is to validate the effectiveness of the proposed hybrid impact localisation method on more complex stiffened structures. This validation is essential, considering that the majority of aircraft structures are intricate and incorporate stiffening elements.

4.5 Optimisation of Group Velocity Profile

The experimental impact data were utilised to validate the proposed hybrid physics-based and data-driven impact localisation method, which optimises the GVP using a two-stage approach based on training impacts and locates the target impact through triangulation based on the optimised GVP. For the composite laminate FP, four experimental impacts numbered 12, 14, 22, and 24, as shown in Fig. 4.3(a), were utilised as the training impacts. Similarly, the same number of training impacts, numbered 7, 9, 17, and 19 and displayed in Fig. 4.3(b), were adopted for the mono-stringer SP. Subsequently, all experimental impacts were treated as testing impacts (target impacts) based on the optimised GVP, aiming to be localised by minimising the difference in TDOA between the optimised GVP and sensor signals.

The accuracy of the GVP and impact localisation hinges on factors such as the optimisation algorithm, the number of sensors employed, and the quantity of training impacts. In this section, the number of sensors was fixed at four, which is a reasonable choice, as in practical scenarios, the aircraft structure can be segmented into numerous substructures using the closest four sensors.

With the aforementioned four training impacts, the proposed two-stage approach was compared with the GA for optimising the GVP as described in Section 4.3.3. The stiffness design variables $D_{ij}, i, j = 1, 2, 6$, and A_{44} are determined using the laminate properties detailed in Table 4.1 and the stacking sequence. A scaling range of $[0.8, 1.2]$ is employed to accommodate stiffness uncertainties in the optimisation. For the frequency ω, the cut-off frequency f_{NSET} utilised in TDOA extraction via the NSET method serves as its nominal value, with the frequency bounded empirically within $[1, 30]f_{NSET}$ during optimisation.

In addition, the GA algorithm utilises an initial population size of 100, determined through Latin hypercube sampling in the eight-dimensional design space, with each iteration employing the same population size. Conversely, the proposed two-stage approach necessitates an initial point defined by the nominal values of the optimisation design variables.

The convergence of the objective loss function, to be minimised during the velocity profile optimisation, is illustrated in Fig. 4.4 for both the flat and stiffened panels. In the figure legend, 'TS' denotes the proposed two-stage approach.

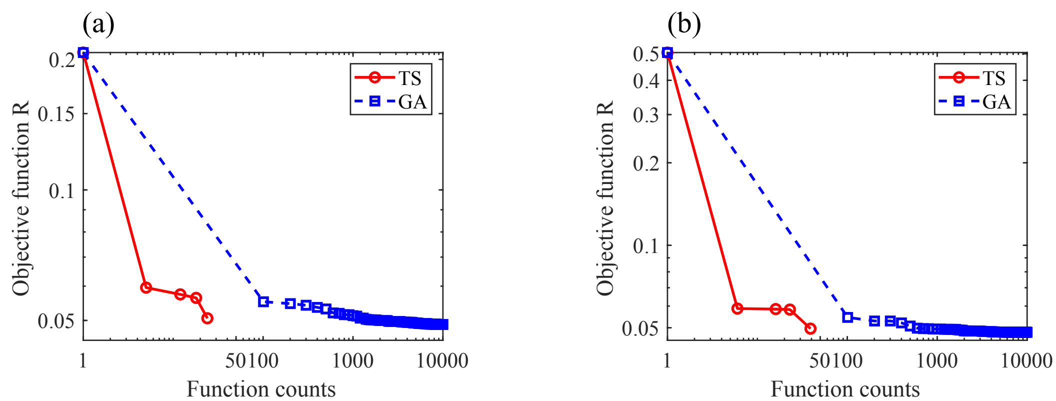

Figure 4.4: Convergence of objective function R for GVP optimisation: (a) FP, (b) SP.

It is evident that the proposed two-stage approach achieves convergence much more rapidly compared to the GA algorithm for both flat and stiffened panels. The proposed method requires fewer than 40 objective loss function evaluations in total to minimise the objective loss function to a value that would typically necessitate 1000 objective loss function evaluations with GA. In the first stage, which optimises the GVP with respect to the frequency using Newton's method, convergence is achieved in less than 5 iterations, with fewer than 5 objective loss function evaluations in each iteration. Subsequently, the second stage, which optimises the GVP with respect to stiffness, further reduces the objective loss function significantly in a single large step. In contrast, the GA algorithm's initial population yields a relatively small value of the objective loss function, with subsequent iterations exploring the design space at a higher computational cost, resulting in limited improvement.

Table 4.3: Computational time for the GVP optimisation using the proposed two-stage algorithm and the GA.

Algorithm	Computational time (FP)	Computational time (SP)
TS	2.24 s	3.59 s
GA (1000 FC)	18.95 s	26.55 s
GA (10000 FC)	179.13 s	242.59 s

*FC: function counts.

The optimised GVP for both the flat and stiffened panels, obtained through the proposed two-stage approach and GA, are depicted in Fig. 4.5. The label 'FS' in the figures denotes the first-stage, representing the GVP optimised with respect to frequency. It is noteworthy that the first-stage optimised velocity profile (FS) closely approximates the final optimised results of the two-stage approach (TS) and GA. This observation underscores the significance of frequency as the primary design variable influencing wave velocity amplitude. Furthermore, the optimised GVP obtained through the two-stage approach (TS) and GA exhibit remarkable similarity, underscoring the effectiveness of the proposed two-stage approach for efficient GVP optimisation.

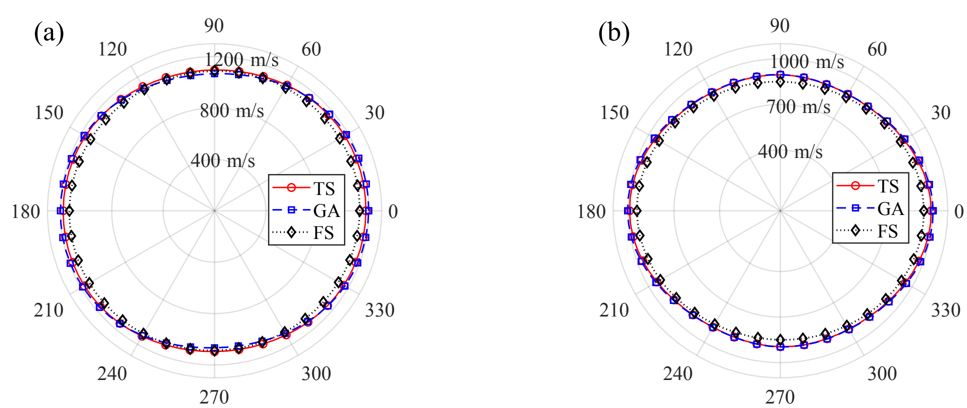

Figure 4.5: The optimised GVP based on four training impacts: (a) FP, (b) SP.

4.6 Impact Localisation on Flat and Stiffened Panels

With the optimised GVP obtained through the proposed two-stage approach, the impact locations and localisation uncertainties for the target impacts can be identified via triangulation. This process involves utilising the TRF algorithm to solve another optimisation problem, as depicted in Algorithm 4.3. This hybrid physics-data impact localisation method is denoted as HPD.

As a reference method, the widely used data-driven impact localisation method employing Multi-layer Perceptron (MLP) is adopted. The MLP architecture aligns with previous research [37], which demonstrated that a configuration comprising 4 layers, each with 10 neurons utilising hyperbolic tangent sigmoid function as activation, and Fletcher-Powell conjugate gradient as the training function, yielded satisfactory localisation accuracy for large-scale SPs. The number of training epochs for the MLP is set to 50000, with a learning rate of 0.01. The MLP training process is repeated 200 times to address model uncertainty. The final location estimation of the target impacts is obtained as the average location prediction from these 200 repetitions, while the localisation uncertainty is quantified by the SD of these 200 predictions.

The structure of this section is organised as follows: the subsequent two subsections present the results of impact localisation by HPD and MLP on the experimental FP and the SP, respectively. Additionally, the final subsection investigates the effects of the number of sensors employed on impact localisation.

4.6.1 Impact localisation on flat panel

As previously stated, for the composite laminate FP, four experimental impacts numbered 12, 14, 22, and 24, as shown in Fig. 4.3(a), were utilised as the training impacts. The target impacts (testing impacts) to be localised encompassed all 35 experimental impacts, some of which were situated outside the coverage area of the four training impacts. The localisation outcomes of the proposed HPD and MLP are depicted in Fig. 4.6, where red circles represent the sensors, hollow black circles denote the training impacts, solid black squares represent the target impacts, magenta diamond indicate the identified locations of the target impacts, and the dashed magenta ellipses represent the uncertainties (SDs) of the identified locations. The uncertainties of the locations estimated by the MLP method are not plotted in the figure because they are so large that including them would distort the presentation of the localisation results.

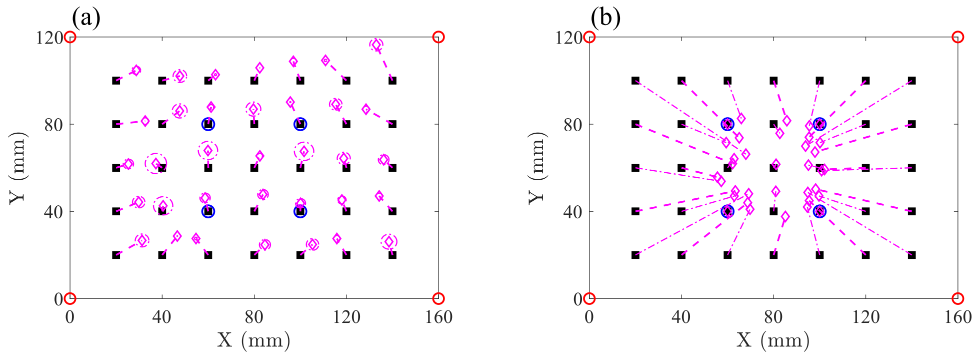

Figure 4.6: Impact localisation of the FP: (a) proposed HPD method, (b) MLP method.

With only four training impacts, the proposed HPD method accurately localises the target impacts regardless of whether they are within or outside the training impact coverage area. In contrast, the MLP method fails to localise impacts outside the training impact coverage area because it relies solely on training impact data without incorporating any physical information. The accuracy of the MLP extrapolation cannot be guaranteed, and its predictions typically tend to closely resemble the training data.

However, the proposed HPD method explicitly derives the GVP through optimisation, which is the exact physics model that the MLP aims to approximate. By integrating physics information with training impact data, the proposed HPD method can effectively locate impacts outside the training impact coverage area. Moreover, the incorporation of physics information also reduces the training impact requirements. The effectiveness of the proposed method is demonstrated by its ability to accurately localise impacts based on only four training impacts.

Table 4.4 presents a summary of the impact localisation outcomes for the FP using both the HPD and MLP methods. The mean error and maximum error in the table represent the average and maximum localisation errors, respectively, across the 35 target impacts. Additionally, the average and maximum SDs indicate the uncertainties associated with these impacts.

Comparing the two methods, the proposed HPD method exhibits higher accuracy, as evidenced by its smaller mean and maximum localisation errors, as well as more reliable location estimation, indicated by its smaller mean and maximum SDs, in contrast to the MLP method. Specifically, the HPD method yields a mean localisation error of 8.27 mm and a mean SD of 2.15 mm, while the corresponding values for the MLP method are 25.67 mm and 11.36 mm, respectively.

Table 4.4: Impact localisation results of the FP by the proposed HPD method and the reference MLP method.

Method	Mean error (mm)	Max error (mm)	Mean SD (mm)	Max SD (mm)
HPD	8.27	17.89	2.15	4.62
MLP	25.67	56.39	11.36	17.52

4.6.2 Impact localisation on mono-stringer stiffened panel

To validate the proposed HPD impact localisation method on stiffened composite structures, impact tests were conducted on a composite laminate mono-stringer SP, as illustrated in Fig. 4.2 and Fig. 4.3. The experimental impacts numbered 7, 9, 17, and 19 were utilised as training impacts to optimise the velocity profile. Subsequently, all 25 impacts were employed as target impacts to assess the localisation accuracy of the proposed HPD method.

Figure 4.7 presents a comparison of impact localisation between the proposed HPD method and MLP on the SP, based on the four selected training impacts. The markers in this figure have the same representation as those in the FP depiction shown in Fig. 4.6. The results demonstrate that, similar to the FP, the proposed HPD method accurately locates the target impacts, regardless of whether they fall within or outside the training impact coverage area. In contrast, MLP fails to localise impacts beyond the training impact coverage area. Additionally, impacts numbered 1-5 and 21-25, located slightly outside the sensor network, are successfully localised by the proposed HPD method.

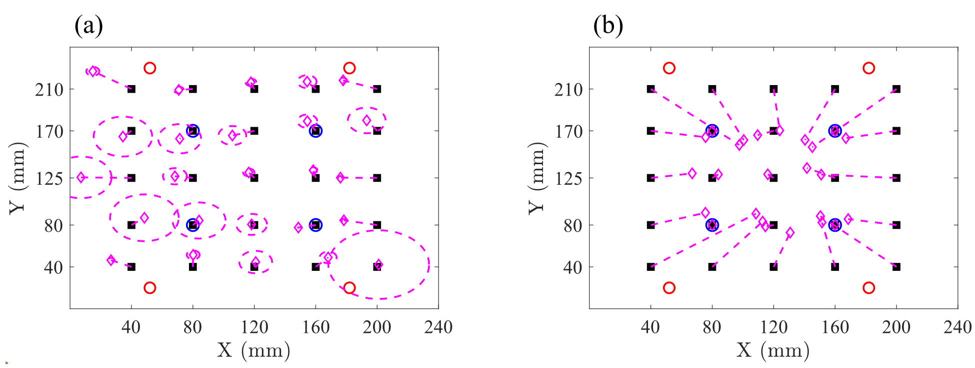

Figure 4.7: Impact localisation of the SP. (a) proposed HPD method, (b) MLP method.

The localisation errors and uncertainties are summarised in Table 4.5. Similar to the FP results, the proposed HPD method offers more accurate and reliable impact location estimation, as indicated by smaller localisation errors and SDs compared to MLP. Specifically, the proposed HPD method achieves a mean localisation error of 12.65 mm and a mean SD of 8.91 mm, whereas MLP exhibits corresponding values of 36.38 mm and 20.13 mm, respectively.

Table 4.5: Impact localisation results on the SP by the proposed HPD method and the reference MLP method.

Method	Mean error (mm)	Max error (mm)	Mean SD (mm)	Max SD (mm)
HPD	12.65	32.90	8.91	32.81
MLP	36.38	89.28	20.13	40.31

The precise impact localisation achieved by the proposed HPD method on the mono-stringer SP validates its applicability to stiffened composite laminate structures. This applicability arises from the fact that stiffened composite laminate panels can be effectively approximated by simple plates with global stiffness [139]. Additionally, the proposed HPD method demonstrates robustness to variations in structural stiffness since the GVP for locating impacts is optimised with respect to wave frequency and stiffness through a two-stage approach based on training impact data. In this optimisation process, the amplitude of the GVP is primarily controlled by the wave frequency, while the shape of the GVP is fine-tuned by variations in material stiffness.

This analysis suggests that the HPD method is suitable for locating impacts on real aircraft composite laminate stiffened structures. Moreover, leveraging physical information from laminate properties and stacking sequences significantly reduces the training data requirements. With just four training impacts, impacts can be located with a localisation error of approximately 10 mm and a SD of 10 mm for both flat and stiffened panels.

4.7 Summary

This chapter introduced a novel hybrid physics-based and data-driven approach—termed the HPD method—for impact localisation in composite laminates. The method leverages the physical dispersion relations of impact-induced flexural waves, derived from the FSDT, to parameterise the GVP as a function of material stiffness and frequency. A two-stage optimisation strategy was developed, using only gradient-based algorithms, to fit the GVP based on a limited set of training impacts. This optimised velocity field is then used in a triangulation-based solver for localisation.

Experimental validation was conducted on both a composite FP and a mono-stringer SP using drop-weight impacts. Results show that the HPD method can accurately localise impacts with as few as four training impacts, maintaining strong performance even outside the training region. Compared to the baseline MLP approach, the HPD method demonstrated superior generalisation and robustness across both isotropic and anisotropic wave fields. Its low training data requirement and reliance on efficient optimisation techniques make it a promising candidate for real-time, on-board SHM applications in aerospace structures.

Nevertheless, the study also has limitations. The assumption of spatially smooth GVP may not hold for highly heterogeneous or complex structural geometries, especially in the presence of multiple stiffeners or curved surfaces. Furthermore, validation was limited to a single material system and two representative geometries. Broader-scale experimental campaigns and integration with real-world flight or maintenance data are needed to confirm the method's scalability and operational readiness.

In conclusion, the HPD framework offers an efficient, physically interpretable, and generalisable solution for impact localisation in composite structures. While it marks a significant step toward practical SHM implementation, further development and rigorous cross-platform validation are essential to realise its full potential in aerospace environments.

Chapter 5

A General Probabilistic Impact Localisation Framework Based on Flexural Wave Propagation

Highlights:

- Develop a data-driven group velocity profile estimation method that enables reliable impact localisation under sparse sensor coverage and limited reference data.
- Formulate a unified localisation framework that integrates physics-based, data-driven, and hybrid approaches to accommodate varying structural complexity and information availability.
- Incorporate Bayesian inference to explicitly quantify uncertainty in model parameters and localisation predictions, enhancing robustness and interpretability.
- Improve localisation performance across diverse wave conditions by enabling multi-frequency wave propagation analysis.

5.1 Introduction

As validated in Chapter 4, integrating a physically informed reference Group Velocity Profile (GVP) with training impact data enables a hybrid GVP calibration and impact localisation method. This approach significantly enhances generalisability, ensuring accurate impact localisation across the entire structure. The physical reference GVP of flexural waves—dominant in low-velocity impact scenarios—can be obtained through various methods, including analytical derivation [29,87,112,114], numerical simulation [21,32], and experimental measurement [26,27,33,68,69].

Analytically, Chow [114] extended Timoshenko's beam theory [140] to cross-ply laminated plates by incorporating a single shear deformation displacement, facilitating the derivation of dispersion relations governing flexural wave propagation. Building on this, Abrate [87] and Jeong et al. [112] refined the formulation using First-order Shear Deformation Theory (FSDT) [141], accounting for independent rotations of normals to the midplane about the x and y axes. However, these studies did not explicitly derive the group velocity from the dispersion relations. Zhu et al. [29] developed an FSDT-based model for GVP estimation and utilised experimental data for model refinement.

Numerical approaches, such as Finite Element Analysis (FEA) [32] and spectral FEA [21], provide an alternative means of accurately measuring GVP, particularly for complex structures, including stiffened configurations. Deng et al. [32] conducted a numerical comparison of the GVPs in stiffened and flat laminated plates, demonstrating that velocity deviations induced by stiffeners remain within 10% across all directions. These numerical methods are particularly advantageous when analytical solutions become impractical due to geometric or material complexities.

Experimental techniques offer another means of measuring GVP, albeit at a higher cost in terms of resources. Meo et al. [26] applied wavelet transforms to extract time difference of arrival (TDOA) data from impact sensor signals, estimating flexural wave GVPs at frequencies below 10 kHz. For higher-frequency waves, Kirkby et al. [33] highlighted the necessity of distinguishing between in-plane and flexural waves to ensure measurement accuracy. However, experimental GVP estimation typically requires precise knowledge of the structural configuration and material properties, as well as an extensive network of sensors and carefully positioned impact excitations, making it time-consuming and resource-intensive.

Given these challenges, a critical question arises: in the absence of detailed structural information, material properties, or direct experimental measurements, can GVP be estimated in a sparse data-driven manner? If so, a general impact localisation framework with high generalisability can be developed, incorporating physics-based (PB), data-driven (DD), and hybrid physics-data (HPD) methods to address varying levels of structural complexity and available information. Table 5.1 summarises the applicable structures, required information, and key characteristics for each method.

Table 5.1: Group velocity profile (GVP) estimation methods and their applications and features.

Method	Structural complexity	Available knowledge	Characteristics
PB	Flat plates	Structural configuration & material properties	Using plate theories (CPT, FSDT)
DD	Complex structures	Reference impact data	GVP parameterised by dispersion relation
HPD	Complex structures with a simpler component	Reference impact data & GVP of simpler component	GVP of simpler component can be from PB method Gradient-based optimisation

These three methods exhibit a high degree of interaction. The PB method, based on plate theories, applies solely to flat plate structures. The GVP for the DD method is parameterised by the dispersion relation from plate theories. The HPD method integrates both the PB and DD approaches: the PB method provides a reference GVP derived from a simpler component of the target complex structure, enhancing the efficiency of the DD estimates. The HPD approach offers scalability in GVP estimation across multiple structural levels—from flat panels to single-stiffener panels, and further to large, metre-scale stiffened panels.

It is also noteworthy that most existing wave-based impact localisation methods follow a deterministic approach [21, 26, 29, 31–35, 37, 41, 42, 61, 62, 69], often neglecting the role of uncertainties. However, quantifying these uncertainties is crucial for improving prediction reliability, particularly when working with sparse passive sensor networks.

Some studies have introduced probabilistic methods to address this issue. For instance, GPR has been explored in a data-driven context [44, 45], but its generalisability remains limited when localising impacts beyond the reference training dataset, as discussed in Chapter 3. The Kalman filter [27, 28] is another widely used technique for uncertainty quantification in wave-based impact localisation. However, this method assumes that impact location, TDOA, and GVP are independent Gaussian variables, which contradicts physical principles, as these factors are inherently correlated. These limitations highlight the need for a more robust impact localisation framework that incorporates uncertainty quantification while remaining physically consistent.

To address these challenges associated with sparse data-driven GVP estimation and uncertainty quantification, a two-step probabilistic framework based on flexural wave propagation is proposed. In the first step, a Bayesian model for GVP estimation is developed, leveraging wave dispersion relations from Classical Plate Theory (CPT) [83, 85] to define the GVP probability space. Three GVP estimation methods are incorporated, tailored to structural complexity and available data: a PB method that analytically derives the GVP based on FSDT; a DD method that estimates GVP using sparse reference impact data; and a HPD approach, which enhances scalability by enabling rapid GVP estimation for complex structures using reference GVP data from simpler components.

In the second step, the estimated GVP is used in multi-frequency probabilistic impact localisation. Within the Bayesian framework, the posterior distribution of impact locations is efficiently determined using fast gradient-based optimisation and Markov Chain Monte Carlo (MCMC) [142, 143], providing reliable localisation while quantifying uncertainties. Experimental impact tests on a flat composite panel, a stiffened composite panel, and a sandwich composite panel validate the framework, showing it to be accurate and efficient in GVP estimation and impact localisation, even for impacts outside sensor-covered regions. For stiffened and sandwich panels, where GVP cannot be analytically derived, the framework efficiently enabled probabilistic GVP estimation and impact localisation with minimal sensor and reference data, underscoring its versatility across complex structures.

5.2 Probabilistic Impact Localisation Framework Based on Flexural Wave Propagation

In practical applications, the TDOAs estimated from impact-induced sensor signals inherently contain uncertainties. These uncertainties stem from both measurement errors—such as sensor noise and environmental influences—and simulation inaccuracies due to limitations in the TDOA extraction techniques. The statistical distribution of TDOA is influenced by the choice of extraction method and its associated kernel, particularly in how it responds to measurement noise.

Assuming that sensor noise—the primary source of measurement error—primarily affects high-frequency signal components, several studies have focused on extracting low-frequency waveforms for impact localisation. Techniques such as the continuous wavelet transform (CWT) [28] and Butterworth filtering [35] have been shown to significantly reduce the sensitivity of TDOA estimates to noise. Furthermore, it is common practice to assume a Gaussian distribution for the extracted TDOAs. For instance, Dehghan-Niri et al. [28] modelled TDOAs as mutually independent Gaussian variables, accounting for Heisenberg uncertainty introduced by the CWT. Other works [27,68] have also adopted independent Gaussian assumptions without explicitly quantifying the underlying uncertainty sources, yet successfully achieved accurate impact localisation.

To investigate the validity of these assumptions, the author conducted a series of drop-mass impact experiments, as reported in [75], which provide empirical evidence supporting the Gaussian and mutually independent nature of the TDOAs. The observed distributions closely align with the Gaussian model and suggest that modelling the TDOAs as statistically independent is a reasonable approximation under controlled experimental conditions.

Based on these findings and experimental validation, the TDOAs in this study are modelled as mutually independent Gaussian random variables. Accordingly, the deterministic wave propagation model in Eq. (2.40) is reformulated to account for TDOA uncertainty as follows:

$$\Delta t_{1j}(\omega) = t_j(\omega) - t_1(\omega) + e(\omega) = \frac{\sqrt{(x-x_j)^2 + (y-y_j)^2}}{v_g(\theta_j,\omega)} - \frac{\sqrt{(x-x_1)^2 + (y-y_1)^2}}{v_g(\theta_1,\omega)} + e(\omega),\ j \in \mathbf{N}_{2N_s}. \tag{5.1}$$

The term $e(\omega)$ is a zero-mean Gaussian variable that accounts for uncertainties in the TDOA, with variance $\sigma^2(\omega)$. Consistent with finds in [75], the variance of Δt_{1j}, where $j \in \mathbb{N}_{2N_s}$, is assumed to be the same across sensors.

Additionally, GVP estimations, particularly those measured by experiments, also contain uncertainties due to material variability and measurement limitations. This study focuses on quantifying the uncertainties in both GVP and TDOA and localising impacts while accounting for these uncertainties. Fig. 5.1 presents impact localisation problem formulation and the developed two-step probabilistic framework for wave propagation-based impact localisation, incorporating the uncertainties in both GVP and TDOA.

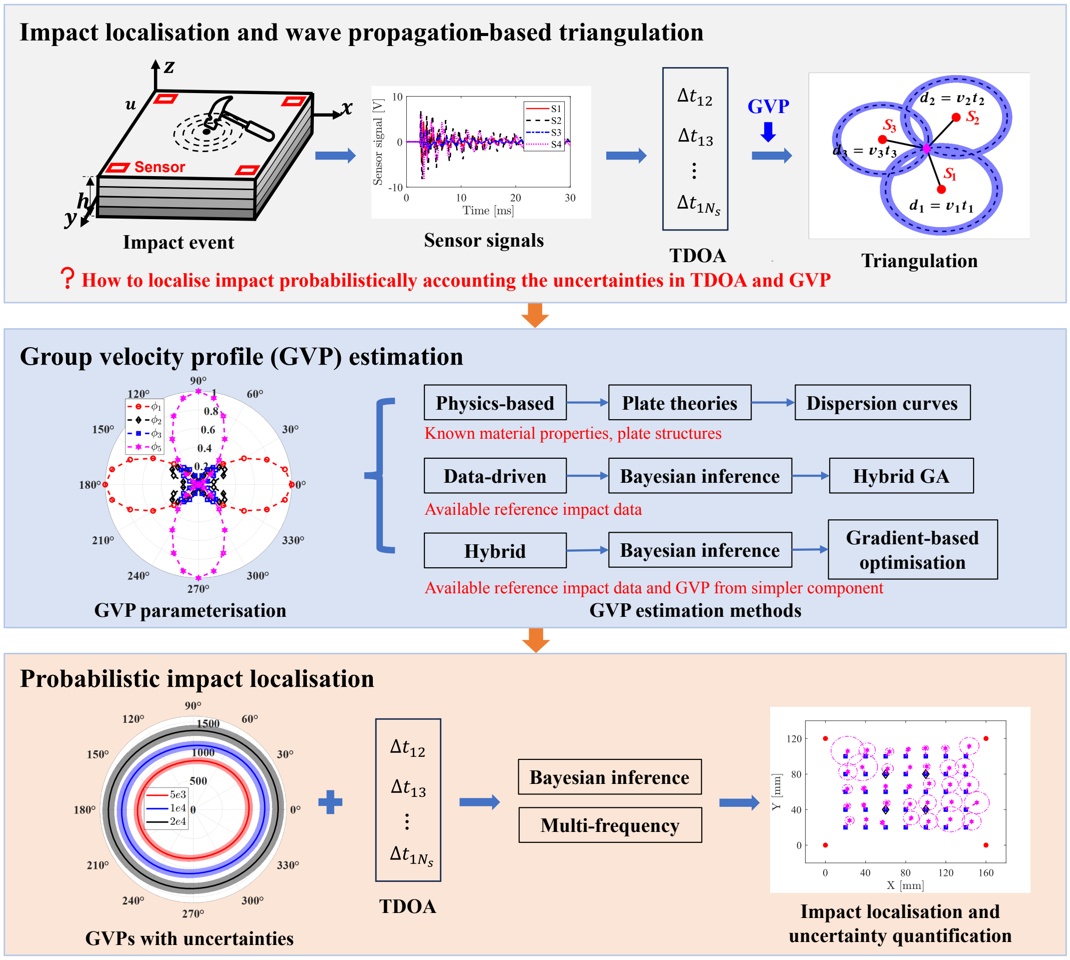

Figure 5.1: Probabilistic impact localisation framework based on flexural wave propagation.

The first step focuses on estimating the GVP and quantifying its uncertainties. Three different cases are considered for GVP estimation based on the structural complexity and the available knowledge: (1) plate structures with known material properties (PB), (2) complex structures with only experimental or numerical reference impact data (DD), and (3) complex structures with reference impact data as well as GVP information from a lower-level structure that is part of the complex structure (HPD). Three corresponding GVP estimation methods are developed for these cases: the PB, DD, and HPD approaches.

The second step involves probabilistic impact localisation using Bayesian inference, based on the previously estimated GVP. To enhance robustness, the localisation is conducted in a multi-frequency manner. Additionally, the GVP parameterisation enables efficient maximum likelihood localisation through gradient-based optimisation. The following sections, Section 5.3 and Section 5.4, focus on detailing the GVP estimation methods and the probabilistic impact localisation process within this two-step framework, respectively.

5.3 Group Velocity Profile (GVP) Estimations

Three GVP estimation methods are developed to address varying levels of structural complexity and available information: the PB, DD, and HPD approaches. A summary of the applicable structures, required information, and key characteristics for each method is provided in Table 5.1.

5.3.1 Physics-based (PB) approach

For plate-like structures with known material properties, flexural wave GVP can be derived analytically using plate theories or calculated numerically via FEA. Experimental studies [144, 145] show that CPT (Eq. (3.1) and Eq. (3.2)) is accurate at very low frequencies in thin plates, while FSDT (Eq. (2.33), Eq. (2.34), and Eq. (2.28)) is more effective for higher frequencies in moderately thick plates. Given that impact-induced waves are predominantly low-frequency (Section 2.1.3), plate theories can provide accurate GVP estimates. This study leverages plate theories for efficient GVP estimation and impact localisation, avoiding the need for FEA.

To evaluate the accuracy of plate theories in composite laminate structures, dispersion curves for the A0 mode were compared using CPT, FSDT, and the SAFEDC software [146], as detailed in [75]. The results show that CPT significantly overestimates phase and group velocities at higher frequencies but aligns well with FSDT and SAFEDC at lower frequencies. FSDT demonstrates superior accuracy across the spectrum, closely matching SAFEDC, particularly for group velocity. These findings highlight FSDT as a reliable and computationally efficient alternative to complex numerical methods for modelling the A0 mode in impact localisation.

5.3.2 Data-driven (DD) approach

For complex structures without prior knowledge of material properties, the GVP can be probabilistically estimated solely using experimental or numerical reference impact data. This reference dataset comprises independent reference impact locations $x^i, y^i,\ i \in \mathbb{N}_{1N_i}$ and their associated TDOA $\Delta\mathbf{t}^i$, $i \in \mathbb{N}_{1N_i}$, extracted from impact sensor signals.

5.3.2.1 Parameterisation of the flexural wave GVP based on dispersion

Based on relation Eq. (3.1), the dispersion relations depicted in Eq. (3.2), serve as a parameterisatoin method for the GVP, which represents the GVP $v_g(\theta)$ with the five basis functions $\phi_j(\theta) = \sin^{(j-1)}\theta\cos^{(5-j)}\theta, j = 1, 2, ..., 5$ and their corresponding coefficient c_j:

$$
\begin{aligned}
&v_g^4(\theta) = 16v_p^4(\theta) = \sum_{j=1}^{5} c_j\phi_j(\theta),\ \phi_j(\theta) = \sin^{(j-1)}\theta\cos^{(5-j)}\theta, \\
&c_1 = \frac{16D_{11}\omega^2}{\rho d}, c_2 = \frac{64D_{16}\omega^2}{\rho d}, c_3 = \frac{32(D_{12}+2D_{66})\omega^2}{\rho d}, c_4 = \frac{64D_{26}\omega^2}{\rho d}, c_5 = \frac{16D_{22}\omega^2}{\rho d}.
\end{aligned} \tag{5.2}
$$

Every realisation of velocity coefficients corresponds to a GVP. Given that wave velocity is greater than zero, the parameter space of the velocity coefficients is defined by positive GVP:

$$
v_g^4(\theta) = \sum_{j=1}^{5} c_j\phi_j(\theta) > 0,\ \phi_1(\theta), \phi_3(\theta), \phi_5(\theta) \geq 0,\ c_1, c_3, c_5 > 0\ c_2, c_4 \geq 0. \tag{5.3}
$$

The velocity coefficients c_2 and c_4 may be negative for certain principal material directions. However, by rotating the principal material direction and coordinate axes transformation during the calculation of GVP, these coefficients can achieve non-negative values [85]. This study advocates for selecting principal material directions that guarantee non-negative velocity coefficients for parameterising and computing the GVP. Detailed derivations of the parameter space for velocity coefficients corresponding to positive GVPs are provided in [75].

5.3.2.2 Probabilistic GVP estimation solely using the reference impact data

By employing Bayesian inference [147,148] in combination with the GVP parameterisation method outlined in Eq. (5.2), the posterior distribution of the GVP velocity coefficients $\mathbf{c} \in \mathbb{R}^{5\times 1}$, given independent observations $x^i, y^i, \Delta\mathbf{t}^i, i \in \mathbb{N}_{1N_i}$, is derived as:

$$P(\mathbf{c},\sigma|x^i,y^i,\Delta\mathbf{t}^i, i\in\mathbb{N}_{1N_i}) = \frac{P(x^i,y^i,\Delta\mathbf{t}^i, i\in\mathbb{N}_{1N_i}|\mathbf{c},\sigma)}{P(x^i,y^i,\Delta\mathbf{t}^i, i\in\mathbb{N}_{1N_i})}P(\mathbf{c},\sigma) = \prod_{i=1}^{N_i}\frac{P(x^i,y^i,\Delta\mathbf{t}^i|\mathbf{c},\sigma)}{P(x^i,y^i,\Delta\mathbf{t}^i)}P(\mathbf{c})P(\sigma), \tag{5.4}$$

where $P(x^i,y^i,\Delta\mathbf{t}^i|\mathbf{c},\sigma)$, $P(x^i,y^i,\Delta\mathbf{t}^i)$, and $P(\mathbf{c},\sigma)$ represents the likelihood, marginal likelihood, and prior, respectively. The prior $\mathcal{P}_{rc} = P(\mathbf{c},\sigma) = P(\mathbf{c})P(\sigma)$ reflects the independence between the GVP (parameterised by $\mathbf{c}$) and TDOA standard deviation (SD) σ, where TDOA uncertainties arise from sensor measurement errors and limitations in TDOA extraction accuracy.

The prior component $P(\mathbf{c})$ represents the distribution of the GVP velocity coefficients absent specific observations $x^i, y^i, \Delta\mathbf{t}^i$. Because the GVP depends on structural properties, and its velocity coefficients are linearly related to bending stiffness, it is typically assumed that the prior distribution of these coefficients follows a Gaussian distribution with a mean $\tilde{\mathbf{c}}$ that accounts for material property uncertainties [149,150]. The SD of the prior depends on the variances of material properties. Assuming the SD ratio of the nominal value of material properties is denoted by η, the prior distribution of velocity coefficients can be expressed as:

$$P(\mathbf{c}) \sim \mathcal{N}(\tilde{\mathbf{c}}, \eta^2\tilde{\mathbf{c}}^2),\ \tilde{\sigma}_c = \eta\tilde{\mathbf{c}} \tag{5.5}$$

where $\tilde{\mathbf{c}}$ and $\tilde{\sigma}_c$ represent the prior mean and SD of the wave velocity coefficients.

In the absence of strong prior information about σ and to facilitate faster computation, this study employs the maximum likelihood approach (treating σ as a fixed parameter). This treatment simplifies the prior and computation, as σ is determined directly by maximising likelihood based on observations $x^i, y^i, \Delta\mathbf{t}^i$. The likelihood $P(x^i,y^i,\Delta\mathbf{t}^i|\mathbf{c},\sigma)$ denotes the probability of the i-th observation given the GVP velocity coefficients $\mathbf{c}$ and TDOA variance, which follows to a multivariate Gaussian distribution, expressed as:

$$\begin{aligned}
\mathcal{L}_c^i &= P(x^i,y^i,\Delta\mathbf{t}^i|\mathbf{c},\sigma) = \prod_{j=2}^{N_s} P(x^i,y^i,\Delta t_j^i|\mathbf{c},\sigma) = \prod_{j=2}^{N_s}\frac{1}{\sqrt{2\pi\sigma^2}}\exp\left(-\frac{(e_j^i)^2}{2\sigma^2}\right), \\
e_j^i &= t_j^i - t_1^i - \Delta t_j^i = \frac{\sqrt{(x^i-x_j)^2+(y^i-y_j)^2}}{v_g(\theta_j^i)} - \frac{\sqrt{(x^i-x_1)^2+(y^i-y_1)^2}}{v_g(\theta_1^i)} - \Delta t_j^i,
\end{aligned} \tag{5.6}$$

based on physical relation of wave propagation Eq. (5.1). In the expression, e_j^i represents the TDOA residual of the j-th sensor for the i-th reference impact, calculated as the difference between the estimation from the GVP $t_j^i - t_1^i$ and the TDOA extracted from the reference sensor signals Δt_j^i. Additionally, d_j^i and θ_j^i represent the distance and wave propagation direction from the i-th reference impact to j-th sensor, respectively. σ^2 denotes the TDOA variance across the reference impacts. The likelihood of all independent reference impacts is the product of the likelihood of each reference impact:

$$\mathcal{L}_c = \prod_{i=1}^{N_i} \mathcal{L}_c^i = \prod_{i=1}^{N_i} \prod_{j=2}^{N_s} P(x^i, y^i, \Delta t_j^i | \mathbf{c}, \sigma) = \prod_{i=1}^{N_i} \prod_{j=2}^{N_s} \frac{1}{\sqrt{2\pi\sigma^2}} \exp\left(-\frac{(e_j^i)^2}{2\sigma^2}\right). \tag{5.7}$$

The log likelihood is further derived as:

$$\ln \mathcal{L}_c = -\frac{N_i(N_s-1)}{2} \ln(2\pi\sigma^2) - \frac{1}{2\sigma^2} \sum_{i=1}^{N_i} \sum_{j=2}^{N_s} (e_j^i)^2. \tag{5.8}$$

The prior mean $\tilde{\mathbf{c}}$ is unknown; thus, it is assumed to be equal to its Maximum Likelihood Estimation (MLE). The Gaussian prior reaches its maximum value when $\mathbf{c}$ is equal to the MLE $\tilde{\mathbf{c}}$. Therefore, the MLE $\tilde{\mathbf{c}}$ serves as the maximum posterior estimation, as the posterior is proportional to the likelihood multiplied by the prior. The maximisation of the log likelihood results in the estimation of the TDOA variance across the reference impacts:

$$\frac{\partial \ln \mathcal{L}_c}{\partial \sigma^2} = -\frac{N_i(N_s-1)}{2\sigma^2} + \frac{1}{2\sigma^4} \sum_{i=1}^{N_i} \sum_{j=2}^{N_s} (e_j^i)^2 = 0 \implies \sigma^2 = \frac{1}{N_i(N_s-1)} \sum_{i=1}^{N_i} \sum_{j=2}^{N_s} (e_j^i)^2. \tag{5.9}$$

Hence, the GVP velocity coefficients with the maximised likelihood (posterior), denoted as $\tilde{\mathbf{c}}$, are estimated by maximising the log likelihood, which is equivalent to minimising the TDOA variance across the reference impacts:

$$\tilde{\mathbf{c}} = \underset{\mathbf{c}}{\operatorname{argmax}} \ln \mathcal{L}_c = \underset{\mathbf{c}}{\operatorname{argmin}}\, \sigma^2 = \underset{\mathbf{c}}{\operatorname{argmin}} \frac{1}{N_i(N_s-1)} \sum_{i=1}^{N_i} \sum_{j=2}^{N_s} (e_j^i)^2. \tag{5.10}$$

5.3.2.3 Maximising likelihood: Hybrid GA (HGA) with gradient-based local search

Genetic algorithm (GA) [138] can be employed to estimate the GVP with the highest probability by maximising the log likelihood (minimising the TDOA variance) as illustrated in Eq. (5.10), with the five GVP velocity coefficients treated as design variables. To expedite the optimisation process, gradient information can be incorporated to facilitate a faster and more efficient local search. These gradients include the first and second-order partial derivatives of the TDOA variance with respect to the five GVP velocity coefficients $c_m, c_n, m, n \in \mathbb{N}_{15}$, which are derived as:

$$\frac{\partial \sigma^2}{\partial c_m} = \frac{2}{N_i(N_s-1)} \sum_{i=1}^{N_i} \sum_{j=2}^{N_s} e_j^i \frac{\partial e_j^i}{\partial c_m},\ \frac{\partial^2 \sigma^2}{\partial c_m \partial c_n} = \frac{2}{N_i(N_s-1)} \sum_{i=1}^{N_i} \sum_{j=2}^{N_s} \frac{\partial e_j^i}{\partial c_m}\frac{\partial e_j^i}{\partial c_n} + e_j^i \frac{\partial^2 e_j^i}{\partial c_m \partial c_n}. \tag{5.11}$$

Based on the expression of the TDOA residual e_j^i defined in Eq. (5.6) and the GVP parameterised by velocity coefficients $c_m, c_n, , m, n \in \mathbb{N}_{15}$ as illustrated in Eq. (5.1), the intermediate derivatives $\frac{\partial e_j^i}{\partial c_m}$ and $\frac{\partial^2 e_j^i}{\partial c_m \partial c_n}$ are further derived using the chain rule:

$$\begin{gathered}\frac{\partial e_j^i}{\partial c_m} = \frac{\partial t_j^i}{\partial c_m} - \frac{\partial t_1^i}{\partial c_m},\ \frac{\partial t_j^i}{\partial c_m} = -\frac{d_j^i}{v_g^2(\theta_j^i)}\frac{\partial v_g(\theta_j^i)}{\partial c_m},\ \frac{\partial v_g(\theta_j^i)}{\partial c_m} = \frac{\phi_m(\theta_j^i)}{4v_g^3(\theta_j^i)},\ \frac{\partial^2 e_j^i}{\partial c_m \partial c_n} = \frac{\partial^2 t_j^i}{\partial c_m \partial c_n} - \frac{\partial^2 t_1^i}{\partial c_m \partial c_n},\\ \frac{\partial^2 t_j^i}{\partial c_m \partial c_n} = \frac{2d_j^i}{v_g^3(\theta_j^i)}\frac{\partial v_g(\theta_j^i)}{\partial c_m}\frac{\partial v_g(\theta_j^i)}{\partial c_n} - \frac{d_j^i}{v_g^2(\theta_j^i)}\frac{\partial^2 v_g(\theta_j^i)}{\partial c_m \partial c_n},\ \frac{\partial^2 v_g(\theta_j^i)}{\partial c_m \partial c_n} = \frac{-3\phi_m(\theta_j^i)\phi_n(\theta_j^i)}{16v_g^7(\theta_j^i)}.\end{gathered} \tag{5.12}$$

Incorporating the gradients illustrated in Eq. (5.11) into the GA for efficient local search, the GVP with the maximised likelihood can be efficiently identified.

5.3.2.4 Bounding velocity coefficients by reference impact data

The maximisation of the log likelihood, as depicted in Eq. (5.10), is significantly influenced by the bounds of these five design variables, namely, the velocity coefficients. The upper and lower bounds of the five velocity coefficients can be determined using the reference impact data $x^i, y^i, \Delta\mathbf{t}^i, i \in \mathbb{N}_{1N_i}$. Based on the physical relation of wave propagation shown in Eq. (5.1), the following inequality can be derived, and the equivalent velocity $\bar{v}(\theta_{1j}^i)$ is defined:

$$\min[v_g(\theta_j^i), v_g(\theta_1^i)] \leq \frac{d_j^i - d_1^i}{\Delta t_j^i + e} \leq \max[v_g(\theta_j^i), v_g(\theta_1^i)],\ \bar{v}(\theta_{1j}^i) = \frac{d_j^i - d_1^i}{\Delta t_j^i}. \tag{5.13}$$

When excluding TDOA uncertainties (e=0), the equivalent velocity $\bar{v}(\theta_{1j}^i)$ lies midway between the actual velocities $v_g(\theta_j^i)$ and $v_g(\theta_1^i)$ of two separate wave propagation paths. However, due to inevitable TDOA uncertainties ($e \neq 0$), the equivalent velocity $\bar{v}(\theta_{1j}^i)$ is not bounded by actual velocities $v_g(\theta_j^i)$ and $v_g(\theta_1^i)$. A large negative TDOA uncertainty ($e < 0$) may leads the equivalent velocity to be greater than $\max[v_g(\theta_j^i), v_g(\theta_1^i)]$ (excluding negative equivalent velocity). A positive TDOA uncertainty ($e > 0$) may leads the equivalent velocity to be smaller than $\min[v_g(\theta_j^i), v_g(\theta_1^i)]$. Across all wave propagation paths in the reference impacts, the equivalent velocity forms a velocity set $\bar{\mathcal{V}} = \{\bar{v}(\theta_{1j}^i), i \in \mathbb{N}_{1N_i}, j \in \mathbb{N}_{2N_s}\}$. Considering the randomness of the TDOA uncertainty, the maximum and minimum of this equivalent velocity set, $\max(\bar{\mathcal{V}})$ and $\min(\bar{\mathcal{V}})$, respectively, bound the actual maximal wave group velocity $\max[v_g(\theta)]$ and minimal wave group velocity $\min[v_g(\theta)]$.

To mitigate the influence of TDOA uncertainty on equivalent velocity, only the equivalent velocities corresponding to a large value of the measured TDOA Δt_j^i should be included in the velocity set. In this study, the TDOA threshold for calculating the equivalent velocity is set to half of the maximal TDOA for all reference impacts. In this way, the actual maximal wave velocity $\max[v_g(\theta)]$ and minimal wave velocity $\min[v_g(\theta)]$ are bounded as:

$$\min(\bar{\mathcal{V}}) \leq \min[v_g(\theta)] \leq \max[v_g(\theta)] \leq \max(\bar{\mathcal{V}}). \tag{5.14}$$

With the bounded wave velocity, the velocity coefficients c_1 and c_5 can be directly bounded since they are only associated with the wave velocity in the $\theta = 0$ and $\theta = \pi/2$ directions, respectively:

$$[\min(\bar{\mathcal{V}})]^4 \leq c_1 = v_g^4(\theta = 0) \leq [\max(\bar{\mathcal{V}})]^4, \; [\min(\bar{\mathcal{V}})]^4 \leq c_5 = v_g^4(\theta = \pi/2) \leq [\max(\bar{\mathcal{V}})]^4. \tag{5.15}$$

To generate a circular wavefront ($v_g(\theta)$ is constant), the conditions $c_3 = 2c_1 = 2c_5$, and $c_2 = c_4 = 0$ should be satisfied. These conditions define the bounds for the velocity coefficient c_3. Additionally, since the lamina placed in the $\theta = 0$ and $\theta = \pi/2$ directions does not contribute to the bending stiffness D_{16} (c_2) and D_{26} (c_4), the laminated composite with a layup of $[0°/45°]_s$ achieves the largest ratio of D_{16}/D_{11} among symmetrically laminated composites [85], which provides an upper bound for c_2 and c_4. Assuming a lamina modulus ratio of $E_1/E_2 = \beta \geq 1$, this largest ratio c_2/c_1

can be estimated based on CPT:

$$\frac{c_2}{c_1} = \frac{4D_{16}}{D_{11}} \leq \frac{4(\beta - 1)}{29.5\beta + 1.5} \leq \frac{4}{29.5}. \tag{5.16}$$

The same analysis can be applied to c_4/c_5. Therefore, the velocity coefficients c_2, c_3, and c_4 are bounded by:

$$2[\min(\bar{\mathcal{V}})]^4 \leq c_3 \leq 2[\max(\bar{\mathcal{V}})]^4,\ -[\max(\bar{\mathcal{V}})]^4/7.375 \leq c_2, c_4 \leq [\max(\bar{\mathcal{V}})]^4/7.375. \tag{5.17}$$

The bounds of c_2 and c_4 are symmetric about 0 since their signs are influenced by the selected principal material direction. By rotating the principal material direction when negative values are present, c_2 and c_4 can be reassessed as positive.

5.3.2.5 Identifying posterior distribution of the GVP

The gradient information derived in Section 5.3.2.3 and the velocity coefficient bounds identified in Section 5.3.2.4 facilitate the rapid determination of the MLEs of the TDOA variance $\tilde{\sigma}^2$, the velocity coefficients $\tilde{\mathbf{c}}$, and the corresponding GVP $\tilde{v}_g(\theta)$. This identified TDOA variance $\tilde{\sigma}^2$ with maximum likelihood refines the posterior distribution from $P(\mathbf{c}, \sigma | x^i, y^i, \Delta\mathbf{t}^i, i \in \mathbb{N}_{1N_i})$ to $P(\mathbf{c}|\tilde{\sigma}, x^i, y^i, \Delta\mathbf{t}^i, i \in \mathbb{N}_{1N_i})$, thereby facilitating efficient posterior estimation via the MCMC [142, 143] method.

In this reaseach, an advanced adaptive MCMC technique, the Delayed Rejection Adaptive Metropolis (DRAM) algorithm [151], is employed. DRAM integrates adaptive Metropolis sampling with delayed rejection to improve both sample accuracy and robustness. The initial proposal covariance for MCMC sampling is set as diag $\eta^2\tilde{\mathbf{c}}^2$, consistent with the Gaussian prior.

Algorithm 5.1 provides the pseudo-algorithm for data-driven GVP estimation, which involves four main steps: TDOA extraction, estimation of velocity coefficient bounds, MLE of velocity coefficients and TDOA variance by Hybrid Genetic Algorithm (HGA), and velocity confidence ratio estimation via MCMC. In the MLE step, the fixed parameter for TDOA variance is identified and subsequently incorporated as known information in the MCMC sampling. This approach reduces the number of probabilistic parameters and enhances computational efficiency and sampling convergence.

Algorithm 5.1: Data-driven GVP estimation with reference impact data.

Input: $x^i, y^i, \boldsymbol{s}^i, L_j(x_j, y_j)$; /* Reference impact data, sensors' locations L_j */

Output: $\tilde{v}_g(\theta), \mathbf{C}_{mc}$; /* GVP with maximum likelihood, posterior velocity coefficients */

Step 1: TDOA extraction from reference impact sensor signals:

$\Delta\mathbf{t}^i \leftarrow \boldsymbol{s}^i$; /* TDOA extraction */

Step 2: Velocity coefficient bounds estimation:

$\bar{\mathcal{V}}, \bar{v}(\theta^i_{1j}) \leftarrow x^i, y^i, x_j, y_j, \Delta\mathbf{t}^i$; /* Equivalent velocity set */

$\mathbf{c}_{lb}, \mathbf{c}_{ub} \leftarrow \bar{\mathcal{V}}$; /* Bounds of velocity coefficients */

Step 3: MLEs of GVP and TDOA variance by HGA:

$e^i_j \leftarrow \phi_m, x^i, y^i, x_j, y_j, \mathbf{c}$; /* TDOA residual function */

$\sigma^2 \leftarrow \frac{1}{N_i(N_s-1)} \sum_{i=1}^{N_i} \sum_{j=2}^{N_s} (e^i_j)^2, \mathbf{c}$; /* TDOA variance function */

$\frac{\partial \sigma^2}{\partial c_m} \leftarrow e^i_j, \phi_m, \mathbf{c}$; /* Gradient function */

$\tilde{\mathbf{c}}, \tilde{\sigma}^2, \tilde{v}_g(\theta) \leftarrow \sigma^2, \frac{\partial \sigma^2}{\partial c_m}, \mathbf{c}_{ub}, \mathbf{c}_{lb}$; /* Maximum likelihood GVP and TDOA variance by HGA */

Step 4: Posterior velocity coefficients by MCMC:

$\mathbf{L}_c, \mathbf{P}_{rc} \leftarrow \tilde{\sigma}^2, \mathbf{c}$; /* Likelihood and prior based on identified TDOA variance */

$\mathbf{C}_{mc} \leftarrow \mathbf{L}_c, \mathbf{P}_{rc}$; /* MCMC samples and posterior distribution of velocity coefficients */

5.3.3 Hybrid physics-data (HPD) approach

In scenarios where limited reference impact data $x^i, y^i, \Delta\mathbf{t}^i$, $i \in \mathbb{N}_{1N_i}$, is available for a target complex structure, and the GVP from a lower-level structure incorporated within the target is known, the GVP of the complex structure can be probabilistically estimated by integrating these two sources of information. This approach demonstrates the scalability of GVP estimation, enabling rapid GVP identification for more complex, higher-level structures by leveraging the reference GVP from their simpler components. For example, complex stiffened plate structures consist of both flat plate and stiffener components. The GVP of the lower-level flat plates can be estimated using the PB method with known material properties, and this estimation can assist in the GVP identification of the overall complex stiffened structure.

5.3.3.1 Gaussian prior and maximum likelihood estimation of the GVP

Assuming that the available reference GVP corresponds to the reference velocity coefficients $\bar{\mathbf{c}}$, these coefficients cannot accurately serve as the prior mean. This is because the reference GVP may not be accurate enough to mimic the wave propagation in the target structure. If the reference GVP is derived from a lower-level structure, it may differ significantly in velocity amplitude from the actual GVP of the target structure, although it may have a similar shape. Therefore, the prior mean of the velocity coefficient again adopts its MLE. However, the reference GVP enables the representation of the prior mean, as the summation of a scaled reference velocity coefficients and small deviations:

$$\tilde{\mathbf{c}} = (1/\gamma)^4 \bar{\mathbf{c}} + \delta_c, \tag{5.18}$$

where γ and δ_c represent the scaling factor and deviations, respectively. In this representation, the scaling factor γ controls the amplitude of the prior mean, and the deviations fine-tune the prior mean. With such representation, the MLE of the velocity coefficients $\mathbf{c}$ can be identified solely based on the two-stage gradient-based optimisation developed in Chapter 4. This two-stage optimisation process involves identifying the scaling factor γ and subsequently the small deviations δ_c until γ converges to 1, using the trust-region-reflective (TRF) algorithm [137] based on the gradient information derived.

5.4 Probabilistic Impact Localisation by Bayesian Inference

5.4.1 Probabilistic impact localisation: Bayesian inference

Given the observations, including the TDOA $\boldsymbol{\Delta}\mathbf{t}$ for an impact estimated from its corresponding sensor signals and the known deterministic GVP $v_g(\theta)$, the impact location can be determined in a probabilistic model using Bayesian inference [148]:

$$P(x, y, \sigma | \boldsymbol{\Delta}\mathbf{t}, v_g) = \frac{P(\boldsymbol{\Delta}\mathbf{t}, v_g | x, y, \sigma)}{P(\boldsymbol{\Delta}\mathbf{t}, v_g)} P(x, y, \sigma) = \frac{P(\boldsymbol{\Delta}\mathbf{t}, v_g | x, y, \sigma)}{P(\boldsymbol{\Delta}\mathbf{t}, v_g)} P(x, y) P(\sigma), \tag{5.19}$$

where $P(x, y, \sigma | \boldsymbol{\Delta}\mathbf{t}, v_g)$, $P(\boldsymbol{\Delta}\mathbf{t}, v_g | x, y, \sigma)$, $P(x, y, \sigma)$ and $P(\boldsymbol{\Delta}\mathbf{t}, v_g)$ represent the posterior, likelihood, prior, and marginal likelihood (evidence), respectively. The prior $\mathcal{P}_{xy} = P(x, y, \sigma) = P(x, y)P(\sigma)$ indicates the independence between impact location and TDOA variance, as TDOA uncertainties arise primarily from sensor measurement errors and the inherent limitations in TDOA extraction methods.

Similar to the data-driven GVP estimation approach in Section 5.3.2, TDOA SD σ is treated as a fixed parameter and estimated using its maximum likelihood [152] (constant σ), rather than using Jeffrey's non-informative prior $P(\sigma) \propto 1/\sigma$ [153] or modelling it as an inverse chi-squared distribution [147,151]. This approach simplifies both the prior and the Bayesian inference process, as σ^2 is automatically determined by the observations (known TDOA $\Delta\mathbf{t}$ and GVP $v_g(\theta)$) through maximum likelihood. Additionally, Section 5.6.3.2 presents a comparison of these three approaches to TDOA variance in impact localisation.

The likelihood $P(\Delta\mathbf{t}, v_g|x, y, \sigma)$ can be derived as the probability of a multivariate Gaussian distribution based on Eq. (5.1). Therefore, the log likelihood is derived as:

$$\begin{aligned} \ln \mathcal{L}_{xy} &= -\frac{(N_s-1)}{2}\ln(2\pi\sigma^2) - \frac{1}{2\sigma^2}\sum_{j=2}^{N_s} e_j^2, \\ e_j &= (t_j - t_1) - \Delta t_{1j} = \frac{\sqrt{(x-x_j)^2+(y-y_j)^2}}{v_g(\theta_j)} - \frac{\sqrt{(x-x_1)^2+(y-y_1)^2}}{v_g(\theta_1)} - \Delta t_{1j}, \end{aligned} \tag{5.20}$$

where $t_j - t_1$ signifies the time difference estimated from the GVP $v_g(\theta)$, while Δt_{1j} denotes the time difference extracted from the impact sensor signals. Consequently, e_j represents the residual of the predicted and measured TDOA.

5.4.2 Maximum likelihood and posterior estimations of impact location

The maximum of the log likelihood is achieved when the first-order partial derivative with respect to σ^2 is zero. Setting $\frac{\partial \ln \mathcal{L}}{\partial \sigma^2}$ equal to zero in Eq. (5.20) yields the estimation of the TDOA variance $\sigma^2 = \frac{1}{N_s-1}\sum_{j=2}^{N_s} e_j^2$. The TDOA variance is estimated as the average residual of sum of the square error of the extracted TODA from sensor signals and the estimated TODA from GVP. The MLE of impact location is equivalent to minimising the TDOA variance:

$$\tilde{x}, \tilde{y} = \underset{x,y}{\operatorname{argmin}}\, \sigma^2 = \underset{x,y}{\operatorname{argmin}} \frac{1}{N_s-1}\sum_{j=2}^{N_s} e_j^2. \tag{5.21}$$

The MLE of TDOA variance $\tilde{\sigma}^2$ (corresponding to the $\tilde{x}, \tilde{y}$) refines the posterior from $P(x, y, \sigma|\Delta\mathbf{t}, v_g)$ to $P(x, y|\Delta\mathbf{t}, v_g, \tilde{\sigma})$. This transformation enables a more focused assessment of impact localisation reliability, which is quantified using a confidence area. This area is defined by a confidence radius, ensuring that the cumulative posterior probability within the overlapping area of circular region centred at the posterior mean and structural domain exceeds a confidence level α. The posterior mean $(\bar{x}, \bar{y})$ and the confidence radius r_α are thus defined by definite integration as follows:

$$
\begin{aligned}
&(\bar{x}, \bar{y}) = \int_{\Omega_{xy}} (x, y) P(x, y|\Delta\mathbf{t}, v_g, \tilde{\sigma}) d(x, y) \\
&r_\alpha = \underset{r}{\operatorname{argmin}} \int_0^r \int_0^{2\pi} P(x, y|\Delta\mathbf{t}, v_g, \tilde{\sigma}) d\phi dr > \alpha,\ x = r\cos\phi + \bar{x},\ y = r\sin\phi + \bar{y}.
\end{aligned}
\tag{5.22}
$$

To approximate the posterior distribution $P(x, y|\Delta\mathbf{t}, v_g, \tilde{\sigma})$, the MCMC method [151], is adopted again. The initial proposal distribution for the MCMC samples is set to a two-dimensional Gaussian distribution with mean $(\tilde{x}, \tilde{y})$ and covariance $\max[v_g(\theta)]^2\tilde{\sigma}^2 I$. Through these MCMC samples, the posterior mean $(\bar{x}, \bar{y})$ and confidence radius r_α are efficiently computed.

The choice of the initial proposal distribution considers the relationship among the confidence radius, TDOA variance, and wave velocity. Since the likelihood follows a Gaussian form, increased TDOA variance and higher wave velocity both result in a more gradual decrease in likelihood as the impact location diverges from its maximum likelihood estimate. Consequently, the confidence radius exhibits a monotonic increase with both TDOA variance and wave velocity. This adaptive covariance, denoted by $\max[v_g(\theta)]^2\tilde{\sigma}^2 I$ based on the maximum wave velocity $\max[v_g(\theta)]$, ensures the proposal distribution maintains adequately heavy tails.

5.4.3 Maximising likelihood: gradient-based optimisation

The process of identifying the impact location with the highest likelihood involves solving a minimisation problem outlined in Eq. (5.21). Traditionally, this problem has been tackled using heuristic optimisation algorithms, such as GA. However, GA-based optimization incurs significant computational costs and requires numerous evaluations of the objective function (specifically, the TDOA variance σ^2) to thoroughly explore the design space. Enhancing computational efficiency is essential for enabling real-time impact localisation directly at the sensor node of a passive impact monitoring system [154], rather than relying on a central computing node. To expedite the optimisation process, this study adopts gradient-based approaches, leveraging the gradient information of the objective function with respect to the impact location. These required gradients are derived using the chain rule:

$$\begin{aligned}&\frac{\partial\sigma^2}{\partial x}=\frac{2}{N_s-1}\sum_{j=2}^{N_s}e_j\frac{\partial e_j}{\partial x},\ \frac{\partial\sigma^2}{\partial y}=\frac{2}{N_s-1}\sum_{j=2}^{N_s}e_j\frac{\partial e_j}{\partial y},\ \frac{\partial^2\sigma^2}{\partial x^2}=\frac{2}{N_s-1}\sum_{j=2}^{N_s}(\frac{\partial e_j}{\partial x})^2+e_j\frac{\partial^2 e_j}{\partial x^2},\\&\frac{\partial^2\sigma^2}{\partial y^2}=\frac{2}{N_s-1}\sum_{j=2}^{N_s}(\frac{\partial e_j}{\partial y})^2+e_j\frac{\partial^2 e_j}{\partial y^2},\ \frac{\partial^2\sigma^2}{\partial x\partial y}=\frac{2}{N_s-1}\sum_{j=2}^{N_s}\frac{\partial e_j}{\partial x}\frac{\partial e_j}{\partial y}+e_j\frac{\partial^2 e_j}{\partial x\partial y}.\end{aligned}\tag{5.23}$$

The intermediate partial derivatives $\frac{\partial e_j}{\partial x}$, $\frac{\partial e_j}{\partial y}$, $\frac{\partial^2 e_j}{\partial x^2}$, $\frac{\partial^2 e_j}{\partial y^2}$, and $\frac{\partial^2 e_j}{\partial x\partial y}$ are further calculated based on the TDOA residual e_j defined in Eq. (5.20). Their detailed derivation is presented in [75]. Utilising these gradients, the TRF algorithm [137], a gradient-based optimisation method well suited to bounded or constrained optimisation problems, efficiently localises impacts by solving Eq. (5.21) in a bounded and finite structural space.

The utilisation of gradient-based optimisation stems from the property that when wavefronts with a convex interior (most often in real structures), such as circles or ellipses, the objective function (σ^2) typically exhibit a simple shape with only one minimum within the sensor coverage area. By initialising the optimisation process with two initial points, one inside and one outside the sensor coverage area, and both closest to the sensor with minimal TDOA, gradient-based optimisation can efficiently locate this minimum and identify the impact localisation with maximised likelihood.

Algorithm 5.2 presents the pseudo-algorithm for probabilistic impact localisation with a known GVP, leveraging Bayesian inference. This algorithm comprises three main steps: TDOA extraction, MLE of the impact location and TDOA variance, and localisation confidence radius estimation via MCMC. During the MLE process, the fixed parameter for TDOA variance is identified. This parameter is then incorporated as known information within the MCMC, thereby reducing the number of probabilistic parameters and enhancing computational efficiency.

5.4.4 Multi-frequency probabilistic impact localisation

Due to the dispersive nature of flexural waves and the availability of TDOAs and GVPs across multiple frequencies, impact localisation can be performed using a multi-frequency approach. Using

Algorithm 5.2: Probabilistic impact localisation with known GVP using Bayesian inference.

Input: $v_g(\theta), \alpha, L_j(x_j, y_j), \boldsymbol{s}_j, N_s$; /* GVP, confidence level, sensors' locations, sensor signals */
Output: $\tilde{x}, \tilde{y}, \tilde{\sigma}$; /* Impact location and TDOA variance with maximum likelihood */
Output: $\bar{x}, \bar{y}, r_\alpha$; /* Posterior mean impact location and confidence radius */
Step 1: TDOA extraction from impact sensor signals:
$\Delta\mathbf{t} \leftarrow \boldsymbol{s}_j$; /* TDOA extraction */
Step 2: MLE of impact location and TDOA variance:
$d_j, \theta_j \leftarrow x, y, x_j, y_j$; /* Impact-to-sensor distances and directions */
$e_j \leftarrow (\frac{d_j}{v_g(\theta_j)} - \frac{d_1}{v_g(\theta_1)}) - \Delta t_{1j}$; /* TDOA residual */
$\sigma^2 \leftarrow \frac{1}{N_s - 1}\sum_{j=2}^{N_s} e_j^2$; /* TDOA variance */
$\frac{\partial e_j}{\partial x}, \frac{\partial e_j}{\partial y} \leftarrow x, y, d_j, \theta_j, v_g(\theta_j)$; /* Derivatives of TDOA residual to impact location */
$\frac{\partial \sigma^2}{\partial x}, \frac{\partial \sigma^2}{\partial y} \leftarrow \frac{\partial e_j}{\partial x}, \frac{\partial e_j}{\partial y}, e_j$; /* Derivatives of TDOA variance to impact location */
$x_0, y_0 \leftarrow \Delta t_{1j}$; /* Initial impact location */
$\tilde{x}, \tilde{y}, \tilde{\sigma}^2 \leftarrow x_0, y_0, \sigma^2, \frac{\partial \sigma^2}{\partial x}, \frac{\partial e_j}{\partial y}$; /* MLE of impact location */
Step 3: Localisation mean and confidence radius estimations by MCMC:
$\mathcal{L}_{xy}, \mathcal{P}_{xy} \leftarrow \tilde{\sigma}^2$; /* Likelihood and prior based on identified TDOA variance */
$X, Y \leftarrow \mathcal{L}_{xy}, \mathcal{P}_{xy}, \tilde{x}, \tilde{y}, \max[v_g(\theta)]^2\tilde{\sigma}^2 I$; /* MCMC samples */
$\bar{x}, \bar{y}, r_\alpha \leftarrow \alpha, X, Y$; /* Estimations of posterior mean impact location and confidence radius */

Bayesian inference again, the posterior impact location x, y, given the observed data (TDOAs and GVPs at different frequencies $\Delta t^i, v_g^i, i \in \mathbb{N}_{1N_f}$), is expressed as:

$$P(x, y, \sigma|\Delta\mathbf{t}^i, v_g^i, i \in \mathbb{N}_{1N_f}) = \frac{P(\Delta\mathbf{t}^i, v_g^i, i \in \mathbb{N}_{1N_f}|x, y, \sigma)P(x, y, \sigma)}{P(\Delta\mathbf{t}^i, v_g^i, i \in \mathbb{N}_{1N_f})}. \tag{5.24}$$

However, the likelihood $P(\Delta\mathbf{t}^i, v_g^i, i \in \mathbb{N}_{1N_f}|x, y, \sigma)$ is intractable due to the unknown explicit correlations between TDOAs and GVPs at each frequency, even though they are highly correlated. In contrast, the likelihood at a single frequency, $P(\Delta\mathbf{t}, v_g|x, y, \sigma)$ is explicitly known, allowing for posterior estimation of the impact location at a single frequency (as shown in Section 5.4.1).

When the likelihood is intractable, arithmetic averaging provides a straightforward approach by estimating the multi-frequency impact location as the average of the uni-frequency estimations. Provided that the posterior mean and 95% localisation radius of the i-th frequency are denoted as $(\bar{x}^i, \bar{y}^i, r_\alpha^i)$, arithmetic averaging merges these uni-frequency estimates into a multi-frequency estimate $(\bar{x}, \bar{y}, r_\alpha)$ as:

$$(\bar{x}, \bar{y}, r_\alpha) = \frac{1}{N_f}\sum_{i=1}^{N_f}(\bar{x}^i, \bar{y}^i, r_\alpha^i). \tag{5.25}$$

This method assumes perfect correlation (a value of 1) between GVPs at different frequencies, which is physically plausible, as GVPs are strongly correlated by the dispersion relations.

Although simple and intuitive, arithmetic averaging is highly sensitive to outliers. Outliers in probabilistic impact localisation may arise from inaccurate GVP estimation and imprecise TDOA extraction from the sensor signals. Based on analysis of three GVP estimation methods, inaccurate TDOA extraction from the sensor signals is the main source of the localisation outlier. The detection and elimination of TDOA outliers at the TDOA extraction stage are illustrated in Section 5.6.1. This procedure significantly decreases the possibility of the presence of uni-frequency impact localisation outlier. Consequently, arithmetic averaging is employed to integrate these uni-frequency impact localisation estimates, where the corresponding TDOAs are not outliers, into a multi-frequency estimation. As the frequency whose TDOA is an outlier is not included in impact localisation, computational costs are reduced as well.

5.5 Experimental Validation

To validate the proposed probabilistic impact localisation framework and assess its generalisability across different structural configurations, impact experiments were conducted on three types of composite panels: a flat panel (FP), a mono-stringer stiffened panel (SP), and a Sandwich Panel (SWP) comprising laminated face sheets and an aluminium honeycomb core. The FP and SP were previously introduced and experimentally validated in Chapter 4, where detailed information on their geometries, layups, material systems (M21/T800s), and boundary conditions is provided (see Section 4.4 and Fig. 4.2). The same experimental configuration, including sensor types and data acquisition system, was retained in this chapter to ensure consistency and comparability.

To further examine the robustness of the proposed localisation methods, the impact testing on the SP was extended in this chapter to include a wider area beyond the sensor network coverage. Specifically, 35 impact locations were tested on the SP, as shown in Fig. 5.3(a), compared to 25 locations shown in Fig. 4.3(b) in Chapter 4. The additional impacts (Nos. 1–5 and 31–35) were placed outside the original sensor region to challenge the model's extrapolative capability. Impact points on the SP were sparsely distributed with grid spacing of approximately 40–45 mm in both directions.

In addition, a new test article—the SWP—was introduced in this chapter to evaluate performance on a more complex structure. The SWP measures 300 mm × 300 mm and consists of 2 mm-thick composite face sheets and a 10 mm-thick aluminium honeycomb core. The laminate layup and material properties of the face sheets are unknown. As shown in Fig. 5.2, the SWP was clamped along two opposite longitudinal edges, with the remaining two edges left free, following the same boundary condition used for the FP. Impact testing on the SWP included 49 impact points, uniformly distributed within the sensor coverage area with a grid spacing of approximately 22 mm.

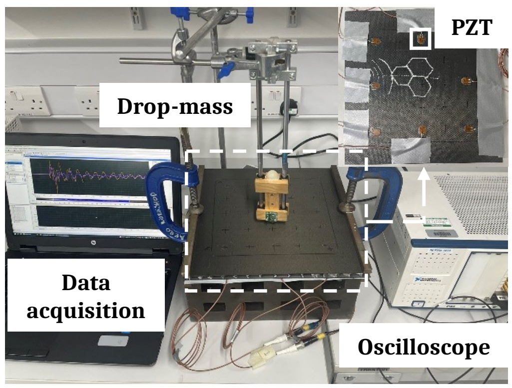

Figure 5.2: Experimental setup for impact testing for SWP with composite face sheets and an aluminium honeycomb core. The experimental setups of FP and SP are detailed in Section 4.4.

Two types of PZT sensors were used across the panels: four PIC 255 sensors were bonded to the FP using super glue, while four PIC DuraAct sensors were bonded to both the SP and SWP using Hexcel Redux 312 epoxy film adhesive. These sensors formed a rectangular sensing region in all cases and were connected to a NI PXI-5105 8-channel oscilloscope, recording signals via NI SignalExpress at a sampling rate of 200 kHz. A 20 mJ impact was generated using a drop mass from a 2 cm height.

The impact locations for the FP and SWP (see Fig. 4.3(a) and Fig. 5.3(b), respectively) were evenly distributed within the sensor region, with grid spacings of 20 mm × 20 mm (FP) and 22 mm × 22 mm (SWP). For all panels, the drop mass was applied on the opposite side of the sensors for the SP and SWP, and on the same side as the sensors for the FP. Accurate localisation across these configurations highlights the robustness of the proposed framework, irrespective of sensor placement.

The implementation of the physics-based component of the hybrid localisation methods also

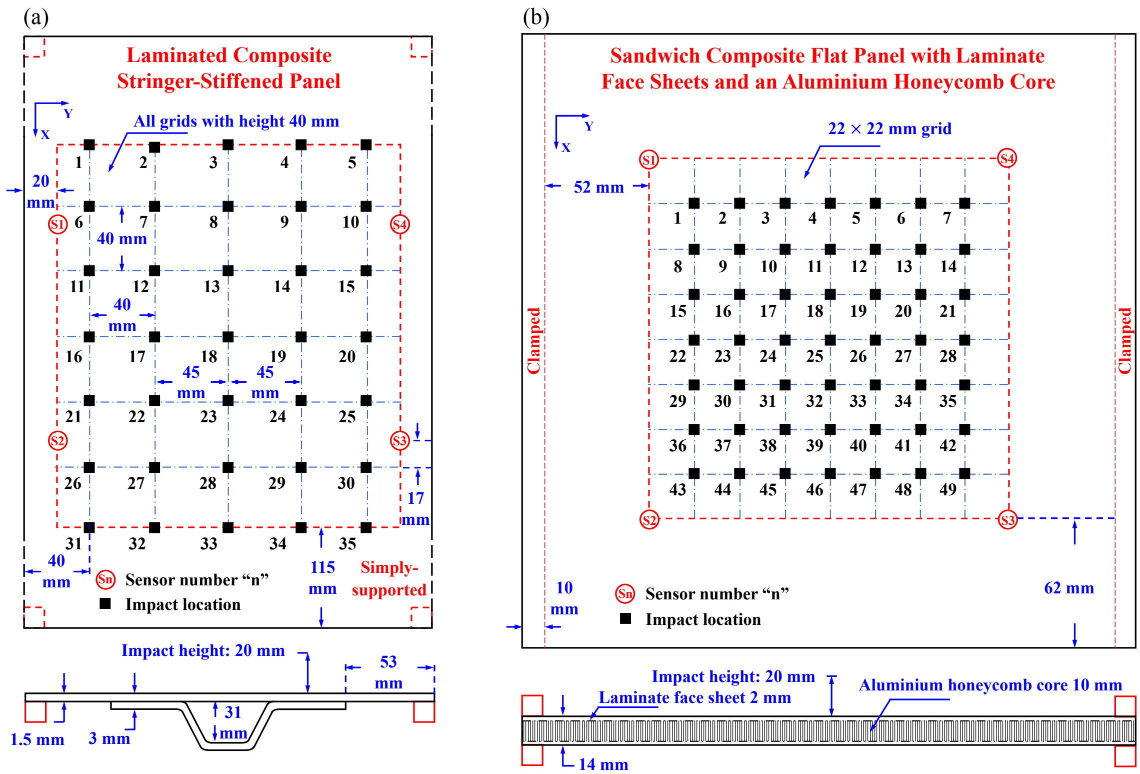

Figure 5.3: Experimental composite panel layup: (a) mono-stringer SP, (b) SWP with laminate face sheets. The layup of FP is depicted in Fig. 4.3(a).

assumes knowledge of material properties, which were available for the FP and SP (see Table 4.1) but not for the SWP. As a result, analytical computation of the GVP was only feasible for the FP and SP.

5.6 Impact Localisation Results and Analysis

This section mainly presents the impact localisation results and analysis for three experimental composite panels using the developed probabilistic framework with three GVP estimation methods (PB, DD, and HPD). For the FP, the GVP is estimated by the PB and DD methods, since analytical GVP is available using plate theories. For the SP, due to the presence of stiffener, DD and HPD are compared in estimating GVP and impact localisation. The impacts on the SWP, without knowing the structural configurations and material properties, are identified using the DD method.

5.6.1 TDOA outlier detection by multi-frequency analysis

The precision of TDOA extraction from sensor signals significantly influences the accuracy of impact localisation. In real-world scenarios where the impact location is unknown, the absence of analytical TDOA poses challenges in evaluating TDOA extraction accuracy. However, since high-frequency flexural waves propagate faster than low-frequency waves, TDOA extraction from high-frequency components yields smaller TDOA values. Leveraging multi-frequency TDOA extractions enables the detection of TDOA outliers and facilitates the evaluation of TDOA accuracy, as demonstrated in Fig. 5.4, which showcases the maximum TDOA for the 35 impacts on the flat panel across various frequencies using NSET and Continuous Wavelet Transform Threshold (CWTT) methods.

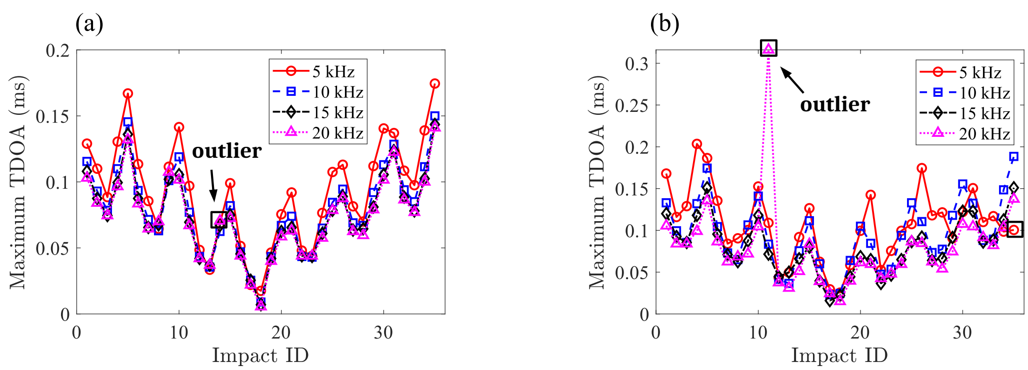

Figure 5.4: Maximum TDOA across various frequencies: (a) NSET, (b) CWTT.

It is evident that with NSET, the lowest frequency of 5 kHz corresponds to the highest maximum TDOA values for all 35 impacts. However, CWTT does not consistently demonstrate this frequency-TDOA relationship across all 35 impacts. For example, impact 11 and 35 yield the highest maximum TDOA values at the higher frequencies of 20 kHz and 15 kHz using CWTT, respectively. If CWTT is used for TDOA extraction to locate impacts, these two TDOA extractions are identified as outliers and should not be utilised. Consistent with the Spearman's Correlation (SC) and Normalised Euclidean Distance (NED) analysis based on analytical TDOA, as compared in [75], NSET exhibits a better frequency-TDOA relationship than CWTT. Therefore, NSET is employed for TDOA extraction to localise impacts in the subsequent study.

5.6.2 Frequency selection for multi-frequency impact localisation

The identification of TDOA outliers also facilitates the selection of frequencies for multi-frequency impact localisation. In the PB method, where no reference impacts are available, the frequencies used for impact localisation are solely determined by the target impact itself. In contrast, in the DD and HPD methods, the available reference impacts aid in determining the frequency candidates for impact localisation, and each target impact to be localised further refines these frequency candidates. Fig. 5.5 illustrates the maximum TDOA as the frequency increases for the three experimental composite panels. Across panels, four experimental impacts were employed as reference impacts for impact localisation using the DD and HPD methods. The reference impacts for the FP and SP are numbered 12, 14, 22, and 24, while the reference impacts for the SWP are numbered 17, 19, 31, and 33.

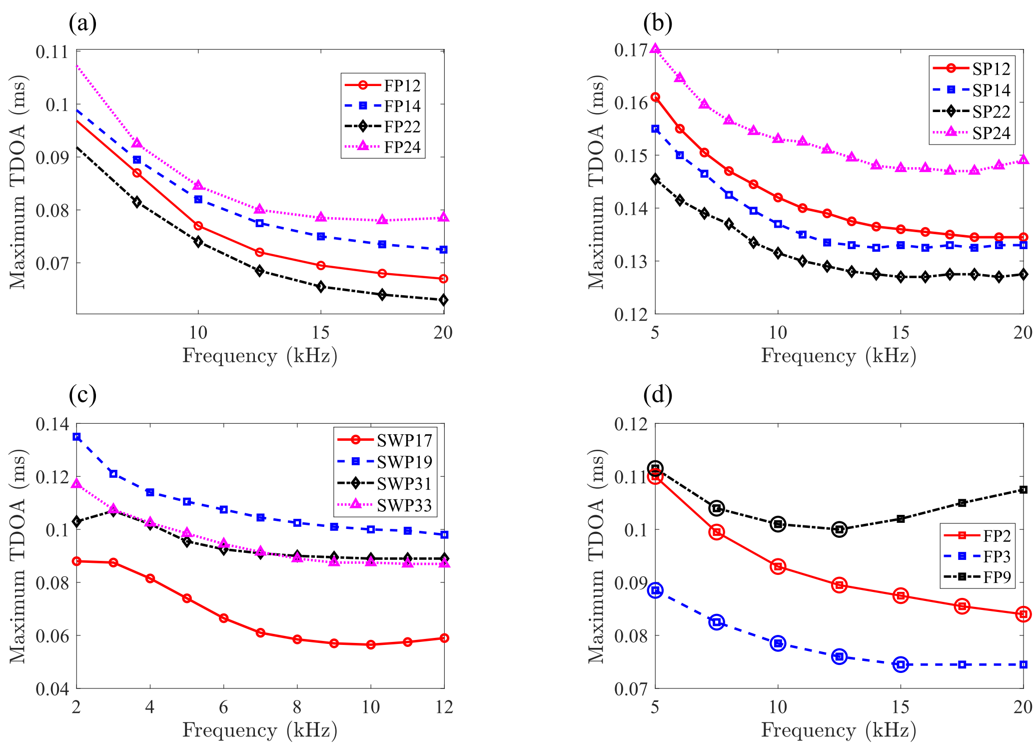

Figure 5.5: Frequency selection for multi-frequency impact localisation.

Figure 5.5(a)-(c) shows that, across the three panels, reference impacts exhibit a decreasing maximum TDOA. This observation aligns with the physical principle that higher frequencies correspond to higher velocities, resulting in smaller maximum TDOA values. However, the critical frequency at which the maximum TDOA converges to a constant value varies across panels due to their different structural configurations. To increase the robustness of impact localisation, the candidate frequencies for impact localisation are cut off at their corresponding critical frequency. Consequently, seven frequencies ranging from 5 kHz to 20 kHz with a step of 2.5 kHz were selected for the FP, eight frequencies (5:1:10, 12, 15 kHz) were chosen for the SP, and six frequencies ranging from 3 kHz to 8 kHz with a step of 1 kHz were identified for the SWP as candidate frequencies for impact localisation.

When employing DD and HPD method for impact localisation, the frequencies used for impact localisation are filtered again based on the maximum TDOA of each target impact to be localised. Figure 5.5(d) illustrates the maximum TDOA of three target impacts numbered 2, 3, and 9 on FP. The decreasing trend persists for impacts 3 and 9 only until 15 kHz and 12.5 kHz, respectively. Therefore, the frequencies for impact 3 and 9 were selected as 5 kHz to 15 kHz and 5 kHz to 12.5 kHz, respectively. These frequencies, characterised by a decreasing maximum TDOA, are chosen for probabilistic impact localisation. The localisation estimations at these individual frequencies are then combined using arithmetic averaging.

5.6.3 Physics-based (PB) impact localisation on FP

Among the three experimental panels, only the FP allows for the analytical estimation of GVP based on plate theories with known material properties.

5.6.3.1 Impact localisation using analytical GVPs obtained from CPT and FSDT

Fig. 5.6 illustrates the impact localisation on the flat panel based on the analytical GVPs calculated using both CPT and FSDT at various frequencies, where the TDOA variance is fixed as its maximum likelihood estimate. In the figures, as indicated in the right-hand legend, the red solid circles, blue solid squares, magenta solid hexagrams, and magenta hollow circles represent the sensors L_j, actual impact locations x, y, the posterior mean location estimates $\bar{x}, \bar{y}$, and the posterior 95% localisation confidence area/radius r_α, respectively. The localisation error is defined as the distance between the actual impact locations x, y and the posterior mean location estimates $\bar{x}, \bar{y}$, calculated as root sum squared error $\sqrt{(x-\bar{x})^2 + (y-\bar{y})^2}$.

The localisation results indicate that the accuracy of impact localisation using CPT decreases

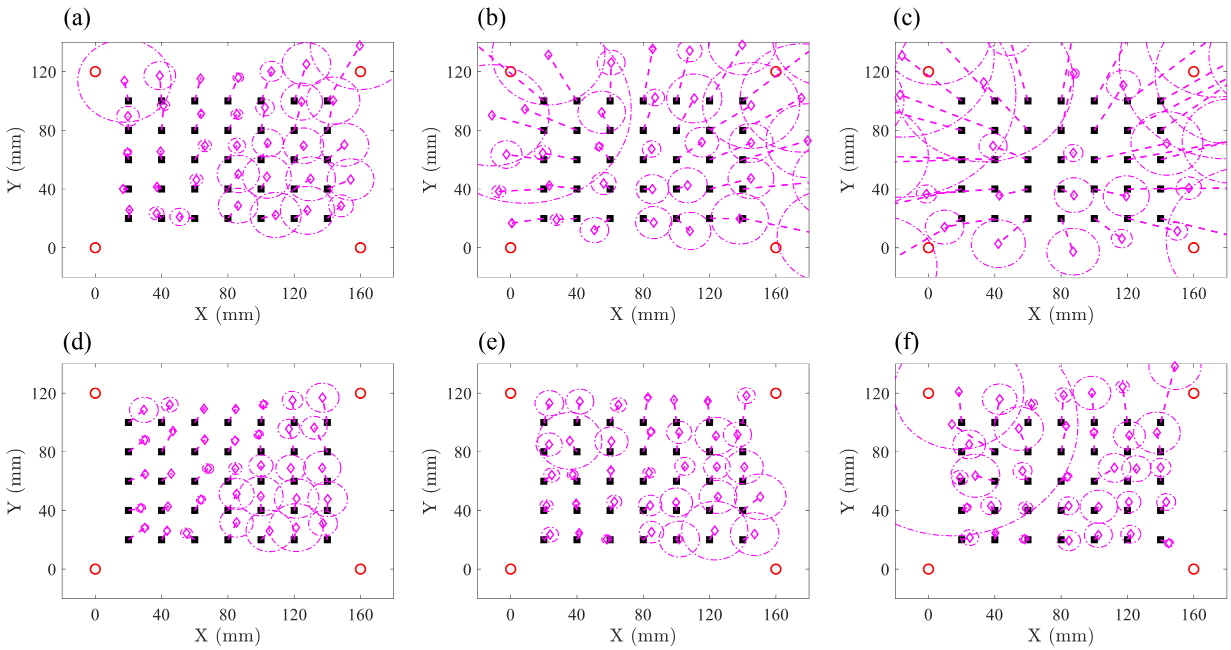

Figure 5.6: Impact localisation on the FP based on analytical GVP and MLE from: (a)-(c) CPT with frequencies 5 kHz, 10kHz and 20 kHz, (d)-(f) FSDT with frequencies 5 kHz, 10kHz and 20 kHz.

as frequency increases. This significant decline in accuracy is primarily due to the fact that the GVP becomes less reliable at higher frequencies, as noted by Abrate [87]. According to CPT, wave group velocities become unbounded as the frequency approaches infinity. Consequently, when using GVPs derived from CPT for impact localisation, it is recommended to focus on lower frequencies. Fortunately, impacts with simple force histories, such as half-sine pulses, predominantly excite structural modes at lower frequencies [76], and these low-frequency waves dominate the sensor signals. Therefore, using GVPs from CPT at lower frequencies remains effective for impact localisation.

Additionally, it can be observed that FSDT consistently provides more accurate impact localisation than CPT across various frequencies. This advantage arises from FSDT's ability to estimate a more precise and bounded GVP, particularly at higher frequencies, as demonstrated in [74]. FSDT demonstrates overwhelming advantage over CPT for GVP estimation and impact localisation for plate-like structures.

However, as the frequency increases from 10 kHz to 20 kHz, impact 9 shows a significantly larger 95% confidence radius and large localisation error (31.9 mm). This increased confidence radius is attributed to errors in TDOA estimation for this impact. As illustrated in Fig. 5.4, the maximum

TDOA for impact 9 at 20 kHz is incorrectly larger than the values at lower frequencies (15 kHz and 10 kHz). This overestimation of maximum TDOA, combined with higher wave velocities, inflates the TDOA variance and results in a larger localisation confidence radius. Therefore, it is crucial to detect and remove TDOA outliers in multi-frequency impact localisation to improve accuracy.

5.6.3.2 Comparison of three TDOA variance treatments in Bayesian inference

Section 5.4.1 outlines three possible treatments of TDOA variance in Bayesian inference: as a fixed parameter estimated by maximum likelihood (CST) [152], using Jeffrey's non-informative prior (JNI) [153], or modeled as an inverse chi-squared distribution (ICS) [147, 151]. This study employed the CST approach due to its efficiency. In Fig. 5.7, impact localisation results on the FP using JNI and ICS methods at a frequency of 10 kHz are illustrated, alongside 10000 MCMC samples for impact FP1. Compared to CST localisation shown in Fig. 5.6(e), the mean localisation accuracy remains similar across methods, but JNI and ICS exhibit larger localisation confidence radii than CST. This is further supported by the MCMC sample distributions, where JNI and ICS show increased variance in localisation predictions, primarily due to their handling of TDOA variance as a variable rather than fixing it at its MLE as in CST.

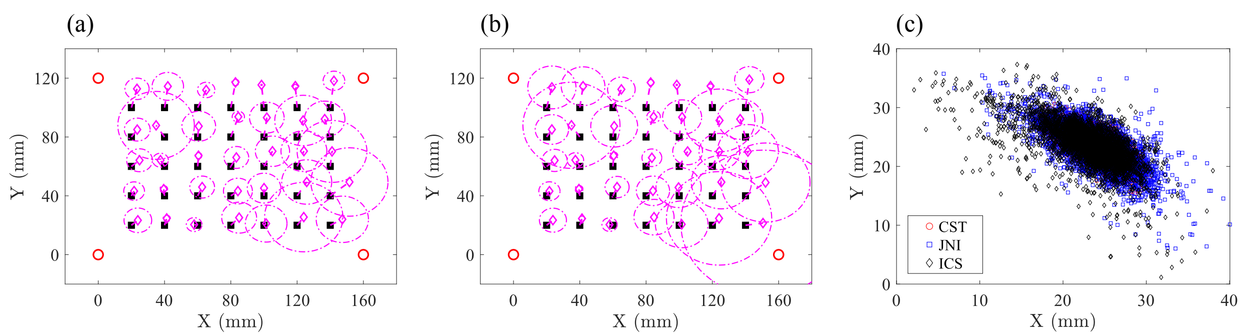

Figure 5.7: Impact localisation on the FP using JNI, ICS at frequency 10 kHz and the MCMC samples illustration for impact FP1: (a) impact localisation with JNI at frequency 10 kHz, (b) impact localisation with ICS frequency 10 kHz, (c) 10000 MCMC samples of three methods for impact FP1.

MCMC sampling convergence for the three methods was also analysed. Fig. 5.8 illustrates the localisation error of the posterior mean, the SD of the posterior distribution, and the distance between location estimates derived from the posterior mean and MLE (by gradient-based optimisation) for impact FP11, all measured with increasing MCMC sample sizes. In the CST method, the localisation error and SD converge steadily at a sample size of 1000, displaying minimal variation as the sample size increases. By contrast, the ICS and JNI methods show significant variability in localisation SD, requiring larger sample sizes to ensure convergence. At a sample size of 10000, both ICS and JNI methods converge, with the distance between the posterior mean and MLE estimates remaining under 0.5 mm. Using MCMC to estimate the posterior distribution (posterior mean and variance) of impact location yields reliable results, while gradient-based optimization for MLE of TDOA variance and impact location efficiently provides initial spatial information on the impact.

Although all three methods deliver accurate localisation, with the posterior mean closely matching the actual impact location and the true impact point falling within the 95% confidence radius for most impacts, this study selected the CST approach due to its rapid convergence and the availability of an accurate MLE estimate of impact location without requiring MCMC. A sample size of 10000 was chosen to balance convergence reliability with computational efficiency, costing approximately 5 seconds for all three TDOA variance treatments.

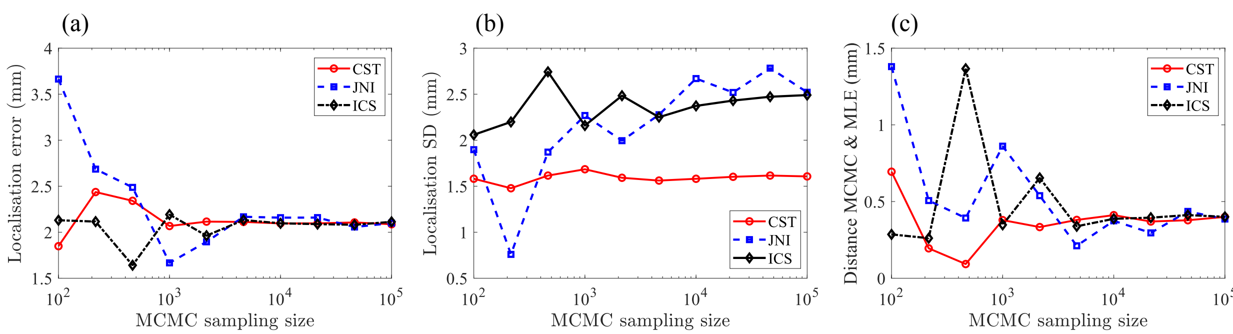

Figure 5.8: MCMC convergence: (a) localisation error of the posterior mean, (b) SD of the posterior distribution, and (c) distance between posterior mean and MLE for impact FP11.

5.6.3.3 Multi-frequency impact localisation on FP with analytical GVPs

As identified in Section 5.6.2, a total of 7 frequencies ranging from 5 kHz to 20 kHz with increments of 2.5 kHz are considered for impact localisation. For each impact on the flat panel, a multi-frequency analysis of the maximum TDOA is conducted to identify and remove frequency outliers from the impact localisation process. Figure 5.9 provides a comparison of multi-frequency impact localisation with and without the removal of frequency outliers. The mean localisation errors across these 35 impacts are nearly identical, at approximately 10 mm for both cases. However, the removal of frequency outliers results in a smaller mean confidence radius of 6.9 mm, compared to 7.7 mm without removing frequency outliers. The reason behind this lies in the 95% confidence radius of impact 9. For impact 9, removing the frequency outliers at 15 kHz, 17.5 kHz, and 20 kHz leads to a reduction in the confidence radius from 34.4 mm to 18.3 mm. This reduced confidence radius encompasses the actual impact location, indicating a robust estimation. The multi-frequency impact localisation with the removal of frequency outliers demonstrates to be accurate and robust.

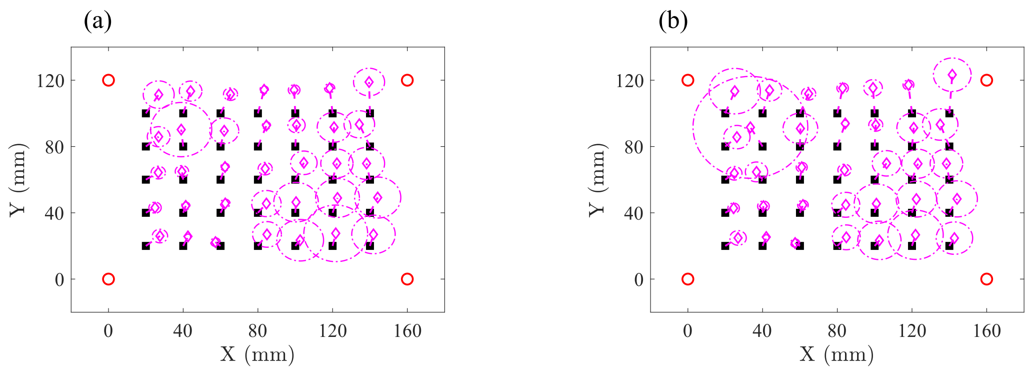

Figure 5.9: Multi-frequency impact localisation on the flat panel with analytical GVP: (a) removal of frequency outliers, (b) without removing frequency outliers.

5.6.4 Data-driven (DD) impact localisation on FP

In data-driven impact localisation, the GVP is probabilistically estimated solely based on reference impact data. Bounding the GVP velocity coefficients is crucial as it determines the optimisation space for MLE of GVP. The size of reference impacts significantly influences both the bounding of velocity coefficients and the likelihood to be maximised. In the following subsections, the effects of reference impact size on the bounding of the GVP velocity coefficients and estimation of the GVP are investigated. Additionally, impact localisation based on GVPs estimated in a data-driven approach are conducted.

5.6.4.1 Bounding GVP velocity coefficients

A total of 9 impacts, numbered [12, 14, 24, 22, 13, 19, 23, 17, 18], located within a small rectangular area, as illustrated in Fig. 5.3, are considered as reference impacts. The TDOA extracted by the NSET method is utilised to calculate the equivalent velocity defined in Eq. (5.13). Its minimum and maximum values serve as the velocity bounds. Fig. 5.10 presents the lower (LB) and upper (UB) bounds of equivalent velocity with increasing reference impact size and varying frequencies for TDOA extraction.

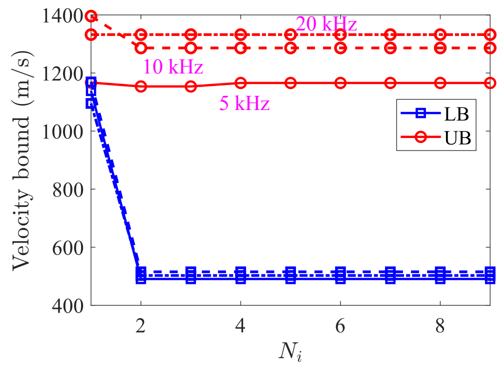

Figure 5.10: Equivalent velocity bounds estimated with increasing reference impact size and varying frequencies for TDOA extraction.

It is observed that involving only 1 reference impact is insufficient to accurately identify the velocity bounds. The velocity bounds converge when the reference impact size is increased to 2. Further increasing the reference impact size does not alter the identified velocity bounds. This information suggests that a minimum of 2 reference impacts is required in the developed data-driven GVP estimation method.

Additionally, analysing the bounds across TDOA extraction frequencies, it is found that a higher frequency for TDOA extraction corresponds to a higher upper bound of the velocity, while the lower bounds are close. This finding is consistent with the dispersion of flexural waves, where higher-frequency waves have higher propagation velocities. Based on the identified lower and upper bounds of equivalent velocity, the bounds for the GVP velocity coefficients **c** can be directly estimated using Eq. (5.15) and Eq. (5.17).

5.6.4.2 GVP estimations by data-driven method with HGA

The GVP with maximised likelihood is identified by maximising the log-likelihood within the bounds of the velocity coefficients. This optimisation task is addressed using a HGA with gradient-based local search, as outlined in Section 5.3.2.3. To incorporate additional randomness through GA's crossover, mutation, and selection processes, the optimisation is iterated 10 times to identify the global optimum. Leveraging gradient information, this HGA demonstrates approximately four times greater computational efficiency than the conventional GA. On a PC with an Intel i7-10700 CPU, it takes on 4.42 seconds to identify the GVP with maximised likelihood using the HGA, compared to 15.59 seconds using the conventional GA. Fig. 5.11 provides a comparison of the identified TDOA SD σ between the HGA and conventional GA when maximising the log-likelihood (minimising the TDOA variance) with increasing the reference impact size. The TDOA of reference impacts is estimated using the NSET method from impact sensor signals at frequencies of 5 kHz and 10 kHz, respectively. The evidence indicates that both the HGA and conventional GA identified nearly identical GVPs with maximised likelihood for both frequencies. Additionally, as higher frequencies correspond to smaller TDOA values, the 10 kHz frequency exhibits a smaller TDOA SD.

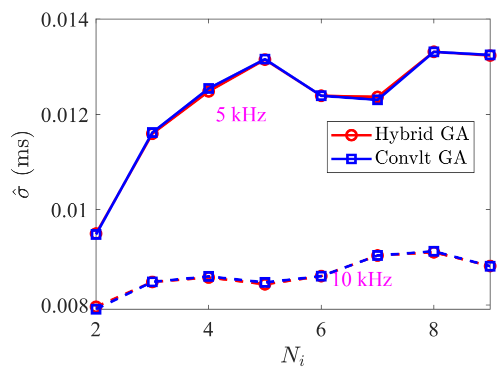

Figure 5.11: Comparison of identified TDOA SD between the HGA and conventional GA.

Fig. 5.12 illustrates the identified GVPs with maximised likelihood across various reference impact sizes, compared with the analytical GVP calculated using known material properties and FSDT. As depicted in Fig. 5.6, the analytical GVPs from FSDT at frequencies of 5 kHz and 10 kHz demonstrate high localisation accuracy and reliability (small confidence radius), serving as reference GVPs. Variations in the GVPs are observed across different reference impact sizes, but they exhibit the same shape. With an increase in the number of reference impacts, the GVP aligns more closely with the analytical GVP. Enhancing the size of the reference impacts improves the reliability of the estimated GVP. It is noted that with a minimum of 2 reference impacts, a significantly accurate GVP can be identified. This smaller number indicates a significant saving in the collection of reference impact data.

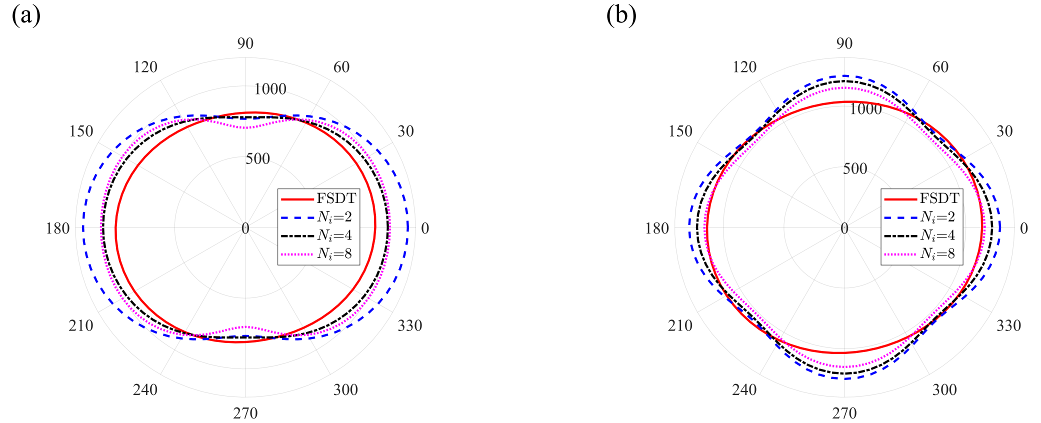

Figure 5.12: Identified GVP with maximised likelihood of the FP based on various reference impact sizes at frequency: (a) 5 kHz, (b) 10 kHz.

5.6.4.3 Data-driven impact localisation based on GVPs with maximised likelihood

The TDOAs of reference impacts can be extracted from sensor signals for any selected frequency, and the corresponding GVP with maximised likelihood at this frequency can be estimated accordingly for impact localisation. Seven frequencies are considered in this study, ranging from 5 kHz to 20 kHz with increments of 2.5 kHz. Fig. 5.13 illustrates the data-driven impact localisation of the flat panel using four reference impacts and TDOAs extracted at single frequencies of 5 kHz and 10 kHz, as well as at multiple frequencies. In the impact localisation illustration shown in Fig. 5.13, the blue hollow circles represent the reference impacts, denoted by x^i, y^i in the figure legend.

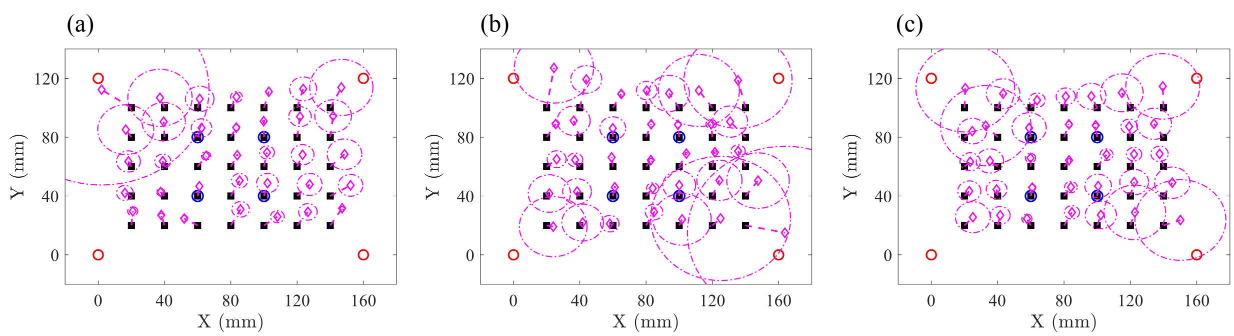

Figure 5.13: Data-driven impact localisation of the FP using 4 reference impacts and TDOAs extracted at (a) uni-frequency 5 kHz, (b) uni-frequency 10 kHz, (c) multi-frequency 5:2.5:20 kHz, respectively.

It is observed that with only four reference impacts, the localisation of impacts on the flat panel based on estimated GVPs, including those outside the coverage area of reference impacts, is quite accurate across single and multiple frequencies. Benefitting from averaging after the removal of frequency outliers, the multi-frequency impact localisation features a smaller confidence radius covering the actual impact location compared to that of uni-frequency methods. This indicates that multi-frequency impact localisation demonstrates higher robustness than uni-frequency methods.

To compare PB impact localisation with DD impact localisation, Table 5.2 presents a comparison of multi-frequency impact localisation results for the FP using the PB and DD methods. The mean and maximum multi-frequency DD localisation errors are 8.9 mm and 16.0 mm, respectively, slightly more accurate than the multi-frequency PB localisation. This enhanced accuracy results from the inclusion of reference impact data, which improves the precision of the estimated GVPs. However, larger variations in the estimated GVPs at different frequencies, as shown in Fig. 5.12, contribute to greater mean and maximum localisation confidence radius in DD localisation. With only 4 reference impacts, the estimation of GVPs at different frequencies can be relatively accurate, leading to precise impact localisation based on these estimated GVPs, even for the impacts occurring outside the reference coverage area. For real-world flat plate structures, depending on the availability of structural material properties, both PB and DD are efficient GVP estimation methods leading to accurate impact localisation.

Table 5.2: Multi-frequency impact localisation results of the FP using GVPs obtained by the PB and DD methods.

Method	Mean error (mm)	Max error (mm)	Mean CR (mm)	Max CR (mm)
PB	9.7	18.6	6.9	18.3
DD	8.9	16.0	9.1	29.7

5.6.5 Impact localisation on SP: DD vs HPD

For complex stiffened composite panel, calculating the analytical GVP using PB method based on plate theories and known lamina properties is not feasible. Instead, estimating the GVP requires FEA to acquire the simulated impact responses at predetermined 'sensorised' points around an impact point. This simulated impact can be regarded as the reference impacts for estimating the GVP by the DD and HPD method. Therefore, this subsection mainly presents the MLE of GVPs and impact localisation by DD and HPD methods for the experimental SP. In the HPD method, the reference GVPs are derived from analytical GVPs estimated by CPT, assuming the SP is flat but with the same size and laminate layup.

5.6.5.1 GVP estimations of SP: DD vs HPD

Figure 5.14(a) illustrates the minimised TDOA SD for the MLE of GVP by both DD and HPD methods across the selected frequencies. It is evident that DD identified smaller TDOA SDs than the HPD method due to the utilisation of global optimisation using HGA. However, the increasing and decreasing trends for both DD and HPD methods remain consistent. Increasing the frequency from 5 kHz to 9 kHz decreases the TDOA SD, indicating good TDOA consistency at these frequencies. However, further increases in frequency do not guarantee a decrease in TDOA SD, as seen at frequencies 10 kHz and 15 kHz. This suggests that at these two frequencies, the TDOA values exhibit greater variability.

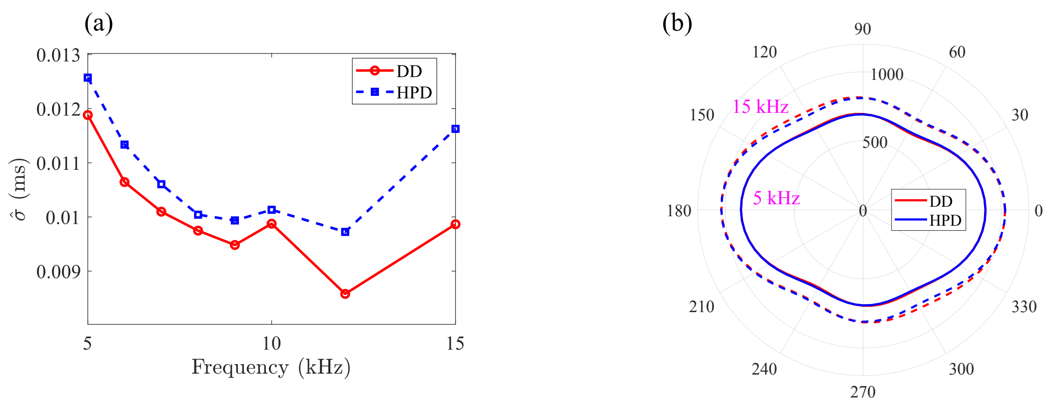

Figure 5.14: TDOA variance identification and GVP optimisation: (a) minimised TDOA SD by the DD and HPD methods of the SP based on 4 reference impacts, (b) identified GVPs with maximised likelihood of the SP by the DD and HPD methods based on 4 reference impacts at frequencies 5 kHz and 15 kHz.

The slight differences in the TDOA SD between the DD and HPD methods are consistent with minor disparities in their corresponding GVPs with maximised likelihood. Figure 5.14(b) depicts the identified GVPs with maximised likelihood by both the DD and HPD methods based on 4 reference impacts at frequencies 5 kHz and 15 kHz. The GVPs identified by both methods are nearly identical. Even for the frequency 15 kHz, which corresponds to the greatest difference in TDOA SD, the maximum difference in GVP is only 18 m/s. It's worth noting that the HPD method, which exclusively employs gradient-based optimization, demonstrates higher computational efficiency compared to the DD method.

5.6.5.2 Impact localisation with identified GVPs: DD vs HPD

Fig. 5.15 illustrates the multi-frequency localisation of 35 impacts on the stiffened panel using 4 reference impacts with both the DD and HPD methods. The confidence radius, represented by the magenta dashed circles in the figures, is scaled by a factor of 0.5 for clarity. Since the DD and HPD methods yield nearly identical GVPs, these impacts are localised at nearly the same locations with almost identical confidence radii between the two methods. Table 5.3 summarises the mean and maximum localisation errors and confidence radii. It is evident that both the DD and HPD methods demonstrate similar accuracy, with mean and maximum localisation error of approximately 15 mm and 50 mm for all 35 impacts, respectively. The mean and maximum confidence radii for all 35 impacts are approximately 43 mm and 110 mm, respectively.

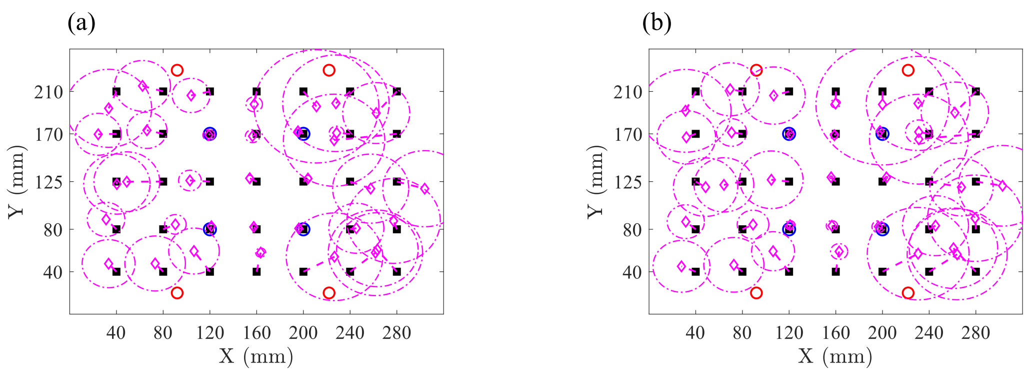

Figure 5.15: Multi-frequency impact localisation of the SP based on 4 reference impacts using: (a) DD, (b) HPD.

Additionally, these 35 impacts can be divided into two groups: 15 impacts numbered 11-25 inside the sensor network, and 20 impacts numbered 1-10, 26-35 outside the sensor network. The impact localisation for impacts inside the sensor network demonstrates higher accuracy and reliability compared to impacts outside the sensor network. As shown in Table 5.3, the DD method localises impacts inside the sensor network with mean and maximum errors of 11.8 mm and 30.1 mm, respectively, compared to higher values of 18.3 mm and 54.1 mm for impacts outside the sensor network. This is primarily because the four reference impacts belong to the impact group inside the sensor network, and the identified GVPs with maximised likelihood exhibit higher generality for impacts closer to the reference impacts.

Table 5.3: Multi-frequency impact localisation results of the SP using the DD and HPD methods.

Localisation Method	Mean error (mm)	Max error (mm)	Mean CR (mm)	Max CR (mm)
DD/HPD (ALL)	15.3/14.5	54.1/49.1	42.2/44.8	106.8/114.1
DD/HPD (IN)	11.8/10.7	30.1/35.0	23.8/27.6	106.8/114.1
DD/HPD (OUT)	18.3/17.3	54.1/49.1	55.9/57.7	91.1/88.8

*ALL: all impacts, IN: impacts inside the sensor network, OUT: impacts outside the sensor network.

5.6.6 Data-driven (DD) impact localisation on SWP

Due to the unknown material properties, the DD method was employed for impact localisation on the sandwich composite panel. Four impacts numbered 17, 19, 31, 33 were utilised for the GVP MLE and probabilistic impact localisation.

5.6.6.1 GVP estimations of SWP by DD method

Fig. 5.16 depicts the MLE of GVPs by the DD method based on 4 reference impacts at frequencies of 3 kHz, 5 kHz, and 8 kHz. As anticipated, higher frequencies correspond to GVPs with larger amplitudes. Furthermore, the GVPs at different frequencies exhibit slight variations in shape, underscoring the importance of including multiple frequencies for impact localisation to enhance reliability and robustness.

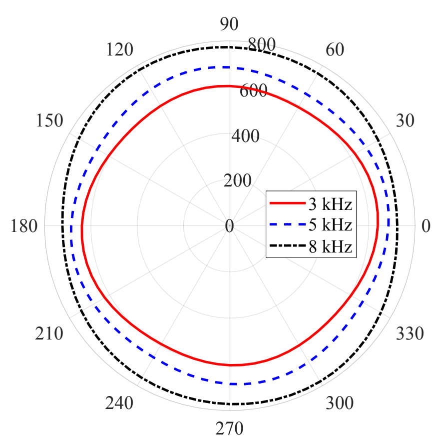

Figure 5.16: Identified GVPs with maximised likelihood of the SWP by the DD method based on 4 reference impacts at frequencies 3 kHz, 5 kHz and 8 kHz.

5.6.6.2 Impact localisation with maximised likelihood GVPs

Fig. 5.17 illustrates the data-driven impact localisation of the SWP using 4 reference impacts at single frequencies of 3 kHz and 8 kHz, as well as multi-frequency localisation spanning from 3 kHz to 8 kHz. Their corresponding mean and maximum localisation errors and confidence radii are summarised in Table 5.4. It is evident that at 3 kHz frequency, the impact localisation achieved higher accuracy and reliability (smaller confidence radii) than at 8 kHz. The multi-frequency impact localisation averages these impact estimates across frequencies that are not outliers, resulting in more intermediate results. Specifically, the multi-frequency impact localisation achieved a very high level of accuracy, with mean and maximum localisation errors of 6.7 mm and 16.9 mm, respectively. Although impacts numbered 1:7:43 exhibited larger confidence radii than the remaining impacts, they were still accurately localised. This indicates that the larger TDOA uncertainties (larger TDOA variance) of these impacts do not degrade the accurate impact localisation (posterior mean) due to the randomness of the TDOA uncertainties.

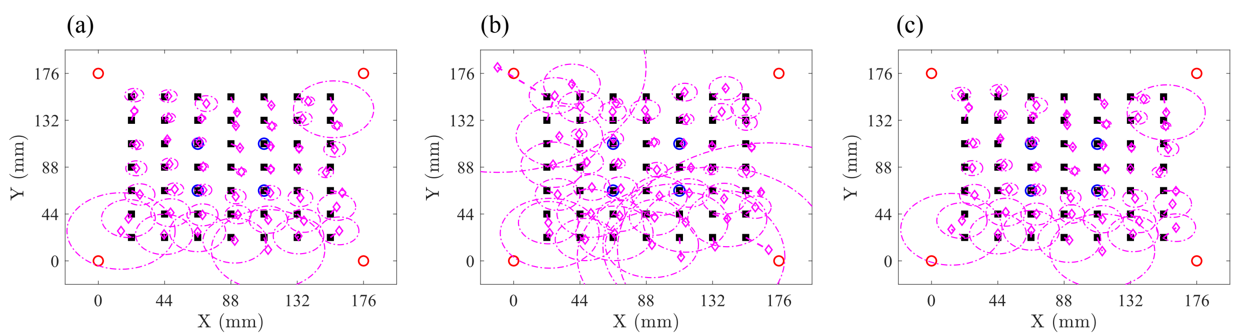

Figure 5.17: Data-driven impact localisation of the SWP using 4 reference impacts at (a) uni-frequency 3 kHz, (b) uni-frequency 8 kHz, (c) multi-frequency 3:1:8 kHz, respectively.

Table 5.4: Impact localisation results of the SWP by the developed DD method: uni-frequency vs. multi-frequency.

Localisation Method	Mean error (mm)	Max error (mm)	Mean CR (mm)	Max CR (mm)
DD (3 kHz)	5.8	15.0	8.3	34.8
DD (8 kHz)	8.6	42.8	16.9	76.5
DD (MF)	6.7	16.9	10.0	48.4

5.6.7 Probabilistic impact localisation: results analysis

The experimental results across three composite structures—a FP, a SP, and a SWP—demonstrate the robustness and flexibility of the proposed probabilistic impact localisation framework. When using the DD approach with only four reference impacts, accurate localisation was achieved across all panels. In particular, for the FP and SWP, where the flexural wavefronts are less disrupted by geometric features, the mean localisation error remained below 10 mm, with a maximum error under 20 mm. This performance validates the effectiveness of the proposed GVP parameterisation in capturing multi-directional wave propagation even with sparse training data and sensors.

The SP, containing a central stringer, presented a more challenging case due to structural discontinuities that distort the wavefronts. Consequently, localisation errors increased—approximately doubling compared to the FP and SWP. Nonetheless, a mean error below 16 mm was still achieved, despite more than half of the impacts being located outside the sensor network. This result reflects the framework's robustness to both geometric complexity and extrapolation beyond the sensing region.

A major innovation of this study lies in its efficient use of reference data. Unlike many existing data-driven methods—which require dense impact training data across the entire surface and are sensitive to sensor placement—the proposed DD method learns the GVP using only a few reference impacts (≤ 4) and a minimal sensor configuration (≤ 4). Once estimated, the GVP serves as a structure-independent, sensor-agnostic parameter that enables localisation to be reused across identical structures with different sensor layouts, eliminating the need for retraining.

Scalability is further enhanced by the HPD approach, which leverages known GVPs from simpler substructures to estimate those of more complex assemblies. This hierarchical inference improves generalisability and minimises data requirements, supporting practical deployment on complex structures with limited prior knowledge.

Computational efficiency was also a key consideration. As shown in the posterior analyses (e.g., Fig. 5.8), the MLE of the impact location aligns closely with the posterior mean derived from MCMC sampling. This enables the use of MLE alone for fast, resource-efficient localisation while still quantifying uncertainty using the estimated GVP and TDOA noise. Such a feature is well-suited for real-time SHM where computational resources are limited.

In summary, the proposed probabilistic impact localisation framework demonstrates a promising combination of accuracy, efficiency, and scalability, supported by a principled integration of physical modelling and sparse data-driven inference.

5.7 Summary

This chapter introduced a general probabilistic framework for impact localisation in composite structures, grounded in the physics of flexural wave propagation and implemented via Bayesian inference. Central to this framework is the estimation of the GVP, which encapsulates the multi-directional wave propagation characteristics necessary for TDOA-based localisation.

To accommodate various levels of structural complexity and available information, three GVP estimation strategies were developed:

- The PB method derives GVP analytically and is suited to simple, flat laminated plates with known material properties.
- The DD method infers GVP from sparse reference impact data and requires minimal prior knowledge, enabling application to more complex geometries.
- The HPD approach transfers learned GVPs from simpler substructures to more complex assemblies, reducing experimental effort while improving generalisability.

These methods feed into a unified Bayesian localisation scheme that enables both impact position estimation and uncertainty quantification. The posterior distribution can be computed using MCMC sampling, or efficiently approximated via MLE with closed-form uncertainty bounds—an option that is particularly suitable for real-time SHM applications.

Experimental validation on three distinct composite structures—a FP, a SP, and a SWP—demonstrated the framework's robustness, accuracy, and scalability. Notably, accurate localisation was achieved even under sparse sensor layouts and limited reference impacts, outperforming traditional data-driven methods that require extensive training data.

The key innovations of this study include:

- Structure-independent GVP parameterisation enabling generalisation across sensor configurations.
- Sparse data-driven impact localisation reducing reliance on training data.
- Scalable hybrid inference applicable to structurally complex assemblies.
- Efficient localisation with uncertainty quantification via MLE-based estimation.

Despite these strengths, several limitations remain. The current GVP parameterisation assumes spatially smooth wavefront propagation, which may not hold in structures exhibiting severe wave scattering, complex boundaries, joints, or delaminations. Additionally, the framework's robustness under environmental variability—such as temperature and humidity fluctuations—and its extension to curved or highly heterogeneous structures require further investigation. The accuracy of TDOA measurements may also degrade in the presence of high ambient noise or uneven sensor placement.

In conclusion, this chapter presents a physically consistent, scalable, and efficient framework for probabilistic impact localisation in composite structures. While the experimental results are promising, further validation under realistic operational conditions and extension to broader structural classes are essential before deployment in industrial SHM systems.

Chapter 6

Adaptive Wavelet-regularised Impact Force Deconvolution

Highlights:

- Establish a robust theoretical basis for impact force reconstruction by reviewing deconvolution principles and regularisation techniques from a physics-based perspective.
- Develop an adaptive wavelet-based regularisation method that ensures stable and efficient deconvolution under variable signal conditions through multi-resolution analysis.
- Validate the proposed framework experimentally under realistic structural scenarios involving large deformations.

6.1 Introduction

Building on the impact localisation methods presented in earlier chapters, a key challenge lies in reconstructing the impact force, which is closely linked to impact-induced damage. The deconvolution method, a physics-based approach to impact force reconstruction, exploits the convolution relationship between sensor signals and the input impact force within Linear Time-Invariant (LTI) structural systems [91]. In such systems, sensor signals are generated by convolving the system's transfer function with the input impact force history. Since the transfer function is intrinsic to the structural system and remains independent of external impact events, it can be determined experimentally or through simulation. Once identified, the impact force history of a given impact can be reconstructed by deconvolving the corresponding sensor signals.

Studies on deconvolution methods have been widespread, particularly across various fields such as wireless communications [155, 156], image processing [157, 158], and geophysics [159–161]. Depending on whether prior information about the source and transfer function is available, deconvolution methods can be classified into blind deconvolution and non-blind deconvolution. Impact force deconvolution falls under the category of non-blind deconvolution, as the impact force is known to be compactly supported, and the transfer function is the superposition of impulse responses from damped single-degree-of-freedom (SDOF) systems at different damped frequencies [60].

Typically, impact force deconvolution methods can be implemented in the frequency domain [22, 123, 124], time domain [162–175], and wavelet domain [176, 177]. While frequency-domain deconvolution yields deconvoluted forces with broader spectral components without filtering out high-frequency noises, wavelet-domain deconvolution is more time-consuming in projecting quantities into wavelet-domain, the time-domain deconvolution combined with regularisation techniques tends to offer superior accuracy and robustness. In time-domain deconvolution, the impact force identification process is formulated as a Least Squares (LS) optimisation problem, with the objective function being the discrepancy between the predicted responses (through the transfer function) and the sensor-measured responses. However, solving this LS problems often poses challenges due to the ill-posed nature of inverse problems [178]. Extensive research has therefore been devoted to developing time-domain regularisation techniques to mitigate the ill-posedness of inverse problems, including:

- Tikhonov regularisation [162–165]. Tikhonov regularisation, also known as L2 regularisation, is a widely adopted technique that penalises the L2-norm of the solution to the LS optimisation problem. The regularisation parameter, denoted as λ_{reg}, plays a crucial role in controlling the magnitude of this penalty. By carefully selecting an appropriate value for λ_{reg}, a delicate balance can be achieved between the residuals and the L2-norm of the solution. Various criteria have been proposed to guide the selection of the regularisation parameter, with the L-curve (LC) criterion and the Generalized Cross Validation criterion being recognised as reliable and accurate methods [163, 164]. These criteria assist in determining the optimal regularisation parameter, leading to a well-regularised and smooth solution.

- Sparse regularisation [166–169]. Given that the impact force history is typically non-zero within a small impact window, the solution obtained by the LS method for impact force identification tends to exhibit sparsity. This inherent sparsity has driven the development of sparse regularisation techniques. Among these techniques, L1 regularisation is widely employed and has been shown to achieve a sparse solution with comparable accuracy to Tikhonov regularisation [167]. More recently, Lp ($0 < p < 1$) regularisation techniques and their corresponding solving algorithms have been developed. Like L2-regularised LS, the L1-regularised LS is still a convex optimisation problem with only one minimum, which can be solved by several classical optimisation algorithms [167]. However, Lp regularised ($0 < p < 1$) LS has more than one minimum and finding the global minimum is shown to be NP-hard [179]. Nevertheless, the necessity of estimating a sparse solution in the whole sampling window is worth discussing, as in many cases the impact window covering the whole positive force impact duration can be directly identified from the sensor signals.

- Bayesian regularisation [170–172]. Bayesian regularisation assumes that the impact force to be a random vector following Gaussian distribution. Although Bayesian regularisation is often more complex than Tikhonov and sparse regularisation techniques, it offers the advantage of not only identifying the forces but also providing statistical information about them. Furthermore, unlike Tikhonov regularisation, Bayesian regularisation avoids the explicit determination of the regularisation parameter. However, Bayesian regularisation necessitates the knowledge of prior distribution of the impact force (regarding the unknown impact excitation before measuring the impact responses), which typically poses difficulties in quantification and measurement due to impacts originating from various sources.

- Wavelet regularisation [173–175]. Wavelet regularisation represents the impact force using multi-resolution wavelet bases and applies regularisation by selecting and filtering these bases. By reducing the dimension of the LS optimisation problem from the number of sampling points to the number of wavelet bases, wavelet regularisation reduces the complexity and computational cost in impact force identification. As a result, the wavelet regularisation technique has gained attention in recent years. For example, Tran et al. [173, 174] employed Haar wavelets to represent the impact force and achieved regularisation by filtering the wavelet bases using the LC criteria. This wavelet regularisation technique was verified through experiments and simulations, demonstrating good accuracy and robustness to noise. However, the finest scale of the wavelets was determined based on the sampling frequency, which introduced extra effects to filter high-frequency noise components. Additionally, the process of filtering the wavelet bases using the LC criterion could be time-consuming since it was achieved by trial and error.

In summary, time-domain deconvolution methods enhance the accuracy and robustness of impact force identification. However, the inherently ill-posed nature of the LS problem necessitates regularisation techniques. Moreover, the large number of predictors (features) in the LS problem, equivalent to the length of the deconvolved signal (observations), imposes significant computational costs, especially for signals sampled at high frequencies and with long sampling windows. Given that typically impact force has compact support (impact contact duration is finite), wavelet regularisation, leveraging compactly-supported wavelets, holds promise for reducing LS problem features and associated computational expenses. Nonetheless, the wavelet scale selection and wavelet filtering present challenges.

To address these aforementioned shortcomings, this study proposes an adaptive wavelet-regularised time-domain deconvolution method. This adaptive approach comprises two key components: the adaptive determination of the impact window and downsampling of sensor signals through dominant frequency analysis, and the adaptive selection of appropriate wavelet bases (scales) for representing the impact force via multi-resolution analysis of the sensor signals. Subsequently, the impact force in the LS problem undergoes regularisation by filtering out insignificant wavelet bases based on their energy contributions to the sensor signal representation. The process of impact window determination and signal downsampling significantly reduces the length of signals to be deconvoluted, thereby enhancing the computational efficiency of force deconvolution. Moreover, the adaptive determination of wavelet bases and the filtering process further improves computational efficiency by reducing the predictors in the LS problem to the number of remaining wavelet bases, eliminating the need for trial-and-error selection of regularisation parameters.

6.2 Time-domain Impact Force Deconvolution and Regularisation Techniques

For an LTI impact system with a fixed sensor and a given impact location, the convolution relationship among the structural response $s(t)$, transfer function $h(t)$, and exciting force $f(t)$, as defined in Eq. (2.9), can be reformulated as:

$$s\left(t\right) = f(t) \circ h(t) = \int_0^t h\left(t-\tau\right) f\left(\tau\right) d\tau. \tag{6.1}$$

In practice, the integrations of continuous functions involved in the convolution need to be discretised into a set of discrete linear equations:

$$\begin{bmatrix} s_{\Delta t} \\ s_{2\Delta t} \\ \vdots \\ s_{n\Delta t} \end{bmatrix} = \begin{bmatrix} h_{\Delta t} & 0 & \cdots & 0 \\ h_{2\Delta t} & h_{\Delta t} & \ddots & 0 \\ \vdots & \ddots & \ddots & 0 \\ h_{n\Delta t} & h_{(n-1)\Delta t} & \cdots & h_{\Delta t} \end{bmatrix} \begin{bmatrix} f_{\Delta t} \\ f_{2\Delta t} \\ \vdots \\ f_{n\Delta t} \end{bmatrix} \Delta t, \tag{6.2}$$

where Δt denotes the time interval for discretisation, n represents the sampling length. After discretisation, the convolution problem can be represented in a matrix-vector form:

$$\mathbf{s} = \mathbf{H}\mathbf{f}, \tag{6.3}$$

where $\mathbf{s} \in R^{n\times 1}$ is the vector of structural responses, $\mathbf{f} \in R^{n\times 1}$ is the vector of the exciting force, and the transfer matrix $\mathbf{H} \in R^{n\times n}$ is a lower triangular matrix.

The identification of impact forces involves solving an inverse problem, which aims to acquire the impact force given the structural responses. Based on the discretised forward problem, the impact force can be identified by solving a LS optimisation problem:

$$\bar{\mathbf{f}} = \arg\min_{\mathbf{f}} \|\mathbf{Hf} - \mathbf{s}\|_2^2, \tag{6.4}$$

6.2.1 Tikhonov (L2) regularisation

However, solving such an inverse problem is often challenging due to its ill-posed nature. To mitigate the ill-posedness of inverse problems, regularisation techniques such as Tikhonov regularisation, sparse regularisation, Bayesian regularisation, wavelet regularisation have been developed. The most widely-used Tikhonov regularisation, also know as L2 regularisation, penalises the LS problem with the L2-norm of the solution:

$$\bar{\mathbf{f}} = \arg\min_{\mathbf{f}} \|\mathbf{Hf} - \mathbf{s}\|_2^2 + \lambda_{reg}\|\mathbf{f}\|_2^2, \tag{6.5}$$

where the regularisation parameter λ_{reg} controls the magnitude of this penalty. Larger λ_{reg} results in more smooth solution. Fixing λ_{reg}, the Tikhonov regularisation is equivalent to double the observations (data points) as:

$$\begin{bmatrix} \mathbf{s} \\ \mathbf{0} \end{bmatrix} = \begin{bmatrix} \mathbf{H} \\ \lambda_{\mathbf{reg}}\mathbf{I} \end{bmatrix} \mathbf{f}, \tag{6.6}$$

where $\mathbf{I}$, and $\mathbf{0}$ represent the identity matrix, the zero vector of size n. This transformation highlights the importance of the number of observations (data points) in LS problem. An overdetermined LS helps reduce overfitting and improve robustness to outliers. This Tikhonov regularised LS problem has an explicit pseudo solution:

$$\bar{\mathbf{f}} = (\mathbf{H}^{\mathbf{T}}\mathbf{H} + \lambda_{reg}\mathbf{I})^{-\mathbf{1}}\mathbf{H}^{\mathbf{T}}\mathbf{s}. \tag{6.7}$$

6.2.2 Sparse regularisation

Instead of regularising the LS problem with L2-norm of the solution, Lp regularisation ($0 < p \leq 1$) which penalizes with Lp-norm of the solution results in a sparse solution. Consequently, this Lp regularisation with sparse solution is also known as sparse regularisation.

$$\bar{\mathbf{f}} = \arg\min_{\mathbf{f}} \|\mathbf{H}\mathbf{f} - \mathbf{s}\|_2^2 + \lambda_{reg}\|\mathbf{f}\|_p^2. \tag{6.8}$$

6.2.3 Wavelet regularisation

By representing the impact force as a linear combination of basis functions, the dimension of the LS problem can be dramatically decreased. This inspires the wavelet regularisation in which the wavelets are employed as basis functions. Assume the basis matrix $\mathbf{B} \in R^{n\times m}$, $m \leq n$ composed of m wavelet bases, the impact force can be expressed in the matrix-vector form:

$$\mathbf{f} = \mathbf{B}\boldsymbol{\alpha}, \tag{6.9}$$

where $\boldsymbol{\alpha} \in R^{m\times 1}$ is the coefficient vector of wavelet bases. Therefore, the reconstruction of impact force $\mathbf{f}$ turns out to be the estimation the coefficient vector α by solving another low-dimension LS problem. This low-dimension LS problem can be expressed as:

$$\bar{\boldsymbol{\alpha}} = \arg\min_{\boldsymbol{\alpha}} \|\mathbf{W}\boldsymbol{\alpha} - \mathbf{s}\|_2^2, \tag{6.10}$$

where $\mathbf{W} = \mathbf{HB} \in R^{n\times m}$ is the new matrix for the low-dimension wavelet-regularised LS problem.

6.3 Multi-resolution Analysis of Impact Force

The wavelet regularisation is of particular interest in this study, wherein the impact force is represented by the multi-resolution wavelet basis functions. According to discrete wavelet analysis [118], the multi-resolution representation of impact force can be given by:

$$f(t) = \sum_{j=j_0}^{J} \sum_{k=k_0}^{K_j} d_{j,k}\psi_{j,k}(t) + \sum_{k=k_0}^{K_J} c_{J,k}\phi_{J,k}(t), \tag{6.11}$$

where the wavelet function $\psi_{j,k}(t)$, scaling function $\phi_{J,k}(t)$ are worked as representation basis functions. To achieve the multi-resolution characteristics, scaling parameter $j(j_0 \leq j \leq J)$ and shifting parameter $k(k_0 \leq k \leq K_j)$ are integers to scale and shift the wavelet basis functions:

$$\psi_{j,k}(t) = 2^{-j/2}\psi(2^{-j}t - k),\ \phi_{j,k}(t) = 2^{-j/2}\phi(2^{-j}t - k). \tag{6.12}$$

Due to the orthogonality of wavelet basis functions (orthogonal Daubechies wavelet is adopted in this study), the wavelet coefficient $d_{j,k}$, $c_{J,k}$ can be approximately given by the integrals:

$$d_{j,k} = \int f(t)\psi_{j,k}(t)dt,\ c_{J,k} = \int f(t)\phi_{J,k}(t)dt. \tag{6.13}$$

By discretising the impact force and wavelet basis functions in impact window at sampling frequency, the matrix-vector form ($\mathbf{f} = \mathbf{B}\boldsymbol{\alpha}$) of multi-resolution representation is obtained, in which basis matrix $\mathbf{B}$ is given by:

$$\mathbf{B} = \begin{bmatrix} \phi_{J,k}(\Delta t) & \psi_{J,k}(\Delta t) & \psi_{J-1,k}(\Delta t) & \cdots & \psi_{j_0,k}(\Delta t) \\ \phi_{J,k}(2\Delta t) & \psi_{J,k}(2\Delta t) & \psi_{J-1,k}(2\Delta t) & \ddots & \psi_{j_0,k}(2\Delta t) \\ \vdots & \vdots & \vdots & \ddots & \vdots \\ \phi_{J,k}(n\Delta t) & \psi_{J,k}(n\Delta t) & \psi_{J-1,k}(n\Delta t) & \cdots & \psi_{j_0,k}(n\Delta t) \end{bmatrix}. \tag{6.14}$$

And the coefficient vector of wavelet bases is given by:

$$\boldsymbol{\alpha} = \begin{bmatrix} c_{J,k} & d_{J,k} & d_{J-1,k} & \cdots & d_{j_0,k} \end{bmatrix}^\top. \tag{6.15}$$

To apply the multi-resolution analysis in practical applications, it is crucial to determine the appropriate wavelet scales and the shifts for each scale. The shift parameter k can be easily determined for each scale j by the sampling window. Specifically, the shifting parameter k_0 represents the largest k that shifts wavelet $\psi_{j,k}(t)$ to the left of the sampling window, while K_j represents the smallest k that shifts wavelet $\psi_{j,k}(t)$ to the right of the sampling window.

However, determining suitable scales for the multi-resolution representation of impact force presents a significant challenge due to the unknown nature of the impact force in practical scenarios. Previous studies [173,174] have addressed this issue by selecting the finest scale, which corresponds to the highest resolution, based on the sampling frequency. Unfortunately, this approach leads to an overfitting representation of the impact force, as it introduces unnecessary high-frequency components. Additionally, the regularisation of the solution which uses the LC criteria to filter the wavelet bases requires trial and error, making it a time-consuming process.

6.4 Adaptive Wavelet-regularised Impact Force Deconvolution

Passive sensors are commonly used to measure the local response of a structure subjected to an impact. These sensors record data over a specified sampling time window $[0, T_{win}]$ at a designated sampling frequency f_s. It is essential that the length of the time window to covers the entire duration of the impact contact. This ensures that the complete impact force history can be accurately identified from the sensor signals. In addition, according to the Nyquist sampling theorem, the sampling frequency should be at least twice the highest frequency present in the signal to prevent aliasing.

In practical applications, the sampling time window is often set to be long, and the sampling frequency is set to be high to capture sufficient target information in the signals. However, it should be noted that the impact typically occurs within a relatively small portion of the sampling window. Reconstructing the impact force over the entire sampling window is inefficient and unnecessary. Additionally, a higher sampling frequency will result in a larger sample size for a given sampling time window. If the main frequency components of the signals are much smaller than the sampling frequency, downsampling the signals can help reduce the sample size without losing essential information.

It is well-established that the complexity of the impact force deconvolution problem is influenced by both the sample size (length) of the impact signals and the efficiency of the adopted deconvolution algorithm. For example, when the sample size of the signals is n, solving the time-domain force deconvolution LS problem using methods such as LSQR [180] or singular value decomposition [178] has time complexities of $O(n^2)$ and $O(n^3)$, respectively. Therefore, reducing the complexity of the force deconvolution process can be achieved from the aspects of minimising the sample size of the impact signals used for deconvolution and improving the efficiency of the deconvolution algorithm.

This study aims to improve the efficiency of reconstructing the impact force by addressing these two factors: reducing the sample size of deconvoluted signals through adaptively determining an appropriate impact window and downsampling signals, and improving the computational efficiency of solving the force deconvolution LS problem by proposing an Adaptive Wavelet Regularisation (AWT) technique. The proposed AWT method for impact force deconvolution is depicted in Fig. 6.1, which comprises two main components: the adaptive impact window determination and

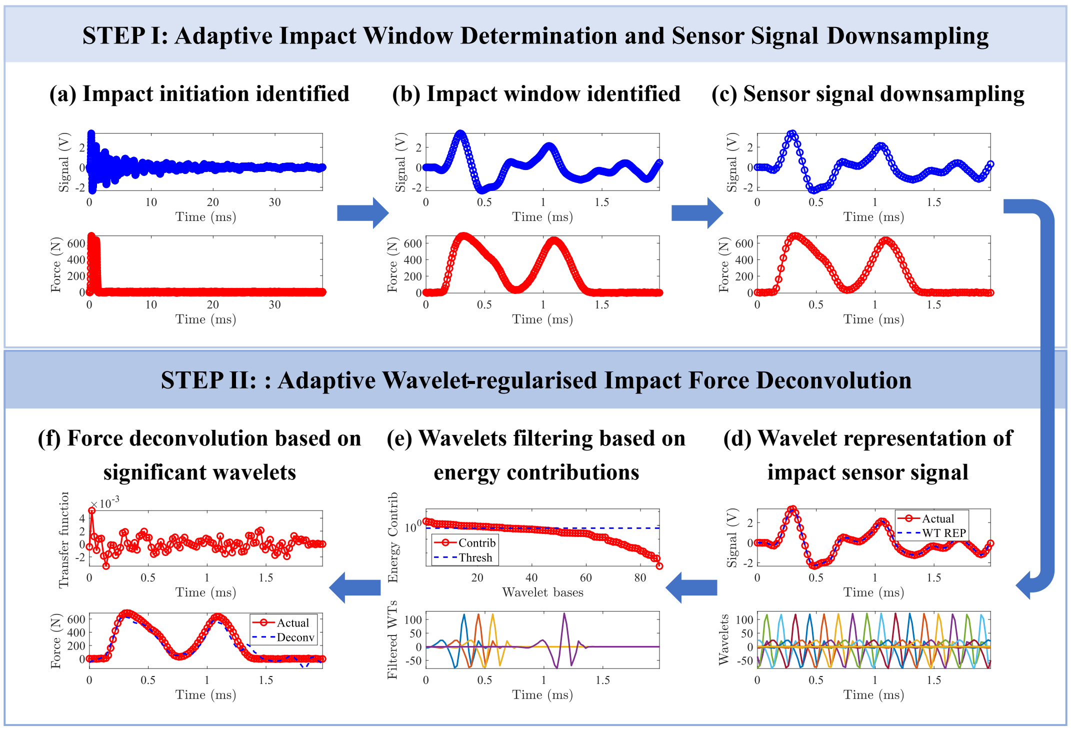

Figure 6.1: Adaptive wavelet-regularised impact force deconvolution method.

signal downsampling method, and the adaptive wavelet-regularised impact force deconvolution method. The first component aims to accurately identify the impact window and downsample the sensor signals to reduce the sample size of the deconvoluted signal based dominant frequency analysis. This reduction in the sample size of the deconvoluted signal is critical to improving the computational efficiency of the impact force deconvolution.

In the second component, the multi-resolution analysis of sensor signals based on wavelets is implemented. Since the frequency components of the impact force and sensor signals are highly correlated, this multi-resolution analysis reveals the appropriate wavelet scales and wavelet bases to represent the impact force. In addition, the energy contributions of the wavelet bases to the sensor signal representation indicate the relative importance of the wavelet bases to the impact force representation. By representing the impact force with filtered significant wavelet bases, the force deconvolution LS problem is naturally regularised with wavelets. This solution of this wavelet-regularised force deconvolution LS problem has a low computational cost, as it reduces the dimension from the signal's sample size to the number of filtered wavelets.

6.4.1 Adaptive impact window determination and signal downsampling

Determining an impact window and downsampling sensor signals enhance computational efficiency by reducing the sample size for impact force deconvolution. This process integrates two key techniques: TDOA extraction and dominant frequency analysis using the wavelet transform (WT). TDOA extraction identifies the precise moment of impact, while dominant frequency analysis provides insights into contact duration and the significant frequency range.

The WT, based on a compactly supported wavelet, offers excellent time-frequency localisation, making it well-suited for analysing transient impact signals. The dominant frequency identified by the WT, as the most significant frequency component within the sensor signals' compact wavelet support, closely corresponds to the dominant frequency of the compactly supported impact force due to their convolution relationship, as expressed in Eq. (6.1).

The implementation of this impact windowing and signal downsampling approach is illustrated in the first three steps of Fig. 6.1, with detailed procedures outlined as follows:

1. Identify an impact event when the sensor signals surpass a threshold.
2. Determine the initiation of the impact event by TOA extraction.
3. Identify the dominant frequency f_d of impact signals using WT. The suitable impact window t_{win} can then be extracted as β_{win}/f_d, where β_{win} represents the impact windowing ratio. A value of 1.2 is used to provide a margin and ensure an adequate impact window covering actual impact duration.
4. Downsample the signals within the impact window if the dominant frequency f_d is 400 times smaller than the sampling frequency f_s. The downsampling ratio is set as $\gamma_{ds} = \left\lfloor \frac{f_s}{200 f_d} \right\rfloor$ to

ensure the downsampling frequency $f_r = f_s/\gamma_{ds}$ larger than $200 f_d$, where $\lfloor\rfloor$ represents the floor function.

To ensure that critical information is preserved in the downsampled signals, an empirical parameter of 200 is used. According to the Nyquist sampling theorem, this ensures that frequency components up to 100 times the dominant frequency remain accurately represented. The spectral characteristics of a half-sine impulse, as shown in Eq. (2.10) and Fig. 2.2, demonstrate a significant decay in spectral amplitude as frequency increases. By setting the downsampling frequency at 200 times the dominant frequency, a substantial safety margin is maintained, ensuring that essential spectral content is retained for accurate impact force reconstruction.

It is noted that when the sampling frequency is not greater than 400 times the dominant frequency, the downsampling procedure is not implemented. In this case, the length of the sensor signals in the determined impact window is of the order of several hundred:

$$n = t_{win} f_s = \frac{1.2}{f_d} f_s \leq 400 \frac{1.2}{f_d} f_d = 480, \tag{6.16}$$

which allows for fast force deconvolution. When the downsampling condition is satisfied, the downsampling is implemented by identifying an upper downsampling ratio γ_{ds} (an integer), ensuring that the resampled frequency exceeds 200 times the dominant frequency. Therefore, the remaining lengths of the sensor signals after downsampling in the determined impact window are slightly greater than 240.

By using this proposed adaptive impact window determination and signal downsampling method, the force deconvolution is conducted on the downsampled signals within the proper impact window identified. The size of the LS force deconvolution problem is dramatically reduced, resulting in greatly improved computational efficiency.

6.4.2 Adaptive wavelet-regularised impact force representation

Utilising the downsampled impact sensor signals, AWT technique is employed to assist in deconvolving the impact force. However, determining the appropriate wavelet scales and filtering the wavelets pose challenges. To address this, the study proposes an adaptive approach for determining wavelet scales through multi-resolution representation of the sensor signals and filtering of the wavelets based on their energy contributions. This involves incrementally increasing the wavelet scale to determine the finest scale corresponding to minimal representation error. The filtering of the wavelets is achieved by evaluating the energy contribution of various wavelet bases within this representation and subsequently filtering out wavelets with insignificant contributions. The implementation procedures are detailed as follows:

1. Utilise Daubechies wavelet at order 4 (db4) to represent the impact sensor signal by incrementally increasing the wavelet scale. Initially, set the scale as 3, with a central frequency of 5.7144 Hz. Determine the finest scale once the representation relative error reaches its minimum as the increase of the scale.

2. Calculate the relative energy contributions (ranging from 0 to 1) of the wavelet bases in representing the sensor signal using their wavelet coefficients.

3. Energy threshold filtering: eliminate the insignificant wavelet bases whose relative energy contributions are less than a threshold value. A small threshold value of 1e-5 was chosen to ensure that trivial wavelets are filtered out.

4. Wavelet size filtering: if the number of remaining wavelets is still greater than half of the sample size, continue to eliminate the insignificant wavelet bases in ascending order of their energy contributions until the number of remaining significant wavelets is half of the sample size.

5. Utilise the filtered wavelet bases to represent the impact force and solve the low-dimensional over-determined LS problem (Eq. (6.10)) to reconstruct the impact forces.

The low-dimensional LS problem, depicted in Eq. (6.10), is typically over-determined, as the number of filtered wavelets is less than or equal to half of the sample size. Considering that the over-determined LS helps reduce overfitting, the LSQR algorithm [180] is adopted for the rapid solution of Eq. (6.10) to reconstruct the impact force without applying explicit regularisation such as L1/L2 regularisation.

It is noteworthy that the initial wavelet scale is set to 3, with a central frequency of 5.7144 Hz, which is significantly smaller than the dominant frequency observed in most practical impact scenarios. This choice enables the inclusion of more high-frequency wavelet bases as the wavelet scale increases, thereby enhancing the representation ability (complexity) of the wavelet space. Typically, as the wavelet scale increases, the representation error of the sensor signal decreases. When the representation error begins to increase, it indicates a significant occurrence of overfitting. This scale-increasing procedure allows for determining the appropriate wavelet scale for the representation of both the impact sensor signals and the impact force history. Additionally, due to the nested properties of the subspace formed by the wavelet bases when increasing the scales, the multi-resolution representation of the sensor signal remains insensitive to the initial scale. The initial scale is simply required, with a central frequency much smaller than that of the dominant frequency of the sensor signals.

The impact force errors analysed in this work is the relative squared error (RSE) ε_{rse}, which are defined as:

$$\varepsilon_{rse} = \frac{\left\|\bar{\mathbf{f}} - \mathbf{f}\right\|_2^2}{\left\|\mathbf{f}\right\|_2^2}. \tag{6.17}$$

The $\bar{\mathbf{f}}$ with a bar denotes the estimated force, $\mathbf{f}$ represents the actual force. The relative squared error ε_{rse} indicates the overall accuracy of the predicted force history in the time-domain.

6.5 Experimental Validation

The proposed adaptive impact force deconvolution method was experimentally validated using the same fibre-reinforced composite flat plate (FP) and sensor configuration introduced in Chapter 3–Chapter 5. Details on the plate geometry, material system (M21/T800s), and sensor placement can be found in Section 4.4 and Table 4.1. The test setup, involving both drop tower and hammer impacts, is shown in Fig. 3.2.

Four surface-mounted PZT sensors (PIC 255) were connected to an 8-channel oscilloscope via 100-fold attenuators. Signals were sampled at 200 kHz over a 100 ms window, producing 20,000 data points per sensor. The impact location was fixed at point D (Fig. 3.3), with the plate securely clamped to maintain consistent boundary conditions.

Three types of impacts were conducted to evaluate the method under varied force and contact characteristics:

- **HAS:** Steel-headed hammer impacts (small-mass, short-duration) to estimate transfer functions between input forces and sensor responses.
- **DT:** Drop tower impacts (large-mass, long-duration) to test force reconstruction using the estimated transfer functions.
- **HAR:** Rubber-headed hammer impacts to assess the effect of contact duration and material on adaptive impact window determination.

The impact characteristics for each case are summarised in Table 6.1. The DT case involved a 5.5 kg mass dropped to generate a nominal energy of 5 J, resulting in a peak force of 1842.6 N and contact duration of 13.4 ms. The HAS impacts, conducted with a 160 g steel hammer, exhibited peak forces around 200 N with contact durations near 1 ms. The HAR impact, using the same hammer mass but with a rubber head, produced a lower peak force (76.4 N) and a longer contact time (5.4 ms).

Table 6.1: Impact cases conducted for validating impact force deconvolution using handheld hammer (steel and rubber heads) and drop tower machine.

Impact case	Impact machine	Mass & energy	Peak force (N)	Impact duration (ms)	Number of & impacts
HAS	Hammer (steel)	m = 160 g, e = rnd	195.2, 202.5	0.94, 1.1	2 (loc D × 2 rep)
HAR	Hammer (rubber)	m = 160 g, e = rnd	76.4	5.4	1 (loc D)
DT	Drop tower	m = 5.5 kg, e = 5 J	1842.6	13.4	1 (loc D)

*Note: m = impact mass, e = impact energy, loc = location, rnd = random, rep = repetition.

This variety of impact scenarios enabled a comprehensive evaluation of the proposed adaptive impact windowing and wavelet scale selection methods, ensuring robustness across different impact dynamics.

6.6 Impact Force Deconvolution Results and Analysis

This section begins by presenting the impact forces and sensor signals recorded during the experimental impacts. Subsequently, the effectiveness of several methods is validated using the experimental data, including adaptive impact window determination and signal downsampling, adaptive wavelet scale determination, and energy-based wavelet basis filtering for force regularisation. Additionally, the proposed adaptive wavelet-regularised time-domain deconvolution method for force reconstruction is compared with reference force deconvolution methods from the literature, with a focus on accuracy and efficiency. Furthermore, the effects of finest wavelet scale, and energy contribution threshold for wavelet filtering are investigated.

6.6.1 Sensor signals and contact forces of hammer and drop tower impacts

Fig. 6.2 presents the impact force histories and sensor signals when the composite plate subject to hammer and drop tower impacts at the same impact location D. These impacts include one steel-headed hammer impact (HAS), rubber-headed hammer impact (HAR), drop tower impact (DT). The sample size of the forces and sensor signals is $n = 20000$, corresponding to a sampling window of $T_{win} = 100$ ms with a sampling frequency of $f_s = 200$ kHz.

The impact energy of the drop tower impacts (DT) is observed to be higher compared to the small-mass hammer impacts with a steel impactor (HAS) and a rubber impactor (HAR). Consequently, the peak force and maximal signal amplitude in the DT case are significantly larger than those in the HAS and HAR cases. Additionally, the impact contact duration for DT is longer due to its larger impact mass (5.5 kg), resulting in lower dominant frequency components in the sensor signals. This finding is consistent with the observation made in [127] where it was noted that the impact response (frequency content of the impact sensor signals) is primarily determined by the impact mass (impactor/plate mass ratio). Moreover, decreasing the impactor stiffness also prolongs the impact contact duration. The rubber-headed hammer impact HAR has a longer duration than the steel-headed hammer impact HAS.

Fig. 6.2d illustrates the relationship between impact force and impact displacement for the

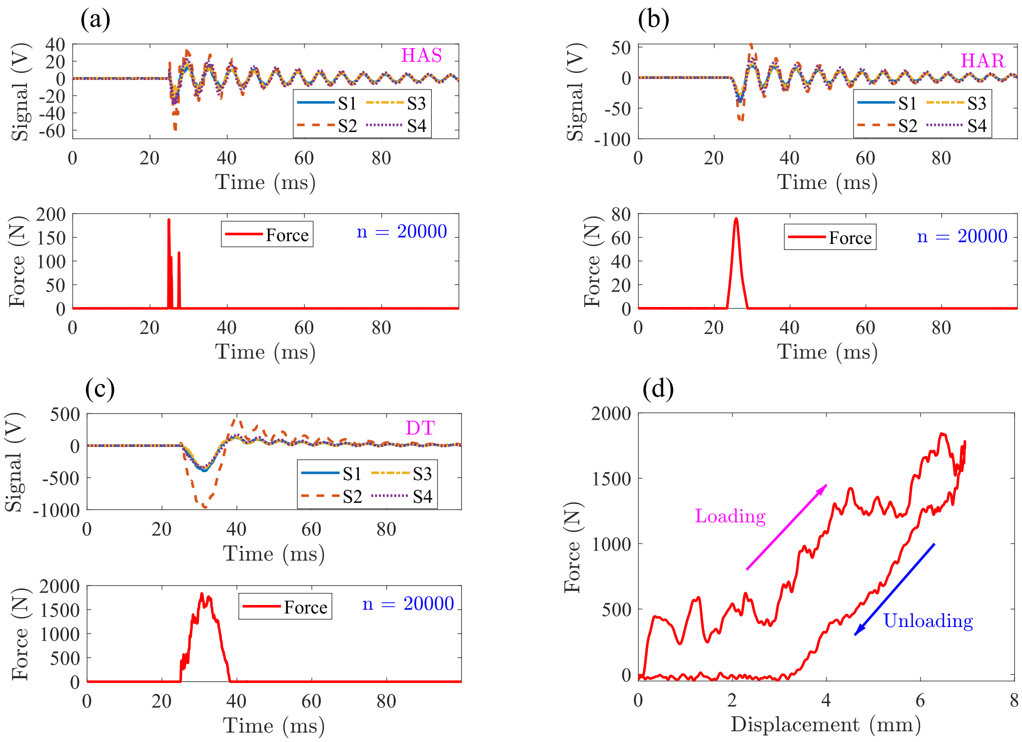

Figure 6.2: Impact force histories and sensor signals: (a) steel-headed hammer impact (HAS), (b) rubber-headed hammer impact (HAR), (c) drop tower impact (DT), (d) impact force - displacement relationship of drop tower impact (DT).

large-mass drop tower impact conducted at 5 J. It can be seen that the maximum deformation is 7 mm, with the plate thickness being 4 mm, meaning that the maximum deformation is 1.75 times the plate thickness. Previous analytical studies have demonstrated clear nonlinear effects for simple plates, even when the maximum deformation was 1.15 times the plate thickness [181]. The composite plate used in this experimental study underwent considerable deformation due to the drop tower impact. Accurately reconstructing the impact force of this large-mass drop tower impact through deconvolution methods would strongly support the effectiveness of deconvolution techniques for impact force identification, even in scenarios involving considerable structural deformation during impact events.

6.6.2 Impact window determination and signal downsampling

The impact window determination and signal downsampling method play a crucial role in capturing the full duration of the impact and reducing the sample size of the sensor signals to be deconvoluted. Fig. 6.3 illustrates the application of the impact window determination and signal downsampling method to the three impact cases conducted. By analysing the magnitude scalogram shown in Fig. 6.3d using WT, it is evident that the proposed method has successfully identified the dominant frequency f_d for each impact case. Subsequently, the appropriate impact windows t_{win} were estimated using $1.2/f_d$. Remarkably, this simple relationship accurately estimates the impact windows covering the actual impact duration for all three cases, despite variations in the impact head material (from steel to rubber) and significant increases in impact mass and energy. The manually measured impact duration from the force history for HAS, HAR and DT cases are 3.0 ms, 5.4 ms and 13.4 ms, respectively. In comparison, the impact windows determined by the proposed method are 5.9 ms, 7.8 ms and 16.7 ms for the respective cases.

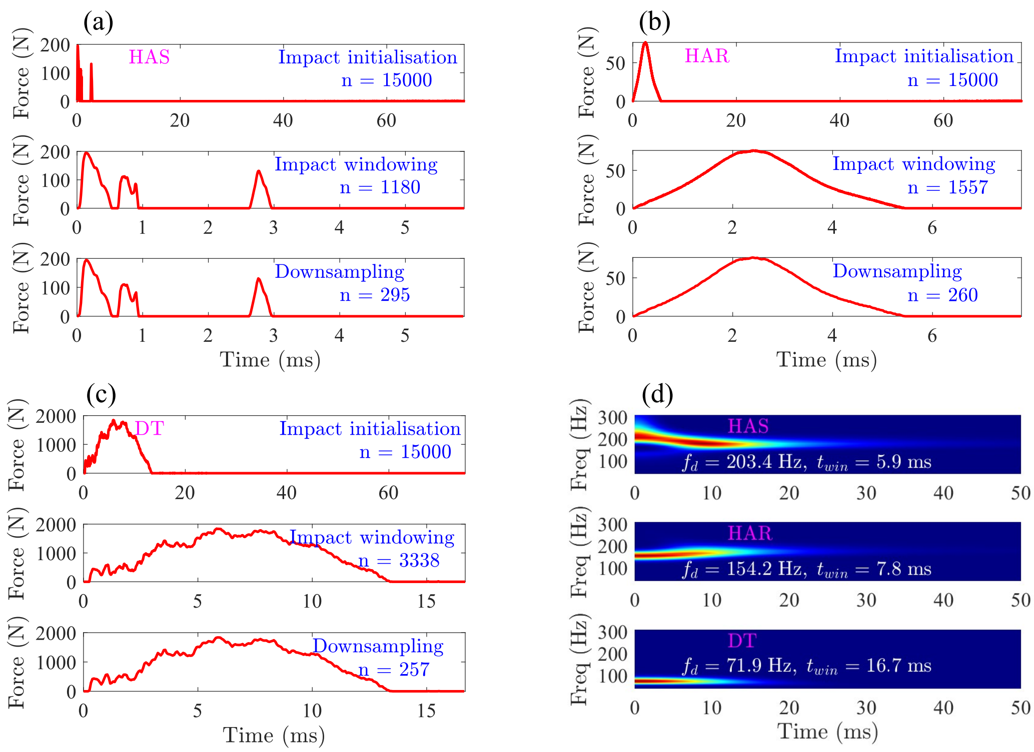

Figure 6.3: Impact window determination and signal downsampling: (a) steel-headed hammer impact (HAS), (b) rubber-headed hammer impact (HAR), (c) drop tower impact (DT), (d) dominant frequency analysis by WT.

After determining the impact window based on dominant frequency, the signals underwent downsampling with a downsampling ratio γ_{ds} of $\left\lfloor \frac{f_s}{200 f_d} \right\rfloor$. The identified downsampling ratio for HAS, HAR, and DT impacts are [4, 6, 13] respectively, corresponding to a downsampling frequency of 2e5/[4, 6, 13] Hz respectively. Both impact windowing and downsampling procedures significantly reduce the sample size of the sensor signals. The original sample size of 20,000 is reduced to several thousand by the impact windowing, and subsequently, the downsampling process further reduces the sample size to several hundred. This considerable reduction in the sample size of the sensor signals leads to a notable enhancement in the computational efficiency of the impact force deconvolution.

The reliability and robustness of the proposed impact window determination and signal downsampling method were further evaluated by considering different numbers of sensors. The effects of the number of sensors on the identified impact window were investigated, as shown in Fig. 6.4. The window lengths identified by the proposed method are normalised by their corresponding actual values. The results demonstrate that the proposed impact window determination method exhibits remarkable robustness with respect to different numbers of sensors. Regardless of the number of sensors employed, the method consistently provides accurate and reliable estimates of the dominant frequency and impact window length. This highlights the effectiveness and versatility of the proposed method in practical applications, where the number of available sensors may vary.

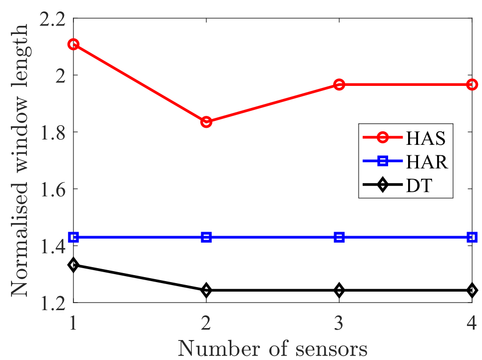

Figure 6.4: The effects of number of sensors on impact window determination.

6.6.3 Wavelet scale determination by multi-resolution analysis of sensor signal

In the multi-resolution analysis of impact force, selecting appropriate scales of wavelet bases is a critical aspect. Previous studies [173, 174] have typically selected the finest scale corresponding to the highest resolution based on the sampling frequency. This approach ensures that the wavelet bases cover frequencies above half the sampling frequency. However, including high frequency wavelet bases can lead to an overfitting representation that may not contribute to the force deconvolution. To address this issue, this study proposes an adaptive wavelet scale determination method through multi-resolution analysis of sensor signals. By incrementally increasing the wavelet scale from low to high resolution to represent the sensor signals, an appropriate finest scale can be determined at which the sensor signal representation error is minimised. The existence of the minimal representation error is validated in the following Section 6.6.3.1. And the wavelet scale determination for the three experimental impact cases is presented in Section 6.6.3.2.

6.6.3.1 Effectiveness of the proposed wavelet scale determination method

The proposed adaptive wavelet scale determination identifies the finest scale at which the representation error of the known sensor signal is minimised. This minimum represents a characteristic feature of the multi-resolution representation of discrete signals, arising from inherent discretisation errors caused by sampling the signal at the predetermined sampling frequency. As depicted in Eq. (6.13), the wavelet coefficient in the multi-resolution representation is derived by integrating the product of the signal and the wavelet in the time domain. This integral equals zero only when the continuous signal and continuous wavelets are orthogonal. However, due to discretisation errors, non-zero coefficients are present for almost all wavelet bases in the multi-resolution representation of the discrete signal, even when the original continuous signal is orthogonal to the continuous wavelets. Notably, when the central frequency of the wavelet exceeds the sampling frequency, particularly when the wavelet support is smaller than the sampling interval, numerical integration necessitates signal interpolation within that interval, leading to significant non-zero wavelet coefficients. This critical scale, where the central frequency of the wavelet exceeds the sampling frequency, can be calculated using the formula:

$$J_c = \left\lceil \log_2\left(\frac{f_s}{2f_0}\right) \right\rceil , \tag{6.18}$$

where $\lceil \cdot \rceil$ represents the ceiling function, and f_0 denotes the central frequency of the wavelets at scale 0 for multi-resolution representation. In this study, it amounts to 0.7143 Hz when using db4 wavelets.

Fig. 6.5 presents the db4 wavelets employed for the multi-resolution representation and an examination of the representation error for a db4 wavelet at scale 5. This particular wavelet at scale

5 is one of the orthogonal wavelets utilised in the multi-resolution representation. Consequently, when wavelet scales are below 5, the relative error in the multi-resolution representation approaches 1. However, increasing the wavelet scale to 5 leads to a significant reduction in the representation error. Furthermore, at higher sampling frequencies, improved representation accuracy is observed due to improved numerical integration accuracy resulting from an increased number of samples, as evidenced by the comparison of representation accuracies at sampling frequencies of 1024 Hz and 2048 Hz. Nevertheless, the critical scales at which the central frequency of the wavelets exceeds the sampling frequency (1024 Hz and 2048 Hz) are determined to be 10 and 11, respectively, based on Eq. (6.18). Consequently, the representation error begins to increase at these scales for the discrete db4 signals at these sampling frequencies. This example of a db4 wavelet representation demonstrates the effectiveness of the proposed adaptive wavelet scale determination method, as the sampling frequency ensures the presence of the minimal representation error and critical scale serves as the upper bound for the adaptive finest scale identified.

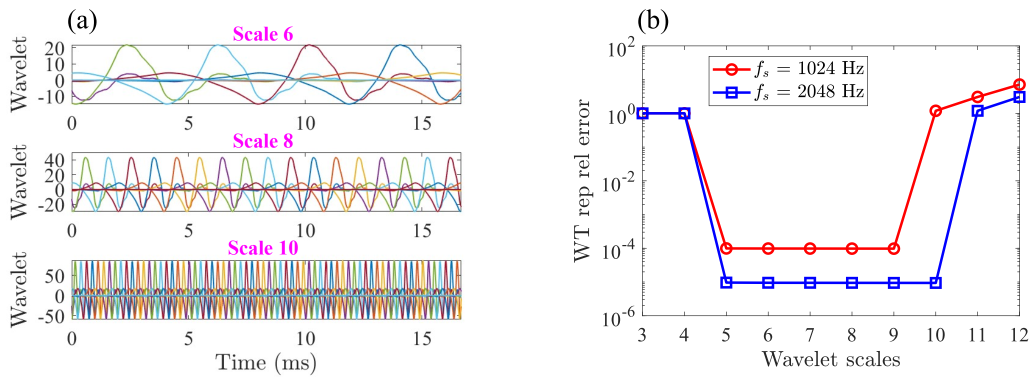

Figure 6.5: Multi-resolution representation of a db4 wavelet at scale 5: (a) db4 wavelets, (b) representation error.

6.6.3.2 Wavelet scale determination for the experimental impacts

In practical applications, due to the various frequency components in the sensor signals, the finest scale identified by the proposed adaptive method may be smaller than the critical scale determined by the sampling frequency. Fig. 6.6 presents the multi-resolution representation error for sensor signals from the impacts of a small-mass steel-headed hammer (HAS), a small-mass rubber-headed hammer (HAR), and a large-mass drop tower (DT). In this scenario, ensuring that the central frequency of the corresponding wavelets exceeds half of the original sampling frequency $f_s = 2e5$

Hz necessitates a minimum scale of 18. However, the finest scales identified to represent the impact signals within the identified impact window with minimal error are 13, 14, and 13 for HAS, HAR, and DT impacts, respectively. At these identified scales, the relative representation error for these three impacts is all below 1e-3. Determining the finest scale solely based on the sampling frequency may introduce unnecessary high-frequency components and complicate the force deconvolution calculation.

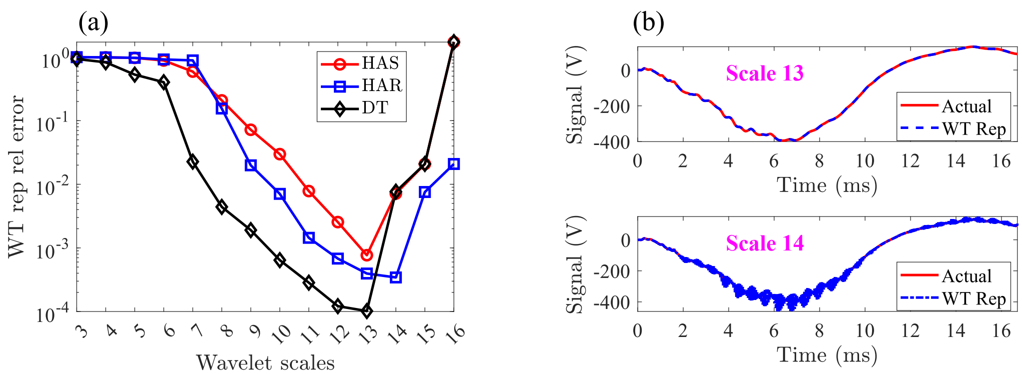

Figure 6.6: Multi-resolution representation of impact sensor signals: (a) wavelet scale determination for HAS, HAR, DT impacts, (b) representation of DT signal with finest scale at 13 and 14.

The findings illustrated in Fig. 6.6 also reveal that as the scale increases from low to high resolution, the relative error of the wavelet representation initially experiences a substantial decrease. This decline signifies an enhanced fidelity of the wavelet representation to the original signal. As illustrated in Section 6.6.3.1, it becomes evident that the representation error cannot continuously decrease with the increase of the wavelet scale. Once the representation error reaches its minimum, further increase in the scale leads to a rise in the representation error. Specifically, in the representation of the DT impact signal, when the scale reaches 10, the relative error of the wavelet representation drops below the millisecond level, indicating a highly accurate representation. The minimal representation error is achieved at scale 13, with a relative representation error of 1e-4. However, there is a significant increase in the representation error from scale 13 to 14, suggesting considerable overfitting is occurring. This surge in the relative error serves as a valuable indicator for determining the appropriate finest scale to represent the sensor signal and impact force. By incrementally increasing the scale and analysing the representation error, the suitable finest scale is adaptively determined, in this case for DT impact, as 13.

Fig. 6.6 also provides a comparison of the wavelet representation of sensor signals and impact force for the DT impact when truncating the finest scale to 13 and 14. The results suggest that truncating the finest scale to 14 results in an overfitting representation, with the introduction of significant high frequency components. Both the sensor signal and impact force can be accurately illustrated with wavelet bases truncated at the finest scale of 13. The multi-resolution analysis of the sensor signals enables the identification of an appropriate wavelet scale for multi-resolution representation of the impact force. By truncating the finest scale to 13 instead of 18 determined by the original sampling frequency, the number of wavelet bases for a 10 ms time window is notably reduced from 5354 to 243. This substantial reduction in the dimension of the force deconvolution LS problem improves computational efficiency. The adaptive wavelet scale determination method proposed in this study offers a solution to the overfitting issue associated with high-frequency wavelet bases. By carefully selecting the finest scale based on the analysis of representation error of sensor signals, the method achieves an optimal balance between accuracy and computational efficiency in the multi-resolution analysis of impact force.

6.6.4 Energy-based Filtering of Wavelet Bases

Indeed, the multi-resolution analysis of sensor signals plays a crucial role not only in determining the appropriate wavelet scales but also in providing insights into the energy contributions of wavelet bases in the representation of sensor signals. By decomposing the sensor signals into different wavelet bases, researchers can gain insights into the relative importance of each wavelet base in capturing the signal characteristics.

In this study, an adaptive wavelet base filtering technique is proposed based on the wavelet representation coefficients of the sensor signals. Within the multi-resolution representation framework, the energy of the represented signal is computed as the sum of the squares of these wavelet coefficients. Consequently, the significance of the wavelets to the representation is denoted by their respective coefficients and quantified by the relative energy contributions. The relative energy contribution of each wavelet is calculated as the ratio between the square of the wavelet coefficient and the energy of the sensor signal, bounded between 0 and 1. By eliminating insignificant wavelets with trivial energy contributions (those with extremely small coefficients), the significant wavelets in a number of half of the sample size, are used to represent and regularise the impact force in force deconvolution.

6.6.4.1 Significant wavelets for the representation of sensor signal and impact force

Once an approximate impact window covering the impact duration has been determined, it becomes evident that the significant wavelets used to represent the impact force are essential components of the significant wavelets for the wavelet representation of responses within the identified impact window. In other words, the wavelets lacking significance in response representation also prove insignificant in representing impact forces. Filtering out these insignificant wavelets, characterised by trivial energy contributions to the response representation, results in a more refined set of wavelet bases for representing impact force.

Fig. 6.7 provides a visualisation of the relative energy contributions of these wavelet bases in representing the sensor signal and impact force for HAS and DT impacts. These relative energy contributions are normalised between 0 and 1 by the actual energies of the sensor signal and impact force history, respectively. Each wavelet's contributions for representing the sensor signal and impact force are connected by a thin black line. In the figures, the numbers in magenta denote the wavelet scales. Higher scales (12 to 13 for DT) have coefficients close to zero and are not displayed here to highlight the significant wavelet bases in lower scales. Particularly, it is evident that the wavelet coefficients of scales larger than 9 for the representation of the DT impact sensor signal and impact force are of small value. The lower scales, corresponding to larger wavelet coefficients, contributes most to the representation. This observation aligns with the impact modal analysis, where lower modes with lower natural frequencies carry the majority of the response energy.

Furthermore, it is notable that the wavelets significant for representing impact force also holds significance in sensor signal representation. For wavelets with a relative energy contribution greater than 1e-5, the short black lines connecting contributions of sensor signal and force for both HAS and DT impacts indicates this strong similarity. Additionally, these significant wavelets are observed to be at lower scales (low frequency), aligning with the structural modal analysis. Consequently, when filtering the wavelets based on increasing energy contribution, most of the insignificant wavelets

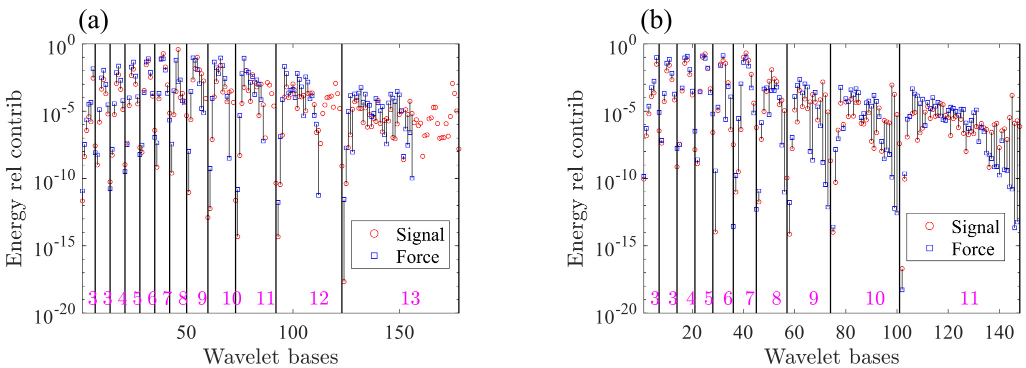

Figure 6.7: Energy contributions of wavelets to represent the sensor signal and impact force: (a) HAS, (b) DT.

filtered out are at higher scales. As the number of wavelets increases with the scale, the remaining significant wavelets are predominantly smaller in size and mostly from lower scales. Utilising these significant wavelet bases allows for the regularisation of the impact force representation, focusing on the relevant bandwidth-limited wavelet bases. Moreover, since the number of significant wavelets for force deconvolution is less than the sample size, the over-determined LS force deconvolution problem alleviates the overfitting phenomenon. This over-determined LS problem can be directly solved by LSQR without the need for additional explicit regularisation such as L2 regularisation.

6.6.4.2 Sample size and the wavelet size before and after energy-based filtering

As depicted in Eq. (6.10), force deconvolution aims to address a LS problem with n samples and m variables. Here, n denotes the sample size of the deconvoluted signal, while m represents the number of wavelet bases. Prior to applying the energy-based filtering, the candidate wavelet bases are determined by the time window and the finest wavelet scale. Meanwhile, the sample size is determined by the time window and the downsampling frequency. To investigate the relationship between sample size and the number of wavelets, Fig. 6.8 illustrates these relationships at a finest scale of 14 and at the critical scale, while varying the time window from 1 ms to 10 ms and considering three different sampling frequencies. The three different sampling frequencies (2e5, 1e5, and 5e4 Hz) correspond to critical scales determined by Eq. (6.18) as 18, 17, and 16, respectively.

It is evident that a clear linear relationship exists between the number of wavelets and the sample size. This relationship arises from the linear increase in the number of samples when extending the time window, under a constant sampling frequency and finest wavelet scale, thus

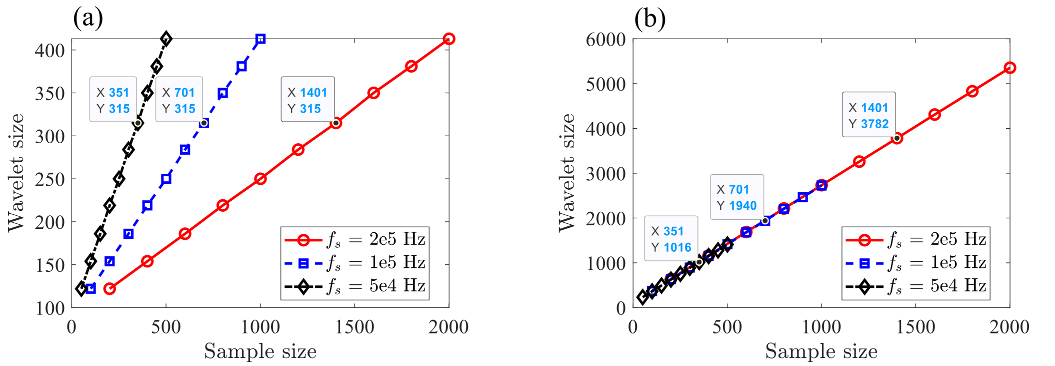

Figure 6.8: Sample size and wavelet size before energy-based filtering (a) finest scale at 14, (b) critical scales.

incorporating more wavelet bases linearly. However, the gradient of this relationship depends on both the finest scale and the sampling frequency. When the finest scale is chosen as the critical scale, as illustrated in Fig. 6.8b, this gradient remains nearly constant across different sampling frequencies. Moreover, the gradient exceeds 2, indicating that the number of wavelets surpasses twice that of the sample size.

In contrast, if the finest scale is determined by the proposed adaptive method, such as 14 for the HAR impacts, the number of wavelets significantly decreases compared to those obtained from the critical scales, as shown in Fig. 6.8a. Furthermore, with a fixed finest scale, a higher sampling frequency leads to a smaller gradient. For a 7 ms time window, sampling frequencies of 2e5, 1e5, and 5e4 Hz yield sample sizes of 1401, 701, and 351, respectively, while the number of wavelets is 315. Given that the sample size exceeds the number of wavelets in this scenario, resulting in an over-determined LS problem, filtering wavelets may not significantly contribute to force deconvolution.

It is noteworthy that while a higher sampling frequency allows for a larger sample size in force deconvolution, but it may lead to an increase in the finest scale identified by the proposed adaptive method. The signal downsampling procedure is significant as it reduces both the sample size and the number of candidate wavelets simultaneously, leading to computational savings. Table 6.2 provides a summary of the sample size and wavelet size for the three impact cases within their respective identified impact windows at the corresponding downsampling frequencies. It is apparent that, before wavelet filtering, the sample size closely matches the wavelet size for these impacts, ranging from two to three hundred. Specifically, for the HAS impact, with a small impact window and a fine scale of 13, the sample size surpasses the wavelet size, implying that wavelet filtering may not substantially improve force deconvolution accuracy. Following the filtering process, the number of remaining significant wavelets is consistently below 100 for these impacts, which is less than half of the sample size. This filtering effectively identifies the significant wavelets for impact force deconvolution, resulting in a well-regularised deconvoluted force.

Table 6.2: Wavelet size and sample size for impact force deconvolution after applying impact window determination, signal downsampling, and energy-based filtering.

Impact	Impact time window (ms)	Downsampling frequency (Hz)	Finest scale	Critical scale	Sample size	Wavelet size	Significant wavelets
HAS	5.9	$f_s/4$	13	16	295	178	97
HAR	7.8	$f_s/6$	14	15	260	338	71
DT	16.7	$f_s/13$	13	14	257	354	69

*Note: f_s: original sampling frequency (2e5 Hz).

6.6.5 Impact force identification by adaptive wavelet-regularised deconvolution

To validate the effectiveness of the proposed AWT for impact force deconvolution, one of the HAS impact was used to estimate the transfer function and the impact forces of other two impacts (HAS, DT) were deconvoluted. Several existing methods from the literature were used as references, including frequency-domain deconvolution method (Freq) [124], Tikhonov-regularised time-domain deconvolution method (L2) [163], sparse-regularised time-domain deconvolution method (L1) [167], and Haar wavelet-regularised time-domain deconvolution method (Haar) [174].

In terms of implementation, the frequency-domain deconvolution technique estimates the impact force by dividing the Fourier transforms of the sensor signals and the corresponding transfer functions in the frequency domain. The Tikhonov-regularised time-domain deconvolution method and the sparse-regularised time-domain deconvolution method rely on the selection of the regularisation parameter, which is recognised to vary depending on the specific problem [163,164]. Therefore, in this study, the regularisation parameter is determined through a comparison of the LC and Generalised Cross Validation (GCV) to ensure effective regularisation. Additionally, the associated L2-regularised and L1-regularised least squares problems are solved using the LSQR [180] and primal-dual interior point algorithm [182], respectively. The Haar wavelet-regularised time-domain deconvolution method employs Haar wavelets to represent the impact force. In this method, the finest scale of the wavelets is determined based on the sampling frequency, and wavelet base filtering is achieved through the utilisation of an adapted LC criteria. This adapted criteria involves plotting the log-log plot of the norm of a regularised solution versus the norm of the corresponding residual as the number of wavelet bases employed decreases in a frequency-decreasing order [174].

6.6.5.1 Force deconvolution and accuracy analysis of DT impact

Fig. 6.9 presents a comparative analysis of these methods for the reconstruction of impact forces for the DT impact, based on the transfer function estimated through one of the HAS impacts. Two distinct deconvoluted signal lengths, namely 20 ms and 25 ms, were considered for the deconvolution process.

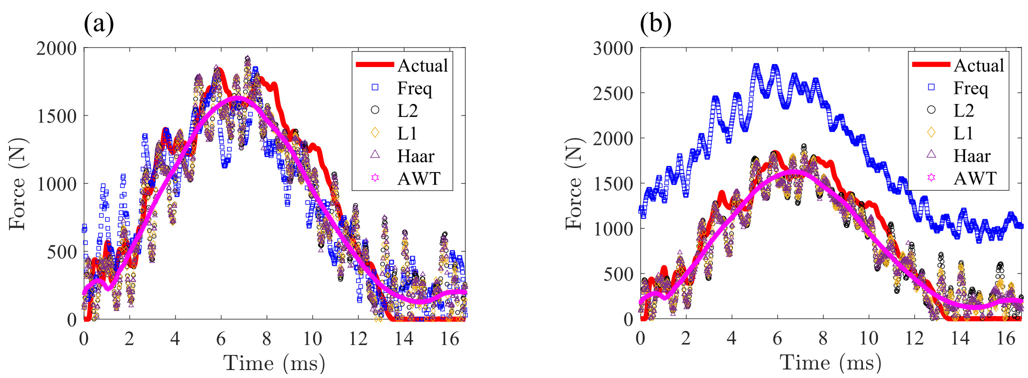

Figure 6.9: Force of DT impact identified by the deconvolution methods: (a) time window 20 ms, (b) time window 25 ms.

Upon thorough examination, it becomes clear that the proposed wavelet-regularised impact force deconvolution method, denoted as AWT, demonstrates highly favorable attributes in terms of continuity and robustness compared to reference methods. The reconstructed impact force using the proposed method exhibits a notable absence of high-frequency noise, indicating its effectiveness in accurately capturing the complex dynamics of the underlying force.

In contrast, the frequency-domain deconvolution method displays significant sensitivity to the time window of the deconvoluted signal. While the force deconvoluted with a window length of 20 ms closely approximates the actual force, a slight increase in the time window (to 25 ms) causes the deconvoluted force to shift upwards. This phenomenon occurs because the mean of the deconvoluted force sequence equals the frequency component $\hat{f}(0) = \hat{s}(0)/\hat{h}(0)$, as determined from the fast Fourier transform (FFT) analysis. The extension of the deconvoluted signal's length beyond the contact duration window substantially affects the mean values of sensor signals, thereby altering the mean value of the deconvoluted force. Moreover, employing a larger time window in FFT enhances the resolution in the frequency domain [91], suggesting that a larger time window is preferable for frequency-domain deconvolution methods in terms of accuracy and resolution.

The time-domain deconvolution methods demonstrate a notable feature of being insensitive to the deconvolved time window, thereby effectively leveraging the pre-processing steps such as impact window determination and signal downsampling. Specifically, the L2-regularised time-domain deconvolution method exhibits well regularised force, albeit slightly inferior to the proposed AWT method. This effective regularisation stems from the meticulous selection of the regularisation parameter through a comparative analysis of two parameter selection techniques, namely LC and GCV. The L2-regularised impact force deconvolution, as illustrated in Fig. 6.10, presents distinct outcomes based on these two regularisation parameter selection techniques. It is observed that LC identifies a smaller regularisation parameter, resulting in a force history with greater fluctuation and an abundance of high-frequency components. Conversely, the use of GCV yields superior force regularisation, capturing both the energy and shape of the impact force more accurately. The superiority of GCV over LC is also observed in the L1 regularisation for the DT impact force deconvolution. The integration of both LC and GCV methods within the L2/L1-regularisation framework enables more reliable and precise force deconvolution. Given the superior performance of GCV in this context, it is employed to determine the optimal regularisation parameter in L2/L1 regularisation, and its deconvoluted forces for L2/L1-regularisation are illustrated in Fig. 6.9.

The sparse-regularised (L1) time-domain deconvolution method and the Haar wavelet-regularised time-domain deconvolution method (Haar) demonstrate pronounced high-frequency fluctuations in the reconstructed impact force compared to the proposed AWT method. These fluctuations become particularly notable towards the end of the deconvolution time window. Both of these methods exhibit inferior regularisation, primarily due to inherent characteristics of their regularisation approaches. L1 regularisation prioritises achieving sparsity in the solution, often at the expense of

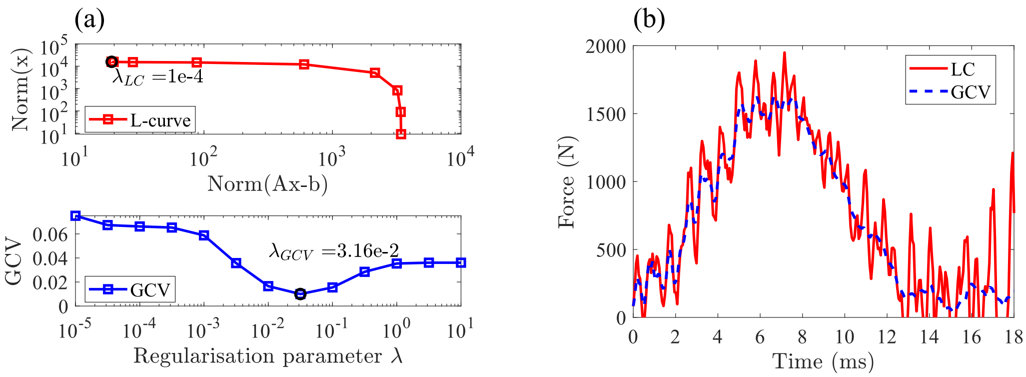

Figure 6.10: L2-regularised impact force deconvolution using LC and GCV: (a) regularisation parameter selection, (b) impact forces identified.

smoothness. Conversely, Haar regularisation introduces numerous high-frequency wavelet bases determined by the sampling frequency, and the adapted LC method fails to effectively filter out insignificant wavelet bases.

Fig. 6.11 provides a comprehensive analysis of the force relative squared error across various time windows for the time-domain deconvolution methods discussed. The force error is computed within the 18 ms time window, which encompasses the entire impact contact duration. The results clearly demonstrate that the proposed adaptive wavelet-regularised time-domain deconvolution method (AWT) achieves the highest accuracy, with a relative squared error of approximately 3%. Conversely, the L2-regularised time-domain deconvolution method employing the LC technique exhibits the lowest accuracy, particularly evident for shorter time windows, yet maintaining a relative squared error of approximately 10%. On the other hand, the L2-regularised time-domain deconvolution method employing the GCV technique showcases commendable force reconstruction capabilities, albeit slightly inferior to the proposed AWT method. This underscores the effectiveness of GCV in this L2-regularised force deconvolution problem. In contrast, the L1 regularised time domain deconvolution method and the Haar wavelet regularised time domain deconvolution method display moderate and similar accuracy.

Moreover, the proposed adaptive wavelet-regularised time-domain deconvolution method demonstrates a higher degree of insensitivity to variations in time windows and achieves greater accuracy compared to the other three time-domain deconvolution methods. Notably, unlike the other methods, increasing the time window does not necessarily improve force deconvolution accuracy. This difference stems from the capability of the proposed method to adaptively identify the suitable

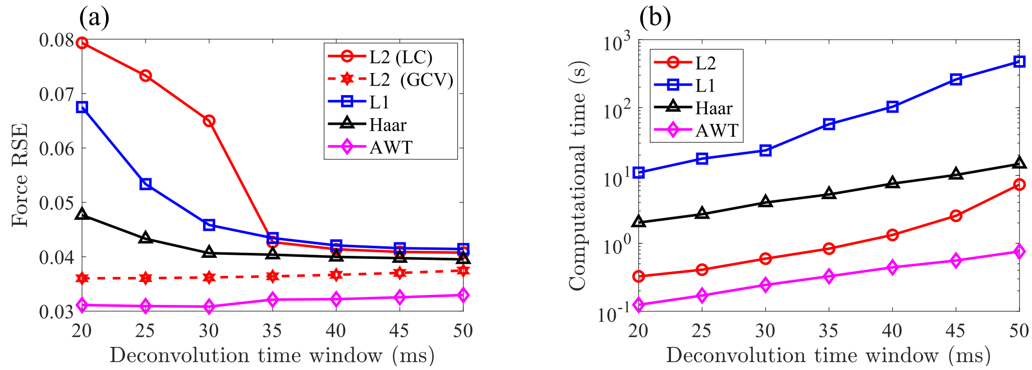

Figure 6.11: Force deconvolution accuracy and computational time of DT impact: (a) relative squared error, (b) computational time.

wavelet bases to represent the impact force, regardless of time window duration. In contrast, the Haar wavelet-regularised method, the L1-regularised method and L2-regularised method with LC technique prove inefficient and less accurate for shorter time windows. Moreover, the use of L2 regularisation with GCV also showcases this insensitivity, highlighting the importance of the regularisation parameter selection. The proposed AWT method maximises the utilisation of signal pre-processing steps, including impact window determination and signal downsampling, which results in a shorter time window for impact force deconvolution.

6.6.5.2 Computational efficiency (complexity) of impact force deconvolution

The computational efficiency of the aforementioned methods is analysed. In Section 6.6.5.2, a summary of the analytical time complexity for each method is provided, assuming a signal sample size of n. The frequency-domain deconvolution method achieves a complexity of $O(n \log n)$ due to the efficient implementation of the Fast Fourier Transform and Fast Inverse Fourier Transform algorithms. Conversely, the L1-regularised time-domain deconvolution method is the most time-consuming, with a complexity of $O(n^3)$ attributable to the primal-dual interior point algorithm utilised for solving the L1-regularised least squares problem. The computational cost of the L1/L2-regularised time-domain deconvolution method depends not only on the sample length n but also on the size R of candidate regularisation parameters (both for GCV and LC techniques), resulting in a complexity of $RO(n^3)/RO(n^2)$. Similarly, the time complexity of the Haar wavelet-regularised time-domain deconvolution method is influenced by the number of wavelet bases M and the combinations C of wavelet bases tested to determine the optimal wavelet combination.

Table 6.3: Time complexities of deconvolution methods: frequency-domain deconvolution and time-domain deconvolution with various regularisation techniques.

Method	Time complexity	Remark
Frequency-domain deconvolution	$O(n \log n)$	n is the sample size
Tikhonov-regularised time-domain deconvolution	$RO(n^2)$	R represents the number of candidate regularisation parameters from which the regularisation parameter selection techniques identify the optimal value
L1-regularised time-domain deconvolution	$RO(n^3)$	Primal-dual interior point algorithm is adopted to solve L1-regularised LS problem
Haar wavelet-regularised time-domain deconvolution	$CO(nM)$	M is the number of wavelet bases; C is the wavelet bases combinations tested to determine optimal combination by LC criteria
Proposed adaptive wavelet-regularised time-domain deconvolution	$O(nm)$	m is the wavelet bases size adaptively determined by multi-resolution analysis of sensor signals, which can be smaller than one-tenth of M

In contrast, the proposed adaptive wavelet-regularised time-domain deconvolution method (AWT) exhibits a time complexity of $O(nm)$, where m refers to the number of filtered significant wavelet bases adaptively determined through multi-resolution analysis of the sensor signals. Based on the filtering scheme, m is equal to or even less than half of sample size n. In addition, m is significantly less than M used in the Haar method. Fig. 6.11 b presents the actual average computational time of 20 repetitions for force deconvolution using the aforementioned methods on a desktop equipped with an Intel i7-10700 processor, with varying deconvolution time windows. The candidate regularisation parameters in L1/L2-regularisation are set to $10^{(-5:0.5:1)}$, totaling 13. In the Haar-regularised method, since wavelet bases surpass several hundred, the tested wavelet combinations are set to 40 ($C = 40$). The practical computational results align with the analytical analysis. Notably, the proposed AWT method demonstrates the highest computational efficiency among all the time-domain deconvolution methods. On the other hand, the L1-regularised method has the highest computational complexity of order 3, as evident by the steepest gradient of the corresponding curve in Fig. 6.11b. Moreover, the repetitions required to determine the optimal regularisation parameters make it the most time-consuming. Although the L2-regularised method is faster than the Haar-regularised method and L1-regularised method, it is also computationally costly compared to the proposed AWT method.

Although for signals in the same time window, the proposed method is only slightly less efficient in terms of computation than the frequency domain deconvolution method. However, as discussed earlier, the frequency-domain deconvolution method requires a large time window to ensure its accuracy and improve its frequency resolution, and it may result in incorrect force reconstruction when the time window is small. The proposed adaptive wavelet-regularised time-domain deconvolution method combined with impact window determination and downsampling techniques performs well in small time windows, which is an efficient complement and comparison to the frequency-domain deconvolution method.

Furthermore, the proposed adaptive wavelet-regularised time-domain deconvolution method exhibits low space complexity. Since the impact force is represented using a few wavelet bases (m is typically less than 100), the size of the deconvolution matrix reduces from $R^{n\times n}$ to $R^{n\times m}$. Moreover, the sensor signals and impact forces can be compressed and stored as wavelet coefficients, further reducing the storage complexity of the proposed adaptive method.

6.6.5.3 Force deconvolution of the HAS impact

As illustrated in Table 6.1, two HAS impacts were conducted on the experimental plate at the same location. To evaluate the effectiveness of the proposed AWT method for force deconvolution in scenarios characterised by a higher frequency range (short contact duration) and low impact energy, one of the HAS impacts was utilised to compute the transfer function, while the remaining HAS impact was employed to assess the performance of the proposed AWT method for force deconvolution. Fig. 6.12 presents the force deconvolution results for the HAS impact across three different time windows, namely 2 ms, 4 ms and 6 ms.

The proposed AWT method demonstrates notable accuracy in identifying the impact force for the HAS impact, exhibiting robustness across varying time windows. Interestingly, as the time window increases, the accuracy of the proposed AWT method improves, particularly in capturing the second force peak for HAS impacts, where other methods fail to do so. In contrast, the

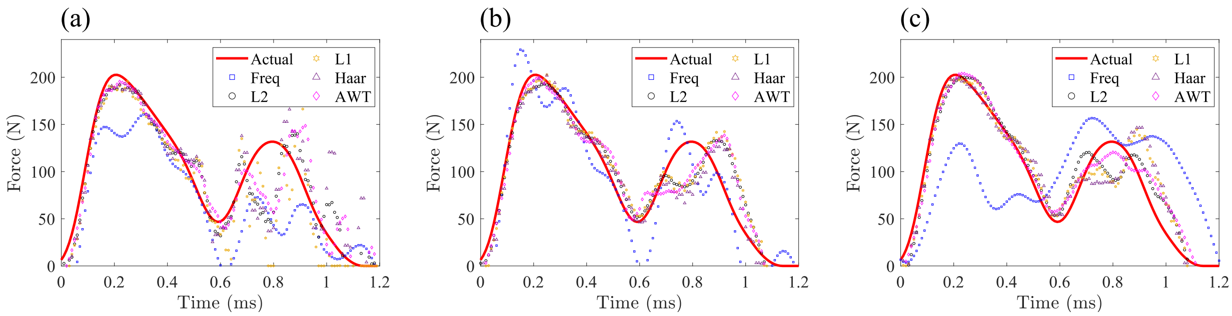

Figure 6.12: Impact force deconvolution for HAS impacts: (a) time window 2 ms, (b) time window 4 ms, (c) time window 6 ms.

performance of the frequency-domain deconvolution method heavily relies on the length of the time window. A longer time window is necessary for frequency-domain deconvolution to achieve higher frequency resolution. The L2 regularisation with GCV technique may underestimate the impact force in the case of large time window (6 ms) due to the selection of a large regularisation parameter. Additionally, the Haar method is computationally intensive for determining the optimal wavelet combination and exhibits slightly more pronounced high-frequency components in the deconvoluted force compared to the proposed AWT method. Overall, the proposed AWT method achieves both high accuracy and robustness for force deconvolution of impacts characterised by a higher frequency range (short contact duration) and low impact energy across varying time windows.

6.6.5.4 Effects of the finest wavelet scale on the impact force deconvolution

The force deconvolution process of the proposed AWT method relies on determining the finest scale, as discussed in detail in Section 6.6.3. This section aims to investigate the impact of the finest wavelet scale on force deconvolution accuracy. As illustrated in Fig. 6.6, the AWT method identifies the finest scale as 13 for both DT and HAS impacts, with a minimal representation error of less than 1e-3. Conversely, scales such as 10 and 16 indicate underfitting and overfitting representations, respectively, with larger representation errors. Fig. 6.13 presents the impact force deconvolution results for HAS and DT impacts based on these three scales within a 4 ms and 20 ms window, respectively.

It is evident that the finest scale of 13, determined by minimal representation error, yields the most accurate and well-regularised deconvoluted force. The higher scale of 16, corresponding to the

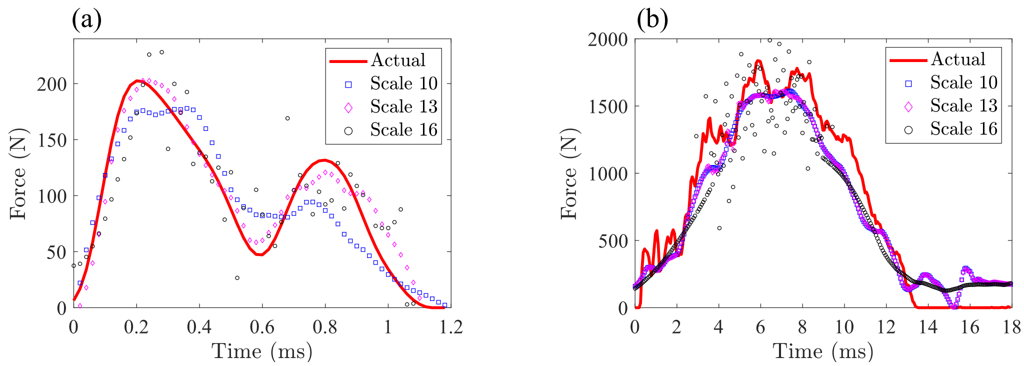

Figure 6.13: Impact force deconvolution based on different finest scales: (a) HAS, (b) DT.

overfitting scenario, exceeds the critical scale, resulting in large wavelet coefficients (contributions) for this higher scale due to numerical integration errors. In this case, wavelets at higher scales are erroneously identified as significant for force deconvolution, leading to distorted deconvoluted force with high-frequency fluctuations. While scale 10 for the DT impact maintains a representation error of less than 1e-3 and identifies nearly the same significant wavelets as scale 13, resulting in a similar deconvoluted force. However, scale 10 for the HAS impact yields a larger representation error of 0.03, leading to underestimated force deconvolution. The proposed AWT method identifies the finest scale based on minimal representation error, proving to be the best choice for force deconvolution.

6.6.5.5 Effects of the energy contribution threshold for wavelet filtering on the impact force deconvolution

The force deconvolution for DT, and HAS impacts by the proposed AWT method utilises an energy contribution threshold of 1e-5. This threshold implies that the top one hundred thousand wavelets, whose relative energy contribution to the multi-resolution of the sensor signal exceeds 1e-5, are employed to represent and regularise the impact force. This low threshold is chosen because, in real-world scenarios, the number of significant wavelets with energy contributions greater than 1e-5 in a small impact window is typically fewer than one hundred. To investigate the effects of the energy contribution threshold on impact force deconvolution, Fig. 6.14 presents the force deconvolution of HAS and DT impacts with four energy contribution thresholds: 1e-7, 1e-5, 1e-3, and 1e-1, in ascending order. The finest scale is determined based on the proposed AWT method as 13. For the HAS impact, the deconvolution window is set to 4 ms, resulting in a sample size of

200 and 147 candidate wavelet bases. Conversely, the 20 ms window for the DT impact leads to 308 samples in the deconvolution signal and 406 candidate wavelet bases.

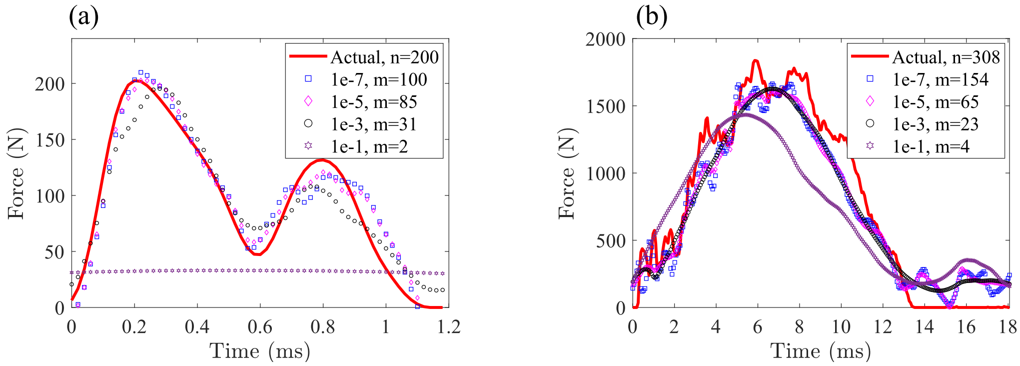

Figure 6.14: Impact force deconvolution based on different energy threshold: (a) HAS, (b) DT.

It can be observed that only 2 and 4 wavelets have energy contributions larger than 1e-1 for HAS and DT impacts, respectively. Consequently, this small number of wavelets cannot fully represent the impact force, leading to erroneous force deconvolution, especially for the HAS impact. Lowering the energy threshold to 1e-3 increases the number of filtered wavelets to 31 and 23, respectively. These filtered wavelets can effectively represent the impact force, resulting in accurate force deconvolution. Further reduction of the energy threshold to 1e-5 yields even more filtered wavelets, although they are fewer than 100 (less than half of the sample size). Only with an energy threshold of 1e-7 do the filtered wavelets exceed half of the sample size. Further filtering based on energy contribution in ascending order is implemented to ensure that the number of filtered wavelets equals half of the sample size. For all three energy thresholds (1e-7, 1e-5, and 1e-3), since the sample size is at least twice as large as the number of wavelets, the deconvoluted forces are close and well-regularised. This highlights the energy contribution as a reliable indicator of wavelet importance, as increasing the energy threshold from 1e-7 to 1e-3 decreases the number of filtered wavelets without degrading the force deconvolution. Additionally, the choice of a small value 1e-5 as the energy contribution threshold in this study is justified. When the number of filtered wavelets at this threshold is less than half of the sample size, further filtering is unnecessary, and the over-determined LS impact force solution remains well-regularised. However, if the number of filtered wavelets by this threshold value exceeds half of the sample size, it indicates that a smaller threshold has been chosen, necessitating additional filtering to remove more insignificant wavelets with trivial coefficients. Further filtering based on energy contribution in ascending order is applied to ensure that the number of filtered wavelets equals half of the sample size.

6.7 Summary

This chapter presents an adaptive wavelet-regularised time-domain deconvolution method for impact force identification using passive sensor signals. The proposed approach aims to improve computational efficiency and robustness by reducing the signal dimension and tailoring the force representation to the characteristics of the structural response.

Efficiency is achieved through two key mechanisms: (1) adaptive determination of the impact time window based on the dominant frequency of the measured response, and (2) selection of an appropriate wavelet scale and subset of wavelets for representing the force history. Since the structural modes excited during impact typically lie near the impact loading frequency, the dominant frequency serves as a proxy for contact duration. This enables estimation of a compact time window and downsampling of the sensor signals, reducing the number of samples for deconvolution to the order of several hundred.

To construct a compact and physically consistent representation of the impact force, a multi-resolution analysis is applied to the sensor signal. The optimal wavelet scale is identified based on the minimisation of signal reconstruction error. Within this scale, wavelets contributing negligibly to the signal are pruned based on their energy content, ensuring an overdetermined deconvolution problem and mitigating overfitting.

Experimental validation on a composite flat panel confirms that the proposed method reliably identifies appropriate impact windows across different scenarios, including changes in impactor material (steel to rubber) and increases in impact mass and energy. The method achieves high accuracy in reconstructing force histories while substantially reducing computation time, especially when compared to conventional deconvolution techniques. It remains effective even in cases involving large-mass impacts that induce significant local deformation—conditions that may slightly violate the linearity assumption of the system model.

Nevertheless, the proposed method is built on the assumption of a known, time-invariant transfer function derived under conditions of linear elastic structural behaviour. This transfer function is empirically estimated and assumed to remain stable across EOV. In reality, however, it may be sensitive to changes in temperature, humidity, and boundary conditions, potentially compromising the accuracy of the deconvolution. Moreover, in scenarios where impact damage occurs during the impact event, the structure may exhibit nonlinear responses due to stiffness degradation, delamination, or other damage mechanisms. Under such conditions, the linear transfer function model becomes invalid, and the force reconstruction may degrade or fail entirely.

These limitations suggest that future work should focus on EOV-adaptive or online transfer function estimation, and explore nonlinear or damage-aware deconvolution frameworks capable of handling dynamic changes in system behaviour during and after impact.

Chapter 7

Physics-guided Impact Identification with Uncertainty Quantification

Highlights:

- Establish a sparse data-driven plate modelling approach based on First-order Shear Deformation Theory (FSDT) to enable structural characterisation from limited impact reference data.
- Improve localisation accuracy and generalisability by integrating multi-frequency guided wave behaviour into a dispersion-relation-augmented machine learning framework.
- Enhance the robustness and interpretability of force reconstruction by incorporating FSDT-based modal characteristics into adaptive regularisation, enabling adaptive deconvolution under sparse and variable data conditions.

7.1 Introduction

As demonstrated in Chapter 6, the deconvolution method enables highly accurate impact force estimation, independent of impact-related parameters such as mass and velocity. However, its accuracy is contingent upon the precise determination of the system transfer function, $h(t; L, q)$, which characterises the response at sensor location L due to an excitation at impact location q. Since it is impractical to experimentally measure transfer functions across all possible impact locations, even a finely calibrated finite element analysis (FEA) model—updated with experimental data—may still exhibit discrepancies from actual sensor measurements. Nonetheless, depending on its fidelity, an updated FEA model can serve as a baseline or prior for refining transfer function estimates using High-Fidelity (HF) experimental data.

In data-driven impact identification, transfer functions $h(t; L, Q)$ at reference impact locations Q are obtained from measured impact forces $F(t)$ and sensor responses $S(t)$. The principal challenge lies in estimating the transfer function at an arbitrary impact location q, particularly in scenarios where reference data are sparse.

Two interpolation methods have been widely employed to estimate transfer functions in a data-driven manner: Radial Basis Function (RBF) interpolation [22] and Shape Function (SF) interpolation [23, 183, 184]. Both methods approximate the transfer function at a target location q as a weighted sum of transfer functions at reference locations Q. The RBF method leverages all available reference locations, with weights determined by the kernel function, while the SF method relies solely on the four nearest reference impact locations surrounding q. This inherent limitation of SF reduces its applicability when the estimated impact location lies outside the reference coverage or when reference data are sparsely distributed. Additionally, the RBF method interpolates each frequency component of the transfer function independently, allowing for frequency-dependent weighting. In contrast, the SF method treats the transfer function as a whole, applying uniform weights across all frequency components.

Both RBF and SF interpolation techniques are inherently location-based, with their accuracy highly dependent on the spatial distribution of reference impacts and their correlation with the target impact. The spatial distribution of reference impacts primarily influences two key aspects:

1. Interpolation vs. Extrapolation: When the target impact is located within the reference impact coverage, the problem is classified as interpolation, which is generally less prone to overfitting. However, when estimating the transfer function for a target impact outside the reference coverage, the problem becomes extrapolation, which is inherently more susceptible to overfitting and reduced accuracy.

2. Mode Shape Resolution: The density of reference impacts dictates the number of structural mode shapes that can be accurately captured. Since higher-frequency modes exhibit finer spatial variations, a denser distribution of reference impacts is required to effectively reconstruct these mode shapes.

This trade-off between generalisability and data dependence highlights the fundamental challenges in developing robust, data-driven impact identification frameworks. A densely distributed, HF experimental dataset is a costly but reliable approach that guarantees accurate impact identification. However, as demonstrated in Chapter 3 and Chapter 5, sparse data-driven impact localisation can achieve high accuracy by directly inferring the Group Velocity Profile (GVP) from data. This even enables impact localisation outside the reference coverage. Investigating sparse data-driven impact identification, particularly for force reconstruction, is of significant interest, as it reduces reliance on extensive pre-existing datasets while maintaining computational efficiency.

To address these challenges, this study proposes a sparse data-driven physics-based modelling strategy, wherein an First-order Shear Deformation Theory (FSDT)-based plate model is developed solely from reference impact data, eliminating the need for prior knowledge of structural material properties and boundary conditions. Structural properties and boundary conditions are subsequently inferred by aligning dispersion relations and modal characteristics (e.g., natural frequencies and transmissibility) between FSDT predictions and reference impact data.

The proposed data-driven FSDT modelling framework enables the construction of a Multi-Fidelity (MF) Gaussian Process Regression (GPR) model for impact localisation, integrating Low-Fidelity (LF) data generated from the FSDT model into a unified, generalisable model. This facilitates accurate localisation, even for impacts occurring outside the reference coverage. Subsequently, transfer function estimation at the identified impact location is performed using RBF interpolation, with adaptive regularisation informed by the identified modal characteristics of the FSDT model. Furthermore, the GPR model provides localisation uncertainties, which are propagated to impact force reconstruction, enabling comprehensive uncertainty quantification in both impact location and force estimation.

By integrating data-driven FSDT modelling, dispersion relations, modal analysis, and machine learning, the proposed framework substantially improves both interpolation and extrapolation accuracy in impact localisation and force reconstruction. This integrated approach enables accurate estimation at previously unseen impact locations and under varying structural responses, while significantly reducing the need for exhaustive experimental measurements.

7.2 Physics-guided Impact Identification by Sparse Data-driven FSDT Modelling

In practical applications, plate-like carbon fiber-reinforced polymer (CFRP) laminated composite structures—such as flat plates, stiffened panels, and sandwich configurations—are extensively used in aerospace and related industries. These structures are therefore the primary focus of this chapter. The geometric dimensions of such components, specifically the length a and width b, are typically determined during the design phase to satisfy manufacturing constraints and ensure effective sensor deployment. Sensor locations, denoted by L, are generally fixed based on these design considerations.

However, in more complex configurations such as stiffened plates and sandwich structures, the plate thickness d exhibits spatial non-uniformity. For instance, stiffened regions may consist of increased local thickness d_s, compared to the nominal plate thickness d_p. Similarly, sandwich structures often integrate aluminium cores with composite laminate facesheets, introducing additional heterogeneity. In such cases, the effective material density ρ is approximated as a volume-weighted average of the constituent materials to account for spatial variation in structural properties.

Given these conditions, the impact identification task within the proposed data-driven framework is cast as a probabilistic inference problem:

$$P\left(\Theta, q, f(t) | s(t), Q, F(t), S(t), L, a, b\right), \tag{7.1}$$

where the plate dimensions (a, b), sensor locations L, reference impact data $(Q, F(t), S(t))$, and measured target responses $s(t)$ are treated as observed inputs. In contrast, uncertain parameters such as the plate thickness $d \in [d_{\mathrm{lb}}, d_{\mathrm{ub}}]$ and effective density $\rho \in [\rho_{\mathrm{lb}}, \rho_{\mathrm{ub}}]$ are treated as bounded equivalents to accommodate material and geometric variability. The goal is to infer the unknown structural parameters Θ and the target impact characteristics $(q, f(t))$ from the observed data.

To enhance the generalisability of impact identification across various types of plate-like CFRP structures, a physics-based model is integrated into the framework. The FSDT is adopted to approximate the behaviour of the target structure as an equivalent flat plate. Despite geometric complexities, such as stiffeners or sandwich cores, FSDT provides a tractable yet sufficiently accurate representation of wave propagation and structural dynamics for these classes of composite systems [139]. This model forms the foundation for coupling physics-based insights with data-driven techniques, thereby enabling robust physics-augmented impact localisation and physics-informed force reconstruction, as illustrated in Fig. 7.1.

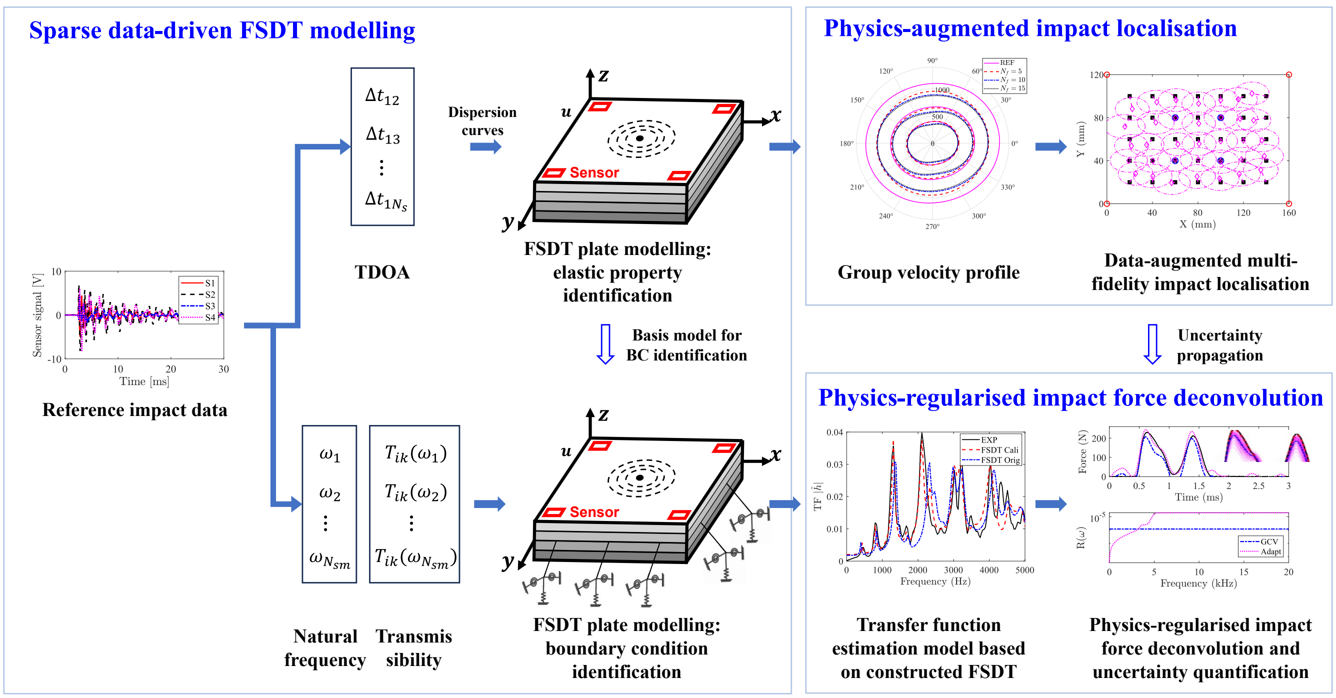

Figure 7.1: Physics-augmented impact identification and uncertainty quantification based on sparse data-driven FSDT modelling.

The model construction is carried out in two phases:

1. Material property identification, by fitting the dispersion curve of the A0 mode; and

2. Boundary condition identification, by matching modal characteristics such as natural frequencies and transmissibility.

These features are extracted from the reference dataset $(Q, F(t), S(t))$, which provides time-difference-of-arrival (TDOA) data related to wave dispersion, and modal information for boundary condition tuning.

Once constructed, the FSDT model enables accurate estimation of the Group Velocity Profile (GVP), which is used to generate synthetic datasets for data-augmented, MF impact localisation. Leveraging these datasets, the localisation model achieves high generalisability across the structure. Additionally, the FSDT model serves as a forward model for transfer function estimation, allowing error quantification in RBF-based interpolation. These interpolation errors are then used to define a frequency-dependent regularisation strategy, which improves impact force reconstruction accuracy compared to traditional L2 regularisation with a constant penalty parameter.

7.2.1 FSDT modelling phase 1: elastic property identification

7.2.1.1 Maximum likelihood estimation of elastic properties

The dispersion relations of a structure are inherently governed by its elastic properties while remaining independent of its boundary conditions. This property enables a hierarchical approach to identifying both structural elastic properties and boundary conditions using sparse reference impact data. Given that low-velocity impacts predominantly generate flexural waves [86, 107], this study focuses specifically on the analysis of out-of-plane flexural wave propagation. For symmetrically laminated composites, the dispersion relation of flexural wave group velocity is formulated in Eq. (2.28) as a function of the structural stiffness parameters $\boldsymbol{D}, \bar{\boldsymbol{A}}$ and inertia terms I_1, I_3:

$$v_g \left(\omega, \theta | \Theta_p : \{\boldsymbol{D}, \bar{\boldsymbol{A}}, I_1, I_3\}\right), \tag{7.2}$$

where $v_g(\omega, \theta)$ represents the group velocity of out-of-plane flexural waves, dependent on wave frequency ω and wave direction θ due to wave dispersion and structural anistropy. The stiffness parameters $\boldsymbol{D}, \bar{\boldsymbol{A}}$ and inertia terms I_1, I_3 are detailed in Eq. (2.16) and Eq. (2.18), respectively.

The GVP v_g is governed by the plate-level material properties Θ_p, which can be further derived from the lamina-level properties Θ_l. These lamina-level properties include the elastic constants of individual plies $E_1, E_2, \nu_{12}, G_{12}$, the lamina thickness t and the stacking sequence Ψ:

$$\Theta_p = \{\boldsymbol{D}, \bar{\boldsymbol{A}}, I_1, I_3\},\ \Theta_l = \{\rho, \Psi, t, E_1, E_2, \nu_{12}, G_{12}\}. \tag{7.3}$$

Here, Ψ is a vector of $2N_l$ elements that define the laminate stacking configuration, while the total plate thickness is given by $2N_l t_{ply}$.

The relationship between reference impact data and wave dispersion is established through TDOA measurements, as described in Eq. (5.1). This is expressed again as:

$$\Delta t_{ij}(\omega) = t_j(\omega) - t_i(\omega) + e(\omega) = \frac{\sqrt{(x-x_j)^2 + (y-y_j)^2}}{v_g(\omega, \theta_j)} - \frac{\sqrt{(x-x_i)^2 + (y-y_i)^2}}{v_g(\omega, \theta_i)} + e(\omega), \quad (7.4)$$

where $\Delta t_{1j}(\omega)$ represents the extracted TDOA between the j-th sensor and the i-th sensor, and $v_g(\omega, \theta_j)$ denote the wave propagation group velocity from the impact point to the j-th sensor. The uncertainties in TDOA, denoted $e(\omega)$, are random variables influenced by wave frequency ω, typically modeled as Gaussian with zero mean and variance $\sigma^2(\omega)$

Since plate-level properties Θ_p primarily capture out-of-plane wave behaviour and do not account for in-plane dynamics, a more comprehensive identification of lamina-level properties Θ_l is necessary. Given the sensor location $L_j = (x_j, y_j)$, independent reference impact locations $Q_i = (x_i, y_i)$ and TDOA estimates $\Delta t^i(\omega)$ from sensor measurements, the material properties at the lamina level can be estimated using a multi-frequency maximum log-likelihood approach:

$$\begin{aligned} &\hat{\Theta}_l = \arg\max_{\Theta_l} \log \mathcal{L} = \arg\max_{\Theta_l} \sum_{m=1}^{N_f} \log \mathcal{L}_m = \arg\max_{\Theta_l} \sum_{m=1}^{N_f} \sum_{i=1}^{N_i} \sum_{j=2}^{N_s} \log \varsigma \left(\frac{e_{1j}^i(\omega_m)}{\hat{\sigma}(\omega_m)} \right), \\ &\hat{\sigma}^2(\omega_m) = \frac{1}{N_i(N_s-1)} \sum_{i=1}^{N_i} \sum_{j=2}^{N_s} \left[e_{1j}^i(\omega_m) \right]^2, \ \mathcal{L}_m = \prod_{i=1}^{N_i} \prod_{j=2}^{N_s} \varsigma \left(\frac{e_{1j}^i(\omega_m)}{\hat{\sigma}(\omega_m)} \right), \end{aligned} \quad (7.5)$$

where ς denotes the probability density function of a standard Gaussian distribution, and $\hat{\sigma}^2(\omega_m)$ is the estimated variance of TDOA at frequency ω_m, obtained by maximising the likelihood function. The likelihood function $\mathcal{L}_m$ at each frequency ω_m is derived based on the wave propagation formulation in Eq. (7.4).

This multi-frequency identification approach leverages the full dispersion curve, reducing dependency on extensive reference datasets and large sensor arrays. Consequently, it enhances the feasibility of sparse data-driven applications in SHM by improving the accuracy and robustness of material property estimation while minimising experimental overhead.

7.2.1.2 Design space of elastic properties of CFRP lamina

In the maximum likelihood estimation (MLE) of the elastic properties of CFRP lamina based on dispersion relations, the definition of the probability spaces for these properties is crucial. CFRP composite lamina are anisotropic, meaning their mechanical properties vary depending on the direction relative to the fibre orientation. The longitudinal modulus, E_1 (along the fibre direction), is significantly higher than the transverse modulus, E_2 (perpendicular to the fibres). For unidirectional CFRP lamina, E_1 typically ranges from 120 to 250 GPa [185], encompassing low-modulus lamina such as T800H fibre/epoxy [185], high-modulus lamina such as GY-70/epoxy [185], and high-tenacity lamina such as T300/T400/T700S fibres/epoxy [185] and AS4/AS6 fibres/epoxy [186].

The ratio E_2/E_1, which depends on both the fibre and matrix properties, typically ranges from 0.05 to 0.1 for CFRP [187]. Another key ratio, G_{12}/E_1, representing the in-plane shear modulus G_{12}, generally falls between 0.02 and 0.05 due to fibre-matrix interactions. These ranges align with values observed in widely used unidirectional lamina [185]. Collectively, these bounds define the probability space for the elastic properties of CFRP lamina, summarised in Table 7.1.

Table 7.1: Probability space of the elastic properties of CFRP lamina and stacking sequence

Properties	E_1 (GPa)	E_2 (GPa)	G_{12} (GPa)	ν_{12}	ρ (kg/m^3)	t_{ply} (mm)	ψ_k (°)	d (mm)
UB	250	25	12.5	0.35	1700	0.3	{45, 90}	d_{ub}
LB	120	6	2.4	0.25	1500	0.1	{-45, 0}	d_{lb}

*Note: UB: upper bound, LB: lower bound E_1: longitudinal modulus along the fibre direction, E_2: transverse modulus perpendicular to the fibre direction, G_{12}: in-plane shear modulus, ν_{12}: in-plane Poisson's ratio, ρ: material density, d: plate equivalent thickness, N_l: half of lamina number, t_{ply}: thickness of lamina.

The in-plane Poisson's ratio, ν_{12}, represents the ratio of transverse to longitudinal strain under uniaxial loading along the fibre direction. While carbon fibres themselves exhibit a low Poisson's ratio ($\nu_{fibre} \approx 0.2 - 0.3$, table 4.4-4 in [185]), their influence on ν_{12} is minimal, as the transverse response is primarily governed by the matrix. The epoxy matrix, which deforms more in the transverse direction, typically has a Poisson's ratio of $\nu_{matrix} \approx 0.3 - 0.4$ (table 3.2-6 in [185]). For aerospace-grade CFRP (fibre volume fraction 60%-70%, table 4.4-5 in [185]) and commercial-grade CFRP (50%-60%), ν_{12} generally falls between 0.25 and 0.35.

The density of CFRP lamina or laminate is determined by the volume-weighted average of fibre and matrix densities. Due to the higher fraction of fibres, they predominantly influence the composite density. Standard carbon fibres and high-modulus carbon fibres have densities of 1750-1900 $\mathrm{Kg/m^3}$ and 1900-2000 $\mathrm{Kg/m^3}$, respectively (table 3.3-1 in [185]), while commonly used epoxy resins have lower densities, typically between 1100 and 1300 $\mathrm{Kg/m^3}$ (table 3.2-7 in [185]). Consequently, for fibre volume fractions of 50%-70%, the overall density of CFRP lamina typically ranges from 1500 to 1700 $\mathrm{Kg/m^3}$.

The equivalent plate thickness is bounded based on the plate type. As illustrated in Fig. 7.2, for a flat plate of thickness d, the equivalent thickness is constrained within $[d-\varepsilon, d+\varepsilon]$, where ε represents measurement uncertainty. For a sandwich plate of total thickness d and face sheet thickness d_{fs}, the equivalent thickness falls within $[2d_{fs}, d]$. For a stringer-stiffened plate, the equivalent thickness is naturally bounded between the thickness of the unstiffened region and that of the stringer toes.

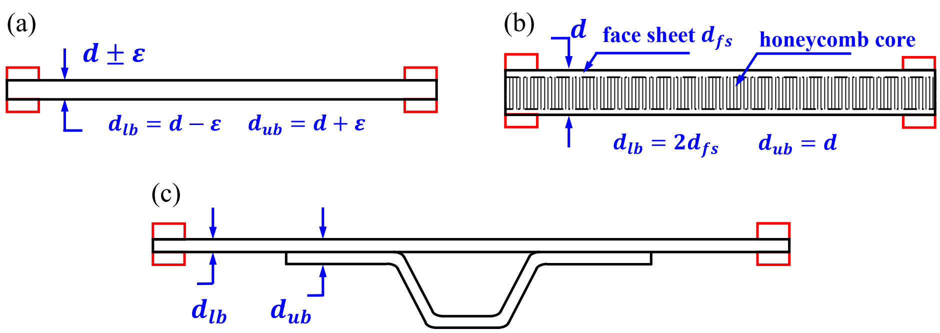

Figure 7.2: Three type of laminated composite plates with bounded thickness: (a) flat plate, (b) sandwich plate, (c) stringer-stiffened plate.

The stacking sequence of the lamina is a key factor in defining the structural anisotropy and mechanical performance of composite laminates. In this study, four of the most commonly used ply orientations in practical applications are considered: 0°, 45°, −45°, and 90°. This selection simplifies the design space of the stacking sequence vector Ψ while maintaining practical relevance. Variations in fibre orientation across individual plies influence both the in-plane and out-of-plane stiffness of the laminate, thereby altering its dispersion relations. The defined parameter spaces for material properties and lamina layup provide a structured basis for the data-driven identification of elastic properties.

The material property identification process, as formulated in Eq. (7.5), is a mixed-integer optimisation problem, where the four candidate ply angles are represented as discrete integer values ranging from 1 to 4. Given that the fitness function, defined as the log-likelihood, can be evaluated at relatively low computational cost—primarily involving calculations of location-to-sensor distances and wave propagation velocities—a mixed-integer genetic algorithm (GA) is employed to efficiently solve this optimisation problem and determine the optimal material properties.

7.2.2 FSDT modelling phase 2: boundary condition identification

The identification of the elastic properties of laminated composites facilitates the subsequent determination of boundary conditions based on modal characteristics.

7.2.2.1 Forward modal analysis by Rayleigh-Ritz variational method with general boundary conditions

Based on the constitutive equations in matrix form, as presented in Eq. (2.15), the strain energy U, kinetic energy T, and potential energy V of external forces for a symmetric plate subjected to a transverse impact load $f(t)$ at a point location q can be expressed as:

$$\begin{aligned} U &= \frac{1}{2}\int_{\Omega}[\boldsymbol{\epsilon}_0^{\top}\boldsymbol{A}\boldsymbol{\epsilon}_0 + \boldsymbol{\kappa}^{\top}\boldsymbol{D}\boldsymbol{\kappa} + \boldsymbol{\gamma}^{\top}\bar{\boldsymbol{A}}\boldsymbol{\gamma}]d\Omega, \\ T &= \frac{1}{2}\int_{\Omega}[I_1\dot{w}_0^2 + I_3(\dot{\varphi}_x^2 + \dot{\varphi}_y^2)]d\Omega, \\ V &= -\int_{\Omega} f w_0 \delta(q) d\Omega, \end{aligned} \tag{7.6}$$

where Ω represents the structural spatial domain in the x-y plane. The boundary conditions also store energy during impact events, depending on their nature. In real-world structures, boundary conditions are rarely purely free, simply supported, or fully clamped. To model general boundary conditions, artificial springs are introduced to simulate the shear force V_s and bending moment M_b acting on the boundary Γ. This is expressed in terms of the spring stiffness as follows:

$$V_s = k_t\mathbf{d}|_{\Gamma},\ M_b = k_r\frac{\partial\mathbf{d}}{\partial\overrightarrow{n}}|_{\Gamma}, \tag{7.7}$$

where k_t and k_r denote the translational and rotational stiffness, respectively. Here, $\mathbf{d} = [u_0, v_0, w_0, \varphi_x, \varphi_y]^{\top}$ represents the displacements resisted by the springs, and $\overrightarrow{n}$ is the tangential direction along the boundary. Consequently, the additional strain energy stored in the elastic boundary is given by:

$$U_b = \frac{1}{2}\int_{\Gamma} k_t \mathbf{d}^2 d\Gamma + \frac{1}{2}\int_{\Gamma} k_r (\frac{\partial \mathbf{d}}{\partial \overrightarrow{n}})^2 d\Gamma. \tag{7.8}$$

Using the Rayleigh-Ritz variational approximation approach [188, 189], the displacements are assumed to take the form:

$$\begin{aligned}
&\mathbf{d} = [u_0, v_0, w_0, \varphi_x, \varphi_y]^\top = [\mathbf{U_0}\mathbf{B}^\top, \mathbf{V_0}\mathbf{B}^\top, \mathbf{W_0}\mathbf{B}^\top, \mathbf{\Phi_x}\mathbf{B}^\top, \mathbf{\Phi_y}\mathbf{B}^\top]^\top = \mathbf{D}\otimes\mathbf{B}^\top,\\
&\mathbf{D} = [\mathbf{U_0}, \mathbf{V_0}, \mathbf{W_0}, \mathbf{\Phi_x}, \mathbf{\Phi_y}]^\top, \mathbf{B} = [b_1(\frac{x}{a})b_1(\frac{y}{b}), b_1(\frac{x}{a})b_2(\frac{y}{b}), ..., b_M(\frac{x}{a})b_N(\frac{y}{b})],
\end{aligned} \tag{7.9}$$

where the basis function $b_j(x)$ is chosen as Legendre polynomials due to their favourable convergence properties [190], and $\mathbf{D}$ represents the coefficients of these basis functions. The operator $\otimes$ denotes the block Kronecker product. Substituting Eq. (7.9) into Eq. (7.6) and Eq. (7.8), and applying Hamilton's principle, the equations of motion are obtained as:

$$\mathbf{M}\ddot{\mathbf{D}} + (\mathbf{K}_p + \mathbf{K}_b)\mathbf{D} = \mathbf{F}, \tag{7.10}$$

where $\mathbf{M}$ and $\mathbf{F}$ denote the generalised mass matrix and force vector, respectively. $\mathbf{K}_p$, $\mathbf{K}_b$ are the stiffness matrixes for the plate structure, boundary conditions, respectively. The expressions of these matrices are given in detail in Appendix E. Solving the eigenvalue problem by letting $\mathbf{F} = 0$ in Eq. (7.10) leads to the estimation of structural mode shapes and natural frequencies.

7.2.2.2 Boundary condition identification by matching modal characteristics

What modal information can be extracted from the reference impact data $Q, F(t), S(t)$? By analysing the structural response in terms of mode shapes and natural frequencies, as illustrated in Eq. (2.9), a key outcome is the identification of significant lower-mode natural frequencies (Fig. 2.5). In addition to natural frequencies, transmissibility serves as another modal property that can be inferred from reference impact data. Two types of transmissibility are considered: sensor transmissibility and excitation transmissibility.

Sensor transmissibility is defined as the ratio of the spectral amplitudes of responses recorded by two sensors at a given natural frequency when the structure is excited by an impact. When piezoelectric transducer (PZT) sensors monitor impacts and record strain responses, the sensor transmissibility between sensor j and sensor n across all reference impacts $i = 1, ..., N_i$ is given by:

$$T^{jn}(\omega_m) = \frac{\sum_{i=1}^{N_i} \hat{s}(\omega_m; q_i, L_j)}{\sum_{i=1}^{N_i} \hat{s}(\omega_m; q_i, L_n)} = \frac{\sum_{i=1}^{N_i} \hat{h}(\omega_m; q_i, L_j)\hat{f}(\omega_m; q_i)}{\sum_{i=1}^{N_i} \hat{h}(\omega_m; q_i, L_n)\hat{f}(\omega_m; q_i)} = \frac{\frac{\partial \phi_m^x}{\partial x}(L_j) + \frac{\partial \phi_m^y}{\partial y}(L_j)}{\frac{\partial \phi_m^x}{\partial x}(L_n) + \frac{\partial \phi_m^y}{\partial y}(L_n)}, \tag{7.11}$$

where $\hat{s}(\omega; q_i, L_j)$ and $\hat{h}(\omega; q_i, L_j)$ denote the spectral response and transfer function at sensor location L_j when excited at q_i, respectively. Here, phi_m^u denotes m-th mode shape in term of u-displacement, and $\frac{\partial \phi_m^u}{\partial x}(L_j)$ is its spatial derivative with respect to the x, evaluated at sensor location L_j. Essentially, sensor transmissibility reflects the ratio of mode shape gradients. However, sensor characteristics, including frequency response variations due to degradation or poor attachment, may introduce errors in the transmissibility estimate.

To address this limitation, excitation transmissibility is defined based on transfer functions (Eq. (2.9)) and depends on the availability of reference impact data rather than sensor characteristics. Considering two independent impacts at locations q_i and q_k, excitation transmissibility is defined as the ratio of the spectral transfer functions $\hat{h}(\omega; q_i, L)$ and $\hat{h}(\omega; q_k, L)$ at natural frequency ω_m, evaluated across all sensors $L_j, j = 1, ..., N_s$:

$$T_{ik}(\omega_m) = \frac{\sum_{j=1}^{N_s} \hat{h}(\omega_m; q_i, L_j)}{\sum_{j=1}^{N_s} \hat{h}(\omega_m; q_k, L_j)} = \frac{\phi_m(q_i)}{\phi_m(q_k)}. \tag{7.12}$$

For both PZT sensors and accelerometers, excitation transmissibility directly corresponds to the ratio of mode shapes. This definition provides a more robust means of estimating modal properties, particularly in cases where sensor performance may be affected by degradation or attachment quality.

By leveraging both natural frequencies and transmissibility, boundary conditions can be identified by minimising the discrepancies between the extracted modal properties and those predicted using the Rayleigh-Ritz method. This optimisation problem is formulated as:

$$\Theta_k = \arg\min_{\Theta_k} L_{nf} + \tau L_{et},\ L_{nf} = \sum_{m=1}^{N_{sm}} (\omega_m - \bar{\omega}_m)^2,\ L_{et} = \sum_{k=1}^{N_i} \sum_{i=k+1}^{N_i} [T_{ik}(\omega_m) - \bar{T}_{ik}(\omega_m)]^2, \tag{7.13}$$

where Θ_k represents the stiffness of artificial springs applied at the boundaries. L_{nf} and L_{et} are the mean sqaure error loss of natural frequencies and excitation transmissibility, respectively. N_{sm} denotes the number of significant identified modes from reference impact data. By optimising the artificial spring stiffness, the mode shapes and natural frequencies of the FSDT plate can be determined, facilitating the process of impact force identification.

7.2.3 Physics-augmented impact localisation and uncertainty quantification

The GVPs $v_g(\theta;\omega)$ are identified based on the FSDT model corresponding to the optimised structural material properties, facilitating impact localisation.

7.2.3.1 Physics-augmented multi-fidelity Gaussian process regression for impact localisation

The integration of physics-generated data enhances the generalisability of the model. By leveraging the identified GVPs $v_g(\theta;\omega)$, from the FSDT model, LF synthetic TDOA data $\Delta_{FSDT}\mathbf{t}(\omega_m)$ can be generated across the entire structure. Since these GVPs are inferred from experimental data, the simulated TDOAs maintain an intermediate level of accuracy, capturing the primary wave propagation characteristics while exhibiting some deviations from HF experimental data.

To improve the reliability of impact localisation, a MF GPR framework is employed, which integrates both simulated and experimental data. This approach enables accurate localisation across the structure by modelling the HF output as a scaled LF prediction with an additional correction term:

$$y_{HF}(\mathbf{x}) = \beta y_{LF}(\mathbf{x}) + \delta(\mathbf{x}), \tag{7.14}$$

where $y_{LF}(\mathbf{x})$ represents the LF model trained on the synthetic TDOA data $\Delta_{FSDT}\mathbf{t}(\omega_m)$. The scaling factor β adjusts for systematic discrepancies between low- and HF data, while the correction term $\delta(\mathbf{x})$ is modelled as a GP trained on sparse HF TDOA data from experimental measurements. This MF learning framework effectively compensates for the limitations of the LF model, enabling robust and accurate impact localisation across the structure.

To effectively fuse multi-frequency TDOA data within a single GPR model, a tailored multi-frequency kernel is designed as a summation of uni-frequency Squared Exponential Kernel (SEK) kernel(also referred to as the RBF kernel; the term 'squared exponential' is used here to avoid ambiguity with RBF interpolation):

$$k(\mathbf{x}, \mathbf{x}') = \sum_{m=1}^{N_f} k_{sek}(\mathbf{x}(\omega_m), \mathbf{x}'(\omega_m)). \tag{7.15}$$

The SEK kernel k_{sek} contains a length-scale parameter: l_{sek}. A key consideration is whether these length scales should be independently modelled for each frequency, particularly since TDOAs at higher frequencies tend to have lower magnitudes, significantly affecting the kernel values for a fixed l_{sek}. However, increasing the number of hyperparameters in the GPR model elevates model complexity and raises the risk of overfitting.

The simulated impact locations are typically derived from structured experimental designs, such as uniform sampling over a 20 mm by 20 mm grid. Given the intermediate dataset size, reducing model complexity is crucial to achieving high generalisability. Therefore, it is preferable to model the multi-frequency composite kernel using a shared set of length scales l_{sek}. To facilitate this, normalisation preprocessing of the TDOA data is required to ensure comparability across different frequencies. This normalisation is achieved using the dispersion relations $v_g(\omega; \theta)$:

$$\Delta\mathbf{t}_{nor}(\omega_m) = \Delta\mathbf{t}(\omega_m) v_g(\omega_m; \theta = 0). \tag{7.16}$$

By combining physics-augmented data generation with multi-frequency kernel design, the proposed GPR model is expected to achieve accurate and robust impact localisation with enhanced generalisability while also providing uncertainty quantification.

7.2.4 Physics-regularised impact force deconvolution and uncertainty quantification

7.2.4.1 Regularised force deconvolution in frequency domain

Once the transfer function $\hat{h}(\omega; q, L_j)$ at the target location q is identified for each sensor $j \in \mathbb{N}_{1N_s}$, the impact force can be reconstructed using multi-sensor deconvolution in the frequency domain.

This process is formulated as a regularised inverse problem, as shown in Eq. (2.42), where Tikhonov(L2) regularisation—commonly known as Wiener deconvolution [22, 123, 124]—can be employed. The choice of the regularisation parameter λ_{reg} is crucial to balancing data fidelity and solution stability. Two popular data-driven selection methods are the L-curve criterion [164, 165] and Generalised Cross Validation (GCV) [162, 163]. GCV, in particular, provides a principled and automated approach for selecting λ_{reg} without requiring ground truth information. The GCV functional for multi-sensor frequency-domain deconvolution is given by:

$$\mathrm{GCV}(\lambda_{reg}) = \frac{\sum_{j=1}^{N_s}\sum_{k=1}^{N_f}\left|\frac{\lambda_{reg}}{\left|\hat{h}(\omega_k;q,L_j)\right|^2+\lambda_{reg}}\hat{s}(\omega_k;q,L_j)\right|^2}{\left(\sum_{j=1}^{N_s}\sum_{k=1}^{N_f}\frac{\lambda_{reg}}{\left|\hat{h}(\omega_k;q,L_j)\right|^2+\lambda_{reg}}\right)^2}, \tag{7.17}$$

where the optimal λ_{reg} is the value that minimises the GCV functional.

In addition to frequency-domain Tikhonov (L2) regularisation, various time-domain approaches have been developed to leverage the inherent sparsity of impact forces, which are typically compactly supported over a finite time window. Among these, sparse regularisation techniques [166–169] and wavelet-based regularisation methods [76,173,174] have gained prominence. These methods offer improved temporal resolution and enhanced robustness for impact force deconvolution, particularly in scenarios with limited measurement data.

However, a common limitation of both L1 and L2 regularisation is their tendency to underestimate the true force magnitude [191]. In the case of L2 regularisation, this underestimation is primarily due to excessive penalisation in the low-frequency range, resulting from the use of a constant regularisation parameter across all frequencies, as demonstrated in Eq. (2.42). To address this issue, this chapter adopts a frequency-dependent regularisation strategy, which adaptively adjusts the penalty across the frequency spectrum to improve force reconstruction accuracy.

7.2.4.2 Fidelity of transfer function estimations from FSDT and reference impact data

Although the FSDT model is constructed in a data-driven manner by sequentially identifying material properties and boundary conditions, it cannot fully replicate the sensor response to a given impact. This discrepancy arises from three primary factors:

- Model simplifications: The FSDT plate model neglects transverse normal strain and assumes a constant transverse shear strain through the plate thickness. Additionally, the boundary conditions are modelled using uniform spring stiffness along each edge. These simplifications limit its ability to fully capture the real-world structural dynamics.

- Sparse reference data: The accuracy of material property and boundary condition identification depends on the availability of reference data, which may be insufficiently dense to ensure precise reconstruction.

- Sensor frequency responses function variability: The sensor's inherent frequency responses function is affected by factors such as degradation and attachment quality, introducing further discrepancies.

As a result, the FSDT model serves as a LF approximation, while the reference impact data provide HF information. Accurate impact force reconstruction primarily relies on reference impact data, with the FSDT model serving as a supplementary source for additional physical constraints and calibration.

7.2.4.3 Strategies for transfer function estimation based on FSDT

Based on the constructed LF FSDT model and HF reference impact data, the transfer function $\hat{h}(\omega; q, L)$ for a target impact at an estimated location q can be obtained using various strategies:

1. Physical prior approach: Utilise the transfer function estimated by the FSDT model as an LF physical prior, while the HF reference impact data are employed to model the residual between the physical prior and the reference measurements.

2. Modal kernel design: Incorporate physical modal characteristics into GPR or RBF interpolation. For instance, integrating modal similarity into the GPR kernel ensures that interpolation is influenced not only by spatial proximity but also by modal resemblance, thereby improving accuracy.

3. RBF interpolation with adaptive regularisation: Perform interpolation/extrapolation of the transfer function separately using both HF reference transfer functions and LF FSDT transfer functions. An adaptive regularisation factor is introduced, defined based on the discrepancy between the interpolated FSDT results and theoretical FSDT predictions.

The choice among these depends on the FSDT model's fidelity and reference impact coverage:

- Strategy 1 is preferable for accurate FSDT models with sparse reference data.
- Strategy 2 improves interpolation accuracy but requires careful kernel design and a reliable modal basis.
- Strategy 3 offers a flexible compromise when FSDT accuracy is moderate and HF data are sparse.

In this work, Strategy 3 is adopted due to the intermediate-to-low accuracy of the data-driven FSDT model. While the LF model cannot be used directly as a prior mean or to calibrate HF estimates, it can still provide valuable information about the spatial complexity of local dynamics and the frequency-dependent quality of interpolation. Therefore, it is utilised to guide adaptive regularisation in force deconvolution.

7.2.4.4 Transfer function estimation and force deconvolution with adaptive regularisation

Let the HF and LF transfer function estimates at the reference impact locations Q be denoted by:

- $\hat{H}(\omega; Q, L)$: from experimental data;
- $\hat{H}_{FSDT}(\omega; Q, L)$: from the FSDT model.

Using RBF interpolation, the estimated transfer functions at a new location q are denoted as:

- $\hat{h}^{RBF}(\omega; q, L)$: interpolated from HF reference data,
- $\hat{h}^{RBF}_{FSDT}(\omega; q, L)$: interpolated from LF FSDT data.

The explicit RBF formulations for these interpolants are provided in [22]. Briefly, each interpolant combines a weighted sum of radial basis functions and a low-order polynomial to ensure well-posedness and smoothness:

$$
\begin{aligned}
\hat{h}^{RBF}(\omega; q, L) &= \sum_{i=1}^{N_i} \lambda_i \psi(|q - Q_i|) + \sum_{j=1}^{M} \varsigma_j p_j(q), \\
\hat{h}^{RBF}_{FSDT}(\omega; q, L) &= \sum_{i=1}^{N_i} \lambda_i^{FSDT} \psi(|q - Q_i|) + \sum_{j=1}^{M} \varsigma_j^{FSDT} p_j(q).
\end{aligned}
\tag{7.18}
$$

where $\psi(\cdot)$ represents the chosen radial basis function, and $p_j(\cdot)$ denotes a polynomial term included to ensure the well-posedness of the RBF interpolation.

The theoretical transfer function predicted by the FSDT model at location q is denoted as $\hat{h}_{FSDT}(\omega; q, L)$. The discrepancy between the RBF-interpolated transfer function and the theoretical FSDT prediction is quantified by their difference:

$$
\lambda_{reg}(\omega) = \text{cumsum}\left(\frac{1}{N_s} \sum_{j=1}^{N_s} \left| \hat{h}^{RBF}_{FSDT}(\omega; q, L_j) - \hat{h}_{FSDT}(\omega; q, L_j) \right|^2 \right), \tag{7.19}
$$

where cumsum denotes the cumulative sum operator applied across the frequency range. This adaptive, frequency-dependent regularisation term, $\lambda_{reg}(\omega)$, reflects the degree of mismatch between the physics-based (FSDT) model and the data-driven RBF interpolation. By incorporating this discrepancy into the regularisation term of the frequency-domain deconvolution formulation (see Eq. (2.42)), the solution is penalised more heavily in frequency bands where the interpolation error is high, thereby improving the robustness and accuracy of impact force reconstruction.

In addition to enhancing stability, this framework also enables uncertainty quantification. Specifically, uncertainty in the estimated impact location q—obtained via MF GPR model—can be propagated through the force deconvolution pipeline. By performing Monte Carlo sampling over the posterior distribution of q, and subsequently executing force deconvolution for each sample, a distribution of reconstructed impact forces $f(t)$ can be obtained. This approach allows for the estimation of credible intervals and confidence bounds, thereby quantifying the epistemic uncertainty in the reconstructed force due to localisation ambiguity and model variability.

7.3 Experimental Validation

Experimental impact tests were conducted to capture the structural response and impact force history of a sensorised fibre-reinforced composite flat panel (FP) subjected to hammer impacts, as illustrated in Fig. 7.3(a). This composite FP was also utilised for impact localisation validation

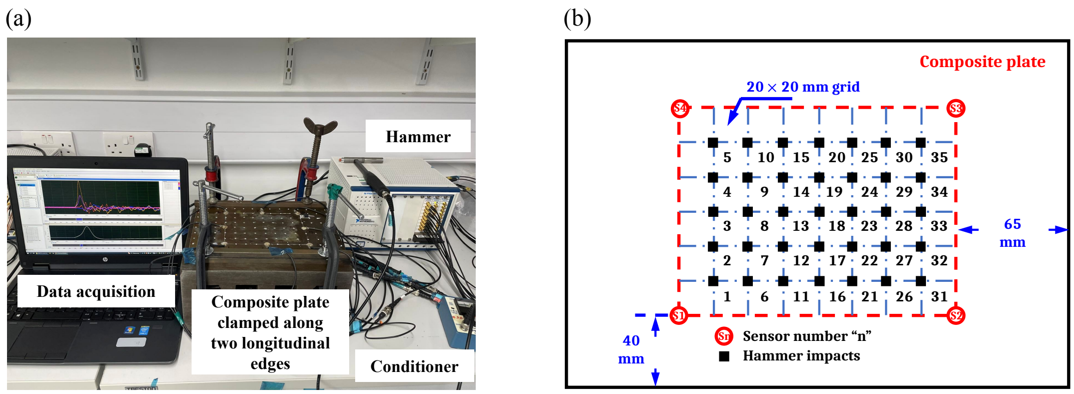

Figure 7.3: Impact testing using handheld hammer on a composite FP: (a) experimental setup, (b) layout of the FP illustration.

in Chapter 3-Chapter 5 and impact force deconvolution in Chapter 6. Detailed specifications of the composite FP are provided in Section 3.4 and Section 4.4, while the reference lamina elastic properties are listed in Table 4.1. As this study focuses on a purely data-driven approach, these reference material properties are used solely for the accuracy validation of the estimated properties.

During impact testing, the FP was clamped along its two longer edges, leaving the two shorter edges free. Impact excitation was generated using a PCB Piezotronics 086C03 hammer, which has a weight of 160 g. The layout of the FP and the hammer impact locations are illustrated in Fig. 7.3(b), where the impact points are marked as black solid squares. These impacts were applied at the vertices of a 20 × 20 mm grid. During each hammer strike, four PZT sensors recorded the structural responses, while the ICP quartz force sensor integrated within the hammer measured the impact force history.

The resulting sensor signals and corresponding impact forces were used to validate the proposed physics-guided impact identification framework with uncertainty quantification. A subset of the data was used to construct the model, while the remaining portion was reserved for independent testing and performance evaluation.

7.4 Impact Identification Results and Analysis

7.4.1 Sparse data-driven FSDT plate modelling

7.4.1.1 Identification of material property

As demonstrated in Chapter 5, the combination of four reference impacts and a sparse sensor network consisting of four PZT sensors enables the identification of GVPs with high accuracy. Given this effectiveness, the same configuration is expected to yield reliable estimates of the material properties. Considering the dominance of low-frequency modes in impact dynamics, material property identification is focused on the dispersion characteristics within the frequency range of 1–10 kHz. By matching the estimated dispersion relations with experimental measurements obtained from the four reference impacts, the material properties of the FSDT plate are identified through the maximisation of the log-likelihood function defined in Eq. (7.5).

As illustrated in Fig. 7.4(a), the log-likelihood function is maximised based on four reference impacts numbered 12, 14, 22, 24 shown in Fig. 3.3, across three frequency ranges, where N_f denotes the number of frequency points considered, spanning from 1 kHz to N_f kHz in 1 kHz increments. With 100 generations in the GA, all three cases ($N_f = 2$, $N_f = 5$, and $N_f = 10$) converge to a stable maximum.

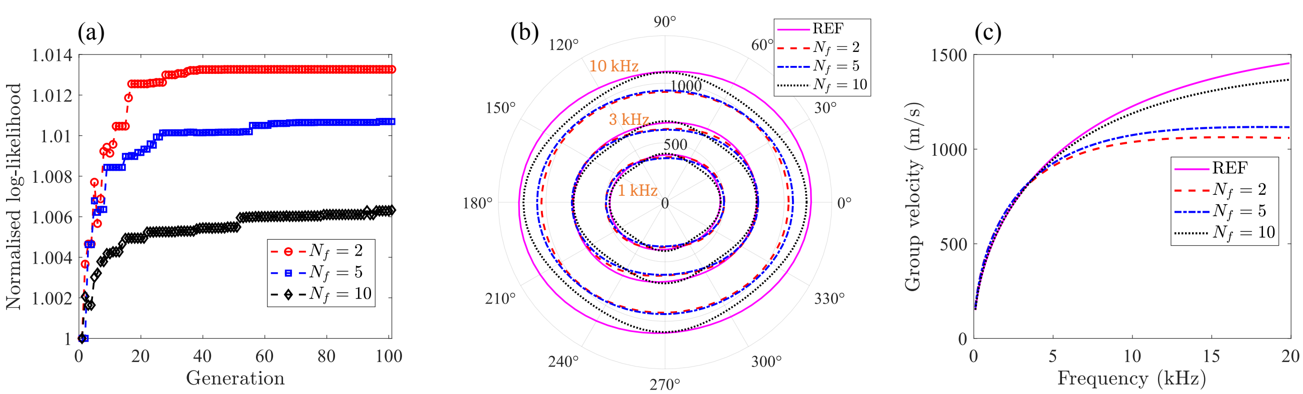

Figure 7.4: Material properties identification with four reference impacts: (a) optimisation convergence, (b) optimised GVPs, (c) optimised dispersion curves (A0 mode).

The comparison between the GVPs derived from the optimised material properties and those corresponding to the reference properties in Table 4.1 is presented in Fig. 7.4(b), where the reference GVPs are depicted as solid magenta lines and the optimised GVPs as dashed lines. Among the three cases, the $N_f = 10$ optimisation yields the most accurate GVPs, as the inclusion of a wider frequency range allows the estimated GVPs to align more closely with those obtained from the reference material properties.

A noticeable trend is observed: as the frequency increases, the reference GVPs tend to be higher than the optimised ones. This discrepancy can be attributed to two main factors: (1) the FSDT model inherently overestimates GVPs at higher frequencies compared to experimental measurements, and (2) at lower frequencies, where the TDOA values are larger, the optimisation process prioritises the low-frequency components to maximise the likelihood function. The comparison of dispersion relations at $\theta = 0°$ between the optimised and reference models is illustrated in Fig. 7.4(c). For $N_f = 2$ and $N_f = 5$, significant deviations from the reference dispersion relations occur at higher frequencies, whereas for $N_f = 10$, the estimated dispersion relations remain more consistent across the entire frequency range. This improvement can be attributed to the integration of a wider frequency spectrum in the optimisation, leading to enhanced accuracy in the high-frequency range.

Despite the observed discrepancies between the reference and optimised GVPs, particularly at higher frequencies, the optimised GVPs remain highly accurate for impact localisation, especially in the low-frequency range. This is because they are directly optimised based on reference experimental impact data, ensuring reliability in practical applications.

Table 7.2 summarises the identified plate-level material properties for different frequency ranges. The reference values (REF) represent the known material properties of the composite FP, while the optimised values correspond to different N_f cases. The density (ρ) and plate thickness (d) remain relatively consistent across the cases, exhibiting only slight variations due to the optimisation process. However, the bending stiffness components (D_{11}, D_{22}, and D_{66}) show more pronounced differences, particularly for D_{11}, which exceeds the reference value.

These variations highlight the inherent complexity of the optimisation problem, which features multiple local minima that yield dispersion relations and GVPs closely matching experimental data. Given that experimental measurements may not perfectly align with the theoretical reference properties due to factors such as manufacturing variations and measurement noise, achieving an exact match with the reference material properties is nearly impossible. Instead, the optimisation process converges to a local minimum that ensures highly accurate GVPs, particularly in the low-frequency range, where wave propagation characteristics are most critical for impact localisation.

Table 7.2: Identified plate-level material properties in modelling FSDT plate from the reference impact data by matching dispersion relations.

Cases	ρ (kg/m^3)	d (mm)	I_1 (kg/m^2)	D_{11} (Pa $\cdot$ m^3)	D_{22} (Pa $\cdot$ m^3)	D_{66} (Pa $\cdot$ m^3)
REF	1600	4.00	6.40	511.0	269.9	125.4
$N_f = 2$	1700	3.92	6.67	755.1	198.6	179.5
$N_f = 5$	1543.8	4.20	6.48	692.8	191.8	114.5
$N_f = 10$	1602.2	4.19	6.73	820.3	396.3	21.5

7.4.1.2 Identification of boundary condition

The modal characteristics of a structure can be estimated from the responses of PZT sensors and transfer functions when the impact forces are known. Impact forces, such as half-sine impulses, exhibit their highest spectral amplitude in the low-frequency range. This amplifies the contribution of low-frequency components in the PZT sensor signals, making it easier to identify low-frequency modes from these signals compared to transfer functions. In contrast, transfer functions tend to exhibit an energy shift towards higher frequencies, facilitating the identification of higher-frequency modes.

To ensure that each reference impact contributes equally to the modal identification process, the spectra and transfer functions of the reference impacts are normalised before averaging. Fig. 7.5(a) illustrates mode identification using PZT sensor signals and transfer functions obtained from the sparse reference impact data. A comparison of the spectral distributions of both the PZT sensor response and the transfer function (TF) reveals that lower-frequency components (below 2000 Hz) dominate the PZT sensor responses. The relatively low spectral amplitude at higher frequencies makes it challenging to accurately identify high-frequency modes from PZT sensor signals alone. In contrast, the transfer function exhibits a spectral energy shift towards higher frequencies, enabling the identification of high-frequency modes while struggling to capture the lowest mode due to a small peak.

The PZT sensor response and the transfer function provide complementary modal information.

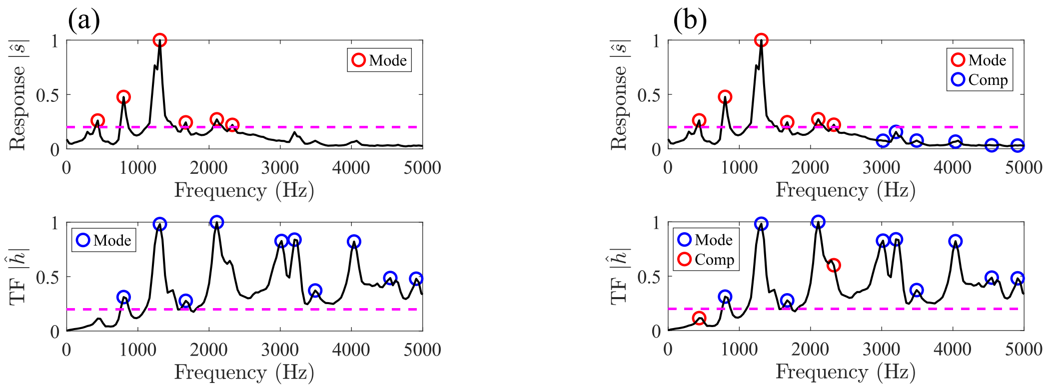

Figure 7.5: Mode identification from PZT sensor signals and transfer functions.

As shown in Fig. 7.5(b), combining both methods allows for the identification of modes across a broader frequency range, capturing both low-frequency and high-frequency modes more effectively. This combined approach enhances the accuracy of mode identification, which is crucial for excitation transmissibility estimation and subsequent boundary condition identification.

As shown in Fig. 7.3, the composite FP was clamped along its longer edges (though not perfectly) while the shorter edges remained free. To model these boundary conditions in a simplified manner, artificial translational and rotational springs were introduced at the plate edges. The design variables consist of four spring stiffness values, one for each edge, with the assumption that the translational and rotational stiffnesses are identical for a given edge.

Although the two shorter edges of the experimental FP are nominally free, their stiffness values were still included in the model, constrained within the range [0, 0.5]. Meanwhile, the stiffness values of the two clamped edges were bounded within [0, 1]. To ensure numerical stability and avoid excessively large stiffness values in optimisation, the stiffness parameters were normalised using the transformation:

$$k_{bc}^{nor} = \frac{\log k_{bc}}{10}, \tag{7.20}$$

where a maximum real stiffness value of 1e10 corresponds to a perfectly clamped edge. Beyond this value, further increases in stiffness do not affect the simulated natural frequencies in the FSDT model.

Fig. 7.6 presents the Pareto front of the minimisation process, balancing the natural frequency loss L_{nf} and excitation transmissibility loss L_{et}. The Pareto front exhibits an L-curve, where significant variations in one loss function occur along the two distinct edges of the 'L', while the other loss remains nearly unchanged. This characteristic suggests that the optimal solution should be selected at the transition point of the L-curve, where a balanced trade-off between the two loss functions is achieved.

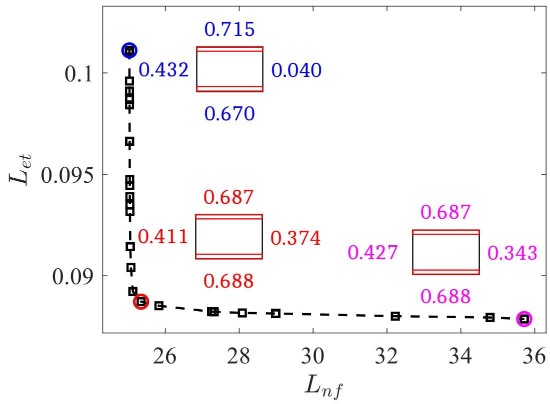

Figure 7.6: The Pareto front in the L-curve shape for boundary condition identification.

At the transition point, marked by the red circle in Fig. 7.6, the identified normalised stiffness values for the two longitudinal edges (clamped but not perfectly rigid) were 0.687 and 0.688. These correspond to real stiffness values more than 100 times greater than those of the two shorter edges, which were nominally free. This indicates that the longitudinal edges serve as the effective boundary conditions, while the shorter edges have a negligible influence. The identified boundary condition configuration aligns well with the experimental setup, thereby validating the effectiveness of the proposed boundary condition identification method.

To further validate the identified boundary conditions, Table 7.3 presents the natural frequencies of the first 10 modes, extracted from the reference impact data and compared with those identified using the optimised FSDT model. The results indicate an average discrepancy of approximately 80 Hz between the experimentally extracted and model-predicted natural frequencies. This frequency deviation suggests that while the identified boundary conditions provide a reasonable approximation, the transfer function estimated from the constructed FSDT model may exhibit slight peak shifts compared to the experimentally obtained transfer function from reference impact data. These discrepancies may arise from unmodelled factors such as localised boundary flexibility, material inhomogeneities, or additional damping effects, which could be further refined in future studies.

Table 7.3: Natural frequencies extracted from the reference impact data and estimated from the constructed FSDT plate model.

Mode	1	2	3	4	5	6	7	8	9	10
Extracted ω_m (Hz)	436.4	800.0	1309.1	1672.7	2109.1	2327.3	2727.3	3018.2	3200.0	3490.9
Estimated $\bar{\omega}_m$ (Hz)	459.9	726.0	1272.0	1545.0	1887.2	2371.7	2774.5	3032.4	3273.8	3514.6

7.4.2 Physics-augmented impact localisation

Based on sparse experimental reference impact data and the identified GVPs (approximated physics), a MF GPR model was constructed and trained to locate a total of 35 experimental impacts on the composite FP. The approximated physics enables the generation of LF physics-augmented data, which provides additional training information for the GPR model. For the target structure, these physics-augmented data points were generated using uniform sampling on a 20 × 20 mm grid across the structure, ensuring comprehensive spatial coverage.

7.4.2.1 Impact localisation: low-fidelity, high-fidelity and multi-fidelity

To evaluate the influence of the identified GVPs (approximated physics) on impact localisation performance, three different localisation approaches were compared: (1) HF localisation using only sparse experimental impact data, (2) LF localisation using solely physics-augmented data, and (3) MF localisation incorporating both experimental and physics-augmented data. Fig. 7.7 illustrates the localisation results for these three approaches, specifically for the frequency range $N_f = 2 \rightarrow 2$. Here, the notation $N_f = f_1 \rightarrow f_2$ indicates that the GVPs (material properties) were identified based on dispersion relations within the frequency range of 1 kHz to f_1 kHz, while the impact localisation process utilised GVPs derived from the frequency range of 1 kHz to f_2 kHz.

The HF GPR model, trained exclusively on four sparse experimental reference impacts, struggles to capture the underlying wave propagation physics that govern the relationship between input TDOA and impact location. Due to data sparsity, the model adopts a constant mean function based on the reference impact data, with a large characteristic length scale. Consequently, the covariance function contributes minimally compared to the noise variance, causing the RBF kernel to fail in capturing variations in the data. Consequently, as depicted in Fig. 7.7(a), while the HF GPR model exhibits high accuracy for localising the reference impacts, it lacks extrapolation

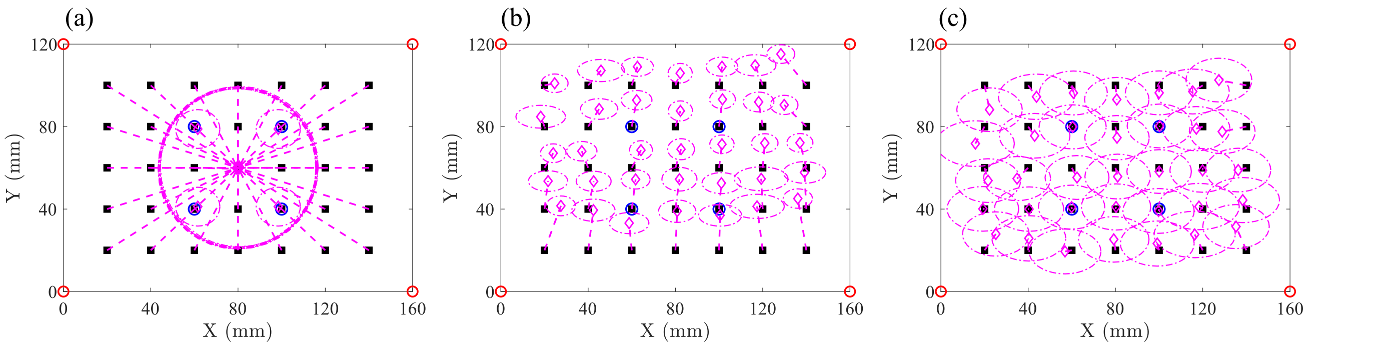

Figure 7.7: Impact localisation based on three approaches: (a) HF estimation based on sparse experimental impact data, (b) LF estimation based on physics-augmented data, (c) MF estimation combining sparse experimental and physics-augmented data.

capability and defaults to predicting impacts outside the reference impact region at the mean of the reference impacts.

By contrast, the LF GPR model, trained on the densely sampled physics-augmented data, achieves intermediate accuracy but significantly improved generalisability across the structure, as shown in Fig. 7.7(b). Since these physics-augmented data points are generated using the approximated GVPs, the LF GPR model can predict impact locations across the entire structure. However, due to the imperfection of the approximated physics and the absence of experimental reference data, the LF GPR model maintains only moderate accuracy, even for the reference impacts used to approximate the GVP physics.

The MF GPR model integrates the strengths of both approaches, combining the high generalisability of physics-augmented data with the high accuracy of sparse experimental reference impacts. As shown in Fig. 7.7(c), this hybrid approach achieves both high localisation accuracy and strong extrapolation capability, demonstrating superior performance across the entire structure. The combination of experimental and physics-augmented data allows the model to refine its predictions, ensuring both precision near reference impacts and reliable localisation in unexplored regions.

7.4.2.2 Impact localisation: variability in frequency ranges

The notation $N_f = f_1 \rightarrow f_2$ underscores the impact of frequency range selection on both material property identification and impact localisation accuracy. Fig. 7.8 presents the results of MF impact localisation using different frequency ranges. A comparison between localisation results for $N_f =$

$5 \rightarrow 2$ in Fig. 7.8(a), $N_f = 10 \rightarrow 2$ in Fig. 7.8(b) and $N_f = 5 \rightarrow 5$ in Fig. 7.7(c) reveals that the $N_f = 2 \rightarrow 2$ case achieves the highest localisation accuracy. In this case, nearly all predicted impact locations fall within the 95 % localisation confidence region, denoted by the dashed ellipse. This improvement can be attributed to the fact that when $f_1 = f_2 = 2$, the identified GVPs at these frequencies align most closely with the experimental TDOA data, leading to the most accurate impact localisation. Conversely, when $f_1 > f_2 = 2$, higher-frequency components contribute to GVP identification but are not utilised in impact localisation, which reduces the accuracy of the estimated GVPs at low frequencies and consequently degrades impact localisation performance.

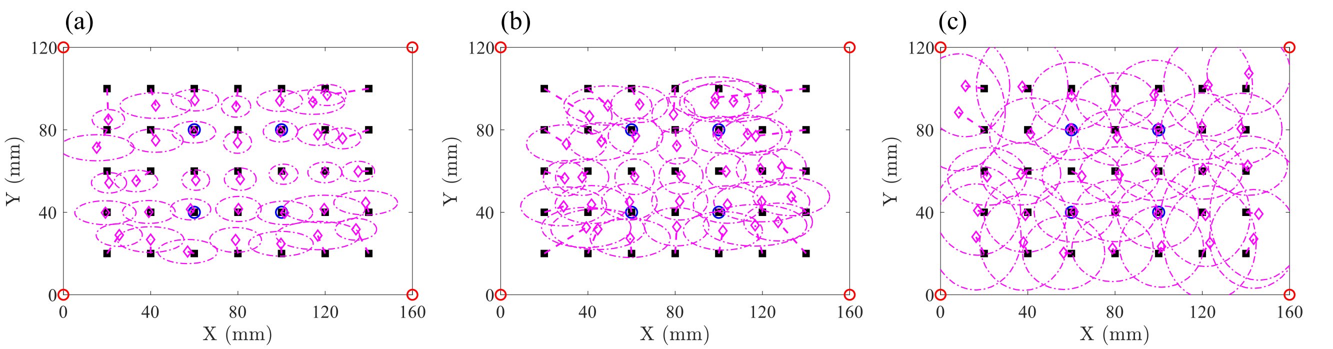

Figure 7.8: Multi-fidelity impact localisation based on different frequency ranges: (a) $N_f = 5 \rightarrow 2$, (b) $N_f = 10 \rightarrow 2$, (c) $N_f = 5 \rightarrow 5$.

Additionally, comparing $N_f = 2 \rightarrow 2$ in Fig. 7.7(c) to $N_f = 5 \rightarrow 5$ in Fig. 7.8(c) further demonstrates that a lower frequency range yields more robust and reliable impact localisation. This observation stems from the fact that higher-frequency GVPs correspond to higher wave velocities, resulting in smaller TDOA values that are more sensitive to random noise. The increased influence of noise at higher frequencies propagates through the GVP identification process, leading to greater uncertainties in the estimated GVPs and, subsequently, in impact localisation. Therefore, it is recommended to prioritise lower-frequency ranges for impact localisation to enhance stability and accuracy.

7.4.2.3 Impact localisation: variability in reference impacts

By carefully selecting the reference impact locations, impact identification can be reformulated as a pure interpolation problem. In contrast, in the previous setup, most impact locations (numbers 1–35) fell outside the four reference impact points, introducing extrapolation errors.

As demonstrated in Chapter 3, using nine strategically chosen reference impacts—numbered [1,3,5,16,18,20,31,33,35]—enables accurate interpolation-based impact localisation, achieving a mean localisation error of approximately 10 mm.

These nine HF reference impacts were utilised for material property identification, facilitating physics-augmented MF impact localisation. Fig. 7.9 presents the localisation results with these nine reference impacts and a frequency reduction from $N_f = 5 \rightarrow 2$. As shown in Fig. 7.9(a), HF estimation based solely on the nine HF experimental reference impacts achieves a high localisation accuracy, with a mean error of 5.9 mm. In comparison, the MF estimation, which integrates the identified GVP physics with the same nine HF reference impacts, results in a mean localisation error of 6.0 mm. As expected, increasing the number of HF data points enhances interpolation accuracy within the reference coverage area. However, the MF model, by incorporating physics-based constraints, improves extrapolation performance beyond the reference coverage.

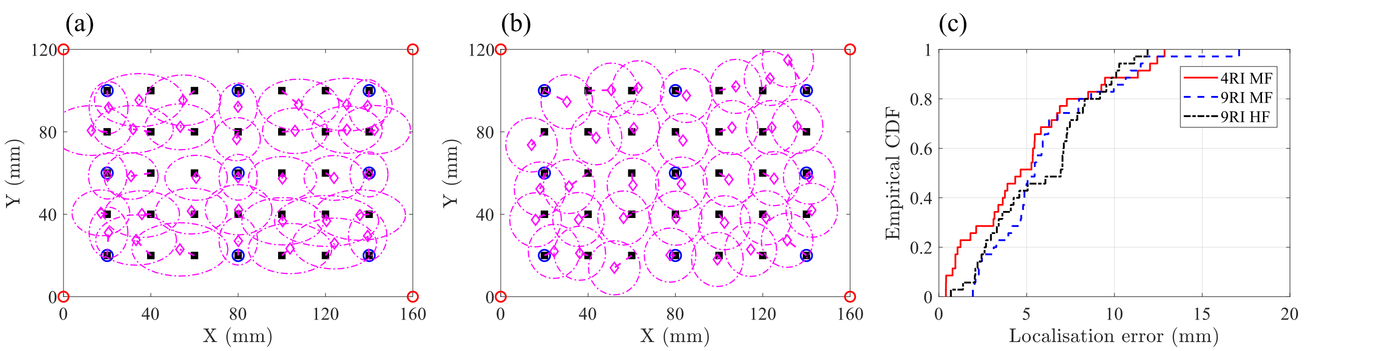

Figure 7.9: Impact localisation with nine reference impacts and $N_f = 5 \rightarrow 2$: (a) HF estimation, (b) MF estimation, (c) empirical CDF of localisation error.

Compared to MF estimation using only four HF reference impacts, as illustrated in Fig. 7.7(c) and Fig. 7.9(c), the MF model with four HF reference impacts achieves a mean localisation error of 5.0 mm, which is comparable to the HF and MF estimations using nine HF reference impacts. This result highlights the efficiency of the proposed MF approach, demonstrating that accurate localisation can be achieved with a minimal amount of HF data, thereby reducing experimental costs while maintaining high performance.

7.4.3 Physics-regularised impact force deconvolution

7.4.3.1 Low-fidelity transfer functions from FSDT model

With the completion of the FSDT model through material property and boundary condition identification, the system transfer function can be derived from the modal characteristics using the principle of superposition. Fig. 7.10 presents the mean transfer function estimates across four sensors for two reference impacts, numbered 12 in (a) and 14 in (b), based on the constructed FSDT model. However, as indicated in Table 7.3, discrepancies exist between the identified natural frequencies and the actual values extracted from the reference impact data. Consequently, the transfer function estimated from the original FSDT model (denoted as 'FSDT Orig' in the figure legend) exhibits slight peak shifts when compared to the experimentally obtained transfer function from reference impact data (denoted as 'EXP').

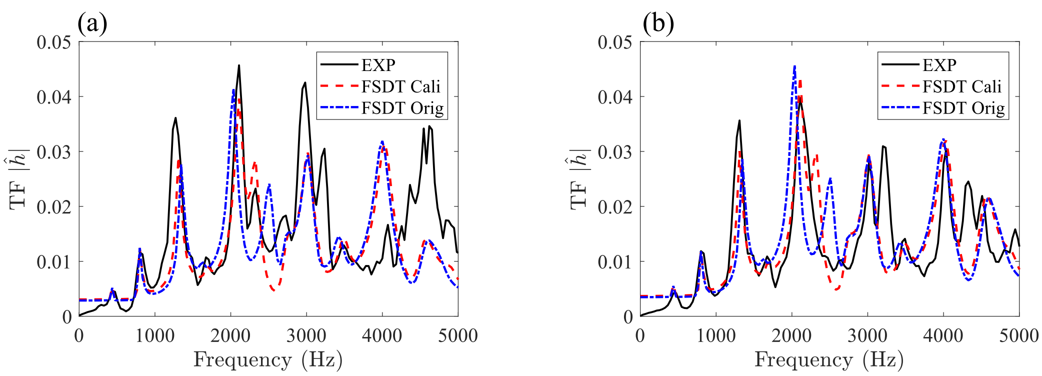

Figure 7.10: Transfer function estimates based on FSDT model: (a) reference impact 12, (a) reference impact 14.

To improve the accuracy of the transfer function, the FSDT model was further calibrated by adjusting the identified natural frequencies to match their experimentally obtained counterparts. This calibration process ensures consistency in the frequency domain, aligning the peak locations of the modelled transfer function with those of the experimental data. As shown in Fig. 7.10, the calibrated FSDT transfer function ('FSDT Cali') demonstrates a significantly improved match with the experimental data in terms of peak positions.

However, despite this calibration, notable discrepancies persist in the peak magnitudes, particularly at higher frequencies. These deviations can be attributed to the simplified assumptions in the FSDT model and the errors in the data-driven FSDT modelling. Consequently, even after calibration, the transfer function estimates derived from the FSDT model remain LF approximations, in contrast to the HF experimental reference data.

7.4.3.2 Transfer function interpolation/extrapolation using RBF method

In location-based transfer function interpolation and extrapolation, the accuracy of the RBF method is highly dependent on the spatial distribution of reference impacts and the spatial correlation between reference impacts and the target impact. To illustrate location-based transfer function interpolation and extrapolation, Fig. 7.11 presents the results based on the calibrated FSDT model and four reference impacts, numbered 12, 14, 22, and 24.

For transfer function interpolation, shown in Fig. 7.11(a), two target impacts, 13 and 18, are considered. Target impact 13 is positioned between reference impacts 12 and 14, while target impact 18 is located centrally among all four reference impacts. It can be observed that for both target impacts, the interpolated transfer functions exhibit higher accuracy in the low-frequency range but reduced accuracy at higher frequencies. Additionally, modes within the 2000 Hz to 3000 Hz range are more pronounced for target impact 13 but relatively weaker for target impact 18. This suggests that the RBF method effectively captures and preserves the mode contributions within the interpolation region.

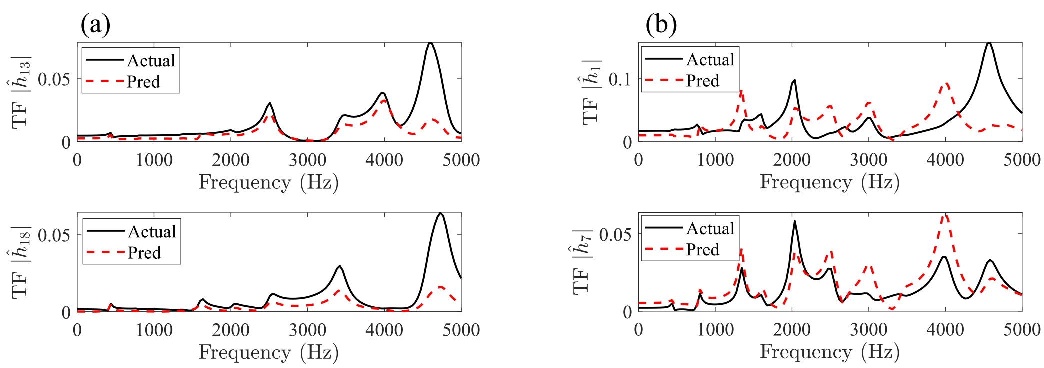

Figure 7.11: Transfer function interpolation/extrapolation based on FSDT model: (a) interpolation of impact 13 and 18, (b) extrapolation of impact 1 and 7.

In contrast, Fig. 7.11(b) illustrates the transfer function extrapolation for target impacts 1 and 7, both of which lie outside the spatial coverage of the four reference impacts. It is evident that the accuracy of the extrapolated transfer functions cannot be guaranteed across the entire frequency range. Both underestimation and overestimation of peak amplitudes are observed, highlighting the limitations of location-based transfer function extrapolation. These errors arise due to the lack of sufficient reference data beyond the known impact region, leading to a less reliable estimation of structural dynamics in extrapolated areas.

The location-based transfer function estimation using the RBF method highlights the critical role of the spatial distribution of reference impacts in achieving high-precision interpolation and capturing higher-frequency modes. Fortunately, due to the dominance of low-frequency modes in impact dynamics, the RBF method remains effective in estimating transfer functions at low frequencies even with sparse data, leading to accurate impact force deconvolution.

7.4.3.3 Constant regularisation (GCV) and adaptive regularisation

For frequency-domain impact force deconvolution, as defined in Eq. (2.42), the regularisation parameter λ_{reg} plays a critical role in suppressing noise amplification caused by uncertainties in sensor signals and transfer function estimates. Traditionally, λ_{reg} is treated as a constant, applying uniform regularisation across all frequencies. The optimal constant value is typically selected using the GCV criterion, as described in Eq. (7.17). However, this global approach often introduces excessive regularisation in the low-frequency range, leading to underestimation of the reconstructed impact force [191].

Fig. 7.12 compares the performance of constant and adaptive regularisation strategies, where the latter is defined based on the FSDT model as in Eq. (7.19). The constant regularisation parameters for impacts 12 and 18 are determined using GCV, which identifies optimal values of 3.455×10^{-6} and 1.193×10^{-6}, respectively, as indicated by the red markers in Fig. 7.12(a).

Impact 12 serves as one of the HF experimental reference impacts used in FSDT modelling and RBF-based transfer function estimation. For this case, the RBF interpolated transfer function exhibits excellent agreement with both experimental and FSDT predictions in both high- and low-frequency regions. Consequently, the adaptive regularisation $\lambda_{reg}(\omega)$ is virtually negligible—on the order of 10^{-40}—due to floating-point numerical limits. As shown in Fig. 7.12(b), this minimal regularisation avoids excessive smoothing and leads to improved force reconstruction compared to constant regularisation, which tends to underestimate the peak force due to oversuppression of low-frequency components.

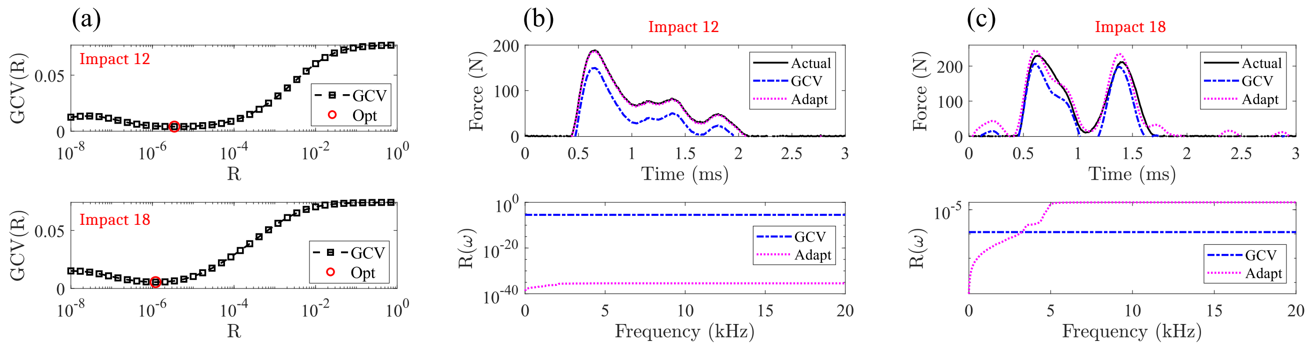

Figure 7.12: Impact force deconvolution based on RBF interpolated transfer function using four reference impacts, with constant and adaptive regularisation: (a) contant regularisation parameter determined by GCV, (b) force deconvolution for impact 12, (c) force deconvolution for impact 18.

In contrast, impact 18 is in the middle of the four HF reference impacts, allowing for imperfect transfer function interpolation. In this case, the adaptive regularisation $\lambda_{reg}(\omega)$ increases significantly with frequency. Below 4 kHz, the adaptive $\lambda_{reg}(\omega)$ remains smaller than the constant GCV-derived value, while at higher frequencies, it surpasses the constant value, as shown in Fig. 7.12(c). Despite this, the adaptive approach results in a more accurate force estimate overall. It avoids the peak underestimation seen with constant regularisation and slightly overestimates the peak force to approximately 15 N—corresponding to a 6.5% deviation from the ground truth. This outcome confirms that low-frequency components, which dominate impact dynamics, are especially sensitive to regularisation strength. To minimise underestimation, regularisation should be carefully modulated across frequencies—lighter at low frequencies and stronger at high frequencies. The adaptive scheme achieves this balance and improves the fidelity of impact force reconstruction.

7.4.3.4 Impact force reconstruction based on extrapolated transfer functions

Force reconstruction deteriorates as the target impact moves further from the region covered by the HF reference impacts, transforming the problem into one of transfer function extrapolation. Fig. 7.13 illustrates the impact force deconvolution for impacts numbered 7 and 2, based on extrapolated transfer functions using the RBF and SF methods. Since these impacts lie outside the four HF reference impacts, their transfer functions are extrapolated and therefore less accurate, leading to an underestimation of the reconstructed forces compared to the actual forces.

The SF method, as detailed in [183], which extrapolates by adopting the nearest reference transfer function, results in the most inaccurate force reconstruction, often distorting the force waveform. In contrast, the RBF method more accurately preserves the force shape, benefiting from its consistency in transfer function estimation and its 'minimum energy' property.

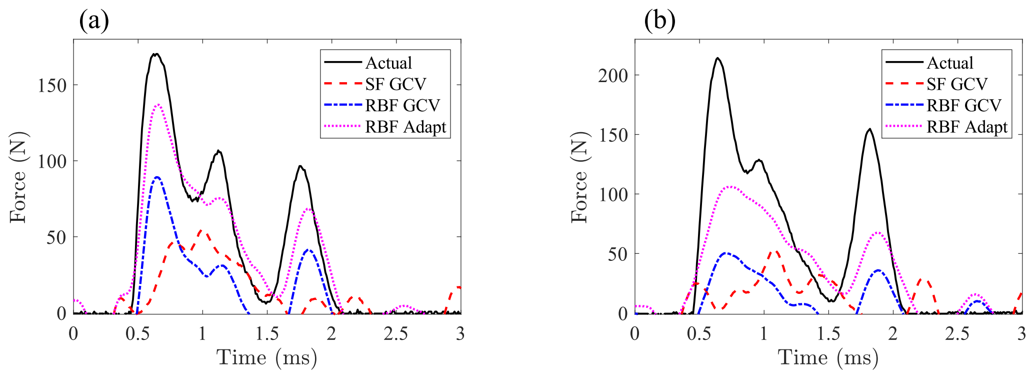

Figure 7.13: Impact force deconvolution based on extrapolated transfer functions using four reference impacts: (a) impact 7, (b) impact 2.

Furthermore, consistent with Section 7.4.3.3, RBF with adaptive regularisation yields a more accurate force estimation compared to constant regularisation. Comparing force reconstructions for the two target impacts, it is evident that greater distance from the reference impacts results in lower reconstructed force magnitudes, due to increased inaccuracies in transfer function extrapolation.

7.4.3.5 Impact force reconstruction with increased HF reference impacts

Two strategies are considered to improve force deconvolution accuracy across the structure: (1) increasing the number of HF reference impacts and (2) enhancing the accuracy/fidelity of the LF model. The first approach is more practical, as increasing the number of HF reference impacts allows for more comprehensive coverage of the structure, facilitating accurate transfer function interpolation. In contrast, improving the LF model's accuracy to replicate HF experimental data requires detailed structural information—such as precise material properties and boundary conditions—and higher-order modelling techniques, such as FEA. Due to its data-driven nature and boundary condition simplification, the FSDT model alone cannot achieve HF accuracy.

By increasing the number of HF reference impacts from 4 to 9, both impacts 7 and 2 fall within the coverage region of these reference impacts. Fig. 7.14 illustrates the force deconvolution results for these two impacts based on interpolated transfer functions using nine reference impacts. Once again, the RBF method demonstrates greater robustness than the SF method in transfer function estimation, consistently capturing the actual force waveform, whereas the SF method fails for impact 2. Additionally, the RBF method exhibits peak force underestimation, though to a lesser extent with adaptive regularisation. Compared to constant regularisation, adaptive regularisation further mitigates peak force underestimation. For both impacts, the relative peak force error remains within 7%.

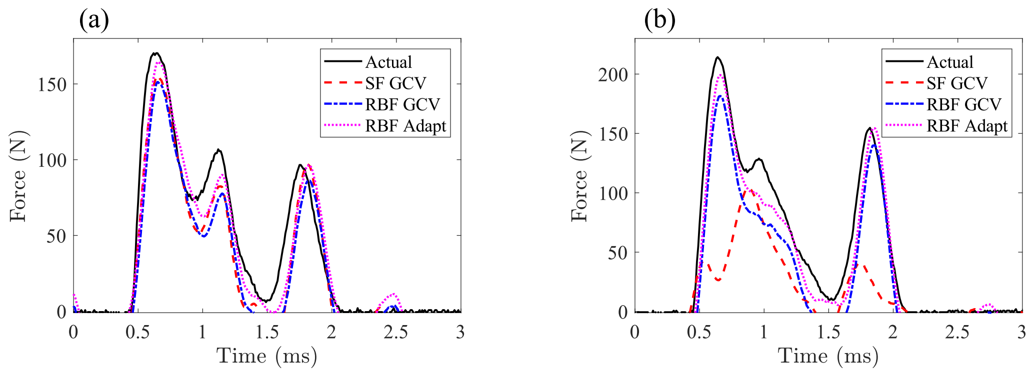

Figure 7.14: Impact force deconvolution based on interpolated transfer functions using nine reference impacts: (a) impact 7, (b) impact 2.

7.4.3.6 Uncertainty quantification of impact force estimation

The preceding analysis of transfer function estimation and impact force deconvolution, presented in Section 7.4.3.3 to Section 7.4.3.5, was conducted under the assumption of known impact locations. However, in practical applications, impact localisation involves estimation with uncertainty. The physics-augmented MF GPR framework used for impact localisation provides both a predictive mean and variance, enabling the propagation of localisation uncertainties into force reconstruction. Fig. 7.15 illustrates the impact force deconvolution and uncertainty quantification for three impacts (numbered 18, 7, and 2), based on GPR-estimated impact location means (with associated variances) and RBF-based transfer function interpolation.

Since transfer function estimation is location-dependent, the discrepancy in force deconvolution between the actual impact location and the GPR-predicted mean location reflects the localisation error. For impacts 18, 7, and 2, these localisation errors are 5.0 mm, 5.5 mm, and 6.9 mm, respectively. The difference between the deconvolved forces at the ‘given location’ (dashed red) and the ‘predicted mean’ (dashed blue) increases from Fig. 7.15(a) to (c). Notably, for impact

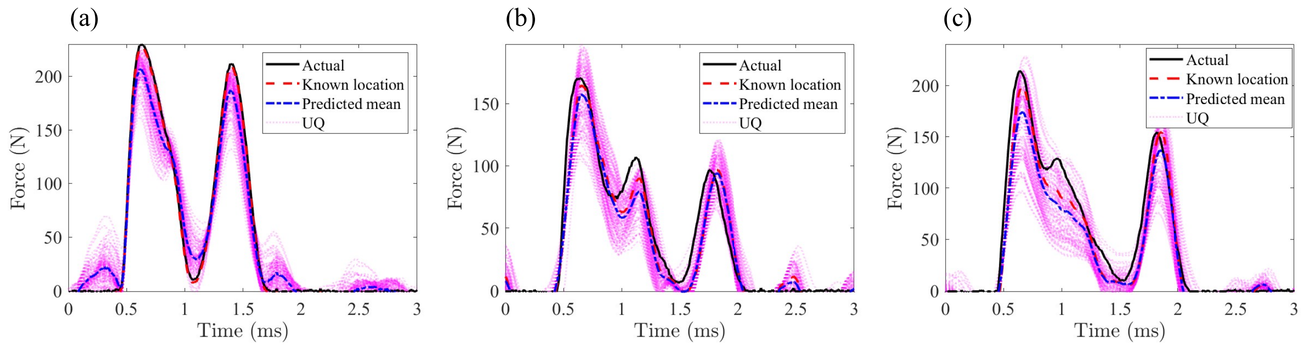

Figure 7.15: Impact force deconvolution and uncertainty quantification based on localised locations using nine HF reference impacts: (a) impact 18, (b) impact 7, (c) impact 2.

2, shown in Fig. 7.15(c), the predicted mean falls outside the coverage region of the nine HF reference impacts. This results in transfer function extrapolation, which significantly overestimates the transfer function, leading to substantial underestimation of the reconstructed impact force. In contrast, for impacts 18 and 7, where the 95% confidence interval of the estimated impact location remains within the HF reference coverage, the mean force deconvolution is more accurate.

The uncertainty in deconvolved forces is influenced by the predictive variance of impact localisation. For impacts 18, 7, and 2, the SDs of localisation errors in the x- and y-coordinates are [8.4, 7.7] mm, [8.8, 7.5] mm, and [9.7, 7.5] mm, respectively. The increasing trend in localisation SDs corresponds to the growing uncertainty in the deconvolved forces observed in Fig. 7.15.

7.5 Summary

Accurate impact force reconstruction via deconvolution requires reliable estimation of transfer functions. However, obtaining these at all potential impact locations is impractical. To overcome this limitation, this study explores sparse, data-driven interpolation using RBF and SF, which estimate transfer functions from a limited number of reference impacts. The effectiveness of these methods depends on the spatial coverage of reference data and the resolution of the corresponding mode shapes.

To improve accuracy and generalisation, a data-driven FSDT model is developed directly from the measured reference data without requiring prior knowledge of the structure's geometry or material properties. This model captures the essential structural dynamics by leveraging dispersion relations and modal characteristics, enabling the augmentation of training data for MF GPR-based localisation. This augmentation significantly improves localisation performance, particularly in extrapolation scenarios beyond the reference impact grid. Furthermore, by incorporating mode shape complexity, the framework allows for adaptive regularisation in impact force deconvolution, while uncertainties in localisation are systematically propagated through to force estimation.

Overall, the proposed approach enhances both interpolation and extrapolation accuracy in impact identification tasks and offers a generalisable and computationally efficient solution for SHM applications. However, it also inherits inherent limitations. The TDOA method and transfer function-based deconvolution are both sensitive to EOV, such as temperature fluctuations or boundary condition changes. Additionally, transfer functions may degrade in accuracy if impact-induced damage is present during the event. The FSDT-based modelling may not be valid for more complex or highly heterogeneous structures, particularly those with multiple stiffeners or curved surfaces. Finally, the framework was validated only on a single flat composite panel, which may limit generalisability until broader testing is conducted on diverse structural configurations.

Chapter 8

Conclusions and Future Work

Highlights:

- Summarise the key contributions and findings of the thesis across impact localisation and force reconstruction.
- Reflect on key modelling assumptions—such as linearity, undamaged media, and data sparsity—and their impact on method development and structural health monitoring applicability.
- Explore future research directions to improve the real-time capability, generalisability, and practical deployment of structural health monitoring systems.

8.1 Conclusions

As outlined in Chapter 1, the central objective of this thesis was to develop robust, efficient, interpretable, and scalable methodologies for impact identification in composite structures by integrating structural dynamics, wave propagation theory, and machine learning. Composite structures, due to their inherent anisotropy, the frequent presence of stiffening elements, and exposure to Environmental and Operational Variability (EOV), pose significant challenges for accurate and generalisable impact localisation and force reconstruction.

To address these challenges, Chapter 2 examined the fundamental principles of structural dynamics, plate theories for efficient structural modelling, and the characteristics of impact-induced waves—including wave types, propagation modes, and dispersion—alongside conventional impact identification methodologies. Building on this foundation, Chapter 3, Chapter 4, and Chapter 5 focused on enhancing the robustness, generalisability, and efficiency of impact localisation methods, while Chapter 6 and Chapter 7 sought to improve the accuracy and computational efficiency of impact force reconstruction.

To improve localisation robustness under EOVs, Chapter 3 introduced a composite kernel for Gaussian Process Regression (GPR) and employed Bayesian-inspired Model Averaging (BIMA) for model fusion. Extensive impact testing was conducted under varying conditions—including changes in impact mass, energy, angle, and temperature—to validate the proposed approach. The key conclusions are as follows:

- Invariant time difference of arrival (TDOA) order: The order of TDOAs between sensors remains consistent under variations in temperature and TDOA extraction frequency.
- Composite kernel design: The integration of distance-based (RBF) and order-based (COS) kernels enables robust handling of EOVs, significantly improving localisation accuracy.
- Adaptive model fusion through BIMA: BIMA enables dynamic weighting of kernel predictions based on global model fit and local predictive confidence, improving both accuracy and uncertainty quantification over single-kernel approaches.
- Independence from boundary conditions: For structures where the initial wavefront from the impact to the sensor is not influenced by boundary reflections, TDOA-based method maintains its effectiveness across different structural boundary configurations.
- Interpolation over extrapolation: Although extrapolation is possible using data-driven models, interpolation settings achieve significantly higher localisation accuracy. Strategic placement of reference impacts is recommended to maximise model coverage and reliability.

To reduce the reliance of data-driven impact localisation on reference data and enhance its generalisability, Chapter 4 introduced a hybrid physics-data approach by incorporating the physical dispersion relations of impact-induced flexural waves into the localisation process. The dispersion relations, derived from the First-order Shear Deformation Theory (FSDT), parameterise the

Group Velocity Profile (GVP) in terms of material stiffness and wave frequency. A two-stage optimisation framework was developed to estimate the GVP from training impacts, employing exclusively gradient-based optimisation algorithms. The optimised GVP was subsequently utilised for impact localisation via the triangulation method. Experimental validation was performed on a flat composite panel and striger stiffened composite panel. The main conclusions are as follows:

- GVP parameterisation: The FSDT-based model characterises the GVP of the S0, A0, SH0, A1, and SH1 modes of guided waves, expressing their velocity profiles as functions of frequency and structural stiffness.
- Efficient optimisation: The GVP can be optimised using an efficient two-stage approach based on gradient-based algorithms, where velocity amplitude is optimised with respect to wave frequency, and wave shape is optimised with respect to structural stiffness.
- High generalisability: Impact localisation via triangulation based on the optimised GVP exhibits high generalisability across different structures, as it is fundamentally grounded in wave propagation physics.

To ensure high generalisability and quantify localisation uncertainties across varying structural complexities, Chapter 5 presents a general probabilistic framework for impact localisation based on flexural wave propagation, employing Bayesian inference to estimate the GVP and probabilistically localise impacts. Depending on the available prior knowledge and structural complexity, three GVP estimation methods were developed: physics-based (PB), data-driven (DD), and hybrid physics-data (HPD). For laminated plates, the PB method utilises known laminate properties to accurately estimate the GVP. In contrast, for more complex structures, the DD and HPD methods provide greater flexibility and improved performance. The DD method, in particular, is highly adaptable and can be applied to a wide range of structures, provided that reference impact data are available. Experimental validation was conducted on a flat composite panel, a mono-stringer stiffened panel, and a composite sandwich panel. The key conclusions are as follows:

- Low-frequency dominance: The physics-based method for GVP estimation and impact localisation, based on Classical Plate Theory (CPT) and FSDT, should prioritise lower frequencies for higher accuracy. This is due to the dominance of low-frequency components in impact dynamics and the superior GVP accuracy at lower frequencies when using plate theories.

- Reduced data dependence: The developed DD method enables GVP estimation even with sparse data and limited sensor arrays (e.g. four reference impacts and four passive sensors), thereby reducing the cost and effort associated with data collection.

- Enhanced scalability: The HPD method improves scalability by enabling rapid GVP identification for complex structures based on simpler components with known GVPs.

- Structural GVP parameterisation: The proposed GVP parameterisation method, derived from flexural wave dispersion relations in CPT, effectively characterises wavefront propagation in plate-like composite structures, particularly in flat laminated and sandwich panels.

- TDOA extraction and outlier detection: The Normalised Smoothed Envelope Threshold (NSET) method reliably extracts TDOAs across different frequencies. Maximum TDOA analysis aids in identifying and excluding outliers, thereby enhancing localisation accuracy.

The previously developed methods enable highly accurate, efficient, and robust impact localisation. To further enhance efficiency and mitigate the ill-posedness of impact force reconstruction, Chapter 6 introduced an adaptive wavelet-regularised time-domain deconvolution method. This approach focuses on two key aspects: (1) reducing the sample size through adaptive impact window determination and signal downsampling, and (2) adaptively selecting the appropriate wavelet scale and filtering wavelet components for impact force representation using multi-resolution analysis of sensor signals (structural responses). Experimental validation was conducted using both hammer and drop tower impacts on composite panels to assess the method's effectiveness. The key conclusions are summarised as follows:

- Adaptive impact window determination and signal downsampling: The dominant frequency of impact-induced signals enables the adaptive identification of a time window that fully encompasses the impact duration. Additionally, adaptive downsampling of sensor signals improves computational efficiency while preserving essential force characteristics.

- Adaptive wavelet regularisation: Multi-resolution analysis of sensor responses using wavelet transforms allows for the identification and selection of an optimal wavelet basis for impact force representation. This adaptive filtering process enhances reconstruction accuracy by suppressing noise while retaining critical force components.

- Preliminary validation under substantial local deformation: Initial experimental results suggest that the proposed deconvolution method remains effective for impact force reconstruction even when the structure experiences noticeable local deformation. While these findings are promising, they represent only a preliminary validation. Further comprehensive studies are needed to fully assess the method's robustness under various nonlinearities.

High-fidelity transfer function estimation is crucial for impact force deconvolution. Since experimental measurements cannot be obtained for all possible impact locations, a data-driven transfer function estimation approach is required. To reduce dependence on extensive reference data and enable uncertainty quantification, Chapter 7 developed a sparse data-driven approach leveraging an FSDT-based model constructed directly from reference impact data, thereby eliminating the need for prior structural knowledge. By identifying structural properties through dispersion relations and modal characteristics, the model facilitates data augmentation for multi-fidelity GPR-based impact localisation, ensuring accurate localisation even beyond the reference impact locations. Additionally, the model captures modal characteristics and mode shape complexity, providing the foundation for adaptive regularisation in impact force deconvolution. The uncertainties in localisation estimates are then systematically propagated into impact force estimation. The key conclusions are summarised as follows:

- Sparse data-driven FSDT modelling: A numerical FSDT model can be constructed in a sparse data-driven manner by identifying material properties through dispersion relations and inferring boundary conditions from modal information. This enables efficient model construction without prior knowledge of structural properties.

- Data augmentation for improved localisation: The ability to generate additional synthetic training data based on modal properties and dispersion relations significantly enhances the generalisability of the impact localisation model, allowing for accurate localisation beyond reference impact locations.

- Enhanced adaptive regularisation: The integration of modal characteristics and mode shape complexity into the force reconstruction framework enables adaptive regularisation, improving robustness against noise and ill-posedness while preserving critical force features.
- Uncertainty propagation in force estimation: The probabilistic modelling of impact localisation uncertainties ensures that these uncertainties are systematically incorporated into impact force reconstruction, improving the reliability of estimated force profiles.

8.2 Reflections on Assumptions and Limitations

Throughout this thesis, several modelling assumptions were made to enable tractable and robust impact identification in composite structures. These assumptions—outlined in Section 1.6—served as foundational simplifications to isolate key physics and reduce experimental or computational burden. However, their implications, influence on methodological development, and potential limitations warrant critical reflection, especially in light of the goal of transitioning the methods towards real-world SHM applications.

1. Linear elastic behaviour and transfer function invariance

- A central assumption was that the composite structures behave in a linear, time-invariant (LTI) manner, which enables the use of transfer function-based deconvolution for impact force reconstruction. This assumption holds for most low-energy impacts where impact damage is not present. While experimental validation showed promising results even under conditions involving substantial local deformation (e.g., drop tower impacts with large masses), these tests did not explicitly include scenarios with induced impact damage. As such, although the method remained stable in the presence of large elastic deformations, its robustness in the presence of BVID remains unverified. This limitation is non-trivial, since damage-induced nonlinearities can degrade transfer function consistency, affecting both localisation and force reconstruction accuracy. Future work should therefore explicitly explore force reconstruction in the presence of damage and investigate whether online transfer function adaptation or nonlinear modelling is necessary.

2. Neglect of damage effects in guided wave propagation

- In Chapter 2, the modelling of wave propagation assumed undamaged media, with the effect of damage on wave propagation neglected. This was a conscious simplification to focus on the development of probabilistic, physics-guided methods for localisation and deconvolution. Given the highly conservative designs for composite aerostructures—partly due to the difficulty of detecting BVID—this assumption remains a reasonable starting point. However, the motivation for developing passive sensing systems is precisely to detect such subtle damage. While the thesis demonstrated that the developed impact localisation methods can operate under EOV, the influence of BVID on both dispersion relations and signal morphology has not been fully quantified. This presents an important avenue for future work, particularly in developing damage-adaptive or damage-informed versions of the proposed models.

3. Environmental and operational variability (EOV)

- Although the probabilistic frameworks incorporated uncertainty quantification to reflect variability in sensor responses, the underlying physical models—particularly transfer functions and TDOA estimations—were assumed to be invariant under EOV. In practice, factors such as temperature, humidity, and boundary condition changes can induce signal drift. This is especially problematic for time-domain deconvolution methods and TDOA-based localisation, which rely on stable transfer paths. Addressing this limitation may require the development of adaptive or online model updating techniques that integrate environmental sensing or leverage unsupervised learning for drift compensation.

4. Data sparsity and generalisation

- A key innovation in this thesis was the development of sparse, data-driven modelling approaches, particularly for GVP estimation and transfer function estimation. While these approaches significantly reduce the need for dense experimental data, their generalisation depends on the representativeness of the selected reference impact locations. In cases of complex wave phenomena or unmodelled dynamics, extrapolation may introduce errors. The integration of active learning or sequential experimental design could further improve data efficiency and robustness.

8.3 Future Work

Building upon the methodologies developed in this study and acknowledging the assumptions and limitations discussed in Section 8.2, future research should focus on enhancing the realism, scalability, and robustness of the proposed impact identification framework. Particular emphasis should be placed on extending these methods for operation under structural damage, nonlinear effects, EOV, and in-service complexity. The following research directions are proposed:

1. Damage-aware modelling for impact identification

- While this study assumed undamaged structural media, future work must address the influence of BVID on guided wave propagation and transfer function invariance. Incorporating damage-sensitive features into wave modelling, and developing adaptive deconvolution or localisation methods that remain valid under structural degradation, are critical next steps. This could include updating transfer functions based on in situ modal or ultrasonic measurements, or applying Bayesian model updating techniques to account for local changes.

2. Nonlinear and time-varying response modelling

- The force reconstruction methods developed here assumed LTI system responses. However, in real impact events—especially those involving damage initiation or large local deformation—nonlinear effects may arise. Future research should explore nonlinear system identification, time-varying transfer function estimation, or surrogate models (e.g., using recurrent neural networks or Volterra series) that can generalise across a broader operational regime.

3. Probabilistic impact identification under EOV

- Although probabilistic frameworks were introduced, they primarily addressed model and sensor uncertainty rather than explicit environmental effects. Future work should extend these models to incorporate EOVs due to temperature, humidity, loading conditions, and structural configurations. This could involve physics-informed Bayesian models with EOV-conditioned priors, or the use of unsupervised drift compensation techniques. Online learning approaches would further support long-term deployment in changing environments.

4. Digital twin for adaptive diagnosis and prognosis

- The integration of the proposed methodologies into a digital twin framework remains a key enabler for real-time structural health management. Future research should focus on the development of adaptive digital twins that not only localise and reconstruct impacts, but also adapt to evolving structural states, detect and characterise damage progression, and forecast remaining useful life. This requires fusion of physics-based and data-driven models, uncertainty propagation, and online updating strategies.

5. Real-time impact damage detection using deep and lightweight learning

- Future systems must offer real-time damage detection despite high data variability and limited computational resources. Deep transfer learning and lightweight neural network architectures (e.g., MobileNet) should be explored for rapid onboard processing. Moreover, incorporating fibre-optic sensing and guided wave data into pre-trained models, coupled with domain adaptation strategies, can facilitate robust and generalisable damage detection under realistic constraints.

6. Multi-scale, multi-modal, and active-passive sensor fusion

- Single-modality monitoring may miss critical damage signatures, particularly for complex structures. Future work should integrate data from passive impact sensors, guided wave transducers, acoustic emission, thermography, and strain fields. Data-driven feature fusion and decision-level integration techniques (e.g., via transformer models or probabilistic graphical models) can enable comprehensive, multi-resolution damage assessment. Incorporating both active and passive sensing will be essential for full lifecycle coverage.

7. Large-scale validation and generalisation to complex geometries

- The proposed methods have been demonstrated on simplified composite panels. Future research should extend validation to full-scale, stiffened, curved, or heterogeneous structures that better represent real aircraft components. This includes benchmarking across varied layups, load conditions, boundary types, and damage scenarios. Model generalisability can be improved using transfer learning, simulation-based training data augmentation, or active learning frameworks for experimental design.

Bibliography

[1] C. Fualdes, X. Jolivet, and C. Chamfroy, "Safe operations with composite aircraft," *Airbus Tech Mag (Safety first)*, July 2014.

[2] A. Safety, "Status of FAA's Actions to Oversee the Safety of Composite Airplanes," Tech. Rep. GAO-11-849, Aviation Safety, Sept. 2011.

[3] J. Pora, "Composite Materials in the Airbus A380 - From History to Future," in *Beijing: Proceedings 13th International Conference on Composite Materials (ICCM-13)*, (Beijing), June 2001.

[4] G. J. Dvorak and N. Laws, "Analysis of Progressive Matrix Cracking In Composite Laminates II. First Ply Failure," *Journal of Composite Materials*, vol. 21, pp. 309–329, Apr. 1987.

[5] R. Olsson, M. V. Donadon, and B. G. Falzon, "Delamination threshold load for dynamic impact on plates," *International Journal of Solids and Structures*, vol. 43, pp. 3124–3141, May 2006.

[6] S. Z. H. Shah, S. Karuppanan, P. S. M. Megat-Yusoff, and Z. Sajid, "Impact resistance and damage tolerance of fiber reinforced composites: A review," *Composite Structures*, vol. 217, pp. 100–121, June 2019.

[7] F. Vincent and M. Emilie, "Damage tolerant composite fuselage sizing, characterization of accidental damage threat," *Airbus Tech Mag (FAST)*, vol. 48, pp. 10–16, 2011.

[8] J. Rouchon, "Certification of large airplane composite structures," in *ICAS Congress Proceedings*, vol. Vol. 2, 1990.

[9] G. a. O. Davies and R. Olsson, "Impact on composite structures," *The Aeronautical Journal*, vol. 108, pp. 541–563, Nov. 2004.

[10] M. H. F. Aliabadi and Z. Sharif Khodaei, *Structural Health Monitoring for Advanced Composite Structures*, vol. 08 of *Computational and Experimental Methods in Structures*. World Scientific (Europe), Feb. 2018.

[11] N. Hu, H. Fukunaga, S. Matsumoto, B. Yan, and X. H. Peng, "An efficient approach for identifying impact force using embedded piezoelectric sensors," *International Journal of Impact Engineering*, vol. 34, pp. 1258–1271, July 2007.

[12] D. Xiao, Z. S. Khodaei, and M. H. F. Aliabadi, "Impact Identification Based on Surrogate-assisted Efficient Global Optimisation," *Procedia Structural Integrity*, vol. 52, pp. 667–678, Jan. 2024.

[13] Y. Liu and L. Wang, "Quantification, localization, and reconstruction of impact force on interval composite structures," *International Journal of Mechanical Sciences*, vol. 239, p. 107873, Feb. 2023.

[14] Z. Yu, C. Xu, J. Sun, and F. Du, "Impact localization and force reconstruction for composite plates based on virtual time reversal processing with time-domain spectral finite element method," *Structural Health Monitoring*, vol. 22, pp. 4149–4170, Nov. 2023.

[15] Z. Yu, J. Sun, M. Yue, and C. Xu, "Accelerated strategies for impact identification of composite laminate using sparse sensor networks and model-based virtual time reversal," *Structural Health Monitoring*, p. 14759217241290260, Nov. 2024.

[16] D. Goutaudier, D. Gendre, V. Kehr-Candille, and R. Ohayon, "Impulse identification technique by estimating specific modal ponderations from vibration measurements," *Journal of Sound and Vibration*, vol. 474, p. 115263, May 2020.

[17] D. Goutaudier, D. Gendre, V. Kehr-Candille, and R. Ohayon, "Single-sensor approach for impact localization and force reconstruction by using discriminating vibration modes," *Mechanical Systems and Signal Processing*, vol. 138, p. 106534, Apr. 2020.

[18] L. Zhang, M. Liu, L. Hong, Z. Wang, Z. Zhou, and W. Liao, "An efficient impact force identification methodology via a single sensor utilizing the concept of generalized transmissibility," *Mechanical Systems and Signal Processing*, vol. 211, p. 111222, Apr. 2024.

[19] A. El-Bakari, A. Khamlichi, E. Jacquelin, and R. Dkiouak, "Assessing impact force localization by using a particle swarm optimization algorithm," *Journal of Sound and Vibration*, vol. 333, pp. 1554–1561, Mar. 2014.

[20] S. Atobe, S. Sugimoto, N. Hu, and H. Fukunaga, "Impact damage monitoring of FRP pressure vessels based on impact force identification," *Advanced Composite Materials*, vol. 23, pp. 491–505, Sept. 2014.

[21] F. Ciampa and M. Meo, "Impact detection in anisotropic materials using a time reversal approach," *Structural Health Monitoring*, vol. 11, no. 1, pp. 43–49, 2012.

[22] M. E. D. Simone, F. Ciampa, and M. Meo, "A hierarchical method for the impact force reconstruction in composite structures," *Smart Materials and Structures*, vol. 28, no. 8, p. 085022, 2019.

[23] C. Chen, Y. Li, and F.-G. Yuan, "Impact source identification in finite isotropic plates using a time-reversal method: experimental study," *Smart Materials and Structures*, vol. 21, p. 105025, Aug. 2012.

[24] J. Liu and B. Li, "A novel strategy for response and force reconstruction under impact excitation," *Journal of Mechanical Science and Technology*, vol. 32, pp. 3581–3596, Aug. 2018.

[25] T. Kundu, "Acoustic source localization," *Ultrasonics*, vol. 54, pp. 25–38, Jan. 2014.

[26] M. Meo, G. Zumpano, M. Piggott, and G. Marengo, "Impact identification on a sandwich plate from wave propagation responses," *Composite Structures*, vol. 71, pp. 302–306, Dec. 2005.

[27] E. Dehghan Niri, A. Farhidzadeh, and S. Salamone, "Nonlinear Kalman Filtering for acoustic emission source localization in anisotropic panels," *Ultrasonics*, vol. 54, pp. 486–501, Feb. 2014.

[28] E. D. Niri and S. Salamone, "A probabilistic framework for acoustic emission source localization in plate-like structures," *Smart Materials and Structures*, vol. 21, no. 3, p. 035009, 2012.

[29] K. Zhu, X. P. Qing, and B. Liu, "A two-step impact localization method for composite structures with a parameterized laminate model," *Composite Structures*, vol. 192, pp. 500–506, May 2018.

[30] K. Zhu, X. P. Qing, B. Liu, and T. He, "A passive localization method for stiffened composite structures with a parameterized laminate model," *Journal of Sound and Vibration*, vol. 489, p. 115683, Dec. 2020.

[31] F. Ciampa and M. Meo, "Acoustic emission source localization and velocity determination of the fundamental mode A0 using wavelet analysis and a Newton-based optimization technique," *Smart Materials and Structures*, vol. 19, p. 045027, Mar. 2010.

[32] D. Deng, X. Zeng, Z. Yang, Y. Yang, S. Zhang, S. Ma, H. Xu, L. Yang, and Z. Wu, "Multi-frequency probabilistic imaging fusion for impact localization on aircraft composite structures," *Structural Health Monitoring*, p. 14759217241233181, Mar. 2024.

[33] E. Kirkby, R. de Oliveira, V. Michaud, and J. A. Månson, "Impact localisation with FBG for a self-healing carbon fibre composite structure," *Composite Structures*, vol. 94, pp. 8–14, Dec. 2011.

[34] S. Sikdar, P. Mirgal, and S. Banerjee, "Low-velocity impact source localization in a composite sandwich structure using a broadband piezoelectric sensor network," *Composite Structures*, vol. 291, p. 115619, July 2022.

[35] A. H. Seno, Z. Sharif Khodaei, and M. H. F. Aliabadi, "Passive sensing method for impact localisation in composite plates under simulated environmental and operational conditions," *Mechanical Systems and Signal Processing*, vol. 129, pp. 20–36, 2019.

[36] A. H. Seno and M. H. F. Aliabadi, "Impact Localisation in Composite Plates of Different Stiffness Impactors under Simulated Environmental and Operational Conditions," *Sensors*, vol. 19, p. 3659, Jan. 2019.

[37] Z. Sharif-Khodaei, M. Ghajari, and M. H. Aliabadi, "Determination of impact location on composite stiffened panels," *Smart Materials and Structures*, vol. 21, no. 10, p. 105026, 2012.

[38] M. Ghajari, Z. Sharif-Khodaei, M. H. Aliabadi, and A. Apicella, "Identification of impact force for smart composite stiffened panels," *Smart Materials and Structures*, vol. 22, no. 8, p. 085014, 2013.

[39] M. S. Hossain, Z. C. Ong, S.-C. Ng, Z. Ismail, and S. Y. Khoo, "Inverse identification of impact locations using multilayer perceptron with effective time-domain feature," *Inverse Problems in Science and Engineering*, vol. 26, pp. 443–461, Mar. 2018.

[40] L. Morse, Z. Sharif Khodaei, and M. H. Aliabadi, "Reliability based impact localization in composite panels using Bayesian updating and the Kalman filter," *Mechanical Systems and Signal Processing*, vol. 99, pp. 107–128, 2018.

[41] B.-W. Jang and C.-G. Kim, "Impact localization of composite stiffened panel with triangulation method using normalized magnitudes of fiber optic sensor signals," *Composite Structures*, vol. 211, pp. 522–529, Mar. 2019.

[42] P. Balasubramanian, V. Kaushik, S. Y. Altamimi, M. Amabili, and M. Alteneiji, "Comparison of neural networks based on accuracy and robustness in identifying impact location for structural health monitoring applications," *Structural Health Monitoring*, vol. 22, pp. 417–432, Jan. 2023.

[43] A. Hami Seno and M. H. Ferri Aliabadi, "Multifidelity data augmentation for data driven passive impact location and force estimation in composite structures under simulated environmental and operational conditions," *Mechanical Systems and Signal Processing*, vol. 195, p. 110288, July 2023.

[44] A. H. Seno and M. F. Aliabadi, "Uncertainty quantification for impact location and force estimation in composite structures," *Structural Health Monitoring*, p. 147592172110202, June 2021.

[45] M. R. Jones, T. J. Rogers, K. Worden, and E. J. Cross, "A Bayesian methodology for localising acoustic emission sources in complex structures," *Mechanical Systems and Signal Processing*, vol. 163, p. 108143, Jan. 2022.

[46] S. Ojha, N. Jangid, A. Shelke, and A. Habib, "Probabilistic impact localization in composites using wavelet scattering transform and multi-output Gaussian process regression," *Measurement*, p. 115078, June 2024.

[47] J. Hensman, R. Mills, S. G. Pierce, K. Worden, and M. Eaton, "Locating acoustic emission sources in complex structures using Gaussian processes," *Mechanical Systems and Signal Processing*, vol. 24, pp. 211–223, Jan. 2010.

[48] I. Tabian, H. Fu, and Z. Sharif Khodaei, "A Convolutional Neural Network for Impact Detection and Characterization of Complex Composite Structures," *Sensors*, vol. 19, p. 4933, Jan. 2019.

[49] B. Zhao, Y. Zhang, Q. Liu, and X. Qing, "Impact monitoring of large size complex metal structures based on sparse sensor array and transfer learning," *Ultrasonics*, vol. 140, p. 107305, May 2024.

[50] M. Hamadneh, S. Mustapha, and M. A. Fakih, "Impact-force identification using deep learning and Bayesian inference with application on pipeline structures," *Structural Health Monitoring*, p. 14759217241297572, Dec. 2024.

[51] D. F. Hesser, S. Mostafavi, G. K. Kocur, and B. Markert, "Identification of acoustic emission sources for structural health monitoring applications based on convolutional neural networks and deep transfer learning," *Neurocomputing*, vol. 453, pp. 1–12, Sept. 2021.

[52] D. del Río-Velilla, A. Pedraza, and A. Fernández-López, “Impact localization in composite structures with Deep Neural Networks,” *Structural Health Monitoring*, p. 14759217241270946, Aug. 2024.

[53] R. Zhou, B. Qiao, J. Liu, W. Cheng, and X. Chen, “Impact force localization and reconstruction via gated temporal convolutional network,” *Aerospace Science and Technology*, vol. 144, p. 108819, Jan. 2024.

[54] C. Huang, W. Liao, H. Sun, Y. Wang, and X. Qing, “A hybrid FCN-BiGRU with transfer learning for low-velocity impact identification on aircraft structure,” *Smart Materials and Structures*, vol. 32, p. 055012, Apr. 2023.

[55] J. Zhou, Y. Cai, L. Dong, B. Zhang, and Z. Peng, “Data-physics hybrid-driven deep learning method for impact force identification,” *Mechanical Systems and Signal Processing*, vol. 211, p. 111238, Apr. 2024.

[56] Z. Zhao and N.-Z. Chen, “Spatial-temporal graph convolutional networks (STGCN) based method for localizing acoustic emission sources in composite panels,” *Composite Structures*, vol. 323, p. 117496, Nov. 2023.

[57] C. Huang, C. Tao, H. Ji, and J. Qiu, “Impact force reconstruction and localization using Distance-assisted Graph Neural Network,” *Mechanical Systems and Signal Processing*, vol. 200, p. 110606, Oct. 2023.

[58] C. Huang, C. Tao, H. Ji, and J. Qiu, “Impact time history reconstruction using dynamic weighted graph neural network under sensor fault situations,” *Structural Health Monitoring*, p. 14759217241313177, Jan. 2025.

[59] H. Yan, W. Xie, B. Gao, F. Yang, and S. Meng, “A deep learning approach to impact localization and uncertainty assessment in CFRP composites using sparse PZTs: Integrating experiments and simulations,” *Thin-Walled Structures*, vol. 212, p. 113143, July 2025.

[60] M. Geradin and D. J. Rixen, *Mechanical Vibrations: Theory and Application to Structural Dynamics*. John Wiley & Sons, Dec. 2014.

[61] T. Kundu, X. Yang, H. Nakatani, and N. Takeda, “A two-step hybrid technique for accurately localizing acoustic source in anisotropic structures without knowing their material properties,” *Ultrasonics*, vol. 56, pp. 271–278, Feb. 2015.

[62] M. E. D. Simone, F. Ciampa, S. Boccardi, and M. Meo, "Impact source localisation in aerospace composite structures," *Smart Materials and Structures*, vol. 26, p. 125026, Nov. 2017.

[63] X. Zeng, D. Deng, H. Yang, Z. Yang, L. Yang, and Z. Wu, "Hybrid DoA-TDoA method for impact localization on thin-walled structures using sensor clusters," *IEEE Sensors Journal*, pp. 1–1, 2025.

[64] V. Giammaria, G. Del Bianco, E. Raponi, D. Fiumarella, R. Ciardiello, S. Boria, F. Duddeck, and G. Belingardi, "Material parameter optimization of flax/epoxy composite laminates under low-velocity impact," *Composite Structures*, vol. 321, p. 117303, Oct. 2023.

[65] T. Xu, Z. Wang, Y. Hu, S. Du, A. Du, Z. Yu, and Y. Lei, "A FEM-based direct method for identification of Young's modulus and boundary conditions in three-dimensional linear elasticity from local observation," *International Journal of Mechanical Sciences*, vol. 237, p. 107797, Jan. 2023.

[66] S. Ereiz, I. Duvnjak, and J. Fernando Jiménez-Alonso, "Review of finite element model updating methods for structural applications," *Structures*, vol. 41, pp. 684–723, July 2022.

[67] B. Szabó and I. Babuška, *Finite Element Analysis: Method, Verification and Validation*. John Wiley & Sons, June 2021.

[68] N. M. M. Kalimullah, A. Shelke, and A. Habib, "A probabilistic framework for source localization in anisotropic composite using transfer learning based multi-fidelity physics informed neural network (mfPINN)," *Mechanical Systems and Signal Processing*, vol. 197, p. 110360, Aug. 2023.

[69] T. Kundu, S. Das, and K. V. Jata, "Detection of the point of impact on a stiffened plate by the acoustic emission technique," *Smart Materials and Structures*, vol. 18, p. 035006, Jan. 2009.

[70] B. J. Schwarz and M. H. Richardson, "EXPERIMENTAL MODAL ANALYSIS," 1999.

[71] L. Grasboeck, A. Humer, and A. Benjeddou, "Detection and time-of-arrival estimation of impact-induced waves in composite laminates," *Structural Health Monitoring*, July 2024.

[72] D. Xiao, Z. Sharif-Khodaei, and M. H. Aliabadi, "Time of Arrival Extraction for Impact Localisation on Composite Structures," *e-Journal of Nondestructive Testing*, vol. 29, July 2024.

[73] D. Xiao, Z. Sharif-Khodaei, and M. H. Aliabadi, "Robust impact localisation on composite aerostructures using kernel design and Bayesian fusion under environmental and operational uncertainties," Jan. 2025. arXiv:2501.18393 [stat].

[74] D. Xiao, Z. Sharif-Khodaei, and M. H. Aliabadi, "Hybrid physics-based and data-driven impact localisation for composite laminates," *International Journal of Mechanical Sciences*, vol. 274, p. 109222, July 2024.

[75] D. Xiao, F. d. S. Rodrigues, Z. Sharif-Khodaei, and M. H. Aliabadi, "A general probabilistic framework for impact localisation based on flexural wave propagation," *Mechanical Systems and Signal Processing*, vol. 226, p. 112320, Mar. 2025.

[76] D. Xiao, Z. Sharif-Khodaei, and M. H. Aliabadi, "Impact force identification for composite structures using adaptive wavelet-regularised deconvolution," *Mechanical Systems and Signal Processing*, vol. 220, p. 111608, Nov. 2024.

[77] D. Xiao, Z. Sharif-Khodaei, and M. H. Aliabadi, "Physics-guided impact localisation and force estimation in composite plates with uncertainty quantification," July 2025. arXiv:2507.13376 [physics].

[78] D. Deng, X. Zeng, Y. Yang, S. Zhang, H. Xu, Z. Yang, L. Yang, and Z. Wu, "Data fusion based impact localization on aircraft composite structures using Bayesian estimation and weighted averaging," *Mechanical Systems and Signal Processing*, vol. 230, p. 112675, May 2025.

[79] K. N. Shivakumar, W. Elber, and W. Illg, "Prediction of Impact Force and Duration Due to Low-Velocity Impact on Circular Composite Laminates," *Journal of Applied Mechanics*, vol. 52, pp. 674–680, Sept. 1985.

[80] S. D. Casey and D. F. Walnut, "Systems of Convolution Equations, Deconvolution, Shannon Sampling, and the Wavelet and Gabor Transforms," *SIAM Review*, vol. 36, pp. 537–577, Dec. 1994.

[81] R. S. Strichartz, *A Guide To Distribution Theory And Fourier Transforms.* World Scientific Publishing Company, June 2003.

[82] C. Lalanne, *Mechanical Vibration and Shock Analysis, Mechanical Shock.* John Wiley & Sons, Mar. 2013.

[83] S. Timoshenko and S. Woinowsky-Krieger, *Theory of Plates and Shells.* McGraw-Hill, 1959.

[84] G. Staab, *Laminar Composites.* Butterworth-Heinemann, Aug. 2015.

[85] J. N. Reddy, *Mechanics of Laminated Composite Plates and Shells: Theory and Analysis.* CRC Press, Nov. 2003.

[86] T. M. Tan and C. T. Sun, "Wave propagation in graphite/epoxy laminates due to impact," Tech. Rep. NASA-CR-168057, NASA, Dec. 1982.

[87] S. Abrate, *Impact on Composite Structures.* Cambridge: Cambridge University Press, 1998.

[88] F. C. Moon, "Theoretical analysis of impact in composite plates," Tech. Rep. AMS-1099, NASA, Jan. 1973.

[89] B. S. Tang, "Lamb wave propagation in laminated composite plates," 1988.

[90] R. Seydel and F.-K. Chang, "Impact identification of stiffened composite panels: I. System development," *Smart Materials and Structures*, vol. 10, no. 2, pp. 354–369, 2001.

[91] J. F. Doyle, "Wave Propagation in Structures," in *Wave Propagation in Structures: An FFT-Based Spectral Analysis Methodology* (J. F. Doyle, ed.), pp. 126–156, New York, NY: Springer US, 1989.

[92] J. Achenbach, *Wave Propagation in Elastic Solids.* Elsevier, Dec. 2012.

[93] H. Kolsky, *Stress Waves in Solids.* Courier Corporation, Jan. 1963.

[94] F. C. Moon, *Wave propagation and impact in composite materials*, vol. 7 of *Composite Materials.* Elsevier, 1975.

[95] A. H. Nayfeh, *Wave Propagation in Layered Anisotropic Media: with Application to Composites.* Elsevier, Sept. 1995.

[96] D. C. Gazis, "Three-Dimensional Investigation of the Propagation of Waves in Hollow Circular Cylinders. I. Analytical Foundation," *The Journal of the Acoustical Society of America*, vol. 31, pp. 568–573, May 1959.

[97] Y. Li and R. B. Thompson, "Influence of anisotropy on the dispersion characteristics of guided ultrasonic plate modes," *The Journal of the Acoustical Society of America*, vol. 87, pp. 1911–1931, May 1990.

[98] D. ROYER and E. Dieulesaint, *Elastic Waves in Solids I: Free and Guided Propagation.* Springer Science & Business Media, Nov. 1999.

[99] K. F. Graff, *Wave Motion in Elastic Solids.* Courier Corporation, Apr. 2012.

[100] J. Miklowitz, *The Theory of Elastic Waves and Waveguides.* Elsevier, Dec. 2012.

[101] B. A. Auld, *Acoustic fields and waves in solids*. Ripol Classic, 1973.

[102] J. L. Rose, *Ultrasonic Guided Waves in Solid Media*. Cambridge: Cambridge University Press, 2014.

[103] V. Giurgiutiu, *Structural Health Monitoring with Piezoelectric Wafer Active Sensors*. Elsevier, June 2014.

[104] A. Huber, "The Dispersion Calculator: A Free Software for Calculating Dispersion Curves of Guided Waves," in *20th World Conference on Non-Destructive Testing (WCNDT 2024)*, vol. 29, (Incheon, Südkorea), pp. 1–17, NDT.net, May 2024.

[105] F. C. Moon, "A critical survey of wave propagation and impact in composite materials," Tech. Rep. CR-121226, NASA, May 1973.

[106] B. S. Kim and F. Moon, "Impact Induced Stress Waves in an Anisotropic Plate," *AIAA Journal*, vol. 17, pp. 1126–1133, Oct. 1979.

[107] I. M. Daniel, T. Liber, and R. H. LaBedz, "Wave propagation in transversely impacted composite laminates," *Experimental Mechanics*, vol. 19, no. 1, p. 9, 1979.

[108] L. Capineri and A. Bulletti, "A Versatile Analog Electronic Interface for Piezoelectric Sensors Used for Impacts Detection and Positioning in Structural Health Monitoring (SHM) Systems," *Electronics*, vol. 10, p. 1047, Jan. 2021.

[109] A. Bulletti, E. M. Merlo, and L. Capineri, "Analysis of the accuracy in impact localization using piezoelectric sensors for Structural Health Monitoring with multichannel real-time electronics," in *2020 IEEE 7th International Workshop on Metrology for AeroSpace (MetroAeroSpace)*, pp. 480–484, June 2020.

[110] A. H. Orta, J. Vandendriessche, M. Kersemans, W. Van Paepegem, N. B. Roozen, and K. Van Den Abeele, "Modeling lamb wave propagation in visco-elastic composite plates using a fifth-order plate theory," *Ultrasonics*, vol. 116, p. 106482, Sept. 2021.

[111] R. S. Langley, "Wave Motion and Energy Flow in Cylindrical Shells," *Journal of Sound and Vibration*, vol. 169, pp. 29–42, Jan. 1994.

[112] H. Jeong and Y.-S. Jang, "Wavelet analysis of plate wave propagation in composite laminates," *Composite Structures*, vol. 49, pp. 443–450, Aug. 2000.

[113] F. C. Moon, "Wave Surfaces Due to Impact on Anisotropic Plates," *Journal of Composite Materials*, vol. 6, pp. 62–79, Jan. 1972.

[114] T. Chow, "On the Propagation of Flexural Waves in an Orthotropic Laminated Plate and Its Response to an Impulsive Load," *Journal of Composite Materials*, vol. 5, pp. 306–319, Mar. 1971.

[115] N. E. Huang, Z. Shen, S. R. Long, M. C. Wu, H. H. Shih, Q. Zheng, N.-C. Yen, C. C. Tung, and H. H. Liu, "The empirical mode decomposition and the Hilbert spectrum for nonlinear and non-stationary time series analysis," *Proceedings of the Royal Society of London. Series A: Mathematical, Physical and Engineering Sciences*, vol. 454, pp. 903–995, Mar. 1998.

[116] I. N. Sneddon, *Fourier Transforms.* Courier Corporation, Jan. 1995.

[117] E. O. Brigham and R. E. Morrow, "The fast Fourier transform," *IEEE Spectrum*, vol. 4, pp. 63–70, Dec. 1967.

[118] I. Daubechies, *Ten Lectures on Wavelets.* CBMS-NSF Regional Conference Series in Applied Mathematics, Society for Industrial and Applied Mathematics, Jan. 1992.

[119] A. Tobias, "Acoustic-emission source location in two dimensions by an array of three sensors," *Non-Destructive Testing*, vol. 9, pp. 9–12, Feb. 1976.

[120] V. Mallardo, Z. Sharif Khodaei, and F. M. H. Aliabadi, "A Bayesian Approach for Sensor Optimisation in Impact Identification," *Materials*, vol. 9, p. 946, Nov. 2016.

[121] W. Ostachowicz, R. Soman, and P. Malinowski, "Optimization of sensor placement for structural health monitoring: a review," *Structural Health Monitoring*, vol. 18, pp. 963–988, May 2019.

[122] Z. Sharif-Khodaei and M. H. Aliabadi, "An optimization strategy for best sensor placement for damage detection and localization in complex composite structures," *8th European Workshop On Structural Health Monitoring (EWSHM 2016)*, July 2016.

[123] M. T. Martin and J. F. Doyle, "Impact force identification from wave propagation responses," *International Journal of Impact Engineering*, vol. 18, pp. 65–77, Jan. 1996.

[124] M. Thiene, M. Ghajari, U. Galvanetto, and M. H. Aliabadi, "Effects of the transfer function evaluation on the impact force reconstruction with application to composite panels," *Composite Structures*, vol. 114, pp. 1–9, Aug. 2014.

[125] E. Schulz, M. Speekenbrink, and A. Krause, "A tutorial on Gaussian process regression: Modelling, exploring, and exploiting functions," *Journal of Mathematical Psychology*, vol. 85, pp. 1–16, Aug. 2018.

[126] A. I. J. Forrester, A. Sbester, and A. J. Keane, *Engineering Design via Surrogate Modelling*. Chichester, UK: John Wiley & Sons, Ltd, July 2008.

[127] R. Olsson, "Mass criterion for wave controlled impact response of composite plates," *Composites Part A: Applied Science and Manufacturing*, vol. 31, pp. 879–887, Aug. 2000.

[128] F. Ren, I. N. Giannakeas, Z. Sharif Khodaei, and M. H. F. Aliabadi, "Theoretical and experimental investigation of guided wave temperature compensation for composite structures with different thicknesses," *Mechanical Systems and Signal Processing*, vol. 200, p. 110594, Oct. 2023.

[129] F. Ren, I. N. Giannakeas, Z. Sharif Khodaei, and M. H. F. Aliabadi, "The temperature effects on embedded PZT signals in structural health monitoring for composite structures with different thicknesses," *NDT & E International*, vol. 141, p. 102988, Jan. 2024.

[130] C. Fendzi, M. Rébillat, N. Mechbal, M. Guskov, and G. Coffignal, "A data-driven temperature compensation approach for Structural Health Monitoring using Lamb waves," *Structural Health Monitoring*, vol. 15, pp. 525–540, Sept. 2016.

[131] M. Nabati, S. A. Ghorashi, and R. Shahbazian, "JGPR: a computationally efficient multi-target Gaussian process regression algorithm," *Machine Learning*, vol. 111, pp. 1987–2010, June 2022.

[132] L. Wasserman, "Bayesian Model Selection and Model Averaging," *Journal of Mathematical Psychology*, vol. 44, pp. 92–107, Mar. 2000.

[133] J. Gardner, G. Pleiss, K. Q. Weinberger, D. Bindel, and A. G. Wilson, "GPyTorch: Blackbox Matrix-Matrix Gaussian Process Inference with GPU Acceleration," in *Advances in Neural Information Processing Systems*, vol. 31, pp. 1–11, Curran Associates, Inc., 2018.

[134] D. P. Kingma and J. Ba, "Adam: A Method for Stochastic Optimization," Jan. 2017. arXiv:1412.6980.

[135] H. Suemasu and O. Majima, "Multiple Delaminations and their Severity in Circular Axisymmetric Plates Subjected to Transverse Loading," *Journal of Composite Materials*, vol. 30, pp. 441–453, Mar. 1996.

[136] R. Olsson, "Analytical prediction of large mass impact damage in composite laminates," *Composites Part A: Applied Science and Manufacturing*, vol. 32, pp. 1207–1215, Sept. 2001.

[137] T. F. Coleman and Y. Li, "An Interior Trust Region Approach for Nonlinear Minimization Subject to Bounds," *SIAM Journal on Optimization*, vol. 6, pp. 418–445, May 1996.

[138] J. H. Holland, "Genetic Algorithms," *Scientific American*, vol. 267, no. 1, pp. 66–73, 1992.

[139] A. C. Correas, A. C. Crespo, H. Ghasemnejad, and G. Roshan, "Analytical Solutions to Predict Impact Behaviour of Stringer Stiffened Composite Aircraft Panels," *Applied Composite Materials*, vol. 28, pp. 1237–1254, Aug. 2021.

[140] S. Timoshenko, "On the correction for shear of the differential equation for transverse vibrations of prismatic bars," *The London, Edinburgh, and Dublin Philosophical Magazine and Journal of Science*, vol. 41, pp. 744–746, May 1921.

[141] R. D. Mindlin, "Influence of Rotatory Inertia and Shear on Flexural Motions of Isotropic, Elastic Plates," *Journal of Applied Mechanics*, vol. 18, pp. 31–38, Mar. 1951.

[142] S. Jackman, "Estimation and Inference via Bayesian Simulation: An Introduction to Markov Chain Monte Carlo," *American Journal of Political Science*, vol. 44, no. 2, pp. 375–404, 2000.

[143] B. P. Carlin and S. Chib, "Bayesian Model Choice Via Markov Chain Monte Carlo Methods," *Journal of the Royal Statistical Society: Series B (Methodological)*, vol. 57, pp. 473–484, Jan. 1995.

[144] L. Maio, V. Memmolo, F. Ricci, N. D. Boffa, E. Monaco, and R. Pecora, "Ultrasonic wave propagation in composite laminates by numerical simulation," *Composite Structures*, vol. 121, pp. 64–74, Mar. 2015.

[145] F. Ricci, E. Monaco, N. D. Boffa, L. Maio, and V. Memmolo, "Guided waves for structural health monitoring in composites: A review and implementation strategies," *Progress in Aerospace Sciences*, vol. 129, p. 100790, Feb. 2022.

[146] M. Liu, W. Zhang, X. Chen, L. Li, K. Wang, H. Wang, F. Cui, and Z. Su, "Modelling guided waves in acoustoelastic and complex waveguides: From SAFE theory to an open-source tool," *Ultrasonics*, vol. 136, p. 107144, Jan. 2024.

[147] A. Gelman, J. B. Carlin, H. S. Stern, and D. B. Rubin, *Bayesian Data Analysis*. New York: Chapman and Hall/CRC, June 1995.

[148] G. E. P. Box and G. C. Tiao, *Bayesian Inference in Statistical Analysis.* John Wiley & Sons, Jan. 2011.

[149] V. Ajith and S. Gopalakrishnan, “Spectral Element Approach to Wave Propagation in Uncertain Composite Beam Structures,” *Journal of Vibration and Acoustics*, vol. 133, July 2011.

[150] F. Bouchoucha, M. N. Ichchou, and M. Haddar, “Guided wave propagation in uncertain elastic media,” *Ultrasonics*, vol. 53, pp. 303–312, Feb. 2013.

[151] H. Haario, M. Laine, A. Mira, and E. Saksman, “DRAM: Efficient adaptive MCMC,” *Statistics and Computing*, vol. 16, pp. 339–354, Dec. 2006.

[152] S. R. Eliason, *Maximum Likelihood Estimation: Logic and Practice.* SAGE, 1993.

[153] A. Gelman, “Bayes, Jeffreys, Prior Distributions and the Philosophy of Statistics,” *Statistical Science*, vol. 24, no. 2, pp. 176–178, 2009.

[154] H. Fu, Z. Sharif Khodaei, and M. H. F. Aliabadi, “An Event-Triggered Energy-Efficient Wireless Structural Health Monitoring System for Impact Detection in Composite Airframes,” *IEEE Internet of Things Journal*, vol. 6, pp. 1183–1192, Feb. 2019.

[155] S. Choudhary and U. Mitra, “Sparse blind deconvolution: What cannot be done,” in *2014 IEEE International Symposium on Information Theory*, (Honolulu, HI, USA), pp. 3002–3006, IEEE, June 2014.

[156] A. Ahmed, B. Recht, and J. Romberg, “Blind Deconvolution Using Convex Programming,” *IEEE Transactions on Information Theory*, vol. 60, pp. 1711–1732, Mar. 2014.

[157] A. Levin, Y. Weiss, F. Durand, and W. T. Freeman, “Understanding Blind Deconvolution Algorithms,” *IEEE Transactions on Pattern Analysis and Machine Intelligence*, vol. 33, pp. 2354–2367, Dec. 2011.

[158] D. Kundur and D. Hatzinakos, “Blind image deconvolution,” *IEEE Signal Processing Magazine*, vol. 13, pp. 43–64, May 1996.

[159] A. Gholami and M. D. Sacchi, “A Fast and Automatic Sparse Deconvolution in the Presence of Outliers,” *IEEE Transactions on Geoscience and Remote Sensing*, vol. 50, pp. 4105–4116, Oct. 2012.

[160] J. A. J. A. Kane, *wavelet domain inversion and joint deconvolution/interpolation of geophysical data.* Thesis, Massachusetts Institute of Technology, 2003.

[161] D. R. Velis, "Stochastic sparse-spike deconvolution," *GEOPHYSICS*, vol. 73, pp. R1–R9, Jan. 2008.

[162] L. Wang, J. Liu, and Z.-R. Lu, "Bandlimited force identification based on sinc-dictionaries and Tikhonov regularization," *Journal of Sound and Vibration*, vol. 464, p. 114988, Jan. 2020.

[163] H. G. Choi, A. N. Thite, and D. J. Thompson, "Comparison of methods for parameter selection in Tikhonov regularization with application to inverse force determination," *Journal of Sound and Vibration*, vol. 304, pp. 894–917, July 2007.

[164] B. Qiu, M. Zhang, Y. Xie, X. Qu, and X. Li, "Impact Force Identification on Carbon Fibre–Epoxy Honeycomb Composite Panel Based on Local Convex Curve Criterion," *Experimental Mechanics*, vol. 59, pp. 1171–1185, Oct. 2019.

[165] Z. Chen, Z. Wang, Z. Wang, and T. H. T. Chan, "Comparative studies on the criteria for regularization parameter selection based on moving force identification," *Inverse Problems in Science and Engineering*, vol. 29, pp. 153–173, Feb. 2021.

[166] B. Qiao, X. Zhang, J. Gao, and X. Chen, "Impact-force sparse reconstruction from highly incomplete and inaccurate measurements," *Journal of Sound and Vibration*, vol. 376, pp. 72–94, Aug. 2016.

[167] B. Qiao, X. Zhang, J. Gao, R. Liu, and X. Chen, "Sparse deconvolution for the large-scale ill-posed inverse problem of impact force reconstruction," *Mechanical Systems and Signal Processing*, vol. 83, pp. 93–115, Jan. 2017.

[168] J. Liu, B. Qiao, W. He, Z. Yang, and X. Chen, "Impact force identification via sparse regularization with generalized minimax-concave penalty," *Journal of Sound and Vibration*, vol. 484, p. 115530, Oct. 2020.

[169] J. Liu, B. Qiao, Y. Wang, W. He, and X. Chen, "Non-convex sparse regularization via convex optimization for impact force identification," *Mechanical Systems and Signal Processing*, vol. 191, p. 110191, May 2023.

[170] G. Yan, H. Sun, and O. Büyüköztürk, "Impact load identification for composite structures using Bayesian regularization and unscented Kalman filter," *Structural Control and Health Monitoring*, vol. 24, no. 5, p. e1910, 2017.

[171] G. Yan and H. Sun, “A non-negative Bayesian learning method for impact force reconstruction,” *Journal of Sound and Vibration*, vol. 457, pp. 354–367, Sept. 2019.

[172] S. Samagassi, E. Jacquelin, A. Khamlichi, and M. Sylla, “Bayesian sparse regularization for multiple force identification and location in time domain,” *Inverse Problems in Science and Engineering*, vol. 27, pp. 1221–1262, Sept. 2019.

[173] H. Tran and H. Inoue, “Development of wavelet deconvolution technique for impact force reconstruction: Application to reconstruction of impact force acting on a load-cell,” *International Journal of Impact Engineering*, vol. 122, pp. 137–147, Dec. 2018.

[174] H. Tran and H. Inoue, “Further development and experimental verification of wavelet deconvolution technique for impact force reconstruction,” *Mechanical Systems and Signal Processing*, vol. 148, p. 107165, Feb. 2021.

[175] H. Tran and T.-H. Le, “Wavelet deconvolution technique for impact force reconstruction: mutual deconvolution approach,” *VNUHCM Journal of Engineering and Technology*, vol. 3, no. SI2, pp. SI60–SI68, 2020.

[176] J. F. Doyle, “A wavelet deconvolution method for impact force identification,” *Experimental Mechanics*, vol. 37, pp. 403–408, Dec. 1997.

[177] Z. Li, Z. Feng, and F. Chu, “A load identification method based on wavelet multi-resolution analysis,” *Journal of Sound and Vibration*, vol. 333, pp. 381–391, Jan. 2014.

[178] P. C. Hansen, *Discrete Inverse Problems.* Fundamentals of Algorithms, Society for Industrial and Applied Mathematics, Jan. 2010.

[179] D. Ge, X. Jiang, and Y. Ye, “A note on the complexity of L p minimization,” *Mathematical Programming*, vol. 129, pp. 285–299, Oct. 2011.

[180] C. C. Paige and M. A. Saunders, “LSQR: An Algorithm for Sparse Linear Equations and Sparse Least Squares,” *ACM Transactions on Mathematical Software*, vol. 8, pp. 43–71, Mar. 1982.

[181] T.-L. Teng, C.-C. Liang, and C.-C. Liao, “Transient Dynamic Large-Deflection Analysis of Panel Structure under Blast Loading,” *JSME international journal. Ser. A, Mechanics and material engineering*, vol. 39, no. 4, pp. 591–597, 1996.

[182] S.-J. Kim, K. Koh, M. Lustig, S. Boyd, and D. Gorinevsky, "An Interior-Point Method for Large-Scale L1-Regularized Least Squares," *IEEE Journal of Selected Topics in Signal Processing*, vol. 1, pp. 606–617, Dec. 2007.

[183] J. Park, S. Ha, and F.-K. Chang, "Monitoring Impact Events Using a System-Identification Method," *AIAA Journal*, vol. 47, no. 9, pp. 2011–2021, 2009.

[184] L. Xu, Y. Wang, Y. Cai, Z. Wu, and W. Peng, "Determination of impact events on a plate-like composite structure," *The Aeronautical Journal*, vol. 120, pp. 984–1004, June 2016.

[185] S. E. C. S. S, "Structural materials handbook-Part 1: Overview and material properties and applications," Tech. Rep. ECSS-E-HB-32-20 Part 1A, Requirements and Standards Division, European Space Agency., 2011.

[186] P. D. Soden, M. J. Hinton, and A. S. Kaddour, "Lamina properties, lay-up configurations and loading conditions for a range of fibre reinforced composite laminates," in *Failure Criteria in Fibre-Reinforced-Polymer Composites* (M. J. Hinton, A. S. Kaddour, and P. D. Soden, eds.), pp. 30–51, Oxford: Elsevier, Jan. 2004.

[187] A. Trauth, D. Bücheler, F. Henning, and K. A. Weidenmann, "Mechanical properties of unidirectional continuous carbon fiber reinforced sheet molding compounds," 2016.

[188] A. S. Sayyad and Y. M. Ghugal, "On the free vibration analysis of laminated composite and sandwich plates: A review of recent literature with some numerical results," *Composite Structures*, vol. 129, pp. 177–201, Oct. 2015.

[189] P. Moreno-García, J. V. A. dos Santos, and H. Lopes, "A Review and Study on Ritz Method Admissible Functions with Emphasis on Buckling and Free Vibration of Isotropic and Anisotropic Beams and Plates," *Archives of Computational Methods in Engineering*, vol. 25, pp. 785–815, July 2018.

[190] Z. Ni, D. Li, L. Ji, and K. Zhou, "Aeroelastic modeling and analysis of honeycomb plates in high-speed airflow with acoustic load and general boundary conditions," *Composite Structures*, vol. 305, p. 116504, Feb. 2023.

[191] B. Qiao, C. Ao, Z. Mao, and X. Chen, "Non-convex sparse regularization for impact force identification," *Journal of Sound and Vibration*, vol. 477, p. 115311, July 2020.

Appendices

Appendix A

Equations of Motion in terms of Displacements for Angle-ply Laminates based on FSDT

The differential operator $\mathcal{L}$ for angle-ply laminates based on the First-order Shear Deformation Theory (FSDT), as expressed in Eq. (2.19), is a 5 by 5 symmetric matrix with upper triangular elements:

$$
\begin{aligned}
&\mathcal{L}_{11} = A_{11}\frac{\partial^2}{\partial x^2} + 2A_{16}\frac{\partial^2}{\partial x \partial y} + A_{66}\frac{\partial^2}{\partial y^2} - I_1\frac{\partial^2}{\partial t^2},\ \mathcal{L}_{12} = A_{16}\frac{\partial^2}{\partial x^2} + (A_{12}+A_{66})\frac{\partial^2}{\partial x \partial y} + A_{26}\frac{\partial^2}{\partial y^2},\\
&\mathcal{L}_{14} = B_{11}\frac{\partial^2}{\partial x^2} + 2B_{16}\frac{\partial^2}{\partial x \partial y} + B_{66}\frac{\partial^2}{\partial y^2} - I_2\frac{\partial^2}{\partial t^2},\ \mathcal{L}_{15} = B_{16}\frac{\partial^2}{\partial x^2} + (B_{12}+B_{66})\frac{\partial^2}{\partial x \partial y} + B_{26}\frac{\partial^2}{\partial y^2},\\
&\mathcal{L}_{22} = A_{66}\frac{\partial^2}{\partial x^2} + 2A_{26}\frac{\partial^2}{\partial x \partial y} + A_{22}\frac{\partial^2}{\partial y^2} - I_1\frac{\partial^2}{\partial t^2},\ \mathcal{L}_{24} = B_{16}\frac{\partial^2}{\partial x^2} + (B_{12}+B_{66})\frac{\partial^2}{\partial x \partial y} + B_{26}\frac{\partial^2}{\partial y^2},\\
&\mathcal{L}_{25} = B_{66}\frac{\partial^2}{\partial x^2} + 2B_{26}\frac{\partial^2}{\partial x \partial y} + B_{22}\frac{\partial^2}{\partial y^2} - I_2\frac{\partial^2}{\partial t^2},\ \mathcal{L}_{33} = (A_{55}\frac{\partial^2}{\partial x^2} + 2A_{45}\frac{\partial^2}{\partial x \partial y} + A_{44}\frac{\partial^2}{\partial y^2}) - I_1\frac{\partial^2}{\partial t^2},\\
&\mathcal{L}_{34} = A_{55}\frac{\partial}{\partial x} + A_{45}\frac{\partial}{\partial y},\ \mathcal{L}_{35} = A_{45}\frac{\partial}{\partial x} + A_{44}\frac{\partial}{\partial y},\ \mathcal{L}_{44} = D_{11}\frac{\partial^2}{\partial x^2} + 2D_{16}\frac{\partial^2}{\partial x \partial y} + D_{66}\frac{\partial^2}{\partial y^2} - A_{55} - I_3\frac{\partial^2}{\partial t^2},\\
&\mathcal{L}_{45} = D_{16}\frac{\partial^2}{\partial x^2} + (D_{12}+D_{66})\frac{\partial^2}{\partial x \partial y} + D_{26}\frac{\partial^2}{\partial y^2} - A_{45},\ \mathcal{L}_{55} = D_{66}\frac{\partial^2}{\partial x^2} + 2D_{26}\frac{\partial^2}{\partial x \partial y} + D_{22}\frac{\partial^2}{\partial y^2} - A_{44} - I_3\frac{\partial^2}{\partial t^2}.
\end{aligned}
\tag{A.1}
$$

The symmetry of $\mathcal{L}$ ensures that $\mathcal{L}_{ij} = \mathcal{L}_{ji}$, with zero elements at $\mathcal{L}_{13}$, and $\mathcal{L}_{23}$. The in-plane and out-of-plane motions are coupled through the nonzero extensional-bending stiffness $\boldsymbol{B}$.

Appendix B

Equations of Motion in terms of Displacements for Angle-ply Laminates based on CPT

The differential operator $\mathcal{L}$ for angle-ply laminates based on the Classical Plate Theory (CPT), as expressed in Eq. (2.22), is a 3 by 3 symmetric matrix with upper triangular elements:

$$
\begin{aligned}
\mathcal{L}_{11} &= A_{11}\frac{\partial^2}{\partial x^2} + 2A_{16}\frac{\partial^2}{\partial x \partial y} + A_{66}\frac{\partial^2}{\partial y^2} - I_1\frac{\partial^2}{\partial t^2}, \\
\mathcal{L}_{12} &= A_{16}\frac{\partial^2}{\partial x^2} + (A_{12} + A_{66})\frac{\partial^2}{\partial x \partial y} + A_{26}\frac{\partial^2}{\partial y^2}, \\
\mathcal{L}_{13} &= -\left[B_{11}\frac{\partial^3}{\partial x^3} + 3B_{16}\frac{\partial^3}{\partial x^2 \partial y} + (B_{12} + 2B_{66})\frac{\partial^3}{\partial x \partial y^2} + B_{26}\frac{\partial^3}{\partial y^3}\right] + I_2\frac{\partial^3}{\partial x \partial t^2}, \\
\mathcal{L}_{22} &= A_{66}\frac{\partial^2}{\partial x^2} + 2A_{26}\frac{\partial^2}{\partial x \partial y} + A_{22}\frac{\partial^2}{\partial y^2} - I_1\frac{\partial^2}{\partial t^2}, \\
\mathcal{L}_{23} &= -\left[B_{16}\frac{\partial^3}{\partial x^3} + (B_{12} + 2B_{66})\frac{\partial^3}{\partial x^2 \partial y} + (3B_{26})\frac{\partial^3}{\partial x \partial y^2} + B_{22}\frac{\partial^3}{\partial y^3}\right] + I_2\frac{\partial^3}{\partial y \partial t^2}, \\
\mathcal{L}_{33} &= D_{11}\frac{\partial^4}{\partial x^4} + 4D_{16}\frac{\partial^4}{\partial x^3 \partial y} + 2(D_{12} + 2D_{66})\frac{\partial^4}{\partial x^2 \partial y^2} + 4D_{26}\frac{\partial^4}{\partial x \partial y^3} + D_{22}\frac{\partial^4}{\partial y^4} + I_1\frac{\partial^2}{\partial t^2}.
\end{aligned}
\tag{B.1}
$$

The symmetry of $\mathcal{L}$ ensures that $\mathcal{L}_{ij} = \mathcal{L}_{ji}$.

Appendix C

Equations of Motion in terms of Displacements for Symmetrical Laminates Using FSDT

In a symmetrically laminated plate, the bending-extensional coupling stiffness $\boldsymbol{B}$ and the coupling inertial I_2 vanish, resulting in a complete decoupling of in-plane and out-of-plane motions [87]. The equations of motion for symmetric laminates under First-order Shear Deformation Theory (FSDT) are obtained by setting $\boldsymbol{B} = 0$ and $I_2 = 0$ in Eq. (A.1):

$$
\begin{aligned}
&\mathcal{L}_{11} = A_{11}\frac{\partial^2}{\partial x^2} + 2A_{16}\frac{\partial^2}{\partial x \partial y} + A_{66}\frac{\partial^2}{\partial y^2} - I_1\frac{\partial^2}{\partial t^2},\ \mathcal{L}_{12} = A_{16}\frac{\partial^2}{\partial x^2} + (A_{12} + A_{66})\frac{\partial^2}{\partial x \partial y} + A_{26}\frac{\partial^2}{\partial y^2},\\
&\mathcal{L}_{22} = A_{66}\frac{\partial^2}{\partial x^2} + 2A_{26}\frac{\partial^2}{\partial x \partial y} + A_{22}\frac{\partial^2}{\partial y^2} - I_1\frac{\partial^2}{\partial t^2},\ \mathcal{L}_{33} = (A_{55}\frac{\partial^2}{\partial x^2} + 2A_{45}\frac{\partial^2}{\partial x \partial y} + A_{44}\frac{\partial^2}{\partial y^2}) - I_1\frac{\partial^2}{\partial t^2},\\
&\mathcal{L}_{34} = A_{55}\frac{\partial}{\partial x} + A_{45}\frac{\partial}{\partial y},\ \mathcal{L}_{44} = D_{11}\frac{\partial^2}{\partial x^2} + 2D_{16}\frac{\partial^2}{\partial x \partial y} + D_{66}\frac{\partial^2}{\partial y^2} - A_{55} - I_3\frac{\partial^2}{\partial t^2},\\
&\mathcal{L}_{35} = A_{45}\frac{\partial}{\partial x} + A_{44}\frac{\partial}{\partial y},\ \mathcal{L}_{45} = D_{16}\frac{\partial^2}{\partial x^2} + (D_{12} + D_{66})\frac{\partial^2}{\partial x \partial y} + D_{26}\frac{\partial^2}{\partial y^2} - A_{45},\\
&\mathcal{L}_{55} = D_{66}\frac{\partial^2}{\partial x^2} + 2D_{26}\frac{\partial^2}{\partial x \partial y} + D_{22}\frac{\partial^2}{\partial y^2} - A_{44} - I_3\frac{\partial^2}{\partial t^2},\\
&\mathcal{L}_{13} = 0,\ \mathcal{L}_{14} = 0,\ \mathcal{L}_{15} = 0,\ \mathcal{L}_{23} = 0,\ \mathcal{L}_{24} = 0,\ \mathcal{L}_{25} = 0.
\end{aligned}
\tag{C.1}
$$

This decoupling is reflected in the governing equations, where $\mathcal{L}_{1j} = \mathcal{L}_{2j} = \mathcal{L}_{j1} = \mathcal{L}_{j2} = 0$ for $j = 3, 4, 5$, ensuring independent in-plane and out-of-plane dynamics.

Appendix D

Equations of Motion in terms of Displacements for Symmetrical Laminates Using CPT

The equations of motion for symmetric laminates under Classical Plate Theory (CPT) are obtained by setting $\boldsymbol{B} = 0$ and $I_2 = 0$ in Eq. (B.1):

$$
\begin{aligned}
\mathcal{L}_{11} &= A_{11}\frac{\partial^2}{\partial x^2} + 2A_{16}\frac{\partial^2}{\partial x \partial y} + A_{66}\frac{\partial^2}{\partial y^2} - I_1\frac{\partial^2}{\partial t^2},\\
\mathcal{L}_{12} &= A_{16}\frac{\partial^2}{\partial x^2} + (A_{12} + A_{66})\frac{\partial^2}{\partial x \partial y} + A_{26}\frac{\partial^2}{\partial y^2},\\
\mathcal{L}_{22} &= A_{66}\frac{\partial^2}{\partial x^2} + 2A_{26}\frac{\partial^2}{\partial x \partial y} + A_{22}\frac{\partial^2}{\partial y^2} - I_1\frac{\partial^2}{\partial t^2},\\
\mathcal{L}_{33} &= D_{11}\frac{\partial^4}{\partial x^4} + 4D_{16}\frac{\partial^4}{\partial x^3 \partial y} + 2(D_{12} + 2D_{66})\frac{\partial^4}{\partial x^2 \partial y^2} + 4D_{26}\frac{\partial^4}{\partial x \partial y^3} + D_{22}\frac{\partial^4}{\partial y^4} + I_1\frac{\partial^2}{\partial t^2},\\
\mathcal{L}_{13} &= 0, \mathcal{L}_{23} = 0.
\end{aligned}
\tag{D.1}
$$

The decoupling of in-plane and out-of-plane motions is reflected in the governing equation that $\mathcal{L}_{13} = \mathcal{L}_{23} = \mathcal{L}_{31} = \mathcal{L}_{32} = 0$.

Appendix E

Mass, Stiffness Matrix for Modal Analysis by Rayleigh-Ritz Variational Method

The mass matrix $\mathbf{M}$ for modal analysis using the Rayleigh–Ritz method for the symmetrically-laminated First-order Shear Deformation Theory (FSDT) plate, as defined in Eq. (7.10), can be obtained by simplification from angle-ply laminated FSDT plate given in [190]:

$$\mathbf{M} = \begin{bmatrix} \mathbf{M}_1 & 0 & 0 & 0 & 0 \\ 0 & \mathbf{M}_1 & 0 & 0 & 0 \\ 0 & 0 & \mathbf{M}_1 & 0 & 0 \\ 0 & 0 & 0 & \mathbf{M}_3 & 0 \\ 0 & 0 & 0 & 0 & \mathbf{M}_3 \end{bmatrix}, \tag{E.1}$$

where $\mathbf{M}_i = \int_\Omega I_i \mathbf{B}^\top \mathbf{B} d\Omega$, $\mathbf{B}$ is the row vector of basis functions, expressed in Eq. (7.9).

The detailed expression of the stiffness matrix $\mathbf{K}_p$ from plate structure is given by:

$$\mathbf{K}_p = \begin{bmatrix} \mathbf{K}_{11} & \mathbf{K}_{12} & 0 & 0 & 0 \\ \mathbf{K}_{12}^\top & \mathbf{K}_{22} & 0 & 0 & 0 \\ 0 & 0 & \mathbf{K}_{33} & \mathbf{K}_{34} & \mathbf{K}_{35} \\ 0 & 0 & \mathbf{K}_{34}^\top & \mathbf{K}_{44} & \mathbf{K}_{45} \\ 0 & 0 & \mathbf{K}_{35}^\top & \mathbf{K}_{45}^\top & \mathbf{K}_{55} \end{bmatrix}, \; \mathbf{K}_{ij} = \int_\Omega \left[\mathbf{B}^\top \; (\frac{\partial \mathbf{B}}{\partial x})^\top \; (\frac{\partial \mathbf{B}}{\partial y})^\top \right] \mathbf{C}_{ij} \begin{bmatrix} \mathbf{B} \\ \frac{\partial \mathbf{B}}{\partial x} \\ \frac{\partial \mathbf{B}}{\partial y} \end{bmatrix} d\Omega, \tag{E.2}$$

where $\mathbf{C}_{ij}$ are 3-by-3 matrix consisting of plate-level stiffness:

$$\begin{aligned} \mathbf{C}_{11} &= \begin{bmatrix} 0 & 0 & 0 \\ 0 & A_{11} & A_{16} \\ 0 & A_{16} & A_{66} \end{bmatrix}, \; \mathbf{C}_{12} = \begin{bmatrix} 0 & 0 & 0 \\ 0 & A_{16} & A_{12} \\ 0 & A_{66} & A_{26} \end{bmatrix}, \; \mathbf{C}_{22} = \begin{bmatrix} 0 & 0 & 0 \\ 0 & A_{66} & A_{26} \\ 0 & A_{26} & A_{22} \end{bmatrix}, \\ \mathbf{C}_{33} &= \begin{bmatrix} 0 & 0 & 0 \\ 0 & A_{55} & A_{45} \\ 0 & A_{45} & A_{44} \end{bmatrix}, \; \mathbf{C}_{34} = \begin{bmatrix} 0 & 0 & 0 \\ A_{55} & 0 & 0 \\ A_{45} & 0 & 0 \end{bmatrix}, \; \mathbf{C}_{35} = \begin{bmatrix} 0 & 0 & 0 \\ A_{45} & 0 & 0 \\ A_{44} & 0 & 0 \end{bmatrix}, \\ \mathbf{C}_{44} &= \begin{bmatrix} A_{55} & 0 & 0 \\ 0 & D_{11} & D_{16} \\ 0 & D_{16} & D_{66} \end{bmatrix}, \; \mathbf{C}_{45} = \begin{bmatrix} A_{45} & 0 & 0 \\ 0 & D_{16} & D_{12} \\ 0 & D_{66} & D_{26} \end{bmatrix}, \; \mathbf{C}_{55} = \begin{bmatrix} A_{44} & 0 & 0 \\ 0 & D_{66} & D_{26} \\ 0 & D_{26} & D_{22} \end{bmatrix}. \end{aligned} \tag{E.3}$$

The detailed expression of the stiffness matrix $\mathbf{K}_b$ from boundary conditions is given by:

$$\mathbf{M}_b = \int_\Gamma \mathbf{B}^\top \operatorname{diag}(k_t^u \mathbf{I}, k_t^v \mathbf{I}, k_t^w \mathbf{I}, k_r^x \mathbf{I}, k_r^y \mathbf{I}) \mathbf{B} d\Gamma, \tag{E.4}$$

where $[k_t^u, k_t^v, k_t^w, k_r^x, k_r^y]$ are three translational stiffness and two rotational stiffness of the artificial springs and acting on boundaries Γ, $\mathbf{I}$ is the identity matrix with the size of the number of basis functions in $\mathbf{B}$.